Actinide surface chemistry

Alexander James Bishop

ProQuest LLC
789 East Eisenhower Parkway
P.O. Box 1346
Ann Arbor, MI 48106-1346

DECLARATION

This work has not previously been accepted in substance for any degree and is not concurrently submitted in candidature for any degree.

Signed ..... (candidate) Date 23/2/11

STATEMENT 1

This thesis is being submitted in partial fulfillment of the requirements for the degree of PhD

Signed ..... (candidate) Date 23/2/11

STATEMENT 2

This thesis is the result of my own independent work/investigation, except where otherwise stated. Other sources are acknowledged by explicit references.

Signed ..... (candidate) Date 23/2/11

STATEMENT 3

I hereby give consent for my thesis, if accepted, to be available for photocopying and for inter-library loan, and for the title and summary to be made available to outside organisations.

Signed ..... (candidate) Date 23/2/11

Abstract

The surface reactivity of thorium and uranium, and how this links to the 5f electrons, has been investigated under UHV conditions using x-ray photoelectron spectroscopy (XPS), ultra violet photoelectron spectroscopy (UPS), and inverse photoemission spectroscopy (IPES). Water and ammonia adsorption on a polycrystalline thorium surface has been investigated at 100 and 298 K. Water adsorbs and dissociates upon the surface, leading to the formation of oxide and hydroxide species at 298 K, and oxide, hydroxide, and physisorbed water at 100 K. The surfaces after adsorption at both temperatures proved to be unstable when exposed to the low energy electron gun utilised in IPES. Ammonia adsorbs and dissociates upon the surface, leading to the formation of nitride and NH_2 species at 298 K, and nitride, NH_2, and physisorbed ammonia at 100 K. Upon reaction only the mononitride ThN is formed, the metallic nature of which was confirmed by UPS and IPES. The surface was unstable under the low energy electron gun utilised in IPES, with the ThN species being converted to the non-metallic Th_3N_4. Water and ammonia adsorption on a polycrystalline uranium surface has also been investigated at 100 and 298 K. Water adsorbs and dissociates upon the surface, leading to the formation of oxide and hydroxide species at 298 K, and oxide, hydroxide, and physisorbed water at 100 K. The rate of reaction of water with uranium is substantially reduced in the presence of residual oxygen on the surface. The small band-gap of semi-conducting UO_2 can be observed directly with UPS and IPES. Ammonia adsorbs and dissociates upon the surface, leading to the formation of nitride and NH_2 species at 100 and 298 K. The reaction at 100 K was electronically hindered by a combination of residual oxygen contamination on the surface, and the phenomenon of "band banding", which together resulted in the coverage being 16 % of that seen at 298 K. The surface was stable under the low energy electron gun, retaining the metallic nature that was confirmed with UPS and IPES.

Acknowledgments

Well, it's taken a long four years to get to this point, but I wouldn't have made it at all if it wasn't for the help and support of a lot of people:

The first person to thank is Dr. Albert Carley, both for selecting me to undertake this Ph.D, and for your guiding supervision during the time of my studies. Your academic support and remarkable depth of technical knowledge has proven vital during the past four years.

This thesis wouldn't have been possible without the invaluable input of Dr Paul Roussel. I will forever be truly grateful for the huge amount of time and effort you spent on me. Your remarkable knowledge, enthusiasm, and ingenuity have both astounded and inspired me in equal measures.

I would like to thank the AWE for their financial support, and Cardiff University for providing wonderful facilities, and for offering me the opportunity to undertake this project.

The last four years would have been an awful lot more difficult (and certainly duller) if it weren't for the "crew". While there were many members, it's Kareem, Jon, Lee, and Theo who all deserve special thanks for their efforts to keep me sane during our time together. The competitive nature of our little group, and the jokes that this competition led to, inspired me to work hard, fix the "old girl", and get the results I needed. Extra special thanks are reserved for Dave, who had to put up with an incessant stream of questions from me. Dave, your technical skills are without equal, and my time working with you has been truly enlightening.

My final thanks must go to those closest to me. My parents, Andrew and Janet, for your support during my eight years in Cardiff. There have been many ups and downs, but your consistent encouragement has remained one of the few stable things in my life. And finally, Sara, your presence in my life gave me the drive and energy I needed to ultimately finish the writing process. Without your love, persistence, and belief in me I seriously doubt I'd have ever managed to get this far, and for that I will forever be grateful.

Contents

Chapter 1 – Introduction: The actinides and their surface chemistry

1.1 The actinide series

1.1.1 Introduction

The actinides, a series of elements located separately from the main periodic table, have fascinated mankind for many years. From their unusual properties and chemistry, through to their key uses in the nuclear power and weapon industries, the actinides have risen in importance, particularly during the last 60 years, with much research being carried out upon them. However, the elements that make up the actinide series are still some of the least understood of all the periodic table, with much research still needing to be done [1].

In comparison to the rest of the periodic table, the actinide series has not been known for all that long. The earliest found actinides, thorium and uranium, were initially thought to be transition metals and were positioned accordingly in groups 4 and 6 respectively. However the work carried out by G. T. Seaborg in the 1940's into the transuranium elements led to their reclassification [2]. Seaborg proposed in 1944 that the actinides form a transition series analogous to the rare earth series of the lanthanide elements, and as such would contain all the elements of atomic numbers 90 through to 103. The final position of the actinide series and its component elements can be seen in figure 1.1.

At the time of their establishment as a separate series within the periodic table, the actinides were not well understood, with many of them not having been isolated and identified. But since that time the possibilities of nuclear fission, and the vast energy that it can release, have pushed the series to the forefront of chemistry and physics, and led to a variety of interesting and important research being carried out under the banner of "actinide science". This section will detail the important properties and traits of the actinide elements that both inspire and hinder the research and study carried out upon them.

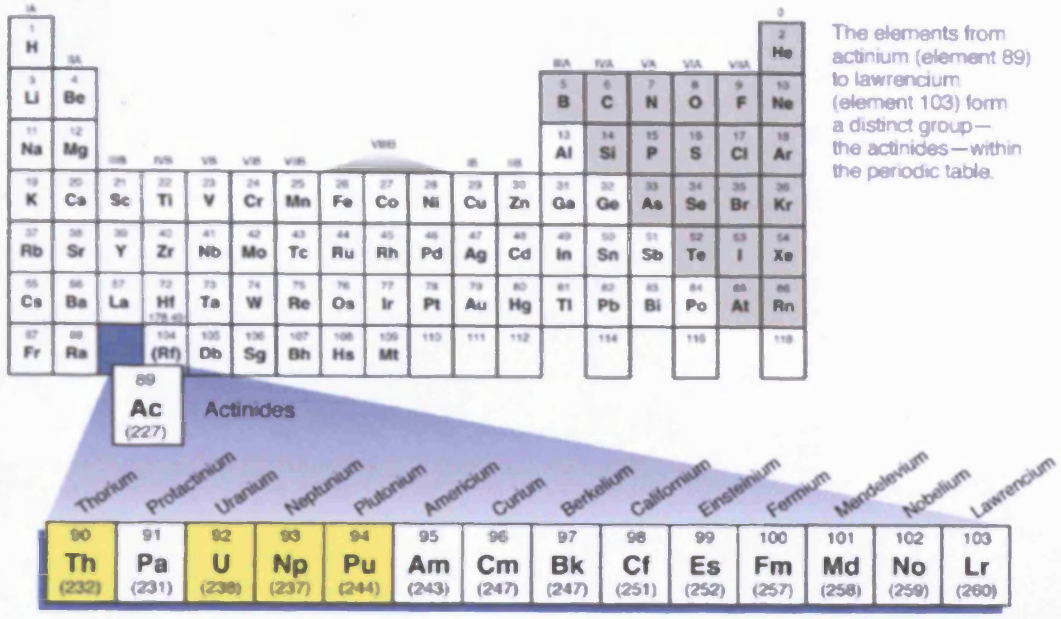

Figure 1.1: The actinide series and its position in the periodic table [3]

1.1.2. Abundance

The actinide series, the second row of the f-block series after the lanthanides, is made up of 14 radioactive elements; however only five of them occur naturally. Thorium, protactinium, uranium, neptunium, and plutonium have all been found in nature, although only thorium and uranium are found in sufficiently large enough quantities to make their refining viable. Protactinium, neptunium, and plutonium have only been found in very small quantities formed through the neutron capture and decay processes associated with radioactive uranium, and not in large enough quantities to make refining a viable method of acquiring them. The remaining actinide elements are considered man-made, and have been generated, along with protactinium, neptunium, and plutonium, through a variety of bombardment processes. The elements were originally formed, inside either nuclear reactors or particle accelerators, *via* means of successive neutron capture followed by radioactive decay [4]. Neutron bombardment can result in a heavy atom capturing a neutron (releasing gamma radiation in the process), which then undergoes radioactive decay, due to its newly unstable state, emitting a β^- particle, the loss of which produces a new atom with an increase in atomic number of one (see equation 1.1).

$$^{238}U + ^{1}n \rightarrow ^{239}U \rightarrow ^{239}Np + \beta^{-}$$ Equation 1.1 [4]

Through the capture of successive neutrons access to multiple actinide elements is possible. Unfortunately as the number of successive captures increases the potential yield dramatically decreases as well, as the process is a slow one. For example, if you began with 1 kg of ^{239}Pu, and subjected it to a neutron flux of 3 x 10^{14} neutrons $cm^{-2}s^{-1}$ (an experimentally feasible value), only 1 mg of ^{252}Cf would be obtained after 5-10 years [4]. An alternative method that can be used involves heavy-ion bombardment, where particles such as ^{11}B, ^{12}C, and ^{16}O are used instead of neutrons; however this suffers from the disadvantage of only being applicable to one atom at a time, so cannot be used to produce significant quantities [4].

The lack of abundance and difficulty in accumulating significant quantities of the vast majority of the elements is one of the most serious and specific difficulties associated with actinide research.

1.1.3 Radioactivity

As mentioned above, all the elements that make up the actinide series are radioactive, and as such their isotopes have limited-lives. The radioactivity varies dramatically across the period, with a general trend being that it increases, and the half-lives decrease, as the period is traversed from left to right. Table 1.1 features a list of the longest lived isotopes for each of the elements, combined with the means by which they decay.

The radioactivity is another of the most challenging aspects that have to be managed when studying the actinide elements. However, the careful use of specialist handling techniques and facilities can sufficiently minimise the risks, allowing the safe study of the interesting properties and characteristics of the elements that make up the series.

	Mass	Half-life	Means of decay
Thorium	232	1.14×10^{10} years	α
Protactinium	231	3.28×10^{4} years	α
Uranium	238	4.47×10^{9} years	α
Neptunium	237	2.14×10^{6} years	α
Plutonium	244	8.26×10^{7} years	α
Americium	243	7380 years	α
Curium	247	1.56×10^{7} years	α
Berkelium	247	1380 years	α
Californium	251	898 years	α
Einsteinium	252	472 days	α
Fermium	257	100.4 days	α
Mendelevium	258	55 days	α
Nobelium	259	1 hour	α
Lawrencium	260	3 minutes	α

Table 1.1: The longest lived isotopes of the actinide elements [4]

1.1.4 Uses

A number of uses have been found for the actinide elements since their discoveries, ranging from the trivial through to the vitally important. Thorium, often in the form of thorium dioxide (thoria) has been used considerably in industry. Thorium, when applied to the surface of tungsten filaments leads to an increase in electron emission at lower temperatures, which has led to its use in the electronics and lighting industries. Thoria itself has one of the highest melting points of any oxide (>3600 K), which has led to its use in welding electrodes and heat resistant ceramics. Thoria has also been added to glass to increase the refractive index, necessary for the manufacture of high quality lenses for cameras and scientific instruments [5]. Americium, in the form of the dioxide, is found within many smoke detectors where it is used as a source of ionising radiation. Curium is a strong alpha emitter, and as such has been used as the source in alpha particle x-ray spectrometers which are used in the field of space exploration. Plutonium has found use as a power source in early pacemakers, and as a radioisotope heat source in the field of space exploration [6]. Uranium compounds have been utilised as stains and dyes in the ceramic industry, as toner in the photographic industry, and as a contrasting agent for biological specimens [7]. However all of these examples are dwarfed in scale by the single most important use

of the actinides; the generation of energy through nuclear fission for both civilian and military purposes.

1.1.5 Ground state electronic structure

The actinide series has garnered much of its interest due to the unusual and striking properties of the elements that are the result of their electronic structures. The actinides, along with the lanthanides, are the only elements in the periodic table that possess valence f electrons, and it is the filling of this set of orbitals that has been of greatest interest. Table 1.2 provides a list of the ground state gas phase electronic configurations of both the lanthanides and actinides, detailing the specific way in which the valence f orbitals fill for the elements of both series. It can be seen that the filling of the 5f orbitals is not as regular as that seen for the 4f orbitals, with the lack of any f electrons in thorium of particular note. The reason for the unusual and irregular way in which the 5f orbitals of the actinide series fill, as you progress across the period, is down to their relative position with respect to the 6d orbitals. For the early members of the actinide series the 6d orbitals are located at a lower energy than those of the 5f, and as such become partially filled. It is only then that the additional electrons begin to enter the 5f levels. The addition of electrons to the 5f shell results in its relative energy decreasing with respect to others such as the 6d. As it moves to lower energy it becomes preferably filled over that of the 6d, and as such the 6d states become completely empty. It is for this reason that the 6d orbitals, while partially filled at the start of the actinide series, gradually become completely vacant upon moving through the period as the total number of electrons increases. This is all in complete contrast to the lanthanide series, where the 4f orbitals are always at a considerably lower energy level than those of the 5d, and are thus occupied first, and continue to be filled in a more regular manner as the period is traversed.

The unusual orders in which the orbitals of the actinide series fill up, and the reasoning behind it, are both a symptom and a cause of the unusual reactivity and behaviour of the actinide elements, particularly when compared to those of the lanthanide series, which also contain valence f electrons. This concept will be explored in the next section.

Lanthanides: [Xe] core			Actinides: [Rn] core		
	Atomic No.	Ground state		Atomic No.	Ground state
Cerium	58	$4f^{1}5d^{1}6s^{2}$	Thorium	90	$6d^{2}7s^{2}$
Praseodymium	59	$4f^{3}6s^{2}$	Protactinium	91	$5f^{2}6d^{1}7s^{2}$
Neodymium	60	$4f^{4}6s^{2}$	Uranium	92	$5f^{3}6d^{1}7s^{2}$
Promethium	61	$4f^{5}6s^{2}$	Neptunium	93	$5f^{4}6d^{1}7s^{2}$
Samarium	62	$4f^{6}6s^{2}$	Plutonium	94	$5f^{6}7s^{2}$
Europium	63	$4f^{7}6s^{2}$	Americium	95	$5f^{7}7s^{2}$
Gadolinium	64	$4f^{7}5d^{1}6s^{2}$	Curium	96	$5f^{7}6d^{1}7s^{2}$
Terbium	65	$4f^{9}6s^{2}$	Berkelium	97	$5f^{9}7s^{2}$
Dysprosium	66	$4f^{10}6s^{2}$	Californium	98	$5f^{10}7s^{2}$
Holmium	67	$4f^{11}6s^{2}$	Einsteinium	99	$5f^{11}7s^{2}$
Erbium	68	$4f^{12}6s^{2}$	Fermium	100	$5f^{12}7s^{2}$
Thulium	69	$4f^{13}6s^{2}$	Mendelevium	101	$5f^{13}7s^{2}$
Ytterbium	70	$4f^{14}6s^{2}$	Nobelium	102	$5f^{14}7s^{2}$
Lutetium	71	$4f^{14}5d^{1}6s^{2}$	Lawrencium	103	$5f^{14}7s^{2}7p^{1}$

Table 1.2: Ground state electronic configuration of the lanthanide and actinide elements [8]

1.1.6 The f-orbitals and oxidation states

To fully understand the attraction of the actinides and their unusual properties it is first necessary to consider the other elemental series in the f-block – the lanthanides. For the lanthanides, the chemical and physical differences between adjacent elements in the series are very small. Chemically, the elements all behave in a relatively homogenous fashion, especially when in aqueous solution. Table 1.3 lists the most common oxidation states seen for the elements of the lanthanide series. It can be seen that the trivalent ion is the most commonly formed by all the elements, with there being only very occasional occurrences of divalent or tetravalent ions. In addition to the homogenous nature seen with the oxidation states, the lanthanides all tend to form largely identical compounds, where the specific element bound has little to no effect upon the properties of the compound.

The lack of variation in the oxidation state and the similarity in bonding characteristics are both due to the location of the 4f valence orbitals (the shapes of which can be seen in figure 1.2). These orbitals are characterised by their small radial extension as they are bound tightly to the nucleus, and as such are located lower in

energy, with respect to the Fermi level, than the spatially more extended 6s and 5d levels. The 4f electrons are sufficiently constrained to be considered localised and non-interacting, and as such are incapable of participating in chemical bond formation. It is because of this that the 4f electrons have essentially no effect upon the properties of the lanthanides, and why all the different elements of the series, defined by the total number of 4f electrons they contain, behave in such a similar fashion [8]

Ce	Pr	Nd	Pm	Sm	Eu	Gd	Tb	Dy	Ho	Er	Tm	Yb	Lu
				(2)	2						(2)	2	(2)
3	**3**	**3**	**3**	**3**	**3**	**3**	**3**	**3**	**3**	**3**	**3**	**3**	**3**
4	(4)	(4)					(4)	(4)					

Table 1.3: The oxidation states exhibited by the lanthanides. Numbers in bold signify the most common while numbers in brackets signify uncommon or uncertain states [8]

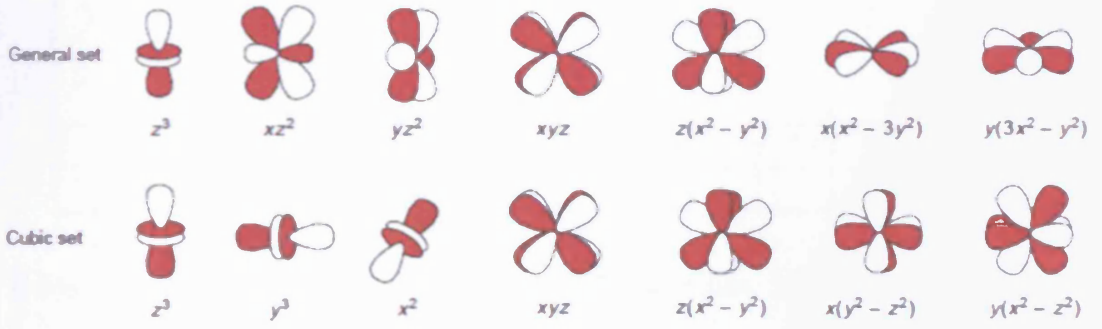

Figure 1.2: The shapes of the seven f orbitals, in both general and cubic form [9]

Because the valence electrons are the ones that ultimately dictate chemical behaviour, it could be expected that the actinides would be chemically similar to the lanthanides, which also have f electrons in their valence shell. However, as was hinted at before when considering the ground electronic states of the actinides, the properties of the actinides, and the 5f valence orbitals, differ significantly from those of the lanthanides, and the 4f orbitals. The first example of this can be seen in table 1.4, which details the oxidation states observed to exist for the elements. While trivalent ions are still formed by all the elements, a great number of other oxidations states are also observed, especially for the "light" actinides (thorium through to plutonium). In

addition, when looking at the most commonly observed states, the steadily increasing then decreasing values seen for the light actinides are extremely similar in form to that observed for the transition metals. The reason for the wide variety of oxidation states is that compared to the 4f orbitals of the lanthanides, the 5f orbitals have a far greater radial extension, and as such are located at a comparable energy to those of the 6d. It is the core 4f electrons of the light actinides partially screening the nuclear charge that leads to the 5f orbitals being extended and delocalised. For the light actinides the energies of the 5f and 6d orbitals are so close that the electrons find it relatively easy to switch between the two configurations. It is this ability to fill the d orbitals that leads the light actinides to display so many traits reminiscent of the transition elements, whose properties are also based upon the filling of d orbitals. In addition to the large variety of oxidation states, the light actinides also display a greater chemical variety, which is also in keeping with the transition elements.

Th	Pa	U	Np	Pu	Am	Cm	Bk	Cf	Es	Fm	Md	No	Lr
					(2)			(2)	(2)	2	2	**2**	
3	3	3	3	3	**3**	**3**	**3**	**3**	**3**	**3**	**3**	3	**3**
4	4	4	4	**4**	4	4	4	(4)	(4)				
	5	5	**5**	5	5	(5)							
		6	6	6	6	(6)							
			7	7	(7)	(7)							

Table 1.4: The oxidation states exhibited by the actinides. Numbers in bold signify the most common while numbers in brackets signify uncommon or uncertain states [8,10]

The contrast seen between the oxidation states of the light actinides and those of the "heavy" actinides (curium through to lawrencium), is one of a number of ways in which the behaviour of the two halves of the actinide series differ. While the light actinide elements are known to form a wide variety of different compounds, with the properties of otherwise identical compounds varying significantly between elements (in a manner similar to the transition elements), the heavy actinides all behave in a largely similar fashion. The lack of variation in the chemical and physical properties of the heavy actinide elements is reminiscent of that seen for the lanthanides, with the explanation for the behaviour of both being largely the same. As with the lanthanides,

the reason the heavy actinides all behave chemically very similarly is that the 5f orbitals are effectively non-bonding. The delocalised 5f system of the early actinides is affected by a dramatic actinide contraction, where an increase in the nuclear charge across the actinide series causes the atomic radii to contract, resulting in the 5f states gradually being pulled in closer to the atomic core. This slight contraction pulls the 5f electrons closer into the core, so that from americium/curium onwards they become localised, and no longer participate in any chemical bonding. It is because of this localised nature of the 5f electrons in the heavy actinides that the elements all behave largely identically, and in a similar fashion to the lanthanides [9-11].

1.2 Actinide surface science and the 5f electrons

The unique and unusual electronic properties of the actinides have led to there being a great quantity of research carried out in the hope of understanding them better [12-18]. As was explained above, it is the nature of the 5f valence electrons that is responsible for those same properties, and as such a large section of the published work has been focussed upon them [1,19-27]. Photoelectron spectroscopy has especially shown its value as a tool for the study of the 5f electrons, in particular the ability to determine the presence of band like or localised behaviour [21,23,28-31].

1.2.1 Actinide metal surfaces

Investigation of the actinides in their metal forms through photoemission spectroscopy has proved extremely useful for understanding the electronic interactions of the 5f band and others. However, owing to the high reactivity of the actinides, the generation of a clean surface for study is not a trivial thing, as has been shown by Allen and Wild [32], McLean *et al* [33], Winer *et al* [34], and Morrall *et al* [35]. The two principle methods involve either removing contaminants from an actinide sample through ion bombardment and annealing cycles, or preparing a new surface *in situ via* the sputtering of an actinide onto a supporting material [36].

The study of thorium metal has proven a useful tool for the investigation of the 5f electrons precisely because it is the only element of the series that lacks them entirely. By taking the results acquired with thorium as a "base-level" for the 6d7s electrons, it

has been possible to elucidate the actual bonding effects brought about through the presence of 5f valence electrons [15,23,37-41]. The valence band spectra, in both the occupied and unoccupied regions, have shown that the f states are almost entirely situated above the Fermi level, as expected based upon the ground state configuration of the metal [23,42]. Even though the 5f states are empty in the metal, their presence above the Fermi level still has an effect upon the 4f photoemission spectra. The positions of the main peaks are influenced by a screening effect of the 5f states, which become populated in the presence of a core hole [43,44]. The Th(4f) peaks that have been reported have shown pronounced peak asymmetry that is indicative of a delocalised actinide metal [41,43,45]. The asymmetry is the result of high density of states (DOS), particularly 5f states, at the Fermi level that cause significant low-energy losses by electrons scattered at the Fermi level into empty states [46,47]. The Th(4f) peaks also possess large satellites at 2.5 eV higher binding energy, that are the result of screening of the 4f hole by 6d electrons [38,41].

Compared to all the other actinides, uranium metal is by far the most understood, with large reviews by both Lander *et al* [48] and Fisher [49] testament to the quantity of research carried out upon the element. The great number of studies undertaken on uranium, and the knowledge they have uncovered, are due to its technological relevance, particularly when compared to other members of the actinide series. As a prime example of an actinide with delocalised 5f electrons capable of bonding, uranium has been compared to thorium in multiple studies in the hope of isolating their effect upon reactions, and any changes in stability or reactivity caused by them [15,23,37-41]. The valence band spectra for uranium show a narrow intense emission just below the Fermi edge in the occupied region, up to 2.5 eV wide, that is due in part to the delocalised 5f electrons [23,37,38,40,50-53]. The unoccupied region, studied by means of bremsstrahlung isochromat spectroscopy (BIS) and theoretical calculations, is noted for an intense signal at the Fermi edge indicative of the unoccupied 5f states and their itinerant character [23]. The U(4f) peaks reported have demonstrated the same asymmetric nature observed for Th(4f), but not the satellite due to screening effects [37,38,40,41,50].

With its six distinct allotropes, and the extreme changes in density (~20 %) associated with them, plutonium has proven to be the most complex of the actinides to

understand (see figure 1.3) [1,11,54,55]. The majority of the work has focused on the ground state monoclinic α and the high temperature fcc δ phases [1]. Plutonium is of particular interest for the study of the 5f electrons because of its unique position on the boundary between the actinides with localised or delocalised 5f electrons.

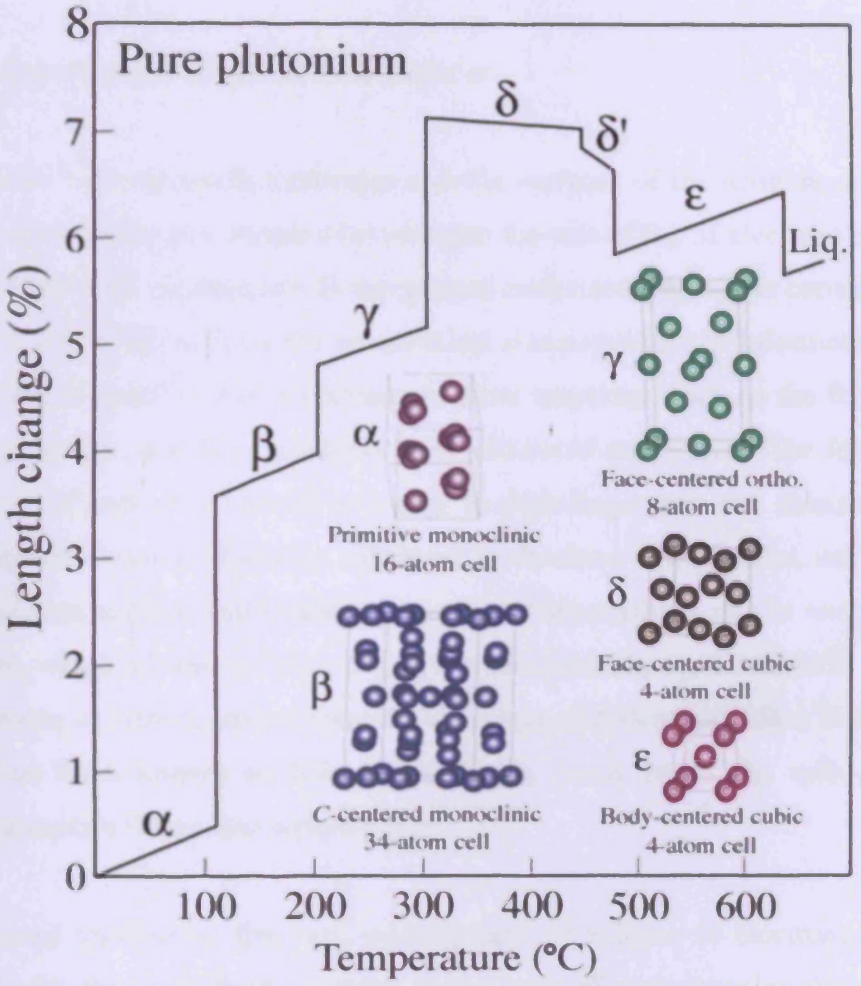

Figure 1.3: The atomic volume of plutonium as a function of temperature, featuring the 6 key allotropes and the liquid phase [1,11]

The valence bands of both the α and δ phases show a sharp feature at the Fermi edge with additional fine structure located at higher energy [21,30,36,56-60]. The fine structure is due to localisation of the 5f states, with the size and intensity observed being indicative of the extent of the localisation [1]. The fine structure reported for δ-plutonium is considerably larger than for α-plutonium, revealing that the 5f states in the higher temperature allotrope are more localised [1]. The Pu(4f) spectra reveal the same asymmetric peaks that are indicative of a fairly delocalised actinide metal

[29,30,35,36,56-64]. However the effects of the partial localisation of the 5f states can be seen in the form of poorly screened satellite peaks present on the high energy sides of the main peaks. As with the valence spectra, the satellites are larger for δ-plutonium, supporting the belief that its 5f states are more localised than those in α-plutonium [1,63,64]

1.2.2 Small molecules and the actinide surfaces

The reactions between small molecules and the surfaces of the actinide metals have been used extensively as a means to investigate the role of the 5f electrons in bonding [33,40,41,44,65-68]. In addition to the general understanding of the contributions of 5f electrons to the interactions, the research has also provided key information about a large number of specific and important chemical reactions, such as the formation of the actinide oxides, and their reactions with additional molecules. The formation of the oxides is of particular interest as owing to their large sizes and electropositivity, the light actinides that are found in nature are in the form of the oxides, and any clean metallic actinide surface will oxidise almost instantaneously in air. In contrast to the lanthanides, which all tend to form Ln_2O_3 sesquioxides, the light actinides, with their multiple stable oxidations states, form a wide range of different oxides. For example, uranium has been known to form: UO_2, U_4O_9, U_3O_8 and UO_3, with additional non-stoichiometric forms also reported [69].

As mentioned previously, thorium, with its lack of valence 5f electrons, has been compared with the other light actinides in the hope of understanding the effect that they have upon reactivity and bonding [15,23,37-41]. It is because of this that a significant amount of research has been carried out exploring and documenting the reactions between the surface of thorium and small molecules. The reactions that have earned most interest are those with oxygen and water [33,37,39-41,70,71]. McLean *et al* [33] studied the effect of exposure to O_2 and showed that upon reaction electrons transfer from the valence 6d7s orbitals to the 2p levels of the oxygen ions. Owing to the loss of intensity at the Fermi edge the Th(4f) peaks appear symmetrical. Analysis showed that exposure of a clean thorium surface in vacuum conditions to pure oxygen resulted in the formation of only the dioxide, and none of the sesquioxide [33,37]. Additional recent work has suggested that the formation of the oxide

following exposure to O_2 retards further oxidation *via* the hindrance of diffusion through the surface layer [72]. The reaction with water, studied by Nornes and Meisenheimer [40], has been shown to proceed rapidly, resulting in the formation of the dioxide with additional hydroxide components. Like the reaction with pure O_2, the reaction with H_2O has also been shown to form multiple layers of oxide upon the surface. It was also reported that the photoemission spectra from the reaction of water with thorium largely matched those of water with uranium, suggesting that the 5f valence electrons have little effect upon the reaction [40].

The reaction of thorium with CO and CO_2 was also studied by McLean *et al* [33]. They showed that both molecules dissociated upon the surface to form both the oxide and the carbide. The presence of both molecular CO and CO_2 was also confirmed in the C(1s) spectra. The C to O ratio observed upon exposure did not match that of the reagents, which was taken as evidence that free carbon from the dissociation upon the surface dissolved into the thorium bulk. This belief was then confirmed through depth profiling that showed its presence far further into the bulk than the oxygen that was also released in the dissociation [33].

The formation of the nitride of thorium has been studied by both Norton *et al* [41] and Gouder *et al* [44]. Both studies utilised N_2 as the reactant gas; however Gouder *et al* used a method whereby the N_2 gas was added to the argon stream used in the reactive sputtering process that is normally used to clean the surface. By varying the partial pressure of the N_2 with the argon it was possible to control whether ThN or Th_3N_4 was formed [44]. With the more conventional method that Norton *et al* used, whereby the clean surface was exposed to pure N_2 at 1200 K, only ThN was reported [41]. The valence and Th(4f) spectra of ThN, and the conclusions taken from them, varied considerably between the two studies. Norton *et al* reported a loss in intensity at the Fermi edge combined with symmetric 4f peaks, which would suggest a non-conducting or semi-conducting nature to the material [41]. These findings were disputed by Gouder *et al*, whose own photoemission spectra revealed a prominent signal at the Fermi level and asymmetric 4f peaks for ThN. Their spectra of Th_3N_4 however did match up with those acquired by Norton *et al*, which suggested that the higher oxidation state nitride had actually been formed in the previous study. In

conclusion Gouder *et al* reported that ThN is a metallic conductor while Th_3N_4, which has more ionic character, is non-metallic [44].

Uranium, as highlighted previously, has been studied to a greater extent than all other actinide elements because of its important technological relevance. Two reactions that have attracted particular interest are those of uranium with oxygen and uranium with water [32-34,38-41,51,52,73-81]. The interest is due to the corrosion reactions that occur on the surface of uranium involving the two reactants [76]. Uranium that is kept in nuclear storage facilities, potentially for decades at a time, can come into contact with the two reagents, and thus a great deal of research has been undertaken to understand the reactions from a safety viewpoint [77]. A big concern is that radiolytic processes will reduce adsorbed H_2O to H_2 and O_2, and the build-up of the two gases could lead to explosive conditions, which would be potentially catastrophic inside the closely packed storage infrastructure [77].

The reaction of clean uranium with O_2 has proven to be a complicated system, due both to the large number of oxide phases, and also the deviation from specific stoichiometry that has been reported to occur [69,82]. For example, high surface coverages have been reported to lead to the formation of stoichiometric UO_2 or hyperstoichiometric UO_{2+x} [51], while low coverages, due to low exposure to O_2, have been reported to lead to the formation of either substoichiometric UO_{2-x} or islands of stoichiometric UO_2 on the U metal [33]. In addition to the variations caused by general changes in exposure magnitude and surface coverage, the temperature at which the experiment is undertaken has also been shown to affect the oxides formed [40,41,52,83,84]. A study by Gouder *et al* [52] revealed that dissociative adsorption of O_2 on uranium at 73, 300, and 573 K leads to the formation of substoichiometric UO_{2-x}; however only at 73 K does the surface continue to oxidise, first to $UO_{2.0}$, and then to hyperstoichiometric UO_{2+x}. Photoemission spectroscopy has proven to be the ideal tool for the investigation of the uranium/oxygen system because of its ability to distinguish between the many different oxides. Allen *et al* [85] used the technique to study $UO_{2.0}$, $UO_{2.1}$, $UO_{2.2}$, U_4O_9, U_3O_7, U_3O_8, and γ-UO_3. They showed that the 4f signal increased in energy as the oxidation state of the uranium increased, with the variation significant enough for the technique to be used to successfully identify which oxide was formed. The

variations in the reported photoemission values for UO_2 seen in the literature can be explained by the fact that substoichiometric UO_{2-x} and hyperstoichiometric UO_{2+x} are so easily formed that it is extremely difficult to guarantee purely stoichiometric $UO_{2.0}$ is formed [33,38,51,85]. Studies of the valence band have also been undertaken to help with the understanding of the uranium/oxygen system. The oxidation of uranium results in a sharp intense peak at 1.4 eV above the Fermi level, which is a signal that is lacking from the valence band spectra of ThO_2 [86]. As U^{IV} has a $5f^2$ state and Th^{IV} a non-occupied $5f^0$ state, the signal was attributed to 5f electrons. The small gap from the signal to the Fermi edge is expected due to the fact that UO_2 is considered to be a semi-conductor [34,37,39,52]. Additional work looking at the unoccupied states above the Fermi level has also been undertaken, using both BIS [87] and inverse photoemission spectroscopy (IPES) [68,88]. The two techniques produced largely identical spectra for stoichiometric UO_2, with large signals centred at 5.1 eV above the Fermi level that were concluded to be due to the $5f^3$ final state. An additional smaller signal on the lower energy side of the peak, which was reported in two of the studies, has been attributed to the $6d^1$ final states [68,87]. Rousell *et al* [68] also reported the considerably less intense unoccupied orbital spectra of the mixed valency $UO_{2.2}$ species. They noted that the signal from the 5f states, now a combination of $5f^3$ and $5f^2$ final states, was located at 0.9 eV higher energy than that seen for UO_2, with the signal attributed to the 6d states now more pronounced and centred at 3.3 eV [68].

The reaction of clean uranium with water has been studied a number of times, at multiple temperatures, and with multiple techniques [34,40,73,75-80]. H_2O has been shown to dissociate upon the surface of uranium, forming both oxide and hydroxide species. The process forms H_2, which is lost to the gas phase, as a by-product of the oxide formation, and as such presents potential safety issues [34,76]. Like the reaction with pure O_2, the reaction with H_2O has also been shown to form multiple layers of oxide upon the surface. It was also reported that the photoemission spectra from the reaction of water with uranium largely matched those of water with thorium, suggesting that the 5f valence electrons have little effect upon the reaction [40]. The reaction rate for the adsorption of water has proven to be a contentious issue, as varying reports have suggested that it proceeds at a comparable or greater rate than that of oxygen adsorption [34,73], while others have reported the rate of reaction to be significantly slower [40]. The conflicting reports were explained by Winer *et al* [34],

amongst others, as being due to the presence of oxygen either on the surface or in the vacuum system, which severely retards the reaction with H_2O [15,73]. Specific studies looking at the issue revealed that the presence of oxygen can prevent dissociation upon the surface [89], and even reduce the initial adsorption of water vapour [90]. Multiple mechanisms have been put forward to explain the observed drop in reaction rate. Allen *et al* [73] concluded that the presence of oxygen promotes the formation of defect complexes which diffuse more slowly through the oxide layer than the OH^- ions created through dissociation, and thus inhibit the transport of OH^- ions to the uranium/oxide interface. Fuller *et al* [91] suggested that the hydrogen released through dissociation of H_2O aids further oxidation through a process related to hydrogen embrittlement, and that any oxygen present would scavenge those hydrogen atoms, thus retarding the reaction. Finally, Colmenares [15] proposed that oxygen is preferentially adsorbed at the surface, and that its presence reduces the available sites for the dissociation of incoming H_2O molecules. A review of the different mechanisms by Winer *et al* [34] concluded that preferential adsorption was the only answer that justified and explained the accumulated data.

The reaction of uranium with CO and CO_2 at 300 K has been studied by McLean *et al* [33]. They showed that both molecules dissociated upon the surface to form both the oxide and the carbide. Examination of the C(1s) spectra revealed that only the carbide was present, with no evidence for either molecular CO or CO_2. This was taken to indicate that all the reacting gases dissociated upon the surface, and at a fast rate [33]. The results agreed with those by Gouder *et al* [74] who studied the reaction at 300 and 573 K. Gouder *et al* [74] also repeated the experiment at 73 K, and found that at that colder temperature the binding of molecular CO and CO_2 to the surface did occur at high surface coverages. The C to O ratio observed by Mclean *et al* [33] upon exposure at 300 K did not match that of the reagents, which was taken as evidence that free carbon from the dissociation upon the surface dissolved into the uranium bulk. This belief was then confirmed through depth profiling that showed its presence far further into the bulk than the oxygen that was also released in the dissociation [33].

Uranium nitride is an important compound currently being considered for use as a fuel in future advanced nuclear reactors [67,92,93]. The formation of the nitride *via*

exposure to N_2 has been explored by both Allen and Holmes [94] and Black *et al* [67]. Allen and Holmes left a clean uranium surface in 1 atmosphere of N_2 at 300 K for 16 hours, yet saw no sign of a reaction between the two regents. Instead the surface entirely converted to UO_2 through reaction with the 0.1 ppm of O_2 present in the research-grade N_2. Their solution to the problem was to bombard the clean uranium with N_2 that was accelerated by 4 kV in a fast ion bombardment (FAB) gun. Using this method they successfully produced a surface of UN [94]. Black *et al* used a largely similar method whereby the nitride was produced through reactive DC sputtering of clean uranium with an argon and nitrogen mix. By varying the partial pressure of the N_2 with the argon it was possible to control whether UN or U_2N_3 was formed [67]. The reported valence band spectra of UN featured a sharp and intense signal at the Fermi edge, which has been described as indicative of the fact that the 5f electrons retain their delocalised nature, and supports the DFT calculations carried out that report UN to be a metallic based conductor [41,67,94-96]. While the uranium in UN has a formal oxidation state of +3, the actual charge transfer away form the metal atoms has been reported as being 0.6-0.7 electrons, which indicates that the bonding is profoundly covalent in character [67,97]. The 5f electrons in U_2N_3 also remain at least partly delocalised, with visible intensity at the Fermi edge in reported valence band spectra; however some localisation does take place. The difference in the extent of delocalisation remaining is highlighted by the 4f peaks reported by Black *et al* [67], which appeared largely symmetrical for U_2N_3, and asymmetrical for UN.

1.3 Summary

This overview of the literature has covered the basics of why the actinides are of interest, their unusual properties, and some of the important reactions studied. This review has focussed on the reactions of thorium and uranium, as these two elements, when compared, provide a fascinating insight into the effect of valence 5f orbitals upon reactions. It is for this reason that thorium and uranium were the actinide elements chosen for study in this work.

Of the actinide elements, it is the surface chemistry of uranium that has received by far the most interest, which is due to its technological relevance. As for specific reactions, it is the formation of the actinide oxides that has been of most interest to

researchers, owing in part to the propensity of the clean metals to oxidise almost instantaneously when in contact with oxygen. A wide variety of stable oxides exist for the early actinides, as their transition metal like behaviour includes that of having multiple stable oxidation states possible. The 5f electrons of the actinides have understandably received considerable attention owing to their fundamental effect upon the properties and reactivities of the elements, which is highlighted by the 'light' and 'heavy' actinide division. The investigation of the interaction and role of the 5f electrons is best undertaken by means of comparing the reactions between multiple different actinides and a range of small molecules. To that effect the light actinides have been reacted with multiple small molecules including; O_2, H_2O, H_2, N_2, CO, and CO_2. As the research has so far focussed upon utilizing forward photoemission techniques, there remains large scope for the use of inverse photoemission techniques in the study of the reactions, and determining the contribution of the 5f electrons.

variations in the reported photoemission values for UO_2 seen in the literature can be explained by the fact that substoichiometric UO_{2-x} and hyperstoichiometric UO_{2+x} are so easily formed that it is extremely difficult to guarantee purely stoichiometric $UO_{2.0}$ is formed [33,38,51,85]. Studies of the valence band have also been undertaken to help with the understanding of the uranium/oxygen system. The oxidation of uranium results in a sharp intense peak at 1.4 eV above the Fermi level, which is a signal that is lacking from the valence band spectra of ThO_2 [86]. As U^{IV} has a $5f^2$ state and Th^{IV} a non-occupied $5f^0$ state, the signal was attributed to 5f electrons. The small gap from the signal to the Fermi edge is expected due to the fact that UO_2 is considered to be a semi-conductor [34,37,39,52]. Additional work looking at the unoccupied states above the Fermi level has also been undertaken, using both BIS [87] and inverse photoemission spectroscopy (IPES) [68,88]. The two techniques produced largely identical spectra for stoichiometric UO_2, with large signals centred at 5.1 eV above the Fermi level that were concluded to be due to the $5f^3$ final state. An additional smaller signal on the lower energy side of the peak, which was reported in two of the studies, has been attributed to the $6d^1$ final states [68,87]. Rousell *et al* [68] also reported the considerably less intense unoccupied orbital spectra of the mixed valency $UO_{2.2}$ species. They noted that the signal from the 5f states, now a combination of $5f^3$ and $5f^2$ final states, was located at 0.9 eV higher energy than that seen for UO_2, with the signal attributed to the 6d states now more pronounced and centred at 3.3 eV [68].

The reaction of clean uranium with water has been studied a number of times, at multiple temperatures, and with multiple techniques [34,40,73,75-80]. H_2O has been shown to dissociate upon the surface of uranium, forming both oxide and hydroxide species. The process forms H_2, which is lost to the gas phase, as a by-product of the oxide formation, and as such presents potential safety issues [34,76]. Like the reaction with pure O_2, the reaction with H_2O has also been shown to form multiple layers of oxide upon the surface. It was also reported that the photoemission spectra from the reaction of water with uranium largely matched those of water with thorium, suggesting that the 5f valence electrons have little effect upon the reaction [40]. The reaction rate for the adsorption of water has proven to be a contentious issue, as varying reports have suggested that it proceeds at a comparable or greater rate than that of oxygen adsorption [34,73], while others have reported the rate of reaction to be significantly slower [40]. The conflicting reports were explained by Winer *et al* [34],

amongst others, as being due to the presence of oxygen either on the surface or in the vacuum system, which severely retards the reaction with H_2O [15,73]. Specific studies looking at the issue revealed that the presence of oxygen can prevent dissociation upon the surface [89], and even reduce the initial adsorption of water vapour [90]. Multiple mechanisms have been put forward to explain the observed drop in reaction rate. Allen *et al* [73] concluded that the presence of oxygen promotes the formation of defect complexes which diffuse more slowly through the oxide layer than the OH^- ions created through dissociation, and thus inhibit the transport of OH^- ions to the uranium/oxide interface. Fuller *et al* [91] suggested that the hydrogen released through dissociation of H_2O aids further oxidation through a process related to hydrogen embrittlement, and that any oxygen present would scavenge those hydrogen atoms, thus retarding the reaction. Finally, Colmenares [15] proposed that oxygen is preferentially adsorbed at the surface, and that its presence reduces the available sites for the dissociation of incoming H_2O molecules. A review of the different mechanisms by Winer *et al* [34] concluded that preferential adsorption was the only answer that justified and explained the accumulated data.

The reaction of uranium with CO and CO_2 at 300 K has been studied by McLean *et al* [33]. They showed that both molecules dissociated upon the surface to form both the oxide and the carbide. Examination of the C(1s) spectra revealed that only the carbide was present, with no evidence for either molecular CO or CO_2. This was taken to indicate that all the reacting gases dissociated upon the surface, and at a fast rate [33]. The results agreed with those by Gouder *et al* [74] who studied the reaction at 300 and 573 K. Gouder *et al* [74] also repeated the experiment at 73 K, and found that at that colder temperature the binding of molecular CO and CO_2 to the surface did occur at high surface coverages. The C to O ratio observed by Mclean *et al* [33] upon exposure at 300 K did not match that of the reagents, which was taken as evidence that free carbon from the dissociation upon the surface dissolved into the uranium bulk. This belief was then confirmed through depth profiling that showed its presence far further into the bulk than the oxygen that was also released in the dissociation [33].

Uranium nitride is an important compound currently being considered for use as a fuel in future advanced nuclear reactors [67,92,93]. The formation of the nitride *via*

exposure to N_2 has been explored by both Allen and Holmes [94] and Black *et al* [67]. Allen and Holmes left a clean uranium surface in 1 atmosphere of N_2 at 300 K for 16 hours, yet saw no sign of a reaction between the two regents. Instead the surface entirely converted to UO_2 through reaction with the 0.1 ppm of O_2 present in the research-grade N_2. Their solution to the problem was to bombard the clean uranium with N_2 that was accelerated by 4 kV in a fast ion bombardment (FAB) gun. Using this method they successfully produced a surface of UN [94]. Black *et al* used a largely similar method whereby the nitride was produced through reactive DC sputtering of clean uranium with an argon and nitrogen mix. By varying the partial pressure of the N_2 with the argon it was possible to control whether UN or U_2N_3 was formed [67]. The reported valence band spectra of UN featured a sharp and intense signal at the Fermi edge, which has been described as indicative of the fact that the 5f electrons retain their delocalised nature, and supports the DFT calculations carried out that report UN to be a metallic based conductor [41,67,94-96]. While the uranium in UN has a formal oxidation state of +3, the actual charge transfer away form the metal atoms has been reported as being 0.6-0.7 electrons, which indicates that the bonding is profoundly covalent in character [67,97]. The 5f electrons in U_2N_3 also remain at least partly delocalised, with visible intensity at the Fermi edge in reported valence band spectra; however some localisation does take place. The difference in the extent of delocalisation remaining is highlighted by the 4f peaks reported by Black *et al* [67], which appeared largely symmetrical for U_2N_3, and asymmetrical for UN.

1.3 Summary

This overview of the literature has covered the basics of why the actinides are of interest, their unusual properties, and some of the important reactions studied. This review has focussed on the reactions of thorium and uranium, as these two elements, when compared, provide a fascinating insight into the effect of valence 5f orbitals upon reactions. It is for this reason that thorium and uranium were the actinide elements chosen for study in this work.

Of the actinide elements, it is the surface chemistry of uranium that has received by far the most interest, which is due to its technological relevance. As for specific reactions, it is the formation of the actinide oxides that has been of most interest to

researchers, owing in part to the propensity of the clean metals to oxidise almost instantaneously when in contact with oxygen. A wide variety of stable oxides exist for the early actinides, as their transition metal like behaviour includes that of having multiple stable oxidation states possible. The 5f electrons of the actinides have understandably received considerable attention owing to their fundamental effect upon the properties and reactivities of the elements, which is highlighted by the 'light' and 'heavy' actinide division. The investigation of the interaction and role of the 5f electrons is best undertaken by means of comparing the reactions between multiple different actinides and a range of small molecules. To that effect the light actinides have been reacted with multiple small molecules including; O_2, H_2O, H_2, N_2, CO, and CO_2. As the research has so far focussed upon utilizing forward photoemission techniques, there remains large scope for the use of inverse photoemission techniques in the study of the reactions, and determining the contribution of the 5f electrons.

1.4 References

1 K. T. Moore and G. van der Laan, *Reviews of Modern Physics*, 2009, **81**, 235-298.

2 G. T. Seaborg, *Science*, 1946, **104**, 379-386.

3 L. J. Terminello, *Science & Technology Review: Lawrence Livermore National Laboratory Journal*, 2000, **June**, 15-22.

4 S. Cotton, Lanthanide and Actinide Chemistry, **2006**, John Wiley & Sons, Ltd: Chichester, p. 145-147.

5 I. Hore-Lacy. *2009.* "Thorium" In: Encyclopedia of Earth. Eds. Cutler J. [WWW] <URL:http://www.eoearth.org/article/Thorium> [Accessed 20 August 2010]

6 R. G. Lange and W. P. Carroll, *Energy Conversion and Management*, 2008, **49**, 393-401.

7 I. Hore-Lacy. *2009.* "Uranium" In: Encyclopedia of Earth. Eds. Cutler J. [WWW] <URL:http://www.eoearth.org/article/Uranium> [Accessed 20 August 2010]

8 J. M. Fournier and L. Manes, Actinides - Chemistry and Physical Properties, in *Structure and Bonding, Vol. 59/60* (Ed.: L. Manes), **1985**, Springer-Verlag: Berlin, p. 4-6.

9 D. L. Clark, *Los Alamos Science*, 2000, **26**, 364-381.

10 P. Nevitt, *Discovery: The Science & Technology Journal of AWE*, 2005, **11**, 16-25.

11 S. S. Hecker, *Los Alamos Science*, 2000, **26**, 16-23.

12 G. C. Allen and P. M. Tucker, *Chemical Physics Letters*, 1976, **43**, 254-257.

13 H. L. Skriver, O. K. Andersen and B. Johansson, *Physical Review Letters*, 1978, **41**, 42-45.

14 M. Boring, R. D. Cowan and R. L. Martin, *Physical Review B*, 1981, **23**, 445-448.

15 C. A. Colmenares, *Progress in Solid State Chemistry*, 1984, **15**, 257-364.

16 H. L. Skriver, *Physical Review B*, 1985, **31**, 1909-1923.

17 M. O. Krause, R. G. Haire, O. Keskirahkonen and J. R. Peterson, *Journal of Electron Spectroscopy and Related Phenomena*, 1988, **47**, 215-226.

18 I. D. Prodan, G. E. Scuseria and R. L. Martin, *Physical Review B (Condensed Matter and Materials Physics)*, 2007, **76**, 033101-033104.

19 J. M. Fournier and L. Manes, Actinides - Chemistry and Physical Properties, in *Structure and Bonding, Vol. 59/60* (Ed.: L. Manes), **1985**, Springer-Verlag: Berlin, p. 1-56.

20 J. M. Fournier and L. Manes, Actinides - Chemistry and Physical Properties, in *Structure and Bonding, Vol. 59/60* (Ed.: L. Manes), **1985**, Springer-Verlag: Berlin, p. 127-196.

21 J. R. Naegele and J. Ghijsen, Actinides - Chemistry and Physical Properties, in *Structure and Bonding, Vol. 59/60* (Ed.: L. Manes), **1985**, Springer-Verlag: Berlin, p. 197-262.

22 M. S. S. Brooks, Actinides - Chemistry and Physical Properties, in *Structure and Bonding, Vol. 59/60* (Ed.: L. Manes), **1985**, Springer-Verlag: Berlin, p. 263-293.

23 Y. Baer and J. K. Lang, *Physical Review B*, 1980, **21**, 2060-2062.

24 F. Gerken and J. Schmidtmay, *Journal of Physics F-Metal Physics*, 1983, **13**, 1571-1580.

25 J. D. Denlinger, G. H. Gweon, J. W. Allen, C. G. Olson, Y. Dalichaouch, B. W. Lee, M. B. Maple, Z. Fisk, P. C. Canfield and P. E. Armstrong, *Physica B*, 2000, **281**, 716-722.

26 T. Gouder, F. Wastin, J. Rebizant and G. H. Lander, *Mrs Bulletin*, 2001, **26**, 684-688.

27 K. T. Moore, G. van der Laan, M. A. Wall, A. J. Schwartz and R. G. Haire, *Physical Review B*, 2007, **76**, 073105.

28 W. D. Schneider and C. Laubschat, *Physical Review Letters*, 1981, **46**, 1023-1027.

29 J. R. Naegele, L. Manes, J. C. Spirlet and W. Muller, *Physical Review Letters*, 1984, **52**, 1834-1837.

30 T. Gouder, *Journal of Electron Spectroscopy and Related Phenomena*, 1999, **103**, 419-422.

31 G. van der Laan and M. Taguchi, *Physical Review B*, 2007, **82**, 045114.

32 G. C. Allen and R. K. Wild, *Journal of the Chemical Society-Dalton Transactions*, 1974, **5**, 493-498.

33 W. McLean, C. A. Colmenares, R. L. Smith and G. A. Somorjai, *Physical Review B*, 1982, **25**, 8-24.

34 K. Winer, C. A. Colmenares, R. L. Smith and F. Wooten, *Surface Science*, 1987, **183**, 67-99.

35 P. Morrall, P. Roussel, L. Jolly, A. Brevet and F. Delaunay, *Journal of Nuclear Materials*, 2009, **385**, 15-17.

36 T. Gouder, L. Havela, F. Wastin and J. Rebizant, *Europhysics Letters*, 2001, **55**, 705-711.

37 B. W. Veal and D. J. Lam, *Physical Review B*, 1974, **10**, 4902-4908.

38 J. C. Fuggle, A. F. Burr, L. M. Watson, D. J. Fabian and W. Lang, *Journal of Physics F-Metal Physics*, 1974, **4**, 335-342.

39 C. A. Colmenares, *Progress in Solid State Chemistry*, 1975, **9**, 139-239.

40 S. B. Nornes and R. G. Meisenheimer, *Surface Science*, 1979, **88**, 191-203.

41 P. R. Norton, R. L. Tapping, D. K. Creber and W. J. L. Buyers, *Physical Review B*, 1980, **21**, 2572-2577.

42 J. R. Naegele and J. Ghijsen, Actinides - Chemistry and Physical Properties, in *Structure and Bonding, Vol. 59/60* (Ed.: L. Manes), **1985**, Springer-Verlag: Berlin, p. 221-222.

43 J. C. Fuggle, M. Campagna, Z. Zolnierek, R. Lasser and A. Platau, *Physical Review Letters*, 1980, **45**, 1597-1600.

44 T. Gouder, L. Havela, L. Black, F. Wastin, J. Rebizant, P. Boulet, D. Bouexiere, S. Heathman and M. Idiri, *Journal of Alloys and Compounds*, 2002, **336**, 73-76.

45 H. R. Moser, B. Delley, W. D. Schneider and Y. Baer, *Physical Review B*, 1984, **29**, 2947-2955.

46 S. Doniach and M. Sunjic, *Journal of Physics C-Solid State Physics*, 1970, **3**, 285-.

47 A. Kotani and Y. Toyozawa, *Journal of the Physical Society of Japan*, 1974, **37**, 912-919.

48 G. H. Lander, E. S. Fisher and S. D. Bader, *Advances in Physics*, 1994, **43**, 1-111.

49 E. S. Fisher, *Journal of Alloys and Compounds*, 1994, **213**, 254-261.

50 F. Greuter, E. Hauser, P. Oelhafen, H. J. Guntherodt, B. Reihl and O. Vogt, *Physica B & C*, 1980, **102**, 117-121.

51 G. C. Allen, I. R. Trickle and P. M. Tucker, *Philosophical Magazine B-Physics of Condensed Matter Statistical Mechanics Electronic Optical and Magnetic Properties*, 1981, **43**, 689-703.

52 T. Gouder, C. Colmenares, J. R. Naegele and J. Verbist, *Surface Science*, 1990, **235**, 280-286.

53 S. L. Molodtsov, J. Boysen, M. Richter, P. Segovia, C. Laubschat, S. A. Gorovikov, G. V. Prudnikova and V. K. Adamchuk, *Physical Review B*, 1998, **57**, 13241-13245.

54 W. H. Zachariasen and F. H. Ellinger, *Acta Crystallographica*, 1963, **16**, 777.

55 R. C. Albers, *Nature*, 2001, **410**, 759-761.

56 L. E. Cox and J. W. Ward, *Inorganic & Nuclear Chemistry Letters*, 1981, **17**, 265-268.

57 D. Courteix, J. Chayrouse, L. Heintz and R. Baptist, *Solid State Communications*, 1981, **39**, 209-213.

58 R. Baptist, D. Courteix, J. Chayrouse and L. Heintz, *Journal of Physics F-Metal Physics*, 1982, **12**, 2103-2114.

59 L. E. Cox, *Physical Review B*, 1988, **37**, 8480-8483.

60 L. Havela, T. Gouder, F. Wastin and J. Rebizant, *Physical Review B*, 2002, **65**, 235118.

61 D. T. Larson, *Journal of Vacuum Science and Technology*, 1980, **17**, 55-58.

62 L. E. Cox, O. Eriksson and B. R. Cooper, *Physical Review B*, 1992, **46**, 13571-13575.

63 A. J. Arko, J. J. Joyce, L. Morales, J. M. Wills, J. C. lashley, F. Wastin and J. Rebizant, *Physical Review B*, 2000, **62**, 1773-1779.

64 N. Baclet, B. Oudot, R. Grynszpan, L. Jolly, B. Ravat, P. Faure, L. Berlu and G. Jomard, *Journal of Alloys and Compounds*, 2007, **444**, 305-309.

65 L. E. Cox, *Journal of Electron Spectroscopy and Related Phenomena*, 1982, **26**, 167-171.

66 T. Ishii, *Physica B: Condensed Matter*, 1993, **186-188**, 21-25.

67 L. Black, F. Miserque, T. Gouder, L. Havela, J. Rebizant and F. Wastin, *Journal of Alloys and Compounds*, 2001, **315**, 36-41.

68 P. Roussel, P. Morrall and S. J. Tull, *Journal of Nuclear Materials*, 2009, **385**, 53-56.

69 J. R. Naegele and J. Ghijsen, Actinides - Chemistry and Physical Properties, in *Structure and Bonding, Vol. 59/60* (Ed.: L. Manes), **1985**, Springer-Verlag: Berlin, p. 238.

70 P. H. Holloway and E. B. Evans, *Oxidation of Metals*, 1972, **4**, 27.

71 T. N. Taylor, C. A. Colmenares, R. L. Smith and G. A. Somorjai, *Surface Science*, 1976, **54**, 317-339.

72 P. Nevitt, "Photoemission Studies of The Light Actinides", *Ph.D. Thesis*, University of Cardiff, **2006**.

73 G. C. Allen, P. M. Tucker and R. A. Lewis, *Journal of the Chemical Society-Faraday Transactions Ii*, 1984, **80**, 991-1000.

74 T. Gouder, J. Naegele, C. A. Colmenares and J. J. Verbist, *Inorganica Chimica Acta*, 1987, **140**, 35-36.

75 M. Balooch and A. V. Hamza, *Journal of Nuclear Materials*, 1996, **230**, 259-270.

76 W. L. Manner, J. A. Lloyd and M. T. Paffett, *Journal of Nuclear Materials*, 1999, **275**, 37-46.

77 M. N. Hedhili, B. V. Yakshinskiy and T. E. Madey, *Surface Science*, 2000, **445**, 512-525.

78 N. Shamir, E. Tiferet, S. Zalkind and M. H. Mintz, *Surface Science*, 2006, **600**, 657-664.

79 E. Tiferet, S. Zalkind, M. H. Mintz, I. Jacob and N. Shamir, *Surface Science*, 2007, **601**, 936-940.

80 S. D. Senanayake, G. I. N. Waterhouse, A. S. Y. Chan, T. E. Madey, D. R. Mullins and H. Idriss, *Catalysis Today*, 2007, **120**, 151-157.

81 G. C. Allen and R. K. Wild, *Chemical Physics Letters*, 1972, **15**, 279.

82 D. Chadwick and J. Graham, *Nature - Physical Science*, 1972, **237**, 127.

83 G. C. Allen, P. A. Tempest and J. W. Tyler, *Journal of the Chemical Society-Faraday Transactions*, 1987, **83**, 925.

84 S. Tull, *Ph.D. Thesis*, University of Cardiff, **2002**.

85 G. C. Allen, J. A. Crofts, M. T. Curtis, P. M. Tucker, D. Chadwick and P. J. Hampson, *Journal of the Chemical Society-Dalton Transactions*, 1974, 1296-1301.

86 J. R. Naegele and J. Ghijsen, Actinides - Chemistry and Physical Properties, in *Structure and Bonding, Vol. 59/60* (Ed.: L. Manes), **1985**, Springer-Verlag: Berlin, p. 240-241.

87 Y. Baer and J. Schoenes, *Solid State Communications*, 1980, **33**, 885-888.

88 G. Chauvet and R. Baptist, *Solid State Communications*, 1982, **43**, 793-796.

89 J. Jupille, J. Fusy and P. Pareja, *Surface Science*, 1984, **143**, L433-L438.

90 E. M. Stuve, S. W. Jorgensen and R. J. Madix, *Surface Science*, 1984, **146**, 179-198.

91 E. L. Fuller, N. R. Smyrl, J. B. Condon and M. H. Eager, *Journal of Nuclear Materials*, 1984, **120**, 174-194.

92 T. Nakagawa, H. Matsuoka, M. Sawa, M. Hirota, M. Miyake and M. Katsura, *Journal of Nuclear Materials*, 1997, **247**, 127-130.

93 C. B. Yeamans, G. W. C. Silva, G. S. Cerefice, K. R. Czerwinski, T. Hartmann, A. K. Burrell and A. P. Sattelberger, *Journal of Nuclear Materials*, 2008, **374**, 75-78.

94 G. C. Allen and N. R. Holmes, *Journal of Nuclear Materials*, 1988, **152**, 187-193.

95 M. Erbudak and J. Keller, *Zeitschrift Fur Physik B-Condensed Matter*, 1979, **32**, 281-286.

96 R. A. Evarestov, M. V. Losev, A. I. Panin, N. S. Mosyagin and A. V. Titov, *Physica Status Solidi B-Basic Solid State Physics*, 2008, **245**, 114-122.

97 M. S. S. Brooks, *Journal of Physics F-Metal Physics*, 1984, **14**, 639-652.

Chapter 2 – Experimental

2.1 The vacuum system

2.1.1 Introduction

All experiments were carried out in a hybrid photoemission electron spectrometer comprising facilities for photoelectron spectroscopy (VG Scientific), high-resolution electron energy-loss spectroscopy (HREELS; Vacuum Science Workshop), and inverse photoelectron spectroscopy (PSP Vacuum Technology). The system itself comprises of a single large UHV chamber where the experimental samples are mounted. Connected to this are the facilities required to both clean and scan the samples. The system features a hemispherical electron analyser, an x-ray source, an UV source, a photon detector, a low energy electron gun, a quadrupole mass spectrometer, and an ion bombardment gun. These components form the different analytical techniques available for use on the system, such as X-Ray Photoelectron Spectroscopy (XPS), Ultraviolet Photoelectron Spectroscopy (UPS), and Inverse Photoemission Spectroscopy (IPES). A labelled diagram of the system, featuring the key components, can be seen in figure 2.1.

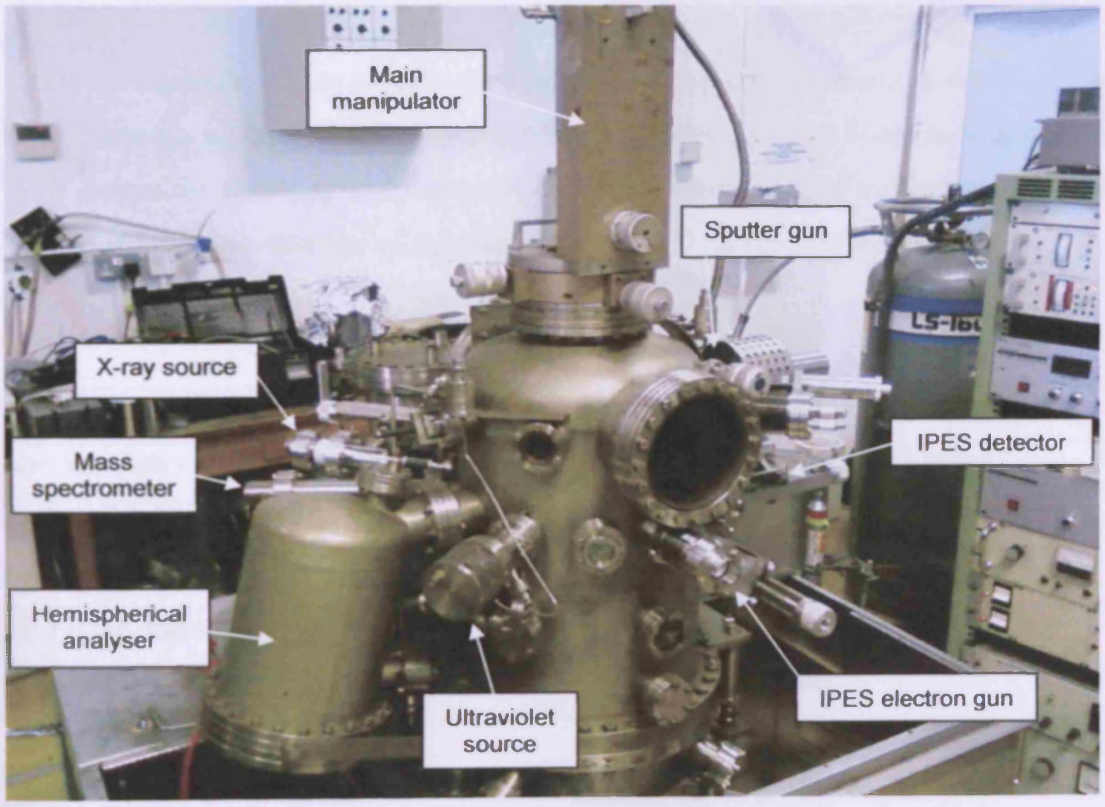

Figure 2.1: A photo of the UHV system with key components labelled

2.1.2 The requirement for Ultra High Vacuum (UHV)

A key requirement for this research, and other research of metal – adsorbate interactions *via* photoelectron spectroscopies, is the use of ultra high vacuum (UHV) conditions, where the pressure is $< 10^{-9}$ mbar. A definition of UHV and the other vacuum "regions" is given in table 2.1. The UHV conditions are required for the research for three main reasons:

1) The photoelectrons emitted from the surface of the sample need to have a sufficiently long mean free path so that they can travel to the analyser without colliding with any gas molecules. For meaningful spectroscopy to be carried out, the photoelectrons must arrive at the detector in exactly the same state that they left the sample surface.

2) To prevent electrical discharges between different components inside the system. The use of high voltages in both the x-ray anode, and the electron multiplier detector, require a minimum of a high vacuum to prevent electrical discharges to the electron analyser.

3) To maintain an atomically clean surface. The surface needs to remain clean throughout the experimental period, which may be many hours in length. The lower the pressure in the system, the lower the number of molecules, and thus the lower the number of contaminating collisions upon the surface.

Vacuum Definition	**Pressure Range**
Low Vacuum (LV)	Atmospheric pressure ↔ 1 mbar
Medium Vacuum (MV)	1 mbar ↔ 10^{-3} mbar
High Vacuum (HV)	10^{-3} mbar ↔ 10^{-8} mbar
Ultra High Vacuum (UHV)	10^{-8} mbar ↔ 10^{-12} mbar
Extreme High Vacuum (XHV)	Less than 10^{-12} mbar

Table 2.1: Pressure definitions for the different vacuum regions [1]

It is the requirement of the atomically clean surface that drives the need for ultra high vacuum conditions, as the mean free path and electrical discharge requirements would be sufficiently met at high vacuum ($<10^{-6}$ mbar). The rate of contamination of the surface can be calculated using the Hertz-Knudsen equation (Equation 2.1).

$$J = \frac{p}{\sqrt{2\pi mkT}} \qquad \text{Equation 2.1 [2]}$$

Where J is the rate of impingement of gas on the surface in cm^{-2} s^{-1}, m is the molecular mass of the gas, k is the Boltzmann constant, T is the temperature in K, and p is the pressure in Pa.

Assuming that the sticking probability is 1 (i.e. all molecules that collide with the surface stick, and remain attached), and that there are approximately 1×10^{15} available sites on any 1 cm^2 of the surface, at 10^{-6} mbar and 298 K the entire surface will be covered by a monolayer of contamination within a few seconds. In contrast, at 10^{-10} mbar the surface takes more than 9 hours to be covered by a monolayer of contamination. So to have enough time available to study the surface while it is still predominantly clean, the maintaining of UHV conditions is absolutely essential.

2.1.3 Achieving UHV

To achieve the required UHV conditions, a certain number of vacuum pumps are needed. Each one is only capable of reaching a specific order of magnitude of vacuum; however when combined they have the capability of achieving UHV conditions (specifically a base pressure of 10^{-10} mbar). One of the key reasons why multiple pumps are needed is that gas behaves in different ways depending upon the pressure. This gas flow behaviour is dependent upon the Knudsen number, which is defined as:

$$K_n = \lambda / D \qquad \text{Equation 2.2}$$

Where K_n is the Knudsen number, λ is the mean free path of the gas molecules, and D is a characteristic dimensional length of the container (for example the width if the container is a cube, or the diameter if it is a cylinder). From atmosphere down to 10^{-2} mbar the Knudsen number will be less than 1, and the mean free path of the molecules present will be smaller than the dimensions of the pipes of the UHV system. Because of this molecule-molecule collisions are far more likely than molecule-surface collisions, and the gas has a fluid-like behaviour. With fluid-like behaviour the gas can be physically withdrawn and extracted out of the chamber by means of 'suction', with the movement of molecules communicated by inter-molecular collisions. However at lower pressures, needed for UHV, the Knudsen number will be greater than 1 and the mean free path of the molecules will be considerably longer than the dimensions of the system. With negligible inter-molecular collisions taking place, and molecules only colliding with the surface walls, the gas will no longer behave as a viscous flow. Instead the gas would be described as a molecular flow, as there is no means of communicating motion between the molecules of gas. In the molecular flow region gases can no longer be 'sucked', and instead pumps need to operate on the 'capture' principle, and focus on capturing any molecules that happen to 'arrive' in that area of the system. This arrival rate is determined by the gas alone, and thus applies an upper limit upon the speed at which any pump can operate within this region.

Initial evacuation of the chamber down to a pressure of 10^{-2} mbar is achieved through the use of mechanical rotary vane pumps. These mechanical pumps, which operate on viscous flow principles, utilise a spinning slotted rotor inside a stator as the basis of their pumping ability. Inside the slots on the rotor are sliding vanes, which are in constant contact with the sides of the stator. As the rotor spins the vanes draw in and trap gases which are then fed to a one-way exhaust valve. All edges and surfaces inside the pump are 'sealed' with oil to provide good seals and drastically improve the performance as opposed to if oil was not present. The rotary pumps are used both for the purpose of 'roughing' down the system to 10^{-2} mbar, and also as the 'backing' pumps required for the operation of the oil diffusion pumps.

The job of reducing the pressure in the system down to useable UHV pressures (10^{-10} mbar) falls on the oil diffusion pumps. These pumps utilise collision theory and

are able to work in the molecular flow region of pressures. A schematic of a diffusion pump can be seen in figure 2.2. The heater at the bottom of the pump heats oil to produce a vapour which travels upwards through the central chimney structure. This oil vapour is then channelled and deflected downwards by the jet assembly into a jet travelling at supersonic speed. The speeding oil molecules collide with the random moving incoming gas molecules from the chamber, imparting a largely directional momentum directed towards the region of the pump outlet. Once the molecules from the chamber reach the pump outlet, where the pressure is considerably higher due to the constant flow of incoming molecules, the backing rotary pump is able to remove them from the chamber. The oil molecules, after colliding with the arriving gas molecules, condense on the water cooled walls of the pump and return to the oil reservoir at the bottom to begin the cycle again. It is important to note that the choice of oil used is critical for the performance of the pump. The oil needs to have a high resistance to thermal degradation, a very low vapour pressure, and be non-reactive with the gases passing through the pump. The oil that fits these parameters, and is used in the diffusion pumps on the system, is a polyphenyl ether oil (Santovac 5, SantoLubes LLC) with a vapour pressure of ~4 x 10^{-10} mbar at 298 K. In between the diffusion pump and the main chamber is a liquid nitrogen cooled cold trap which is needed to prevent 'back-streaming', where the oil in the pump gradually seeps into the system, and facilitate reaching the 10^{-10} mbar base pressure.

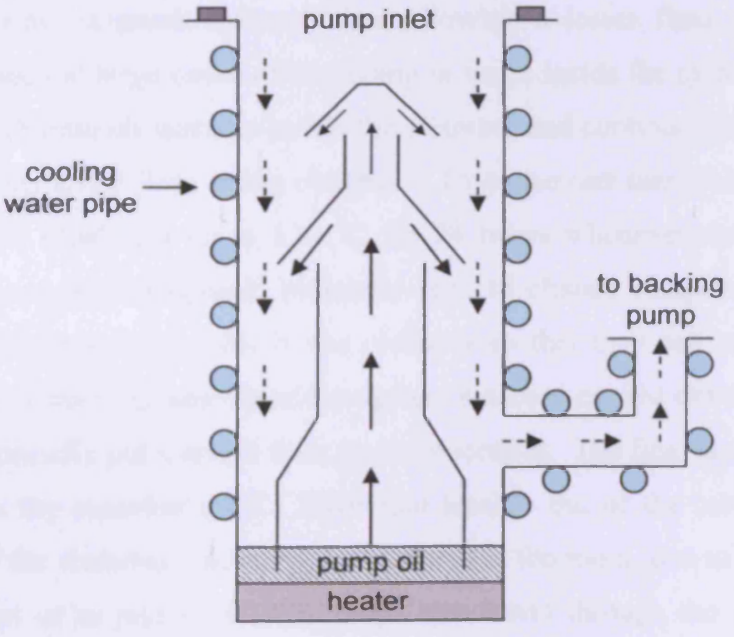

Figure 2.2: Schematic of an oil diffusion pump

The final base pressure for the system is ruled by two factors; 1) the overall pumping speed of the multiple pumps mentioned above, and 2) the combined total of all degassing and leaking components on the system. These two factors work directly against one another, so when they are in equilibrium the system will be at the lowest pressure possible. Therefore to improve the vacuum either the total pumping speed needs to be improved or the amount of degassing within the system need to be reduced (leaking components normally have such a pronounced affect upon the system that they would normally be dealt with long before the degassing issues and pump size are looked at).

The term degassing is used to describe the increase of gaseous molecules in the system. This can either be due to a specific chemical reaction which produces more gaseous molecules than it consumes, or by the process of adsorbed and absorbed molecules on the inside surfaces of the system desorbing (there is also the additional issue of pump 'back-streaming' as mentioned above). One of the most common causes of degassing is the use of hot filaments in the system, which are found both on the ion-gauges, and inside the various analytical technique components (e.g. the filaments in the x-ray gun and quadruple mass spectrometer). To counteract this issue the various filaments are put through an intentional degas procedure, where they are briefly run at higher than normal power with the intention of desorbing the majority of contaminants present. After this has been carried out the rate of continuous degas from the filaments is much reduced, thus allowing a lower final pressure to be reached. The second large cause of degassing is water inside the system. The water molecules adsorb onto all surfaces inside the chamber and continuously degas, which normally prevents UHV from being obtained. To counteract this problem the entire system is heated ("baked") up to 130 °C for 24 hours whenever the inside of the system is exposed to atmospheric pressures (e.g. to change samples), to stimulate desorption of all water molecules in the chamber so that they can be pumped out. Additionally, it is after this heating of the system has been carried out that the various filaments are normally put through their degas procedure. The final significant source of degassing is the chamber itself. Hydrogen leaches out of the metal used in the construction of the chamber, and helium, if present in the room (due to leak checking, use as a reagent or as part of a UPS setup), can travel through the glass windows

designed into the system [3]. Thankfully the combined total of the hydrogen and helium is rarely enough to prevent UHV conditions being achieved.

2.1.4 Pressure measurement

Two different methods are used to measure the pressure inside the vacuum system: pirani gauges and ionisation gauges (an example of each can be seen in figure 2.3). The pirani gauge, which is a type of thermal conductivity gauge, is used to measure relatively high pressures in the system (1-1x10^{-3} mbar). The gauge consists of a resistively heated tungsten filament (subjected to a constant voltage) that is incorporated into a bridge circuit. The bridge circuit sends current through the filament branch, and also through an isolated reference branch, with a detector being used to measure any out-of-balance current between the two branches. Gases present in the system conduct heat away from the filament, resulting in a change of its temperature, and thus a change in its electrical resistance. The resulting change in the out-of-balance current is detected and presented as a pressure reading in nitrogen equivalent mbar. Below 1x10^{-3} mbar the heat losses from the filament due to conduction become overshadowed by the heat losses due to radiation, and the reliability of the gauge becomes compromised.

For the measurement of pressures ranging from 1x10^{-3} down to 1x10^{-11} mbar a thermionic ionisation gauge (ion-gauge) is used. The basic design of the ion-gauge consists of three components; a filament, a grid (anode), and a collector. The filament, which is typically tungsten or thoria coated iridium, emits electrons when a current is passed through it. The electrons emitted are attracted *via* a positive potential towards the grid, where they may collide with any gaseous molecules in the area, and produce positively charged ions. The positively charged ions are then attracted to the negatively charged collector wire resulting in a current, which when measured, is directly proportional to the pressure of the gas.

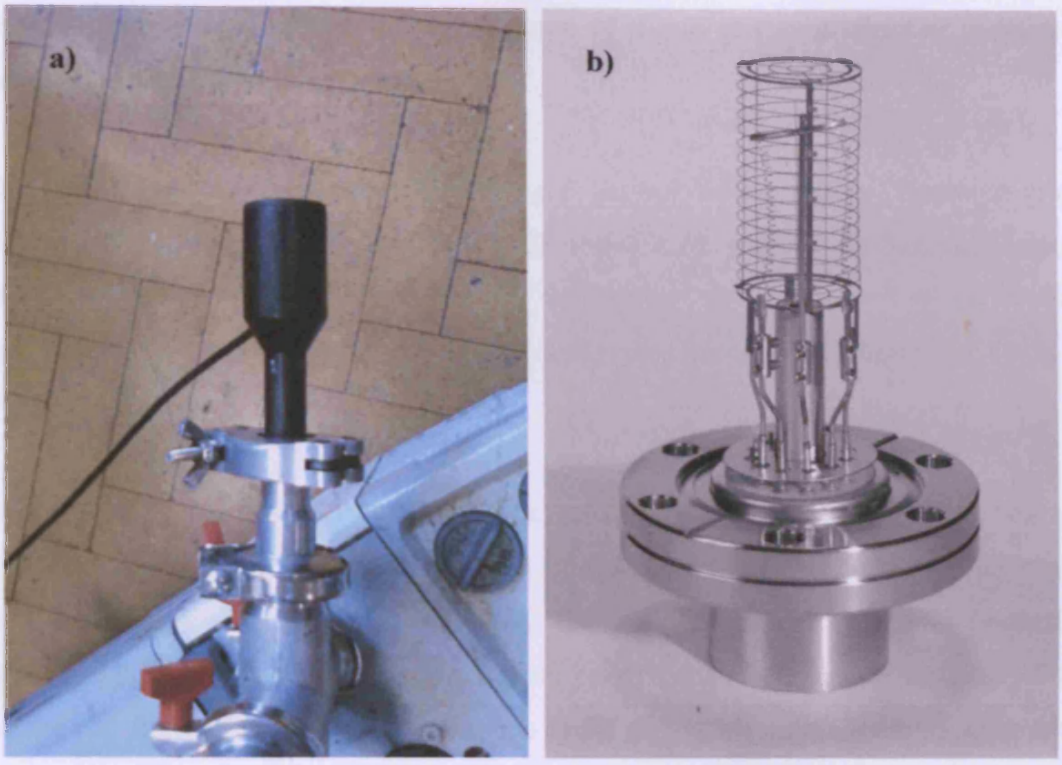

Figure 2.3: a) a pirani gauge attached to a rotary pump and b) a Bayard-Alpert ionisation gauge

2.2 The experimental samples and reagents and their relevant health risks

All experiments were carried out on polycrystalline foils. The thorium foil (19.5 mm x 9.5 mm x 1 mm Goodfellow Metals) was first cleaned in a solution of 50:50 HNO_3 and water plus 0.1 % HF after purchase to remove the thick layer of oxide formed on the surface, before initial mounting in the system. Thereafter nitric acid was sufficient to clean the thorium foil for remounting in the system after use of a different sample. Before each experiment the foil was cleaned *via in situ* argon ion sputtering (8×10^{-6} mbar Ar, 5.0 kV, 30-80 μA sample current). The thorium usually required approximately 120 minutes of argon ion sputtering to produce a surface clean enough to work with. Please see section 2.2.1 for further sputtering procedure details.

The uranium foil (19.5 mm x 9.5 mm x 1 mm Goodfellow Metals) was cleaned in nitric acid to remove the thick layer of oxide on the surface before being mounted inside the system. Before each experiment the uranium was cleaned *via in situ* argon ion sputtering (8×10^{-6} mbar Ar, 5.0 kV, 30-80 μA sample current). The uranium

usually required approximately 120 minutes of argon ion sputtering to produce a surface clean enough to work with.

These foil samples were reacted with oxygen, ammonia, and water. Research-grade oxygen (99.99 %) and ammonia (99.99 %) were used without further purification. The water used was obtained from a MicroPure source therefore no further purification was carried out. All exposures are quoted in Langmuirs (1 L = $1x10^{-6}$ Torr s).

An important issue that needs to be taken into account when dealing with actinide samples, such as thorium and uranium, is their inherent radioactivity and the health risks this brings. During any handling of the samples standard personal protective equipment (gloves, goggles and lab coat) are needed at the very least, preferably with doubled up latex gloves wrapped over the cuffs of the lab coat. Additionally, extra due care and attention is needed when attempting to mount the foil samples onto the probe, specifically to avoid contamination of multiple tools and the surrounding area, and also to avoid inhalation of any radioactive particles given off.

2.2.1 Sputtering procedure

Argon ion sputtering was carried out *in situ* to clean the samples before each experiment. This was carried out using a Vacuum Generators AG2 cold cathode ion bombardment ("sputter") gun (see figure 2.4). This particular sputter gun can operate at a wide range of different energies (from 0-10 kV) and features separate control for the purposes of focussing the beam upon the sample (the beam is normally run in a slightly defocused state to ensure adequate coverage of the large sample). In addition to the actual sputter gun a large retractable cylindrically shaped metal shield with an opening on one side is located inside the system. When extended into the system and placed around the sample, the small opening to allow access to the incoming argon ions from the sputter gun vastly limits the quantity of sputtered material from the sample that would normally be deposited all over the chamber. This is of particular importance as the samples being sputtered inside of the system are radioactive, so anything that can be done to limit the travel of radioactive particles inside the chamber is extremely beneficial.

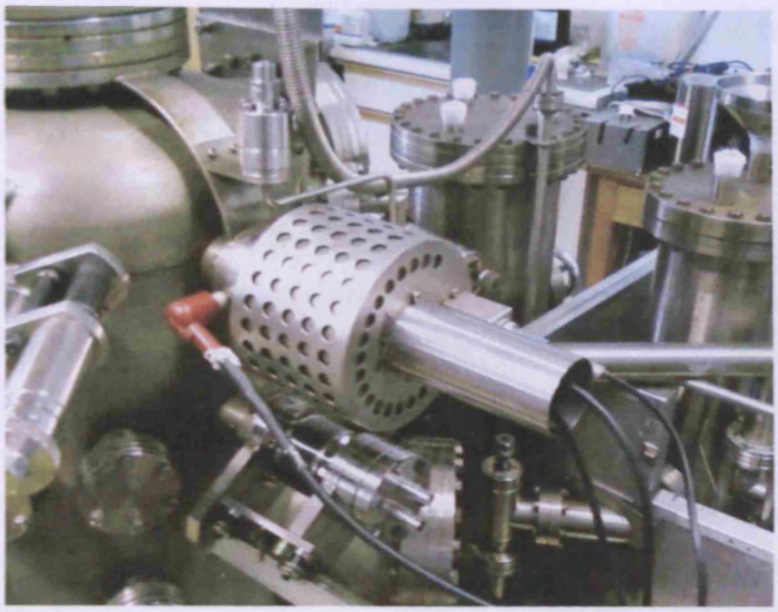

Figure 2.4: The AG2 cold cathode ion gun

2.3 Photoelectron spectroscopy (PES)

2.3.1 Introduction

Photoelectron spectroscopy is one of the most useful and widely used spectroscopic techniques available, not only to surface scientists, but to all scientific disciplines. Involving the excitation and ejection of electrons from atoms through the use of electromagnetic radiation, the technique can provide quantitative information on the atoms involved and their chemical environment. Traditionally probing only a very short distance into the surface of the sample (~50 Å), the technique is ideal for examining adsorbates, of any kind, on a surface.

2.3.2 History of photoelectron spectroscopy

Photoelectron spectroscopy is based upon the investigations of the photoelectric effect carried out by Hertz in 1887 [4]. Hertz was the first to observe the effect, which he encountered while carrying out experiments on the production and reception of electromagnetic waves. He noticed metal contacts in electrical systems exhibit an

enhanced ability to spark when exposed to light; however he did not make any substantial effort to explain this observation [5]. It was only when the effect was subsequently explained by Einstein in 1905 [6] that it was properly understood. By introducing the concept of light quanta (photons) he was able to explain the observed features of the photoelectric effect as being the result of photons of light directly transferring their energy to the electrons within an atom. When a material is hit by a photon of sufficiently high energy, there is a certain probability that it will be absorbed, stimulating emission of an electron (which is often referred to as a photoelectron) whose binding energy is less than the energy of the incident photon. As no energy is lost in the process, the resulting kinetic energy of the released electron is directly related to both the photon energy and the binding energy of the electron. The relationship is represented in both figure 2.5 and in Equation 2.3, where E_B (or BE) is the binding energy of the electron, $h\nu$ is the energy of the photon, E_K (or KE) is the kinetic energy of the resulting photoelectron, and Φ is the work function of the spectrometer. It is possible to remove the work function from the equation if the binding energies are referenced to the Fermi level of the spectrometer used.

$$E_B = h\nu - E_K - \Phi \qquad \text{Equation 2.3}$$

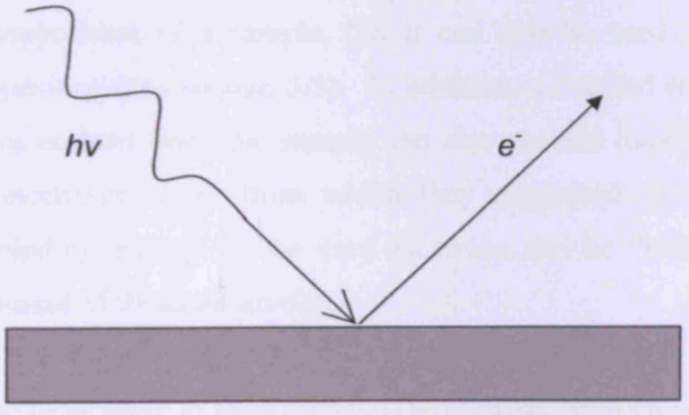

Figure 2.5: The photoelectric effect

The development and harnessing of the photoelectric effect into a useful spectroscopic technique owes a considerable debt to the work Kai Siegbahn carried out in the 1950's and 1960's, and in particular, his seminal 1967 paper [7].

2.3.2.1 The history of x-ray photoelectron spectroscopy (XPS)

The wider technique of photoelectron spectroscopy can be split into two distinct variations dependent upon the energy of the photons used to stimulate the photoemission. There is x-ray photoelectron spectroscopy (XPS), which uses x-ray photons (in the 200-2000 eV energy range) to stimulate emission from the *core* shells, and then there is ultraviolet photoelectron spectroscopy (UPS), which uses ultraviolet photons (in the 10-45 eV energy range) to stimulate emission from the *valence* shells.

The XPS variant of photoelectron spectroscopy focuses on the ejection of core electrons through the use of photons in the x-ray energy range, with two typical energies used being 1486.6 and 1253.6 eV. Figure 2.6 provides a schematic for the photoemission of a core electron due to incident x-ray radiation. These core electrons that are emitted do not participate in bonding, and have energies characteristic of the atom from which they originate. Using this information and the relationship above, Siegbahn and co-workers developed the technology by which the resulting kinetic energy of the released photoelectrons could be determined, thus allowing calculation of the original binding energy of the electrons [7]. As the binding energies are characteristic for each of the elements, the technique is extremely useful for elemental analysis. However, potentially even more important is that XPS can not only identify the elemental composition of a sample, but it can also be used to determine the quantitative composition (see section 3.3). In addition, a detailed energy analysis of the photoelectrons emitted from the sample can also provide important information concerning the electronic states from which they originated (see section 2.3.3.5 below), as the binding energy of the core electrons can be "shifted" due to the chemical environment of the atom involved.

The reason for the large lapse in time between the early research into the photoelectric effect, and the emergence of XPS as a useful technique in the 1960's, is due to the specific experimental requirements needed for the technique. These include the development of a suitably sufficient vacuum system to combat the issue of the extremely short inelastic mean free path of the emitted photoelectrons (see section 2.1.2), the development of intense monochromatised x-ray sources and the high precision voltage supplies need to operate them, and the development of electron

energy analysers of sufficiently high resolving power. All of these parts had to be fully developed before the technique of XPS, as known today, could be realised.

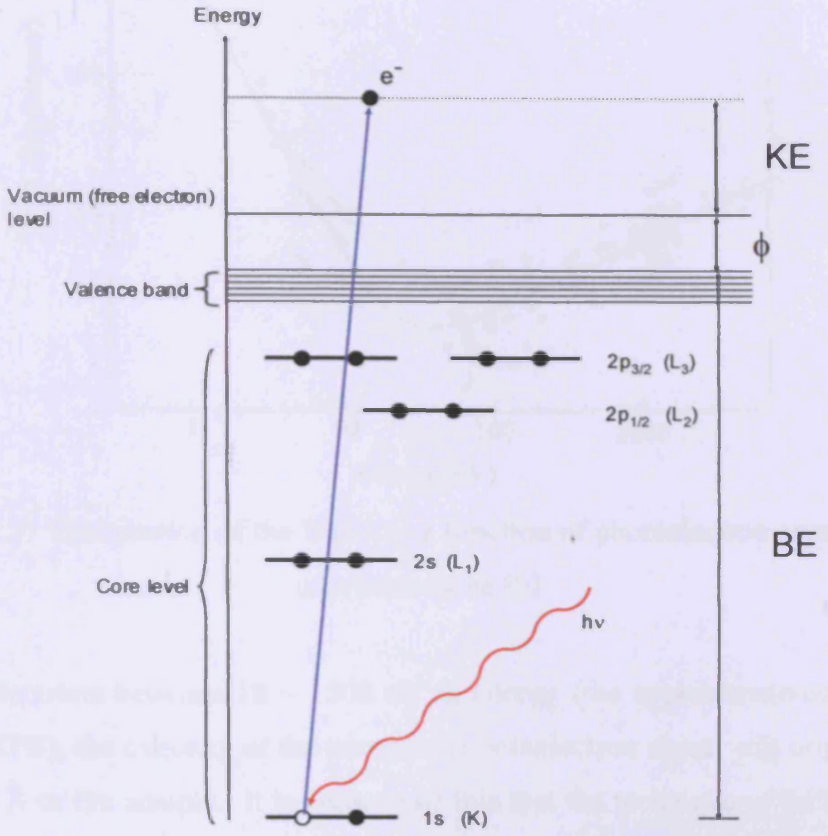

Figure 2.6: A schematic of the photoemission of a core electron due to incident photon energy. The relationship between BE, KE, and Φ can be seen on the side

One of the most important characteristics of the excited electrons utilised in all photoemission techniques is their extremely limited escape depth. The photoelectrons are the limiting factor for the depth at which the sample is probed, as the x-rays can travel microns into the sample. The photoelectron inelastic mean free path (IMFP) for a material, which is the average distance an electron travels between successive inelastic collisions [8], dictates the likelihood of an electron escaping from a material without losing any energy, and is dependent upon the kinetic energy of the electron. The dependence between the kinetic energy and IMFP has been studied extensively [9], and has given rise to the "universal" curve (see figure 2.7), which allows one to estimate the IMFP based on the kinetic energy of the electrons.

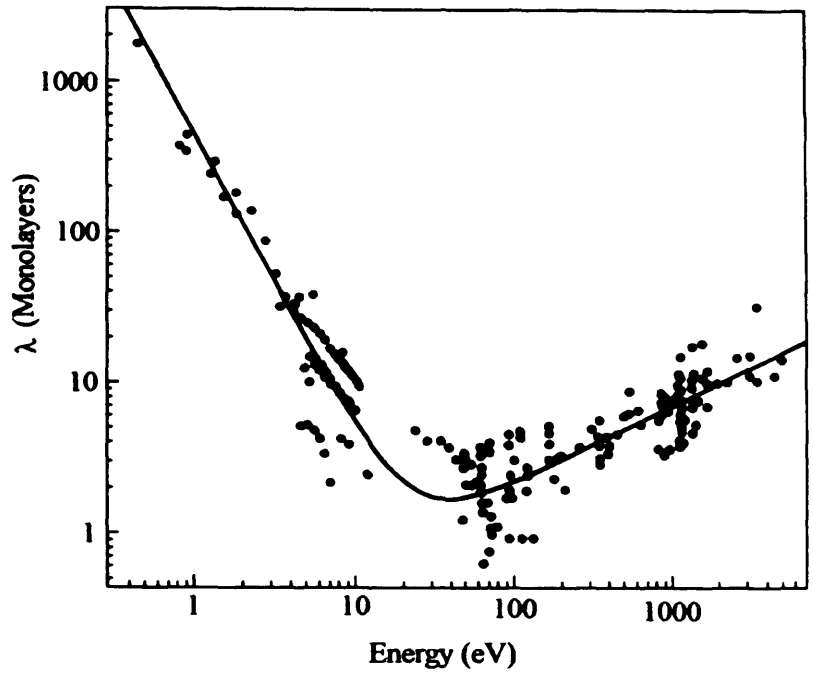

Figure 2.7: Distribution of the IMFP as a function of photoelectron energy – the universal curve [9]

For photoelectrons between 10 – 1500 eV in energy (the approximate energy range seen with XPS), the majority of the measured photoelectron signal will originate from the first 20 Å of the sample. It is because of this that the technique of XPS is so well suited to examining surface adsorbates present in concentrations less than one monolayer.

2.3.2.2 The history of ultraviolet photoelectron spectroscopy (UPS)

The UPS variant of photoelectron spectroscopy is fundamentally very similar to that of XPS; however instead of core electrons being emitted, the ultraviolet radiation used with UPS only has sufficient energy to stimulate emission of valence electrons and electrons from the molecular orbitals of adsorbed species. To highlight the difference in energy of the photons, the two principle energies of the x-rays utilised on the equipment used to produced this work are 1486.6 and 1253.6 eV, while the two typically used ultraviolet energies, used on the same system, are 40.8 and 21.2 eV. Since valence electrons are involved in chemical bonding, UPS is particularly suited to the study of bonding at surfaces. Additionally UPS readily provides measurements of the work function and band structure of the solid, the surface, and adsorbed layers.

As UPS is merely a particular variant of the wider technique of photoelectron spectroscopy, its origins are largely the same as that previously described for XPS in section 2.3.2.1. While Siegbahn and co-workers are largely responsible for XPS being the useful technique it is today, it is down to Eastman and Cashion [10] that UPS is as widely used today as it is. In 1971 they were the first to integrate a differentially pumped helium lamp with a UHV chamber. They showed that even submonolayer quantities of adsorbed gases can significantly modify the measured electron distribution curves at the valence band. While Eastman and Cashion are no doubt largely responsible for the prevalence of the technique today, it is worth mentioning that there were however others who utilised the principles to look at the valence region before them. Quinn and Roberts for example investigated the reactions of hydrogen and oxygen on the surface of nickel with an external mercury-vapour lamp, joined to the chamber *via* a quartz window, which produced the ultraviolet radiation [11].

It is worth mentioning some of the specific benefits of investigating the valence states (with UPS) that you do not get by just studying the core levels (with XPS). The valence electrons that are ejected through the use of the UPS technique come from very near the surface region, and provide information on the density of states (DOS) at the Fermi edge, and molecular orbital occupancy in any adsorbates. By accurately measuring the binding energy of the photoemission peaks, surface molecular dissociation can be monitored from a direct observation of molecular orbital populations. Another additional benefit is that by measuring the DOS at the Fermi edge, a direct measure of the metallic or insulating nature of the material can be gained.

2.3.3 Principles and rules of photoelectron spectroscopy

2.3.3.1 Basic principles

Superficially, the photoelectron energy spectrum should simply show the occupied density of states in the surface transposed up in energy by an amount *hv*. However there are additional complications in the form of final state effects that need to be taken into account. The act of photoemission from an atom results in a final state

containing one less electron than the initial state. Thus in reality photoemission spectroscopy actually measures the final state energies, and can only reveal the initial state energies after certain theoretical considerations have been made.

2.3.3.2 Koopmans' theory

Koopmans assumed that the binding energy of an ejected electron was equal in energy to the orbital from which it came [12]. For this to be true it relies upon the binding energy 'seen' by the photoelectron, E_b, of the state it leaves being the same as it was before the interaction. This means all the other electrons in the system have to remain in the same state as before the photoionisation event. Such a situation reflects Koopmans' theorem and this energy, E_b, is therefore referred to as Koopmans' energy. In this case E_b is referred to the Fermi level, and the emergent kinetic energy is indeed given by Equation 2.4:

$$KE = h\nu - E_b \qquad \text{Equation 2.4}$$

However, as this relies upon the false assumption that the photoelectron emission process does not disturb any of the other orbitals, Equation 2.4 is only approximately correct. Koopmans' theorem completely neglects the fact that, in an attempt to screen the newly formed positively charged core hole, the electron cloud within the ion 'relaxes'. This relaxation leads to a lowering in the binding energy values that are actually seen, which are subsequently attributed to differences between the initial and final states, which in turn result in the higher observed kinetic energy. Specifically, the relaxation energy is the energy necessary for the adjustment of the total system in response to the hole left in a specific orbital due to the photoemission effect.

2.3.3.3 Relaxation and the Core hole

Emission of the photoelectron leaves a core hole and produces a short lived, high energy, ionic system. To neutralise the core hole, and the system itself, a rearrangement takes place where an electron from an outer shell drops down to fill the hole. There are two possible consequences:

X-ray fluorescence – The outer electron falls into the lower energy core hole, and releases the excess energy in the form of an x-ray photon. Therefore the released photon is equal in energy to the difference between the initial and final levels of the electron involved (see figure 2.8 a):

$$h\nu = \varepsilon_A - \varepsilon_B \qquad \text{Equation 2.5}$$

Auger transition – The core hole is again filled by a more energetic electron, however in this case the excess energy is used to ionise one of the outer orbitals. This non-radiative mode of decay emits a secondary electron known as the Auger electron, resulting in a doubly ionised system (see figure 2.8 b):

$$E \approx \varepsilon_A - \varepsilon_B - \varepsilon_C \qquad \text{Equation 2.6}$$

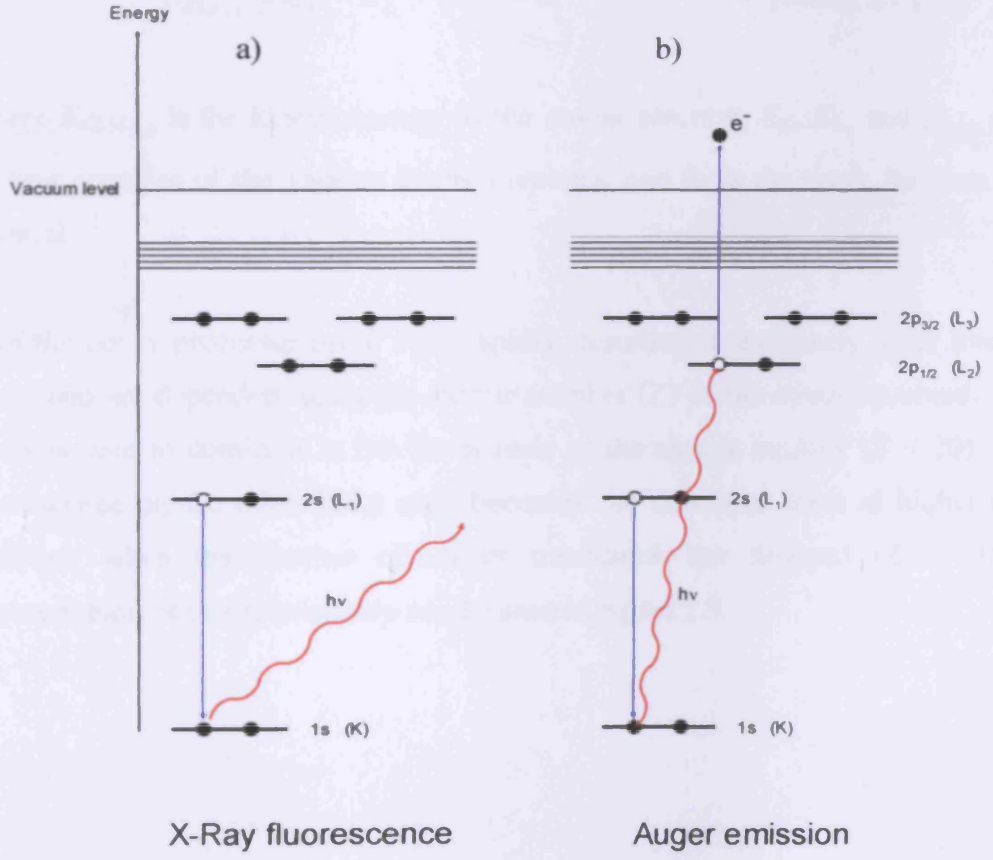

Figure 2.8: Core hole decay *via* a) X-ray fluorescence and b) the Auger process

Auger transition results in the emission of an additional electron, which will be detected along with the directly x-ray induced photoelectrons. The additional Auger electrons will appear as discrete lines on an x-ray photoelectron spectrum. The Auger electrons are easily distinguishable from photoelectrons whose kinetic energies are dependent on the incident photon energy (see section 2.3.4.1). For example the kinetic energy of the nitrogen KLL Auger peak is 375 eV regardless of the incident photon energy, while the kinetic energy of the nitrogen 1s photoemission peak is 855 eV if the photon energy is 1253.6 eV (Mg $K\alpha_{1,2}$) but 1088 eV if it is 1486.6 eV (Al $K\alpha_{1,2}$). The kinetic energy of an Auger electron can be calculated from the binding energies of the various levels involved. Equation 2.7 below provides an example of this based on the KLL levels mentioned above for the nitrogen Auger peak:

$$E_{KL_1L_{2,3}} = E_K - E_{L_1} - E_{L_{2,3}} - \Phi \qquad \text{Equation 2.7 [13]}$$

Where $E_{KL_1L_{2,3}}$ is the kinetic energy of the Auger electron, E_K, E_{L_1} and $E_{L_{2,3}}$ are the binding energies of the various levels involved, and Φ is the work function of the material.

Both the decay processes occur very rapidly, resulting in extremely short lived core holes, and are dependent upon the atomic number (Z) of the atoms involved. Auger decay is seen to dominate at the lower ends of the atomic number ($Z < 20$). X-ray fluorescence on the other hand only becomes the dominant form at higher atomic numbers, when the number of Auger transitions has dropped ($Z > 30$). A representation of this relationship can be seen in figure 2.9.

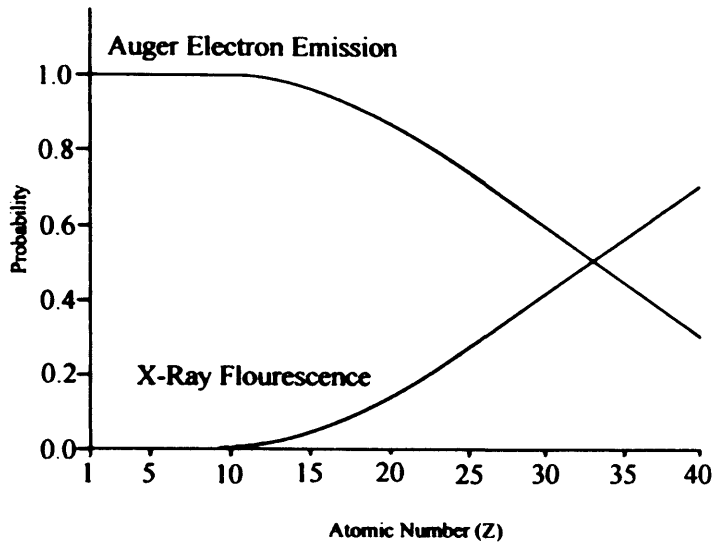

Figure 2.9: The relative probability of x-ray fluorescence and Auger electron emission in relation to the atomic number (Z) of the atom

2.3.3.4 X-ray satellite structure

The brief presence of the core hole following photoemission can have a direct affect upon the many emitted photoelectrons. The energy of these photoelectrons can end up altered, leading to a number of additional different signals located close to the main peaks, which are known as satellites. These can be due to a number of different processes, including:

a) Shake-up satellite

There is a potential for the emitted photoelectrons to interact with the valence electrons contained in the atom. A portion of the kinetic energy of the photoelectron can be imparted to one of the valence electrons, exciting it into a higher unoccupied state. Based on Equation 2.3, as a proportion of the kinetic energy is lost, it gives the photoelectron the appearance of having been bound more strongly. This results in a satellite feature located on the higher binding energy side of the main peak (see figure 2.10). As these satellite features are associated with an electronic excitation, they can provide valuable information about the unoccupied states involved [14].

b) Shake-off satellite

The shake-off process is the result of the whole photoionisation event, and occurs when an outer electron is sufficiently excited so as to leave the atom. This creates a double ionised state which leads to a very broad XPS feature which is most often lost within the general background of inelastically scattered electrons (see figure 2.10). Unlike the shake-up satellites, the shake-off satellites yield no useful spectroscopic information.

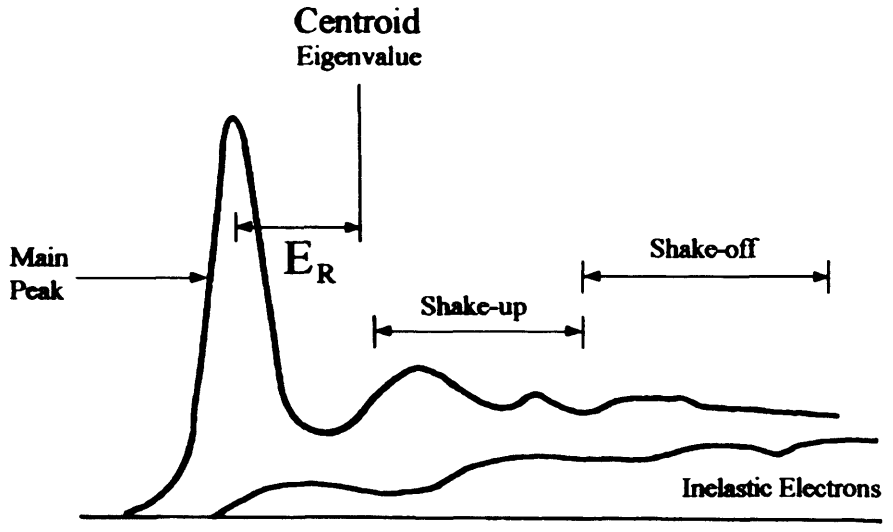

Figure 2.10: The basic elements of an XPS spectrum – including the shake-up and shake-off satellites [15]

c) Multiplet splitting

Multiplet splitting, also known as spin-spin coupling, occurs when an unpaired valence electron interacts with the newly unpaired core electron left after photoemission. This results in two separate final states which are dependant on the alignment of the spin vector(s) of the electrons, either parallel or anti-parallel, resulting in two distinct peaks in the x-ray photoelectron spectrum. Multiplet splitting is most noticeable for the 3s orbitals when unpaired electrons are present in 3d orbitals and as such should not be a significant factor in these studies.

d) Spin-orbit coupling

The magnetic coupling between the spin of an unpaired core electron with its angular momentum can also cause splitting, but of a far greater magnitude than that seen with spin-spin coupling. This particular type of magnetic coupling is known as spin-orbit coupling.

An electron is a charged particle, and as such its orbit around a nucleus induces a magnetic field. The intensity and direction of this field depend on the electron velocity and on the radius of the orbit respectively. It is possible to characterise these by an angular momentum, called the orbital angular momentum, which is quantised due to the fact the electron may only travel in certain discrete orbitals. The quantum number is l, and can take the values 0, 1, 2, 3, 4, ... In addition to the orbit inducing a magnet field, the electrons also possess a spin (positive or negative), which will also induce a magnetic field. This in turn possesses a spin momentum, which is characterised by a spin quantum number s, which can take the values of +½ or -½. By combining the orbital angular momentum with the spin momentum, by summing the two vectors, you get the total electronic angular momentum. However the vector sum can be carried out using two specific methods; j-j coupling or L-S (Russell-Saunders) coupling.

j-j coupling – The total angular momentum of an electron is obtained by summing the vectors of the individual electron spin and angular momenta. This is then characterised by the quantum number j, where $j = l + s$. Based on this it is clear that j can take the values 1/2, 3/2, 5/2, etc. To calculate the total angular momentum of the entire atom, J, the contributions from all the electrons must be summed together, so that $J = \Sigma j$. This description is known as j-j coupling, and is known as a good description of the electronic interaction, especially in elements of high atomic number ($Z > \sim 75$), where it is known as the best description.

L-S coupling – In this method all the individual electronic angular momentum are summed separately from anything else to give the total atomic orbital angular momentum quantum number L, which is equal to Σl. After this the individual electronic spin momenta are summed in the same way to give the total atomic spin

quantum number S, which is equal to Σs. These two total momenta can then be coupled to give total atomic angular momentum, which can be characterised by the quantum number J, which in this case is equal to L ± S (hence the name L-S coupling). Unlike j-j coupling, L-S coupling has been found to give a better description of the electronic interactions in the elements of low atomic number (Z < ~20).

As can be seen in figure 2.11, the splitting bought about by the spin-orbit coupling is large enough to result in a definitive doublet being visible. It is worth pointing out however that the splitting is not always of sufficient size to generate distinct doublets (for example the splitting of the Al(2p) signal is miniscule).

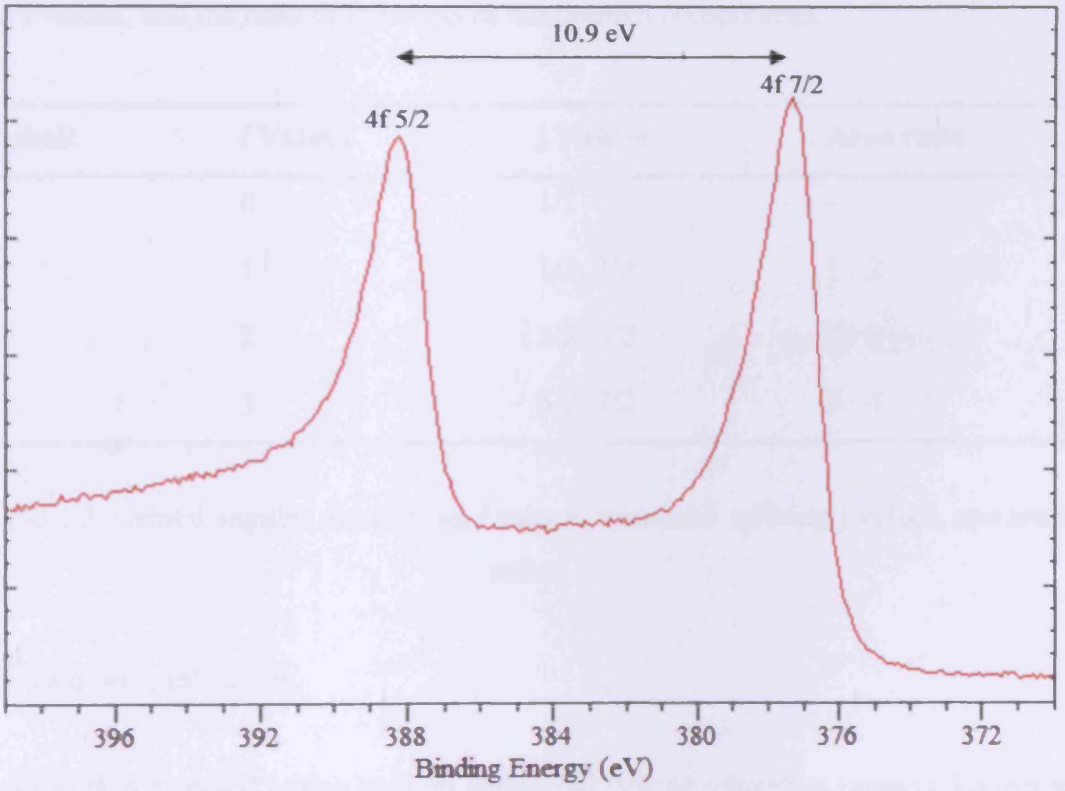

Figure 2.11: U (4f) spectrum of clean uranium to demonstrate the definitive doublet produced by spin-orbit coupling. The splitting between the 5/2 and 7/2 signals is 10.9 eV

The doublets are features of all p, d and f core levels, but not of the s core levels. This is because the two possible states, characterised by the quantum number j (where $j = l + s$, as explained above), only arise when $l > 0$. The difference in energy of the two separate states, ΔE_j, mirrors the parallel and anti-parallel nature of the spin and orbital angular momentum vectors of the remaining electron left after photoemission. The magnitude of the energy separation is proportional to the spin-orbit coupling constant which depends on the expectation value ($1/r^3$) for the particular orbital. The value of ΔE_j increases as Z increases for a given subshell (where n and l are constant), or it increases as l decreases for a constant n (e.g. for thorium the splitting of 4d > 4f).

The relative intensities of the two resultant peaks are given by the ratio of their respective degeneracies (2j + 1). Table 2.2 lists the different subshells, their l values, their j values, and the ratio of the areas of the doublet components.

Subshell	***l* Values**	**j Values**	**Area ratio**
S	0	1/2	-
P	1	1/2, 3/2	1 : 2
D	2	3/2, 5/2	2 : 3
F	3	5/2, 7/2	3 : 4

Table 2.2: Orbital angular momentum l values, spin-orbit splitting j values, and area ratios

e) Extra atomic relaxation

Atoms within a crystal lattice gain an additional unique relaxation process, known as extra atomic relaxation. This occurs when the valence electrons of surrounding atoms contract in an effort to screen the newly formed core hole. The contraction causes a lowering in the final state energy, which leads to the acquired spectrum shifting to lower energy.

f) Plasmon loss effect

A portion of the kinetic energy of outgoing photoelectrons can be lost, inducing collective oscillations in the conduction band, as they pass through the solid. These oscillations are known as plasmons, and are at fixed frequencies characteristic of the material being looked at. The energy losses due to these plasmons manifest themselves as a series of regularly spaced discrete loss features of decreasing intensity in the acquired x-ray photoelectron spectrum. Plasmon loss features are predominantly observed with materials that feature an s- or p- type valence density close to the Fermi edge. As d- and f- type character is not advantageous towards plasmon losses, the effects of this particular loss mechanism are unlikely to be of much concern within the context of this f-block dominated work.

2.3.3.5 Chemical shift

As well as finding out the absolute binding energy of a particular core level, it is also of great interest to determine the change in binding energy between different chemical forms of the same atom. This added capability of being able to measure the binding energy difference between two or more inequivalent chemical environments of the same atom, which is known as the chemical shift, is potentially one of the strongest and most important analytical features of photoemission spectroscopy.

The chemical shifts are due to two different effects working together; the first being final state effects (explained above), and the second being initial state effects. The initial state effects can be thought of as the 'true' chemical shift, as they are due purely to the changes in electronic environment around the atom in question. Even without a true quantitative description of these effects, valuable work can still be performed using the chemical shifts observed in known systems as a fingerprint. Because of this fact extensive work has been carried out to tabulate and compile observed chemical shifts to provide a library of reference data to compare unknown spectra with.

The first person to observe the chemical shift phenomena was Siegbahn [7] who recorded a discrete double peak structure in the spectrum of sodium thiosulphate (see

figure 2.12). He attributed this result to the different chemical states of the two sulphur atoms, with the central sulphur atom being more electropositive due to the electron-withdrawing oxygen atoms.

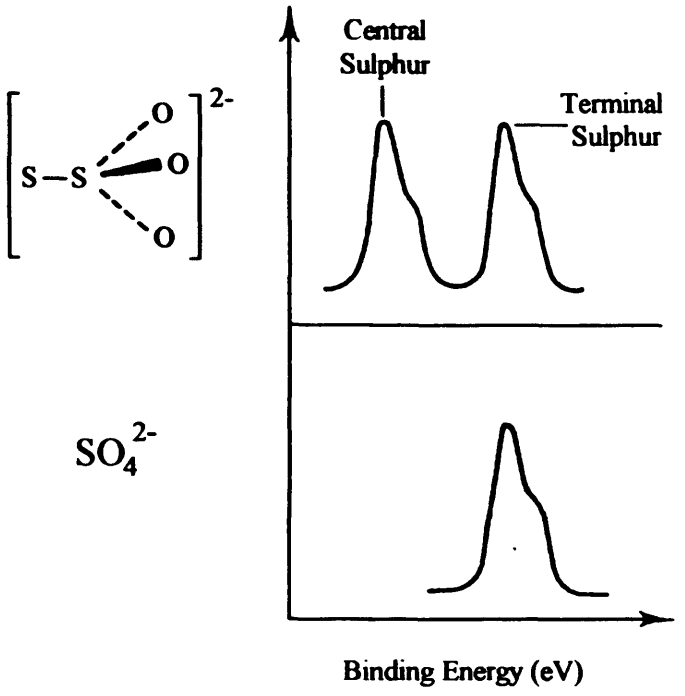

Figure 2.12: An illustration of chemical shift. The central and terminal sulphur atoms produce two different signals in the S(2p) region [7]

2.3.3.6 Angle resolved XPS

For enhanced sensitivity of the outer most layers of the surface, it is possible to vary the collection angle (Φ) between the analyser direction and the normal to the surface. By increasing Φ, photoelectrons collected from a depth d will have to travel further through the material before escaping the surface. Since the inelastic mean free path of the photoelectron (λ) is dictated by its energy, and is thus fixed in this scenario, only photoelectrons from the outermost layers will escape without losing energy. This relationship between the collection angle and the mean escape depth *ED* (the average depth normal to the surface from which the photoelectrons escape [8]) can be described as:

$$ED = \lambda \cos \Phi \qquad \text{Equation 2.8}$$

Figure 2.13 provides a simple visual comparison of the mean escape depths *ED* of a) a sample where the collection angle is 0° to the analyser, and b) a sample where the collection angle is 45° to the analyser. As can be seen by the relative sizes of the arrows labelled *ED*, at a grazing angle of 45° between the analyser and the surface normal, the photoelectrons originate within a smaller depth of the sample, and are thus more surface sensitive.

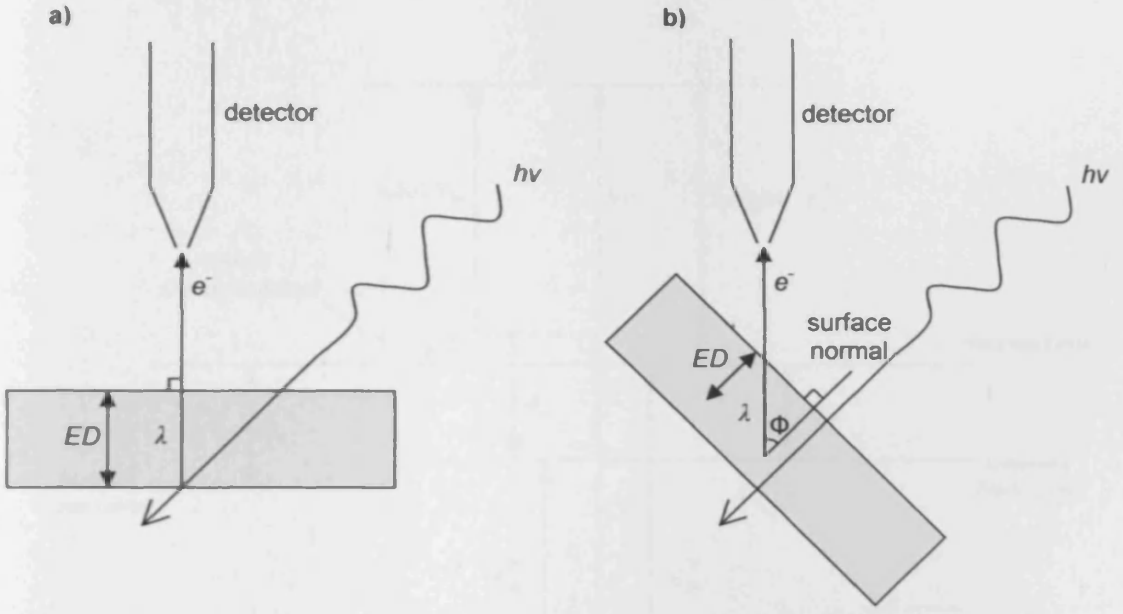

Figure 2.13: A comparison of the mean escape depths *ED* of a) a sample where the collection angle is 0° to the analyser, and b) a sample where the collection angle is 45° to the analyser

The ability to vary the surface sensitivity by varying the collection angle is why angle resolved XPS is thought of as such a useful tool for the identification and characterisation of surface species. While the technique can be extremely useful it is worth noting that this is only for planar systems, as a rough non-uniform surface would lead to false, anomalous or misleading results.

2.3.3.7 The reference level

For accurate comparisons to be made between experimental binding energies, a definitive definition of an energy reference level is required. The reference level for

the electron binding energy scale of gaseous molecules was simply and conveniently chosen as the vacuum level at infinity.

For electrically conducting samples the Fermi level was chosen to be used as the reference level. This relies on the equalisation of the Fermi levels by means of charge sharing across the sample, sample probe, and the earthed spectrometer (an energy level diagram of this can be seen in figure 2.14).

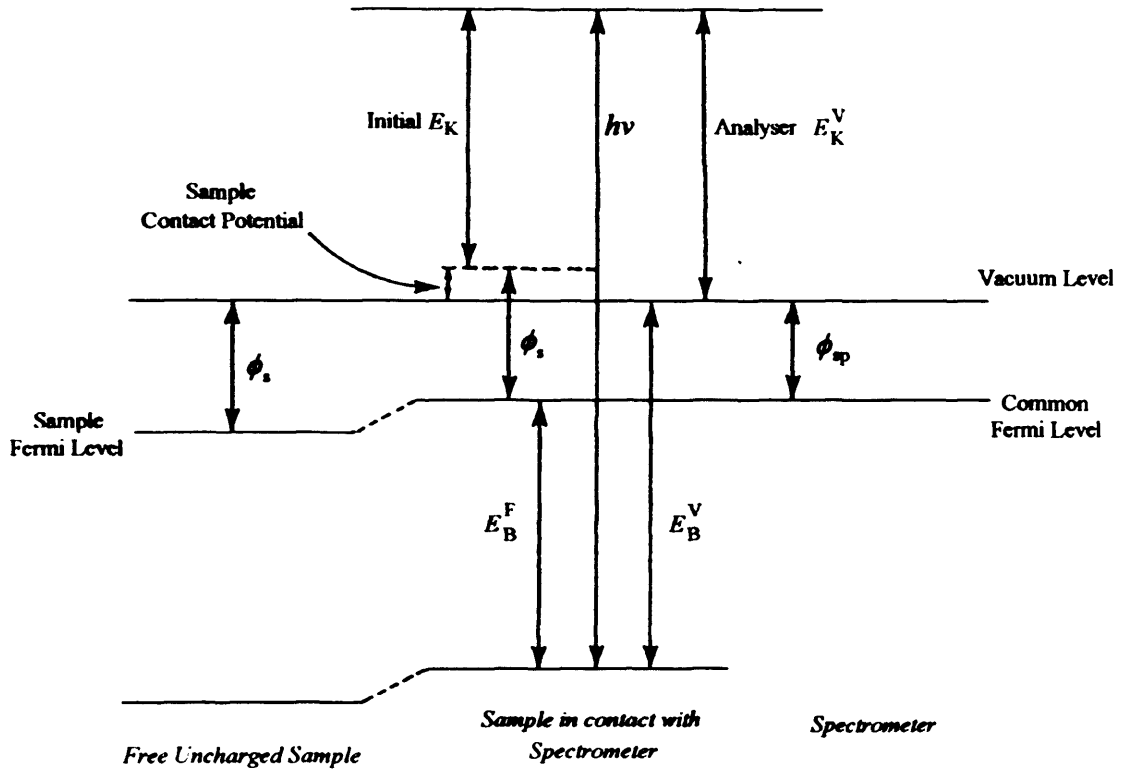

Figure 2.14: An energy level diagram comparing a free uncharged sample, a conducing sample that is in direct contact with the spectrometer, and finally the spectrometer itself [15]

With insulating samples, photoemission spectroscopy measurements suffer charging effects. These arise due to the photoionisation processes creating an electron deficient surface. In addition to this, insulating materials may also suffer from the 'floating' Fermi edge effect brought about by the lack of electrical equilibrium between the sample and the system. These two effects can result in large shifts in the binding energies in the results collected, which can lead to misidentification of signals. This is of particular issue when dealing with real catalytic systems, as the majority of these

are based on insulating metal oxides. The charging effects can be minimised through the use of an electron charge neutraliser, which is designed to neutralise the increasing positive charge on the surface. Alternatively the resulting spectra can be calibrated based on a known constant such as adventitious carbon impurities or a deposited thin gold film, to compensate for the charging effects. However it is worth noting that neither of these are truly effective in obtaining valid binding energies since neither promotes Fermi level coupling [16].

2.3.3.8 Line broadening effects

As the energy levels within atoms are quantised, the acquired photoemission spectrum should theoretically consist of sharp well defined peaks. This however is not the case, as the peaks observed in spectra are commonly broad, which is due to the influence of a number of different factors. Assuming a Gaussian distribution of the components, the peak width (ΔE), which is defined as the full width at half maximum (FWHM), is given by Equation 2.9

$$\Delta E = \left(\Delta E_n^{\,2} + \Delta E_p^{\,2} + \Delta E_a^{\,2}\right)^{1/2} \qquad \text{Equation 2.9}$$

Where ΔE_n is the inherent line width of the core level, ΔE_p is the width of the x-ray line, and ΔE_a is the resolution of the analyser.

The most significant of these contributions, when using a monochromatic x-ray source, is the analyser resolution (ΔE_a), which results in a broadening of approximately 1 eV (this can be lowered through the use of low pass energies).

The second contribution is associated with the width of the x-ray source line itself. The natural line widths (ΔE_p) of the two most commonly used x-ray sources, Al Kα and Mg Kα, are 0.85 eV and 0.70 eV respectively. It is possible to minimise x-ray source broadening through the use of a monochromator. When a monochromator is not used the broadening due to the x-ray source and the analyser are comparable in size.

The final contribution is connected to the lifetime of the core hole produced during photoemission, and is known as the natural width of the photoelectron peak (ΔE_n). The relationship can be expressed in terms of the Heisenburg Uncertainty Relationship.

$$\Delta E_n = \frac{h}{\tau} \qquad \text{Equation 2.10}$$

Where ΔE_n is the natural line width in eV, h is Planck's Constant, and τ is the core hole lifetime in seconds.

Core holes with very short lifetimes, due to the efficient decay of the core hole state will suffer significantly more broadening. In comparison, the longest lived core holes, whose decay is dependent on the rate at which x-ray fluorescence or Auger emission occur, will suffer significantly less broadening.

Additionally, coupling between the core hole and the nuclei within the solid lattice can lead to phonon broadening. Vibrations within the lattice, known as phonons, are induced and can then be observed as Gaussian broadening of the photoelectron peak. This broadening effect is temperature dependent, and is normally not significant enough to cause serious complications.

2.3.4 X-ray photoelectron spectroscopy (XPS)

As mentioned earlier, x-ray photoelectron spectroscopy (also known as Electron Spectroscopy for Chemical Analysis) is a specific variant of photoemission spectroscopy, and is a very useful technique for the analysis, both quantitative and qualitative, of the surface of a sample. It enables identification of the elemental composition and chemical states of the different species in the surface region.

2.3.4.1 XPS instrumentation

There are three main components of the equipment, with the first being the dual x-ray anode source, capable of supplying non-monochromatic x-rays for XPS. The source

provides both Al $K\alpha_{1,2}$ and Mg $K\alpha_{1,2}$ electromagnetic radiation, with photon energies of 1486.6 eV and 1253.6 eV respectively, both of which originate from fluorescence arising from a 2p → 1s electronic transition (a schematic of the anode can be seen in figure 2.15). The big advantage of a dual anode system is the ability to switch between sources and resolve any interference which can occur between the photoelectron and Auger electron signals. As was shown in section 2.3.3.3 (and figure 2.8), this is because the kinetic energy of the Auger electrons is independent of the photoelectron energy, and is instead only dependent on the energy difference between two different levels in the atom. So switching the choice of x-ray anode will result in all photoelectron peaks shifting by 233 eV on the kinetic energy scale (the difference in energy between the two anode sources), while the peaks due to the Auger electrons will remain in the same positions.

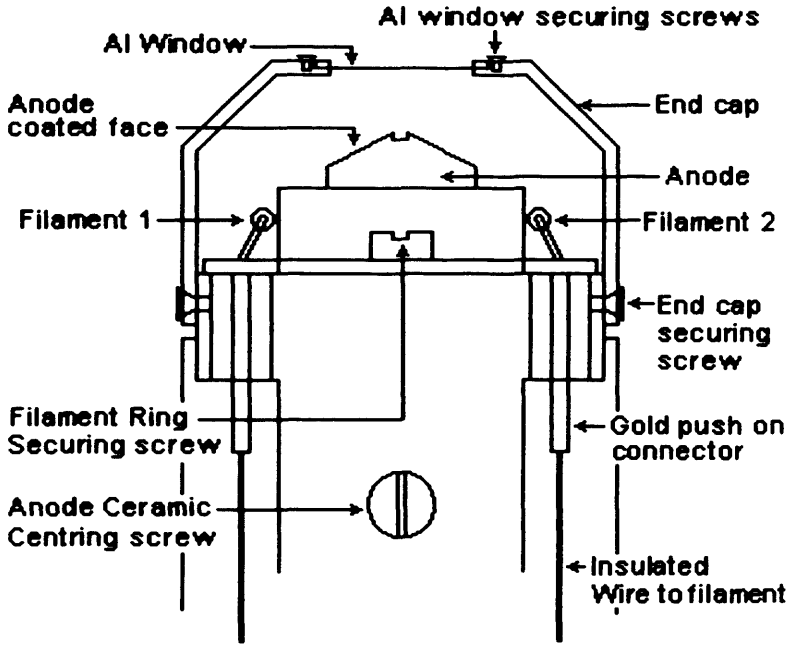

Figure 2.15: A schematic of the end of the x-ray gun. The key components of the gun; the filaments, anodes, and aluminium window are all labelled.

The x-rays are produced when high energy electrons generated by a thoriated iridium filament are accelerated (by an approximately 15 kV potential difference) onto the target anode, which in this case is either aluminium or magnesium. The process of the electrons hitting the target anode produces x-ray radiation in two distinct ways. Firstly, there is the process of incoming high energy electrons knocking core electrons out of the anode nuclei, producing short lived, high energy ionic systems. As was

explained in section 2.3.3.3 (and figure 2.8), to neutralise this core hole a rearrangement can take place where an electron from an outer orbital can drop down into the hole. This releases the excess energy in the system in the form of an x-ray photon or Auger electron (since Z is low for Al and Mg, based on figure 2.9, Auger electron emission dominates). The released photon is equal in energy to the difference between the initial and final level of the rearranging electron. This process of x-ray production is by far the most important and useful of the two for the purposes of this work.

The second of the two processes in which the high energy electrons striking the target anode produce x-rays is based on the principle of radiative deceleration. As the electrons approach and travel through the target material they will pass the positively charged nuclei of the target atoms, leading many of them to be deflected and decelerated from their paths due to the opposite charges they both possess. As the electrons are decelerating the excess energy that they contain is released in the form of x-ray radiation. The continuous spectrum of x-ray energies that this process produces is known as the Bremsstrahlung (meaning "braking radiation").

The two processes that produce the x-rays occur at the same time, resulting in the total x-ray emission spectrum that can be seen in figure 2.16. As it is the defined $K\alpha_{1,2}$ signal that we desire for the technique, the x-rays that are produced travel though a thin aluminium window (approximately 10 μm thick) before heading towards the sample. This has the dual benefits of blocking out approximately 80 % of the Bremsstrahlung, as well preventing any stray electrons (including Auger electrons) and contamination from the x-ray source from entering the chamber.

As the x-rays used were not monochromated additional satellite lines arise on the acquired spectra. These are due to transitions other than the primary $K\alpha_{1,2}$ transitions, such as the $K\alpha_{3,4}$ line (see figure 2.16). The $K\alpha_{1,2}$ and $K\alpha_{3,4}$ expressions are referred to as Siegbahn notation, with the K, α and number indicating precisely which electronic transition is concerned.

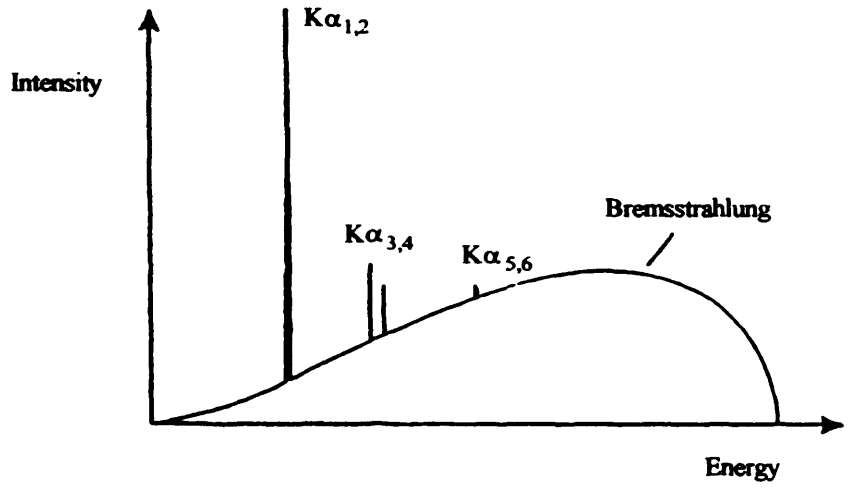

Figure 2.16: X-ray emission spectrum. The principle transitions are superimposed on the rising Bremsstrahlung background.

The desired $K\alpha_{1,2}$ radiation arises from a 2p → 1s electronic transition, the undesired $K\alpha_{3,4}$ radiation also arises from the same transition, however in the presence of additional 2p core holes (referred to as 'spectator holes') which reduce the screening and shift the total energy of the shell upwards in energy, resulting in an increase to the energy released from the 2p → 1s transition. For the aluminium anode the main observed satellite peaks, $K\alpha_{3,4}$, are situated at approximately 10 eV lower binding energy than the main peaks, with their intensities being approximately 10 % that of the main peak. It is particularly important to take the satellites into account, as when you have a doublet signal with a splitting value close to the satellite separation value, the satellite from the higher energy signal will overlap directly with the signal from the lower energy component of the doublet. An example of this can be seen in the thorium spectra of figure 2.17 a). To counteract this problem it is possible to subtract these specific x-ray based satellites, the result of which can be seen in figure 2.17 b). In addition to the obvious loss of satellite signal at around 325 eV, a visible drop in intensity can clearly be seen in the lower energy peak of the doublet, which demonstrates that the size of the satellite component that overlaps it is not insignificant, and cannot be ignored. The value that can be seen at the top of both of the spectra is the residual STD, which provides a measure of the quality of the curve fits applied (see section 3.2.8 for details). In this particular case, the lower the value, the more accurate the combined curves are for emulating the measured signal. It can be seen in the figure that the removal of the satellites led to an improvement in the

quality of the peak fitting, which is another reason why it is so important to take the x-ray induced satellites into consideration.

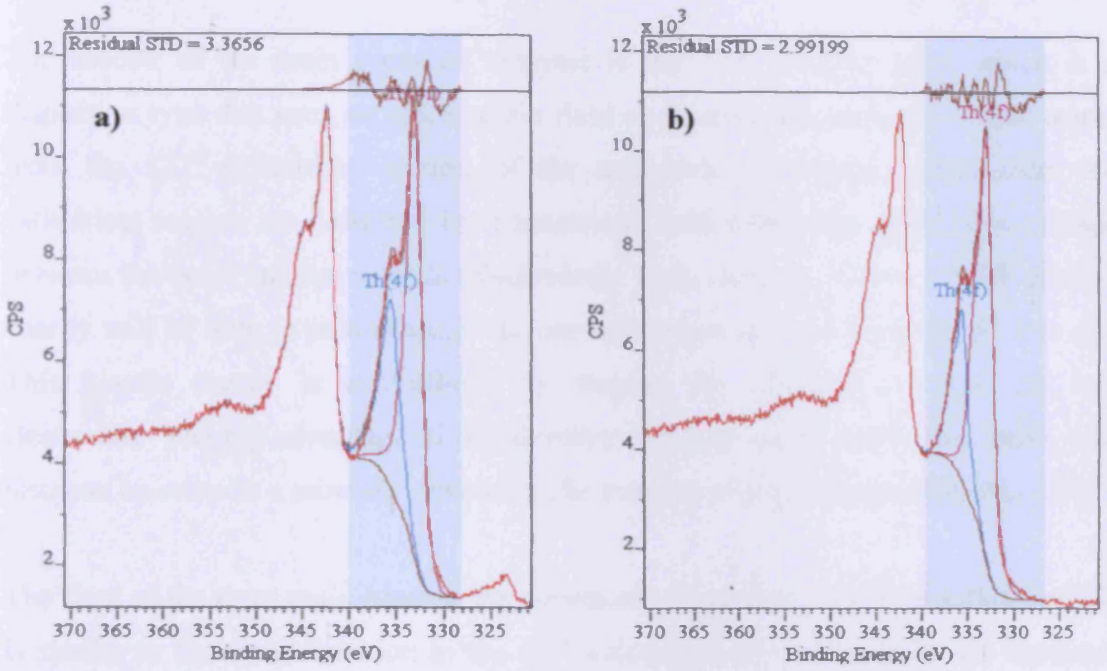

Figure 2.17: Th(4f) spectra of clean thorium metal at ambient temperature – where a) is before removal of the overlapping x-ray satellite while b) is after removal of the overlapping x-ray satellite.

Allowing measurement of the kinetic energies of the photoelectrons, the electron energy analyser is the second vital piece of equipment needed to carry out XPS. There are multiple types of analyser available, each with their own advantages and disadvantages. Possibly the simplest example is the retarding field grid analyser (RFA), which utilises multiple optically highly transparent grids setup between the electron source and collector. When a negative potential V_G is applied between the grids and the sample, only electrons with kinetic energy $E_K > eV_G$ will be able to reach the collector, because of electrostatic deflection. The kinetic energies allowed through can be varied by altering the potential applied, thus providing the equipment with the capability to distinguish and analyse electrons. While a simple experimental setup, and one that features a large angle of electron acceptance (~120°), the RFA has a distinct disadvantage in that it collects *all* emitted electrons whose kinetic energy is enough to overcome the applied potential (there is not a means to filter the high and low energy electrons at the same time). This leads to poor resolution, increased noise, and the need to increase scan time in an effort to counteract these effects.

Furthermore it generates an integral spectrum. This particular analyser is still often used for the purposes of Auger electron spectroscopy [17].

The second of the main types of analyser is the 127° analyser [18], which is a dispersion type that uses an electrostatic field to separate electrons (the name stems from the 127° cylindrical section of the analyser). Electrons which enter the cylindrical section are deflected by a transverse field created by applying a voltage between the outer and inner walls (electrodes). Only electrons with a specific kinetic energy will be able to pass through the curved section and exit through the exit slit. This kinetic energy is controllable by varying the potential between the two electrodes. The big advantage of this detector is that it can be made very small, and thus can be setup as a movable device for the purpose of angle-resolved studies [17].

The final of the three main types is the concentric hemisphere analyser (CHA), which is similar in form and function to the 127° analyser above. This is by far the most popular of the analysers, as it has been highly developed [7], and features very high resolution capabilities. A schematic of the analyser featuring the principles of operation can be seen in figure 2.18. The CHA consists of two hemispherical surfaces of radii R_1 (inner sphere) and R_2 (outer sphere) positioned concentrically. A potential difference is applied to the surfaces so that R_1 is positive and R_2 is negative. These potentials act producing an area of zero potential equidistance from each hemisphere at radius R_0, when ideally,

$$R_0 = \frac{R_1 + R_2}{2} \qquad \text{Equation 2.11}$$

Electrons entering the analyser encounter an applied retarding potential (V_A) between the hemispheres, which decelerates and decreases the energy of the electrons to a constant fixed energy, known as the analyser pass energy (E_A). Only electrons with this specific energy will pass through the analyser without striking either hemisphere surface on the way to the detector. The equation relating pass energy and the applied potential (V_A) is seen in Equation 2.12.

$$E_A = V_A\left[\frac{R_1}{R_2} - \frac{R_2}{R_1}\right] \qquad \text{Equation 2.12}$$

The term in the brackets is the hemispherical constant. Pass energies are fixed and are typically 20, 50, or 100 eV, depending on the desired resolution. A retarding potential (V_R) is applied to the sample to decelerate the photoelectrons, so that: -

$$K.E. = E + eV_R \qquad \text{Equation 2.13}$$

Where $K.E.$ is the kinetic energy of the photoelectron, E is the analyser pass energy, e is the electron charge, and V_R is the retarding potential.

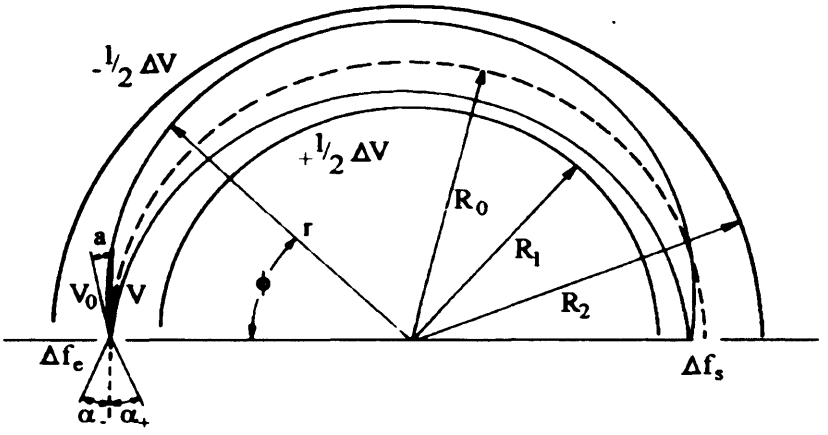

Figure 2.18: A schematic of the principle way in which the concentric hemisphere analyser (CHA) functions [19]

By altering the retarding potential of the electrodes it is possible to vary the kinetic energies of the photoelectrons passing through the analyser to the detector. Normally the retarding potential is linearly ramped so that the electrons of decreasing kinetic energy are analysed. There are two alternative ways in which the spectrometer can be scanned; the first involves varying the retardation voltage between the sample and the entrance slit. This is used for when the analyser setup features a pre-retardation device which is used to increase the resolution at higher electron energies. If the analyser instead features a retarding lens positioned before the actual hemisphere, again to increase resolution of the device, then the spectrometer would instead be scanned by varying the potentials of the lens [20].

The final vital component needed for XPS is the electron multiplier. Due to the extremely small electron current (10^{-16} – 10^{-13} A) emerging from the analyser, amplification by a channel electron multiplier (channeltron®) is required to produce a measurable signal.

The channeltron® consists of a coiled tube made of semi-conduction glass, and coated on the inside with a high secondary electron coefficient material *i.e.* a material that when struck by a photoelectron readily emits more electrons (for example lead oxide). A schematic of a channeltron® can be seen in figure 2.19.

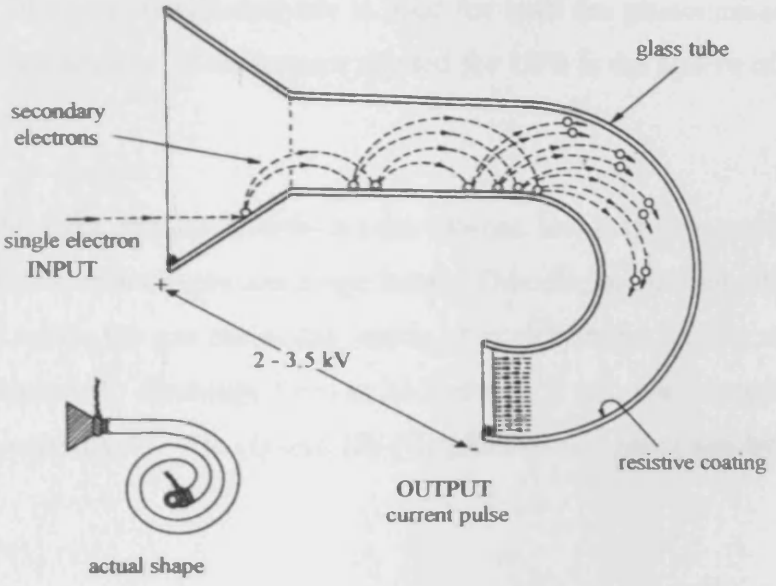

Figure 2.19: A schematic of the channeltron® electron multiplier

Photoelectrons entering the channeltron® *via* a small entrance cone collide with the interior coated walls producing several secondary electrons. These electrons are then accelerated along the channeltron® *via* an applied positive voltage (2-3.5 kV), where they then collide with the walls again, producing more secondary electrons, which are themselves then accelerated, beginning the cycle anew. The entire process results in an amplification of approximately 10^8 times the original signal. The multiplier enables a single photoelectron to become a pulse, which is then passed to a discriminator that removes smaller pulses (which are due to noise), and outputs normalised pulses to the data collection software on the computer for analysis.

2.3.5 Ultraviolet photoelectron spectroscopy (UPS)

As mentioned above, ultraviolet photoelectron spectroscopy is the second specific variant of photoemission spectroscopy, and is an extremely useful technique for looking at the valence bands of the surface of a sample. As UPS focuses on just the valence bands it is a very useful technique for investigating the bonding of molecules adsorbed on the surface.

2.3.5.1 UPS instrumentation

As the same electron energy analyser is used for both the photoemission techniques, the only additional piece of equipment needed for UPS is the source of the ultraviolet radiation itself.

The ultraviolet light employed to probe the valence levels is generated *via* electronic transitions within an inert gas discharge lamp. This discharge lamp utilises a voltage to ionise and excite the gas molecules inside. For this study, helium was used which has two characteristic discharge lines at 21.2 and 40.8 eV, which are labelled He (I) and He (II) respectively. He (I) and He (II) photons are generated by the following processes:

He (I)

$$He \rightarrow He^{+}$$
$$He^{+} \rightarrow He + h\nu_1$$

He (II)

$$He^{+} \rightarrow He^{2+}$$
$$He^{2+} \rightarrow He + h\nu_2$$

The two lines arise due to transitions from 2p to 1s orbitals within the excited helium atoms. Satellite peaks are seen to form from the He (I) β line, arising from the less probable transition from 3p to 1s, appearing as weak features at lower binding energy in the photoelectron spectra.

2.4 Inverse photoemission spectroscopy (IPES)

2.4.1 Introduction

Inverse Photoemission Spectroscopy (IPES) is a lesser used but extremely useful technique for analysing surfaces. In contrast to both XPS and UPS, which allow access to the occupied orbitals in a sample, IPES is entirely concerned with the unoccupied orbitals. This is key, as to get a complete understanding of the electronic properties and reactivity of a material and its surface it is imperative to have information on both the occupied and unoccupied orbitals.

2.4.2 History and principles

Like the standard photoemission techniques of XPS and UPS, IPES also has its basis in the early research into the photoelectric effect carried out by Hertz [4] and Einstein [6]. While their key experimental results showed that the maximum energy of the emitted photoelectrons increase in increments equal to the increases in the photon energy, an additional relationship was observed by Duane and Hunt. They observed an inverse relationship between the short-wavelength cut-off of emitted x-rays and the incident electron energy when a solid is bombarded with electrons [21]. From this the idea of using electrons to stimulate emission of photons from a sample, either in the ultraviolet or x-ray range, was born.

Unlike with forward photoemission, where the early principles were converted into useful workable techniques during the 1960's, the development of the inverse technique took considerably longer. In addition to the requirement of a suitably sufficient vacuum system to combat the issue of the extremely short inelastic mean free path of the probing electrons (see section 2.1.2), a specific detector capable of detecting the small flux of photons released from the sample was also needed. This detection problem is exacerbated by the fact that the inherent cross section for inverse photoemission is considerably lower than that for conventional "forward" photoemission. The ratio of the two cross sections is calculable *via* Equation 2.14, where λ_e is the wavelength of the photoelectron, and λ_p is the wavelength of the photon.

$$r = \frac{\sigma(IPES)}{\sigma(PES)} = \left(\frac{\lambda_e}{\lambda_p}\right)^2$$ Equation 2.14 [22]

At an energy of 10 eV, which is characteristic of the vacuum ultraviolet region, λ_p is approximately 1200 Å and λ_e is approximately 4 Å, leading to an r value of approximately $1x10^{-5}$. At an energy of 1000 eV, which is characteristic of the vacuum x-ray region, λ_p is approximately 12 Å, and the value of r is approximately $1x10^{-3}$. So when using low energy electrons to stimulate emission of photons in the ultraviolet region, the signal will be $1x10^{-5}$ of that encountered during the forward photoemission technique of UPS. It is because of this distinct lack of intensity that IPES (in particular the ultraviolet variant where lower energy photons are being detected) has lagged behind the development of forward photoemission by 10 to 20 years, as the development of sufficiently sensitive detectors has continued.

The basic concept of IPES is that a beam of electrons is fired at a sample, where they proceed to enter the atoms and occupy previously unoccupied orbitals above the vacuum level. The newly created unstable species then undergo a rearrangement in an attempt to return to a lower energy state. The rearrangement involves the decay of the newly entered electrons, which proceed to drop down into lower energy unoccupied orbitals which are located below the vacuum level but above the Fermi level. If the decay is *via* a radiative process, the energy is lost in the form of a photon of specific energy, as can be seen in the schematic in figure 2.20. The photons emitted provide direct information on the nature and density of states (DOS) of the unoccupied orbitals. This in turn provides important information regarding the thermal, optical, and electronic properties of the material, as well as its reactivity and bonding characteristics.

As IPES is concerned with using electrons to stimulate emission of photons from the sample, it is often thought to be, in essence, a time-reversed version of the regular "forward" photoemission techniques (XPS and UPS), where photons are used to stimulate the release of photoelectrons. While this is essentially true for many practical purposes, it is however not a strictly factual statement for a few specific

reasons. Firstly there is the theoretical detail concerning the necessity of quantising the electromagnetic field. Secondly there is the fact that inverse photoemission involves a transition from the $(n \rightarrow n+1)$ electron system, while photoemission involves a transition from the $(n \rightarrow n-1)$ electron system. This is a problem as the electron would experience a different force when approaching an ion, than it would when approaching a neutral atom. While these reasons may cause the forward and inverse photoemission techniques to be poorly comparable when considering atoms and molecules, in the electron delocalised bandstructure of a solid, adding or removing a single electron would create little difference to the overall system. This allows the inverse technique to be treated as a time reversed version of the "forward" photoemission spectroscopies when dealing with solids which have electron band structures.

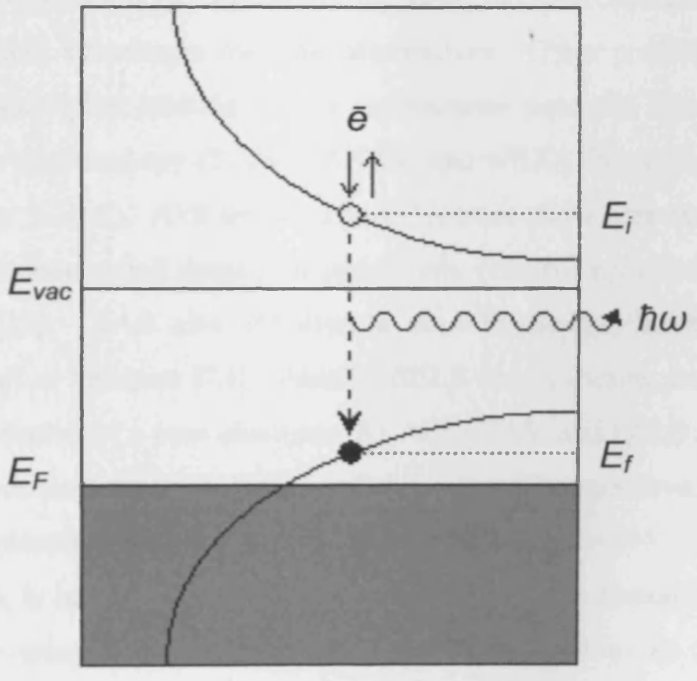

Figure 2.20: Schematic of the inverse photoemission process (adapted from C. N. Borca *et al*, 2002) [23]

As mentioned earlier, the photons released from the sample can be in the ultraviolet or x-ray regions, depending on the energy of the incident electrons. If the technique is based in the x-ray region it is referred to as bremsstrahlung isochromat spectroscopy (BIS), while if it is in the ultraviolet region it is referred to as inverse photoemission spectroscopy (IPES or IPS) [24]. However both the x-ray and ultraviolet versions of

the technique are sometimes referred to as inverse photoemission (IPE) or inverse photoemission spectroscopy (IPES) [22,23].

For both the x-ray and UV versions of the technique, there are two specific variations that are dependent on how the experiment is run. In the first case, which is described as isochromat, the energy of the photon being detected is kept constant, and the energy of the electrons is swept, which is analogous to the energy distribution curve (EDC) mode of PES. In the second case the energy of the electrons is kept constant, while the energy of the photons being detected is swept, which is analogous to the constant initial state (CIS) mode of PES. The isochromat variation is the more used of the two, especially for x-ray-IPES, hence the BIS term being applicable [22,23].

IPES is not the only technique capable of analysing the unoccupied orbitals; however it has some distinct advantages over the alternatives. Other possible techniques for analysing the unoccupied orbitals include; appearance potential spectroscopy (APS), x-ray absorption spectroscopy (XAS, XANES, and NEXAFS), and electron energy-loss spectroscopy (EELS). APS involves two electrons and a core excitation, with the extraction of the unoccupied density of states only possible provided the data allows deconvolution [25]. XAS also involves a core excitation; however the data is relatively difficult to interpret [23]. Finally, EELS is a scattering technique that also relies on the excitation of a core electron. As APS, XAS, and EELS all rely on a core excitation to probe the unoccupied region, the energy of the core level must already be known for any calculation of the unoccupied states to be possible. IPES, unlike the other techniques, is based on a single electron with no core excitations taking place. This means the energy of the core levels does not need to be known, and the subsequent calculations are simpler. Another advantage that IPES has over the other unoccupied orbital techniques is that because only one electron is involved, it is possible to specify the momentum, or wave vector, k of the incident electron. This gives IPES a k-resolved capability (when the technique is known as KRIPES) that the other unoccupied techniques do not have [22]. The KRIPES technique, which is thought of as the time-reversed version of angle resolved XPS (ARXPS) [26], is useful for a lot of the same reasons, as it can determine the energy and wave vector of the states involved in the electronic transition, and also identify which transitions involve bulk states, and which involve surface states. All inverse photoemission is

concerned with characterising the initially unoccupied final states, but KRIPES is especially important as it allows almost complete characterisation of the states, providing information on their energy, lifetime, and k dispersion. A significant disadvantage of IPES however, when compared to the other techniques, is that it cannot distinguish between elements, and as such you cannot look at the unoccupied orbitals of just one specific element in the sample [23,27].

2.4.3 IPES instrumentation

It is worth noting first of all that this work is only concerned with the ultraviolet isochromat variant of the inverse photoemission technique, where the photons released are in the ultraviolet energy range, and the specific energy of the photons detected remains static while the energy of the incident electron beam is swept.

There are three main components of the equipment needed for IPES, with the first being the electron gun. As ultraviolet photons are desired, the electron gun is of the low energy variety, and is capable of providing electrons from 5 – 50 eV in energy. Within this range of energies the electron beam has an approximate energy spread of 0.25 eV. This is due to the BaO filament used, which during normal operation emits electrons at temperatures between 1100 and 1200 K.

The specialised detector needed to record the photons emitted from the sample is the second of the main IPES components. The detector is of the solid state bandpass variety, known as such due to the fixed "band" of energies of which it can detect (a schematic can be seen in figure 2.21). The band effect is achieved through the use of low pass and high pass photon filters. The low pass filter is a SrF_2 window which only allows low energy photons, approximately below 10 eV, to pass through. The high pass filter consists of a tantalum cone (photocathode) coated in NaCl. The photons that pass through the SrF_2 window strike the photocathode, resulting in the production of photoelectrons, with the NaCl serving to increase the quantum efficiency of the process. The photoelectrons produced then pass through to an electron multiplier used to boost the signal (of the same type detailed in 2.3.4.1). It is important to note that only photons of sufficiently high energy are capable of producing the photoelectrons, hence the use of the photocathode as a high pass filter.

The combined effect of the two filters is that the detector only allows photons of approximately 9.5 eV to pass through, and with a resolution of approximately 0.5 eV. The materials used to construct the window and photocathode were chosen specifically to give the best compromise between resolution and quantum efficiency.

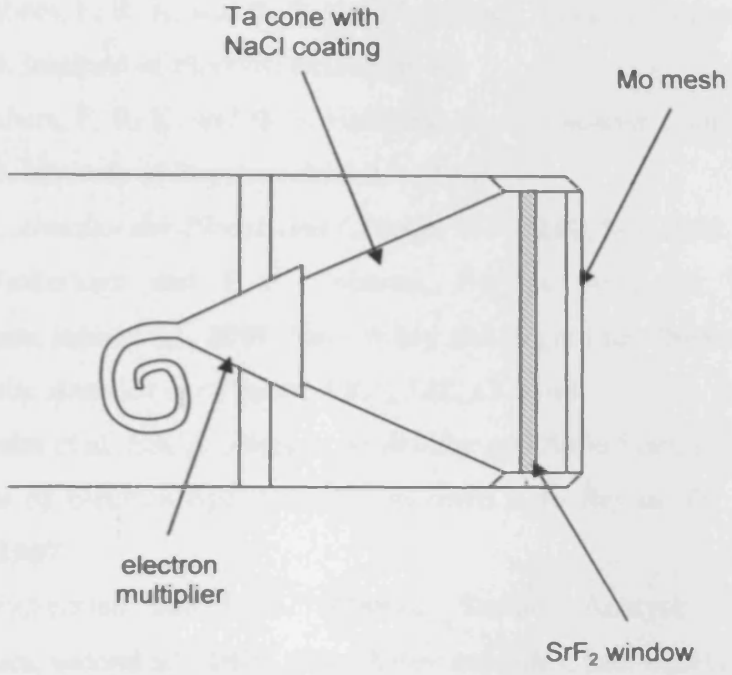

Figure 2.21: A schematic of the IPES bandpass detector

The third and final piece of equipment is needed because of an additional complication that the electron gun produces. The incident sample current generated upon the surface when using the gun varies as the energy of the electrons changes (normally between the ranges of 0-10 μA). As the relationship between the electron energy and sample current is not constant, and can vary considerably from day to day, it needs to be accounted and compensated for. This is achieved by recording the sample current at the same time as the detector signal using a picoammeter (Keithley, Model 6487). The signal acquired by the photon detector at each electron energy is then modified to take into account the actual sample current measured at the time.

2.5 References

1 A. Chambers, F. R. K. and B. S. Halliday, Basic Vacuum Technology, second ed., **1998**, Institute of Physics: Bristol, p. xii.

2 A. Chambers, F. R. K. and B. S. Halliday, Basic Vacuum Technology, second ed., **1998**, Institute of Physics: Bristol, p. 10.

3 A. Chambers, F. R. K. and B. S. Halliday, Basic Vacuum Technology, second ed., **1998**, Institute of Physics: Bristol, p. 144.

4 H. Hertz, *Annalen der Physik und Chemie*, 1887, **267**, 983-1000.

5 J. C. Vickerman and I. S. Gilmore, Surface Analysis: The Principal Techniques, second ed., **2009**, John Wiley and Sons, Ltd: Chichester, p. 49.

6 A. Einstein, *Annalen der Physik*, 1905, **322**, 132-148.

7 K. Siegbahn et al, ESCA: Atomic, Molecular and Solid State Structure Studied by means of Electron Spectroscopy, in *Nova Acta Regiae Sci. Ups., Ser IV, Vol. 20*, **1967**.

8 J. C. Vickerman and I. S. Gilmore, Surface Analysis: The Principal Techniques, second ed., **2009**, John Wiley and Sons, Ltd: Chichester, p. 66.

9 M. P. Seah and W. A. Dench, *Surface and Interface Analysis*, 1979, **1**, 2-11.

10 D. E. Eastman and J. K. Cashion, *Physical Review Letters*, 1971, **27**, 1520-1523.

11 C. M. Quinn and M. W. Roberts, *Transactions of the Farady Society*, 1965, **61**, 1775-1786.

12 T. Koopmans, *Physica*, 1934, **1**, 104-113.

13 K. Oura, V. G. Lifshits, A. A. Saranin, A. V. Zotov and M. Katayama, Surface Science: An Introduction, first ed., **2003**, Springer-Verlag: Berlin, p. 83.

14 G. Ertl and J. Küppers, Low Energy Electrons and Surface Chemistry, **1985**, VCH Verlagsgesellschaft: Weinheim, p. 185.

15 J. N. O'Shea, *Ph.D. Thesis*, University of Cardiff, **1999**.

16 R. T. Lewis and M. A. Kelly, *Journal of Electron Spectroscopy and Related Phenomena*, 1980, **20**, 105-115.

17 G. Ertl and J. Küppers, Low Energy Electrons and Surface Chemistry, **1985**, VCH Verlagsgesellschaft: Weinheim, p. 9-13.

18 A. L. Hughes and V. Rojansky, *Physical Review*, 1929, **34**, 284-290.

19 P. S. Bagus, *Physical Review*, 1965, **139**, A619-634.

20 G. Ertl and J. Küppers, Low Energy Electrons and Surface Chemistry, **1985**, VCH Verlagsgesellschaft: Weinheim, p. 67.

21 W. Duane and F. L. Hunt, *Physical Review*, 1915, **6**, 166.

22 N. V. Smith, *Reports on Progress in Physics*, 1988, **51**, 1227-1294.

23 C. N. Borca, T. Komesu and P. A. Dowben, *Journal of Electron Spectroscopy and Related Phenomena*, 2002, **122**, 259-273.

24 J. C. Fuggle and J. E. Inglesfield, Unoccupied Electronic States, in *Topics in Applied Physics, Vol. 69* (Eds.: J. C. Fuggle, J. E. Inglesfield), **1992**, Springer-Verlag: Berlin, p. 1-21.

25 G. Ertl and J. Küppers, Low Energy Electrons and Surface Chemistry, **1985**, VCH Verlagsgesellschaft: Weinheim, p. 157.

26 J. B. Pendry, *Journal of Physics C-Solid State Physics*, 1981, **14**, 1381-1391.

27 P. T. Andrews, I. R. Collins and J. E. Inglesfield, Unoccupied Electronic States, in *Topics in Applied Physics, Vol. 69* (Eds.: J. C. Fuggle, J. E. Inglesfield), **1992**, Springer-Verlag: Berlin, p. 243-275.

Chapter 3 – Data analysis and quantification

3.1 Introduction

The conversion of the raw photoelectron spectroscopic data into useable values and information requires the use of careful and systematic analysis. This includes determination of the peak positions and areas, which in turn is dependent on the shape of the peaks themselves, and the underlying background signal. In addition supplementary knowledge of the sampling depth is required to correctly estimate the concentration of surface species. These issues are far from trivial, so incorrect or uncritical use of the following methodologies can introduce significant error.

3.2 Data analysis

3.2.1 Inelastic background removal – XPS and UPS

A significant feature in photoelectron spectra is the inelastic background signal. This feature is mainly due to the inelastic scattering of emitted photoelectrons whilst they are travelling through the sub-surface region. The effect of this is a sloping background that increases with decreasing kinetic energy, upon which the actual photoelectron peaks are superimposed. For accurate quantification of the results to be achieved this background intensity must be subtracted. However, before contemplating which method of background subtraction to use, it is important to understand what the three main sources of the background actually are. The most important of the three is the inelastically scattered photoelectrons of the main detected peaks, which result in noticeable 'step' like features after each signal (see figure 3.1).

The second source of background contributions is from inelastically scattered photoelectrons from all photoemission lines at higher kinetic energy. This is best accounted for by a linear function [1]. The final source is only applicable at low kinetic energies (<100 eV), and is due to a background of low energy secondary electrons.

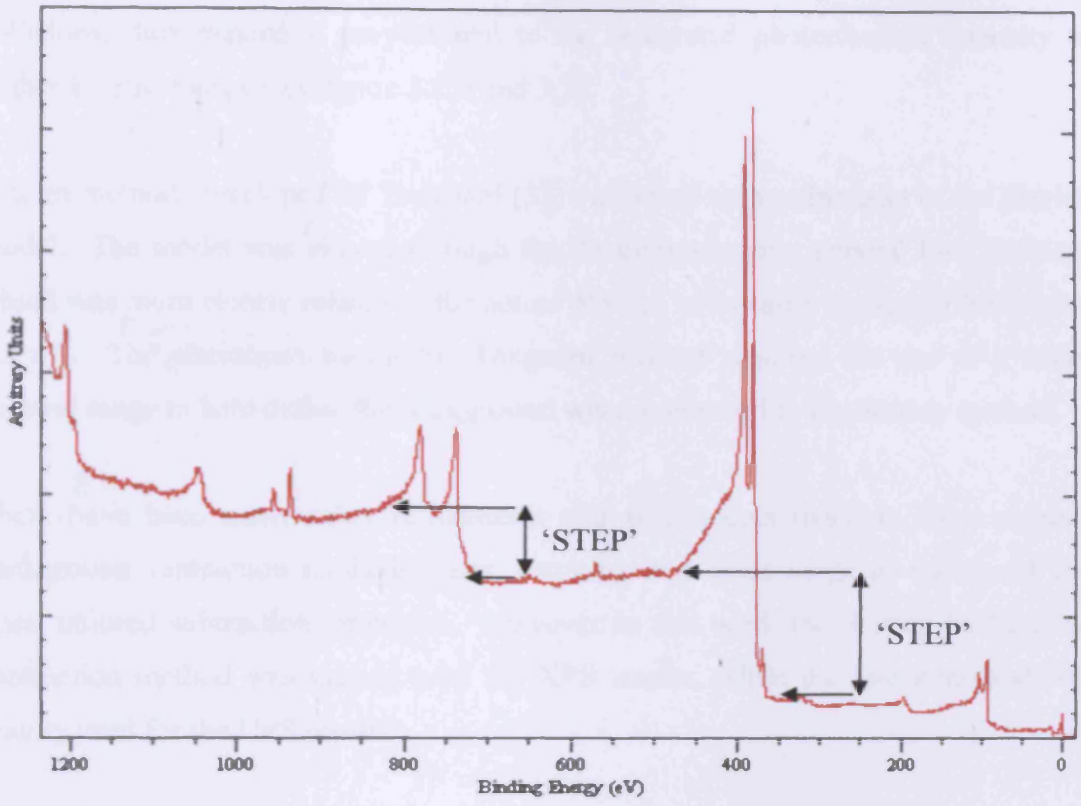

Figure 3.1: Example photoelectron spectrum of uranium detailing the step edges due to inelastically scattered photoelectrons from the primary peaks

While there is no single method of background subtraction that is applicable for all scenarios, there are a number of approaches available that can be used providing the conditions are right. Of the many possible methods of background subtraction, the linear type is by far the simplest. This is achieved by approximating a straight line between the signal on either side of the peak (see figure 3.2 a)). Everything under the base line is then removed from the photoelectron peak. This technique only really works well for photoelectron peaks that produce very small background increases, such as those due to the O(1s) and C(1s) orbitals in adsorbed species, and most of those produced in the valence region using photons in the ultraviolet energy range. It is however not suitable for use with the large background intensities often observed in the metal core-levels for bulk materials.

A second method, based on a numerical treatment devised by Shirley [2], is known as a non-linear background subtraction. It assumes that every point on the background

arises solely from higher kinetic energy photoelectrons losing energy in inelastic collisions, thus making it proportional to the integrated photoelectron intensity to higher kinetic energy (see figure 3.2 b and 3.3).

A third method, developed by Tougaard [3], was based on a refinement of the Shirley model. The model was altered through the development of a general loss function, which was more closely related to the actual physics of inelastic scattering (see figure 3.2 c)). The alterations meant the Tougaard method required the use of a wider spectral range to help define the background when compared to the Shirley method.

There have been many other refinements and adjustments made to these original background subtraction methodologies, resulting in a wide range of additional and often tailored subtraction strategies. However in this work the Shirley background subtraction method was mainly used for XPS results, while the linear method was mainly used for the UPS results.

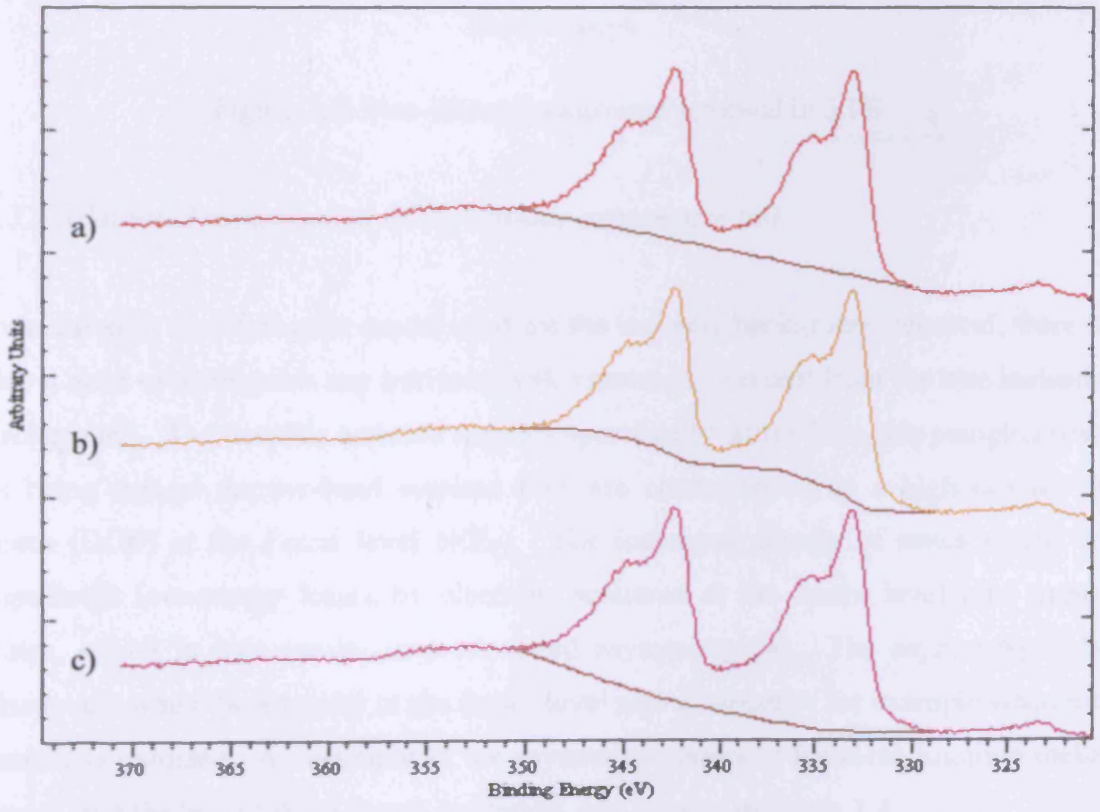

Figure 3.2: Example background removal from clean Th(4f) spectrum – a) Linear, b) Shirley, c) Tougaard methods

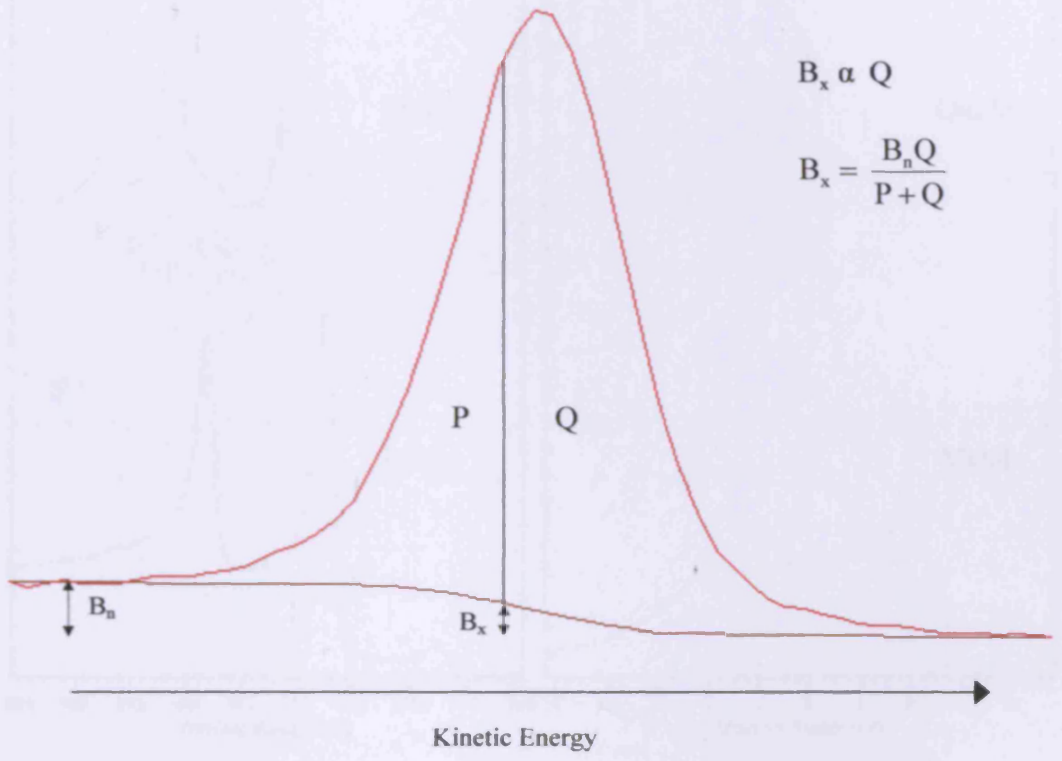

Figure 3.3: Non-linear background removal in XPS

3.2.2 Additional complication of the actinide asymmetric tail

In addition to specifying the model used for the inelastic background removal, there is also a need to distinguish any intrinsic peak asymmetry present from the true inelastic background. The metallic actinide systems specifically suffer from this complication, as being typical narrow-band systems they are characterised by a high density of states (DOS) at the Fermi level $N(E_F)$. The increased density of states results in significant low-energy losses by electrons scattered at the Fermi level into empty states, which in turn results in pronounced asymmetry [4]. The asymmetry only disappears when the intensity at the Fermi level also disappears, for example when the surface is oxidised. An example of the asymmetric peaks in the clean uranium metal signal, and the loss of them due to oxidation, can be seen in figure 3.4.

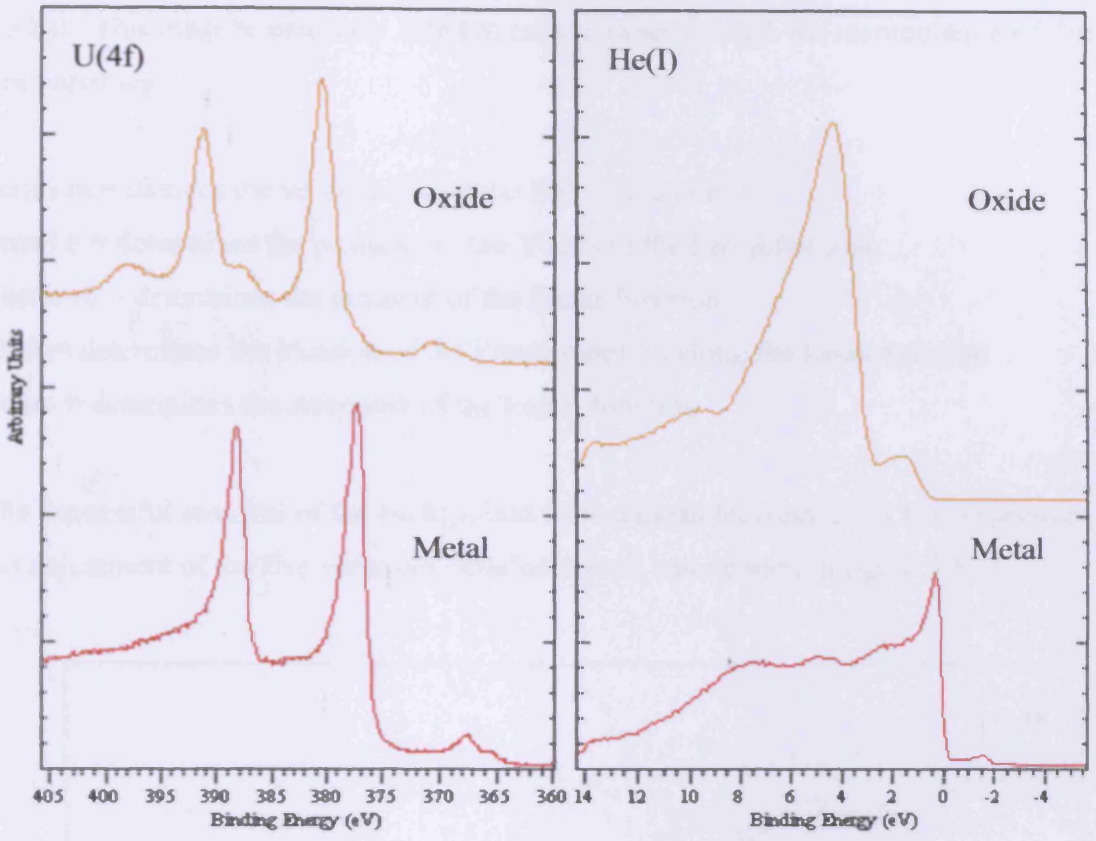

Figure 3.4: U(4f) and He(I) spectra of uranium metal and uranium dioxide to highlight the asymmetric nature of the metal peak when compared to that of the oxide, and the high density of states (DOS) at the Fermi edge that are the cause of it

3.2.3 Inelastic background removal – IPES

As mentioned above, a significant feature of acquired photoemission spectra is that of the inelastic background. However the source of that background can vary slightly, and depends on whether it is the forward (regular) or backward (inverse) version of the technique that is being studied. For inverse photoemission the steadily rising background signal occurs due to inelastic scattering of incident electrons, and is known to increase relative to *decreasing* initial state energy [5].

Unlike the regular photoemission technique, removal of the background from spectra from IPES is a far more subjective process, as there are no easily applicable standard methods (such as the Shirley, or Tougaard) available. The background used instead is

a combination of a reverse Fermi function followed by a linear background (see figure 3.5 b)). This must be manually fitted to each data set through the manipulation of five key variables:

Fermi m = dictates the vertical size of the Fermi function
Fermi c = determines the position on the Y axis of the Fermi function
Linear m = determines the gradient of the linear function
Shift = determines the location of the Fermi function along the linear function
Temp = determines the steepness of the Fermi function

The successful removal of the background from a clean thorium metal IPES spectrum, *via* adjustment of the five variables detailed above, can be seen in figure 3.5 c).

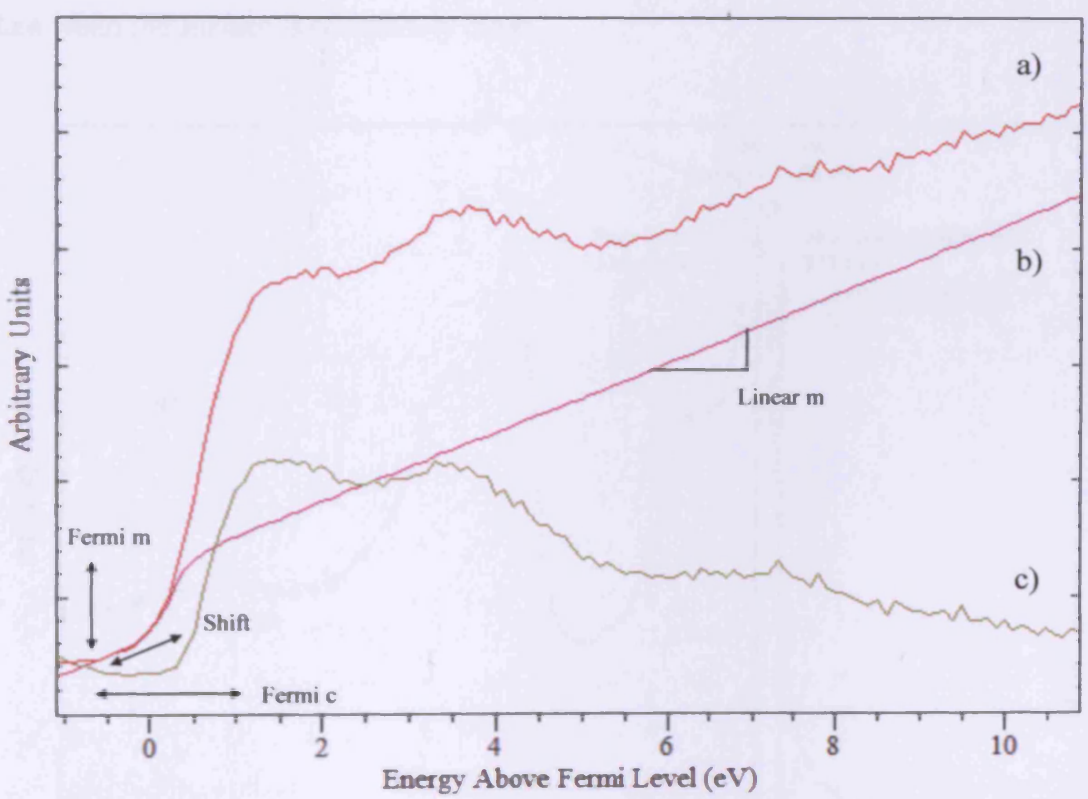

Figure 3.5: a) the raw inverse photoemission data of clean thorium metal, b) the combined Fermi and linear function fitted to this data, and c) the result of the background subtraction.

3.2.4 Calibration

The binding energy scale of all acquired spectra must be correctly calibrated before significant analysis can be carried out upon them. With the case of forward photoemission spectroscopy, the signal must be calibrated to compensate for possible charging effects upon the surface, and for any possible 'drift' from the ideal values due to the electronics used to capture the spectra (in particular the highly sensitive thermionic valves contained within the electronic control boxes). To achieve this, the clean metal signals are compared to the expected values, as obtained from the literature, and then calibrated to match them (an example of the difference in energies can be seen in figure 3.6). This difference between the expected and acquired values is then applied to the other spectra taken during the experiment. Special care has to be taken with this particular method, as it relies entirely upon the original spectrum being taken when the surface is completely clean.

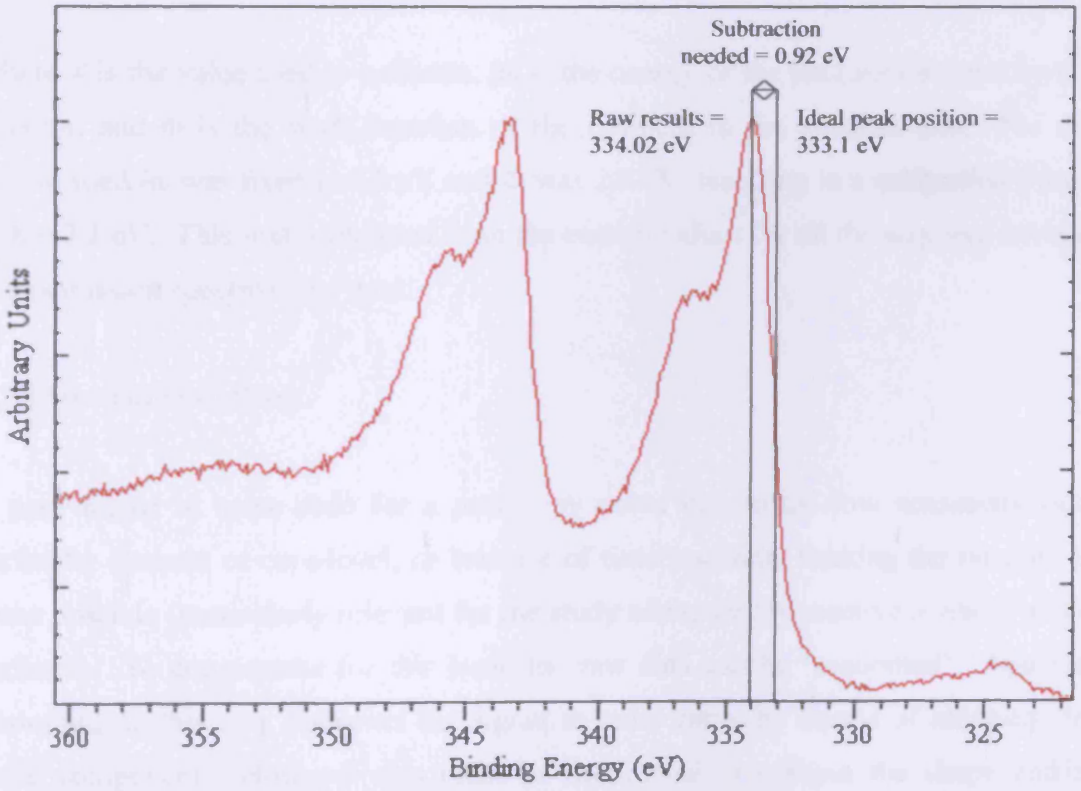

Figure 3.6: A Th(4f) spectrum before calibration. The size of the 'drift' between the recorded value and the ideal value is highlighted.

If pure metal signals are not available then alternative methods utilising the C(1s) and O(1s) are available. Comparison against the pure carbon signal located at 284.7 eV is a common method used for XPS calibration. In a similar fashion, when dealing with an oxide layer, the O(1s) signal can be used to calibrate the other peaks.

The process of calibration for the inverse photoemission spectra is based upon the equipment itself, as opposed to the results acquired. The constant collection energy of the photon detector has to be taken into account and compensated for, as it has the effect of shifting acquired spectra upwards in energy. The work function of the filament in the electron gun also has to be accounted for as it results in a downwards shift in energy of the acquired spectra. To compensate for the two different effects a fixed calibration factor for the equipment can be calculated using the following equation:

$$X = h\upsilon - \Phi \qquad \text{Equation 3.1}$$

Where X is the value used to calibrate, $h\upsilon$ is the energy of the photons detected by the detector, and Φ is the work function of the filament in the electron gun. For the system used $h\upsilon$ was fixed at 9.5 eV and Φ was 2.4 eV, resulting in a calibration figure of X = 7.1 eV. This was subtracted from the energy values for all the acquired inverse photoemission spectroscopy data.

3.2.5 Spectral smoothing

A poor signal to noise ratio for a peak may occur due to the low sensitivity of a particular element or core-level, or because of time restraints limiting the number of scans possible (particularly relevant for the study of the highly reactive actinide metal surfaces). To compensate for this issue the raw data can be "smoothed". Spectral smoothing in this way improves the signal to noise ratio, by means of reducing the noise component. However this must be accomplished without the shape and/or position of the photoelectron peaks changing or distorting, which is something over use of smoothing techniques is prone to cause. One of the most commonly used methods for smoothing data was developed by Savitzky and Golay [6]. This uses a least squares approach, where a polynomial is fitted to the data over an odd number of

points known as the smoothing interval. The degree of smoothing is seen to increase as the number of points in the smoothing interval is increased. The optimal number of points given by Proctor and Sherwood [7] is equivalent to 70 % of the data points comprising the full width half maximum (FWHM) of the peak. An example of smoothed and over-smoothed spectra can be seen in figure 3.7. The over use of the smoothing function has drastically reduced the sharpness of the data, and has significantly reduced the definition of the smaller component contained within the shoulder of the main signal.

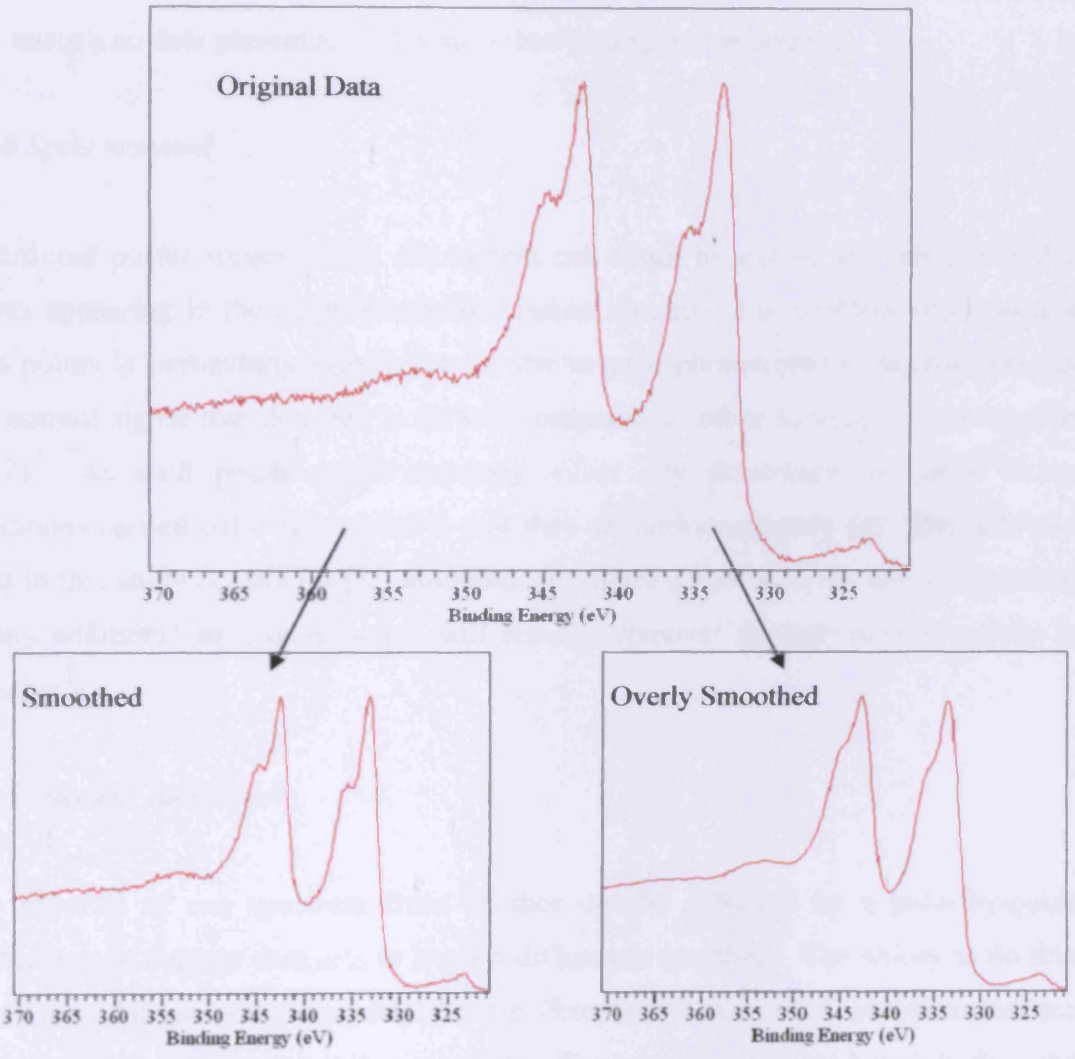

Figure 3.7: Clean thorium metal Th(4f) spectrum followed by the resulting spectra after smoothing (single Savitzky and Golay (SG) Quadratic operation with a smoothing width of 5) and over smoothing (4 SG Linear polynomial operations with a smoothing width of 9) of the signal.

With the standard smoothing featured in figure 3.7 the energies, FWHM, and relative size of the peaks remain almost identical after the smoothing operation has been carried out. This is in contrast to the overly smoothed spectrum where significantly different FWHM measurements (up to 0.5 eV wider) are seen, along with a decrease in the contribution of the smaller satellite (see section 4.2) towards the total acquired signal.

While spectral smoothing can help highlight some features (multiple overlapping oxidation states in particularly noisy data), it can also introduce spectral distortions, and as such no data presented in this work has undergone smoothing.

3.2.6 Spike removal

Occasional power surges within the system can result in spikes, and other irregular points appearing in the acquired photoemission spectra. The problem of erroneous data points is particularly significant for the inverse photoemission experiments, as the normal signal rate detected is so low compared to other techniques (see section 2.4.2). As such points could seriously affect any smoothing or curve fitting operations carried out it is imperative that they are addressed early on. The software used in this study (CasaXPS [8]) automatically detects and removes any such points. If any additional erroneous points still remain, removal through manual means is possible.

3.2.7 Spectral subtraction

The removal of one spectrum from another can be achieved by a point-by-point subtraction of the two data sets to leave a difference spectrum. The ability to do this is of particular use when the peaks from different regions overlap, or when multiple oxidation states are present at the same time. For instance when studying uranium the shake-up satellites of the U(4f) region partially overlap with the N(1s) region. Through removal of the uranium component, a more accurate measurement of the N(1s) peak component is possible. This was of particular use when studying the affects of ammonia adsorption on the uranium surface. The other case where subtraction is particularly useful is when multiple components of the same peak

overlap, and an accurate determination of the intensity of one of those components is needed. For instance, when the surface is only partially oxidised, the clean metal component can be subtracted to leave only the oxidised component, which is often needed to estimate oxide depth. An example of a useful spectral subtraction can be seen in figure 3.8. Figure 3.8 a) features two U(4f) spectra, the one in red being clean uranium, while the one in orange is after exposure to NH_3. The resulting subtraction of the clean spectrum from the NH_3 exposed spectrum gives the signal seen in part b) of the figure. The spectrum after subtraction shows up the peak belonging to the N(1s) at 397 eV, but also demonstrates that the U(4f) signals themselves are altered by the NH_3 exposure (either a broadening effect, or a separate uranium component due to a uranium nitride species), as evidenced by their continued prominence after the subtraction.

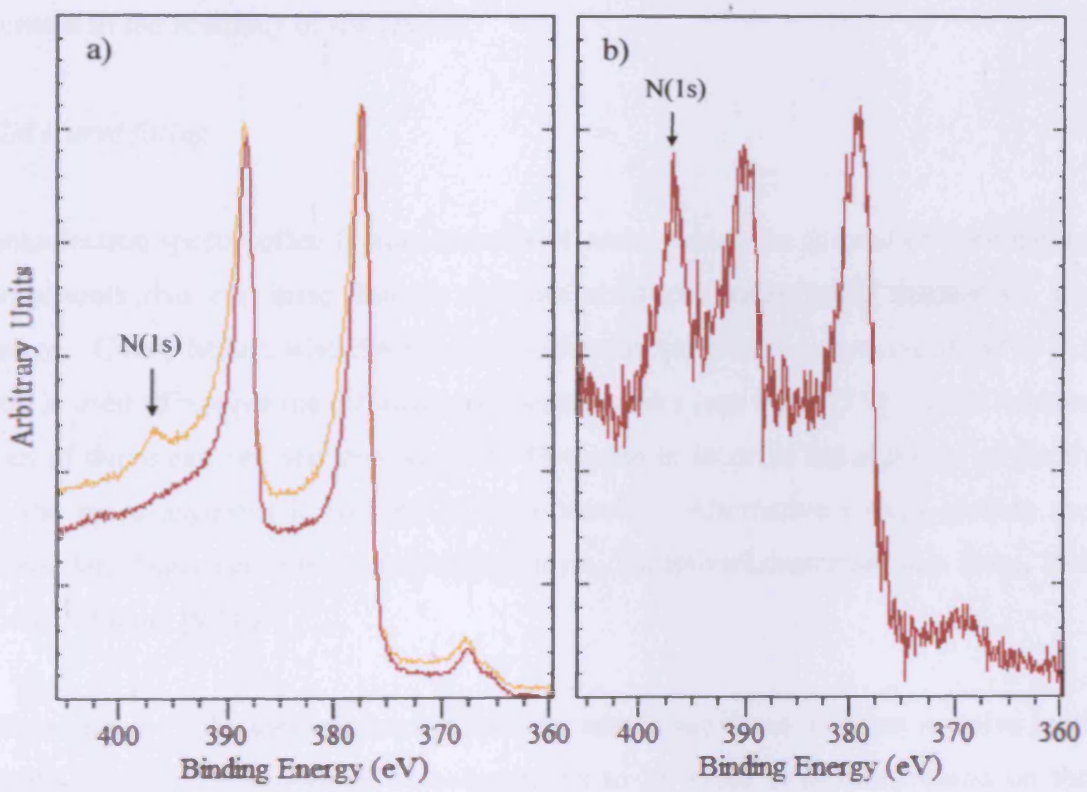

Figure 3.8: An example of the result of spectral subtraction in the U(4f) region. The red spectrum is of clean uranium while the orange spectrum is of uranium exposed to NH_3. a) features the two spectra to be compared (red spectrum to be subtracted from orange spectrum) while b) is the resulting spectrum after subtraction.

Spectral subtraction as a method has both advantages and disadvantages compared to the more general method of curve fitting (see section 3.2.8). One advantage is that spectral subtraction provides a far clearer visual representation of partially or completely obscured signals than merely highlighting it with one of many curve shapes fitted to the data, as would be done as an alternative. Additionally, the actual shape of the signal revealed through subtraction would be more accurate than the standard peak shape assigned through curve fitting, and would thus lead to more accurate measurements of area and position. Probably the biggest of the disadvantages is that it needs a great deal of care and attention to utilise it properly (arguably more than is needed to curve fit). The technique is very sensitive to the alignment and normalisation of spectra, which must be carried out beforehand. Incorrect or careless subtraction can generate false results through the creation of artificial peaks and troughs in the resultant spectrum, and thus lead to an actual decrease in the accuracy of the results.

3.2.8 Curve fitting

Photoelectron spectra often feature composite peaks, which are formed of overlapping components that can arise due to multiple chemical states being present on the surface. Curve fitting, whereby multiple Gaussian (or other) curves are fitted to the data, is used to resolve the different component peaks (see figure 3.9). Other various types of curve can be used instead of the Gaussian to increase the accuracy of the fit for the more asymmetric natured actinide results. Alternative curves include the Lorentzian, Gaussian/Lorentzian product form, Gaussian/Lorentzian sum form, and Doniach Sunjic [9,10].

After removal of the inelastic background the curves are fitted using an iterative least squares fit [11]. The number of components to be fitted is inputted based on the chemistry of the system, and the computer software then varies the positions, peak heights, and FWHM in an effort to match up with the acquired data. Extreme care must be taken in the choice of the number of peaks, as this can be subjective and relies upon some knowledge of the chemistry involved, and the use of reference data. In the event of certain parameters, such as the FWHM, having unreasonable and unrealistic values after fitting, many of the parameters can be specified or constrained

to a set range in an effort to improve the accuracy of the fit. Again due care and prior knowledge is required to ensure that the overall fit and those of the individual components is both realistic and accurate.

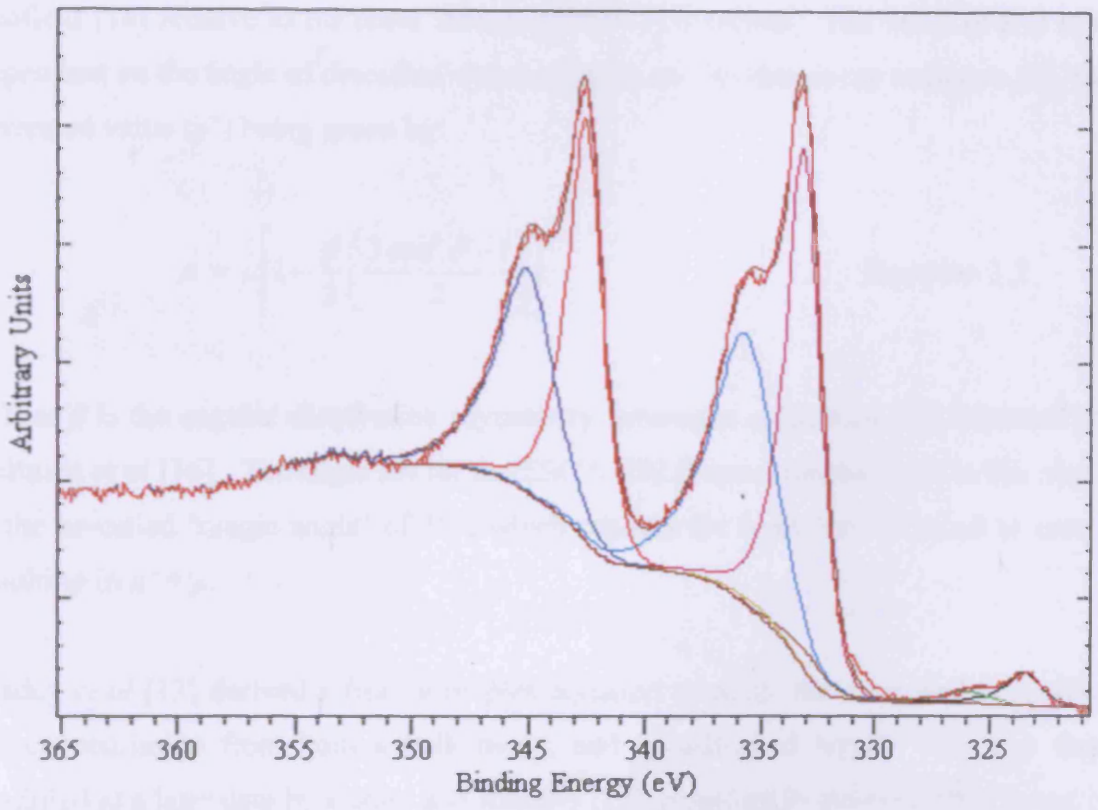

Figure 3.9: Th(4f) spectrum of clean thorium metal curve fitted (with a Shirley background) to separate the main peaks from their associated satellite signals

3.3 Quantification

In order to calculate the surface coverage of the species present on the surface it is first necessary to compute the area of the photoelectron peaks. Accurate peak fitting of the data combined with an appropriate background removal leaves just the photoelectron peak itself, which can then be integrated between two points on either side to calculate the area. Once the area of the photoelectron peaks is known the actual surface coverage of the species can be calculated *via* the Carley and Roberts method [12], which is a development of the original equation due to Madey *et al* [13], modified to include the photo-ionization cross section. The photo-ionization cross section (μ) gives the probability that an electron will be ejected from a particular

orbital of a particular atom. Values of μ depend on the size and shape of the orbital as well as the ionising photon energy [14,15].

The Photo-ionization cross sections for both Mg Kα and Al Kα radiation are given by Scofield [14] relative to the cross section of the C(1s) orbital. The value of μ is also dependent on the angle of detection with respect to the incident x-ray radiation (θ), the corrected value (μ') being given by:

$$\mu' = \mu\left[1 - \frac{\beta}{2}\left(\frac{3\cos^2\theta - 1}{2}\right)\right] \qquad \text{Equation 3.2}$$

Where β is the angular distribution asymmetry parameter calculated and tabulated by Reilman *et al* [16]. The angle (θ) for the ESCA-EELS spectrometer used in this study is the so-called 'magic angle' of 55°, which renders the term $3\cos^2\theta$ equal to unity, resulting in $\mu' = \mu$.

Madey *et al* [13] derived a first principles equation to relate the measured intensities of photoemission from both a bulk metal, and an adsorbed layer. This was then modified at a later date by Carley and Roberts [12], resulting in the simplified form:

$$\frac{I_a(X_a)}{I_m(X_m)} = \frac{\mu_a(\theta, X_a)\sigma_a}{\mu_m(\theta, X_m)n_m\lambda_m(\varepsilon_i)\cos\phi} \qquad \text{Equation 3.3}$$

where $I_a(X_a)$ and $I_m(X_m)$ are the measured intensities of the x-ray photoelectron signals corresponding to the adsorbed layer, and metal substrate, respectively. The density of the emitting atoms in the metal is represented by n_m, $\lambda_m(\varepsilon_i)$ is the mean free path of photoelectrons from level X_m in the metal, and σ_a is the surface concentration of adsorbed species. The $\mu_a(\theta,X_a)$ and $\mu_m(\theta,X_m)$ values are the subshell photoionisation cross sections from the adsorbed and metal layers respectively, and Φ is the angle of collection (with respect to the surface normal) of the photoelectrons.

The equation for calculating surface concentrations was then updated to the following form:

$$\sigma_A = \frac{KE_A}{KE_S} \times \frac{I_A}{I_S} \times \frac{\mu_S N \lambda_S \rho_S \cos\phi}{\mu_A M_S} \qquad \text{Equation 3.4}$$

where,

σ = Surface concentration (cm^{-2})

A = Adsorbate

S = Substrate

I = Integrated peak intensity

KE = Kinetic energy

μ = Modified photoionisation cross section

Φ = Photoelectron take-off angle with respect to the surface normal

N = Avogadro's number

λ_S = Escape depth of photoelectrons through the substrate

M_S = Molar mass of substrate

ρ_s = Substrate density

The equation can be further simplified, as many of the parameters are constant for a particular adsorbate, substrate, and spectrometer. The simplified form is as follows:

$$\sigma_A = \frac{I_A}{I_S} \times A \qquad \text{Equation 3.5}$$

where A is a constant for a particular substrate/adsorbate system.

The Carley-Roberts equation (equations 3.3 and 3.4) relies on the assumption that there is no attenuation of adsorbate photoemission intensity. It is because of this that surface coverages greater than one monolayer are underestimated, as the scattering of the adsorbate above this level of coverage cannot realistically be considered negligible. Once the surface coverage is much greater than a monolayer in size, film thickness calculations must then be undertaken in order to calculate the actual surface coverage.

3.3.1 Inelastic mean free path and film thickness calculations

Calculation of the inelastic mean free path (IMFP) λ, introduced in chapter 2, has recently been improved *via* a modification to take the physics of the scattering process more into consideration. Tanuma *et al* [17] have developed the following analytical expression for λ (referred to as TPP-2):

$$\lambda = E/\left\{E_p^2\left[\beta \ln(\gamma E) - (C/E) + (D/E^2)\right]\right\} \qquad \text{Equation 3.6}$$

Where,

λ = the IMFP (in Å)

E = the electron energy (in eV)

$E_p = 28.8\,(N_v \rho / M)^{1/2}$ and is the free-electron plasmon energy (in eV)

ρ = the density (in g cm^{-3})

N_v = the number of valence electrons per atom (for elements) or molecule (for compounds)

M = the atomic or molecular weight

β, γ, C, and D in equation 3.6 are adjustable parameters used to try and fit the calculated IMFPs to those experimentally measured. Analysis of the various values of β, γ, C, and D derived from the fits to the IMFPs for a variety of elements (27) and organic compounds (14), yielded the following expressions in terms of material parameters [17]:

$$\beta = 0.10 + 0.944/\left(E_p^2 + E_g^2\right)^{1/2} + 0.069\rho^{0.1} \qquad \text{Equation 3.7}$$

$$\gamma = 0.191\rho^{-0.50} \qquad \text{Equation 3.8}$$

$$C = 1.97 - 0.91U \qquad \text{Equation 3.9}$$

$$D = 53.4 - 20.8U \qquad \text{Equation 3.10}$$

$$U = N_v \rho / M = E_p^{\,2} / 829.4 \qquad \text{Equation 3.11}$$

where E_g is the band-gap energy (in eV) for non-conductors (the work was carried out on organic non-conductors such as polyethylene, DNA, and Guanine [17]. This new formalism, TPP-2M as it is known, has been applied to elements, inorganic, and organic compounds and shows much improved and reduced RMS deviations from values calculated from optical data results than was seen with the original TPP-2 formulation [17,18].

To calculate the thickness of an adsorbed layer two different methods were used. One method involved the use of ARXPS [19] and ARCtick [20] computer software, both of which attempted to give an approximation of the thickness of the adsorbed layer. A second method, for use where larger surface coverages are involved, can estimate the thickness (d) of the adsorbate, based on the attenuation of the substrate signal. The equation is;

$$\frac{I}{I_0} = e^{-\frac{d}{\lambda}\cos\phi} \qquad \text{Equation 3.12}$$

where

I = integrated substrate intensity after film deposition

I_0 = integrated intensity of the clean substrate

d = film thickness

λ = inelastic mean free path of the substrate photoelectrons through the adsorbed film

Φ = photoelectron emission angle with respect to the surface normal

Both methods used for calculating the surface thickness of the adsorbate require certain assumptions to be taken into account. For instance both the substrate and adsorbed species are assumed to be homogeneous in composition and structure, with the adsorbed species also assumed to be covering the surface to a uniform depth. It is because of these assumptions that great care must be taken when utilizing either of these methods to predict surface thickness.

3.4 References

1 H. E. Bishop, *Surface and Interface Analysis*, 1981, **3**, 272-274.

2 D. A. Shirley, *Physical Review B*, 1972, **5**, 4709.

3 S. Tougaard, *Surface Science*, 1989, **216**, 343-360.

4 A. Kotani and Y. Toyozawa, *Journal of the Physical Society of Japan*, 1974, **37**, 912-919.

5 V. Dose and G. Reusing, *Applied Physics*, 1980, **23**, 131-134.

6 A. Savitzky and M. J. E. Golay, *Analytical Chemistry*, 1964, **36**, 1627.

7 A. Proctor and P. M. A. Sherwood, *Analytical Chemistry*, 1980, **52**, 2315-2321.

8 CasaXPS; N. Fairley, Version 2.3.15, 2009

9 S. Doniach and M. Sunjic, *Journal of Physics C-Solid State Physics*, 1970, **3**, 285-.

10 S. Evans, *Surface and Interface Analysis*, 1991, **17**, 85-93.

11 A. F. Carley, "Electron Spectroscopic Studies of Solid Surfaces", *Ph.D. Thesis*, University of Bradford, **1980**.

12 A. F. Carley and M. W. Roberts, *Proceedings of the Royal Society of London Series a-Mathematical Physical and Engineering Sciences*, 1978, **363**, 403-424.

13 T. E. Madey, J. T. Yates and N. E. Erickson, *Chemical Physics Letters*, 1973, **19**, 487-492.

14 J. H. Scofield, *Journal of Electron Spectroscopy and Related Phenomena*, 1976, **8**, 129-137.

15 W. J. Carter, G. K. Schweitzer and T. A. Carlson, *Journal of Electron Spectroscopy and Related Phenomena*, 1974, **5**, 827-835.

16 R. F. Reilman, A. Msezane and S. T. Manson, *Journal of Electron Spectroscopy and Related Phenomena*, 1976, **8**, 389-394.

17 S. Tanuma, C. J. Powell and D. R. Penn, *Surface and Interface Analysis*, 1994, **21**, 165-176.

18 C. J. Powell, A. Jablonski, I. S. Tilinin, S. Tanuma and D. R. Penn, *Journal of Electron Spectroscopy and Related Phenomena*, 1999, **99**, 1-15.

19 R. W. Paynter, *Surface and Interface Analysis*, 1999, **27**, 103-113.

20 ARCtick; P. Cumpson, National Physical Laboratory, Version 1.0, 2007

Chapter 4 – The interaction of thorium with water and ammonia

4.1 Introduction

This chapter focuses on the interactions between ammonia, water, oxygen and the surface of thorium metal.

Thorium, the most abundant of the actinide elements [1], has an electronic structure of $[Rn]6d^27s^2$. Being the only element in the actinides to lack any 5f electrons, thorium is an especially useful element for investigating the effect valence f electrons have on surface reactions. As was explained in section 1.1, both the physical and chemical properties of the light actinides are influenced heavily by the 5f electrons, with research into their behaviour being of fundamental interest [2-5]. Through comparison of thorium with other actinide elements (such as uranium) that do possess valence f electrons, researchers have in the past attempted to distil the effect that they have on surface bonding [6-12]. Comparisons can also be made with cerium which occupies an analogous position in the lanthanide series. Cerium, unlike thorium, does contain valence f electrons; however as was mentioned in section 1.1, the 4f electrons of the lanthanides have been shown to behave very differently to the 5f electrons of the actinides [2-5]. While much research has already been undertaken the work is far from complete, as it has been noted that there are still many unanswered questions relating to the 5f valence electrons and the actinides in general [13].

Thorium metal will allow us to investigate a $5f^0$ system and the behaviour of the 6d7s valence electrons, whilst also providing a base to compare and contrast the results acquired from a valence f electron containing element like uranium.

4.2 Clean thorium

Before examining the results of any reactions upon the surface, it is important to understand some key points about photoelectron spectroscopy of thorium. All photoelectron spectra were acquired using *SPECTRA* software [14] and analysed using *CasaXPS* software [15]. For the x-ray photoemission spectra in particular it is important to note that as thorium has an open f shell with two degenerative states, the effect of spin-orbit coupling (see section 2.3.3.4 d) results in the splitting of those degenerate states into two peaks. The two peaks correspond to $f_{5/2}$ and $f_{7/2}$ final states

with the ratio between the peak areas being 3:4. The peak shapes are complicated by satellites, resulting from two specific mechanisms. In addition to those due to the non-monochromated x-ray source, as detailed in section 2.3.4.1, there are additional intense satellites unique to thorium that result in the Th(4f) signals being made up of two distinct components, both of which can be seen in figure 4.1. The smaller component, which made up approximately 30 % of the total signal, was centred at approximately 2.5 eV higher binding energy than the main peak, and was a satellite resulting from a shake-up transition involving the thorium 6d electrons [16,17]. While the satellite was due to the screening of the 4f hole involving the 6d electrons, the main lines were due to screening by the 5f states, which are above E_F in the ground state, but become populated in the presence of the core hole [18]. The satellite is particularly troublesome, as it is located at a binding energy very similar to thorium oxide at 335.2 eV. This will be seen later on in the spectra acquired after exposure to water and oxygen.

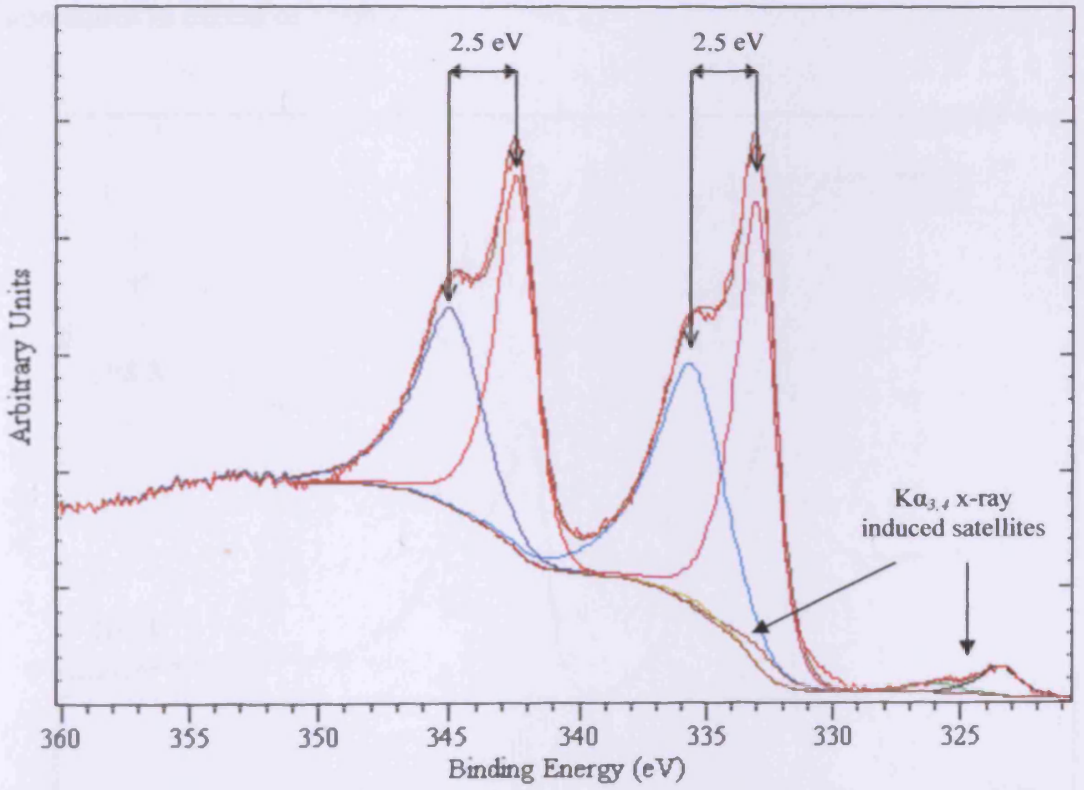

Figure 4.1: Th(4f) spectrum for clean thorium highlighting both the large satellite components situated at 2.5 eV higher binding energy than the principle signals, and the $K\alpha_{3,4}$ x-ray induced satellites

The combination of the distinctive satellite and the asymmetric nature of the actinide metal peaks (explained in section 3.2.2) combine to make thorium a challenging subject for x-ray photoemission studies.

As was explained in section 2.3.2.1, the binding energies observed by XPS are characteristic for each element. In the case of thorium the two primary signals in the Th(4f) region, the $f_{5/2}$ and $f_{7/2}$, have known values for the pure metal. Figure 4.2 shows the Th(4f) spectra of clean thorium at both "ambient" (298 K), and "cryogenic" (100 K) temperatures. For all the cryogenic experiments carried out the sample was cooled down *via* a continuous flow of liquid nitrogen through internal pipes running the length of the sample probe. The peak positions of 342.4 eV and 333.1 eV corresponded to Th $4f_{5/2}$ and Th $4f_{7/2}$ respectively [10,16]. As can be seen in the figure, there were no significant differences between the spectra acquired at the two different temperatures, which was to be expected as the same allotrope of thorium is stable at both temperatures. The alternative allotropes of thorium are only seen at temperatures in excess of 1500 K.

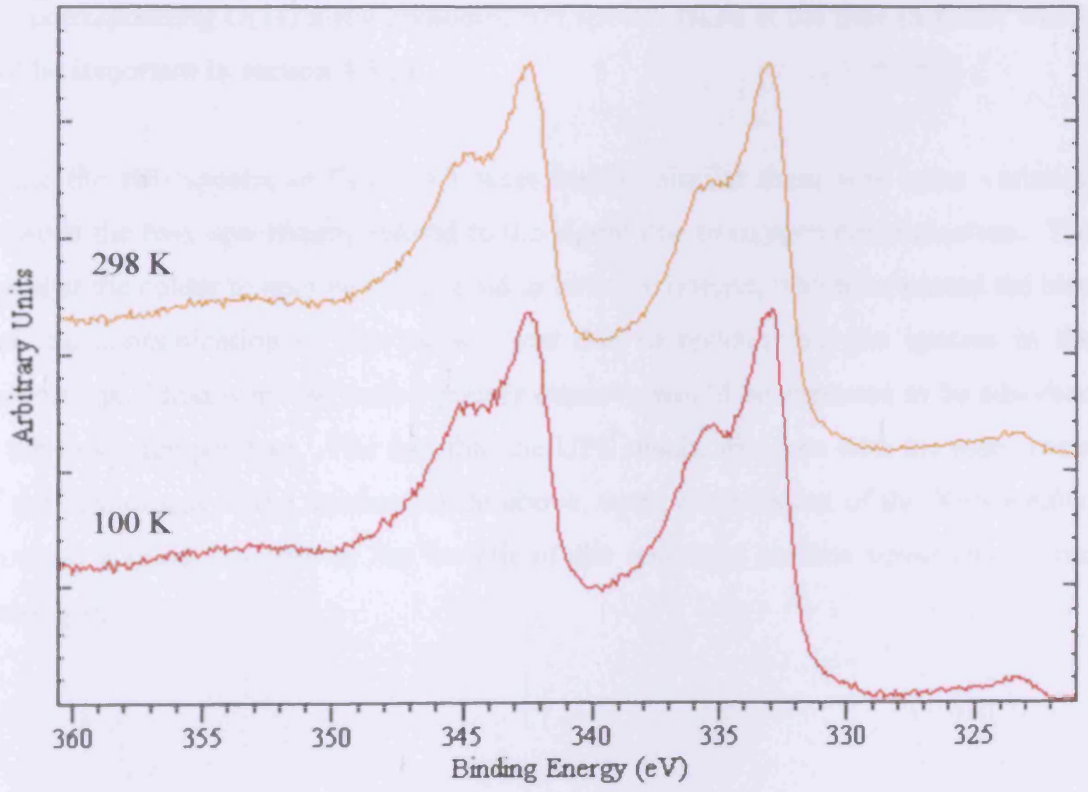

Figure 4.2: Th(4f) spectra for clean thorium acquired at 298 K and at 100 K

As the process of cooling down the sample to cryogenic temperatures takes upwards of 30 minutes, it could be expected that any residual water or other molecules in the vacuum would contaminate the clean surface. That the surface remains largely the same is a strong indicator of the clean condition of the vacuum system.

The ultra-violet photoelectron spectra of thorium, at both ambient and cryogenic temperature, can be seen in figure 4.3. These were both acquired after the surface had been sputtered, removing most of the contaminants, to create a clean surface. The key valence band (6d7s) states could be seen extending from E_f upwards in binding energy towards 4.0 eV, with the two key components at approximately 0.8 and 2.0 eV. At binding energies higher than 4.0 eV, when the signal from the valence states has largely disappeared, a new signal centred at 7.5 eV appeared. The position of this intense broad signal appears to correspond approximately to that of a shifted oxygen species [19,20], the presence of which can be attributed to both residual oxygen in the vacuum, and bulk oxygen in the sample itself. Owing to the increased surface sensitivity of UPS in comparison to XPS, the oxygen contamination seen in the acquired ultra violet spectra of figure 4.3 was considerably more noticeable than in any corresponding O(1s) x-ray photoelectron spectra taken at the time (a factor which will be important in section 4.3.2).

While the two spectra in figure 4.3 were largely similar there was some variation between the two, specifically related to the signal due to oxygen contamination. The signal at the colder temperature appeared to be more intense, which supported the idea that the contamination of the surface was due to residual oxygen species in the vacuum, as if that were the case a greater quantity would be expected to be adsorbed at the lower temperature. The fact that the UPS results disagree with the assessment of the cleanliness of the vacuum made above, upon examination of the XPS results, provides a good example of the benefit of the increased surface sensitivity of the technique.

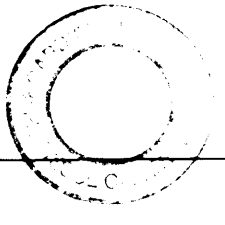

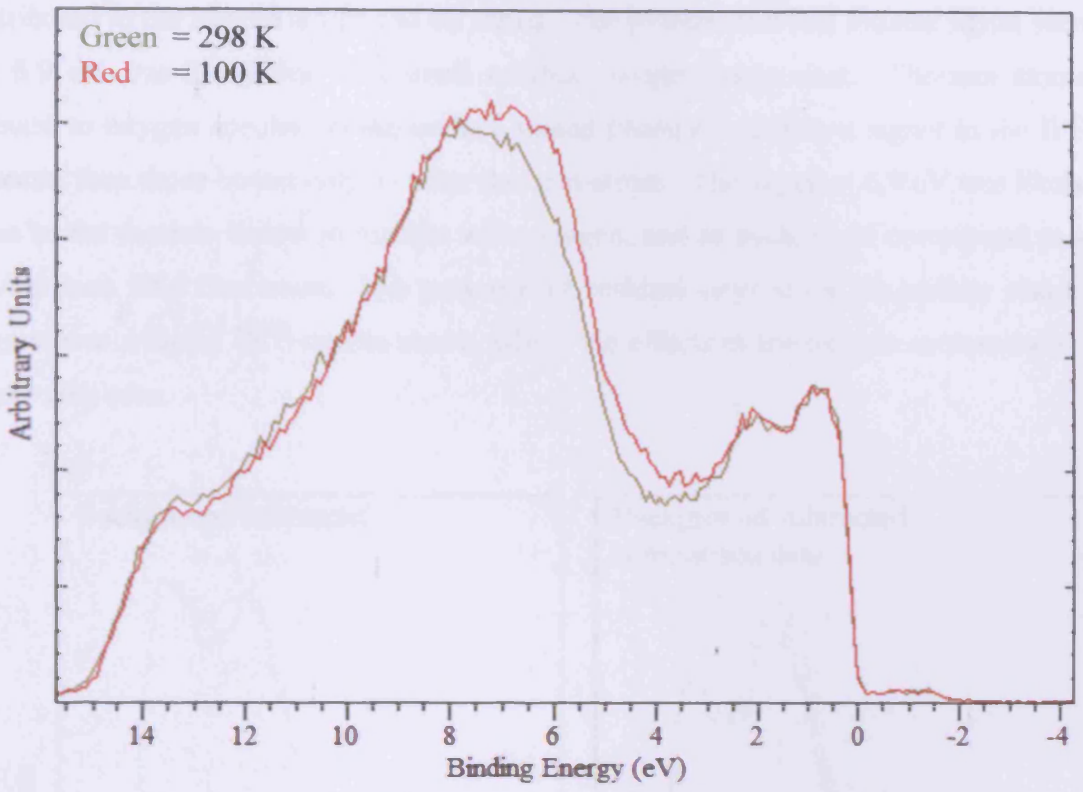

Figure 4.3: Height normalised He(I) spectra of thorium after sputtering, acquired at both 298 K and at 100 K

The inverse photoelectron (IPE) spectra of clean thorium, at both ambient and cryogenic temperatures, can be seen in figure 4.4. The background has already been fitted and subtracted utilising the methodology detailed in section 3.2.3. After processing, three distinct components remained constituting the majority of the spectrum. The two principle signals that can be seen were located at 1.4 and 3.2 eV above the Fermi level. An additional less intense, but broader visible signal was centred at 6.9 eV.

The spectrum of a clean actinide metal should be dominated principally by the unoccupied states that correspond to the spin orbit doublets of the 5f and 6d states. However, as was mentioned in section 2.4.3, the energy of the photons being detected was centred around 9.5 eV. At this energy only the 6d states would be detectable as the photoionisation cross-section towards the 5f orbitals is essentially non-existent [21,22]. However the 5f unoccupied orbitals could be detected if there was band hybridisation in place, which a review by Moore and van der Laan has revealed to be

the case [13]. So the principle signals seen at 1.4 eV and 3.2 eV can be safely attributed to the hybridised 5f and 6d states. The broader and less intense signal seen at 6.9 eV was likely due to a small residual oxygen component. Thorium atoms bound to oxygen species on the surface would produce a different signal in the IPE spectra than those bound only to other thorium atoms. The signal at 6.9 eV was likely due to the thorium atoms in contact with oxygen, and as such could correspond to a hybridised 5f6d final state. The presence of residual oxygen on the surface was in agreement with the UPS results above, where the effects of the oxygen contamination were also seen.

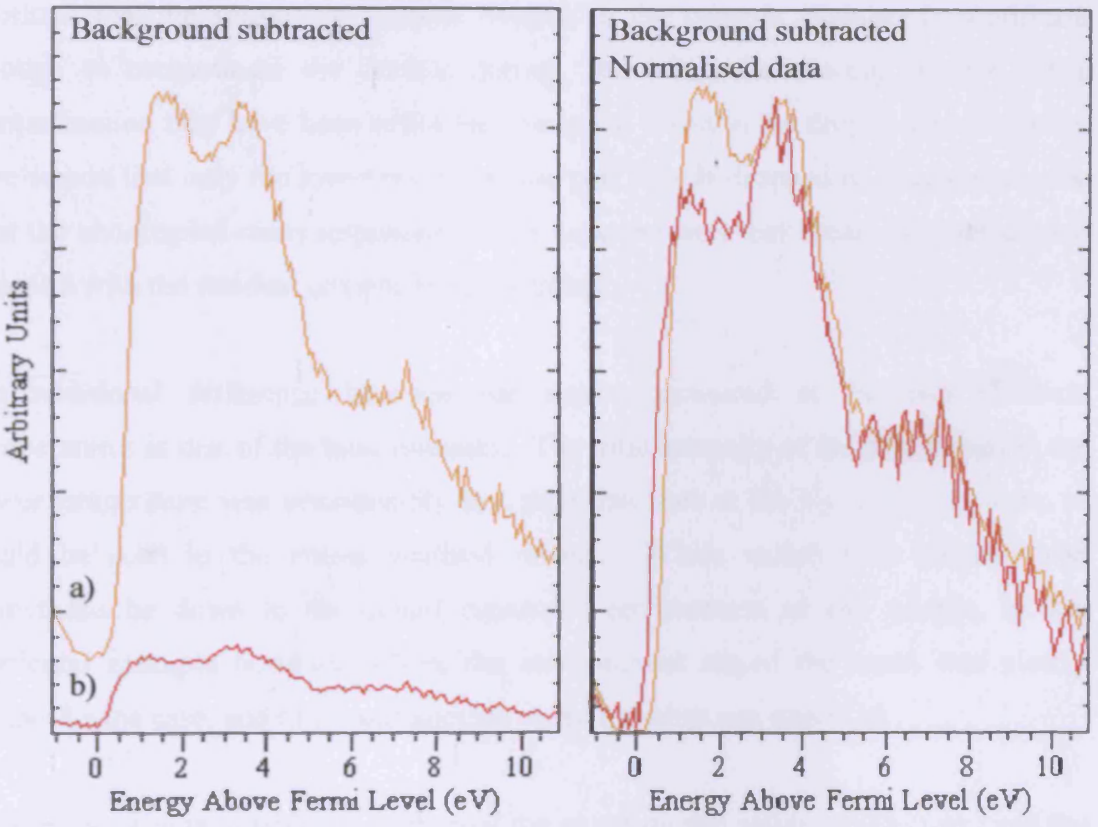

Figure 4.4: Inverse photoemission (IPE) spectra for clean thorium metal at a) 298 K and b) 100 K. The data is presented both before and after normalisation to aid comparison

Figure 4.4 also featured the normalised results of the experiments carried out at both temperatures, allowing direct comparison between the two, which showed up only cosmetic differences. The two principle signals and the single secondary signal were all present at the reduced temperature; however they were located at slightly different

energies. This energy shift was due to both the general decrease in intensity of the signal (mentioned below), but also the specific decrease in intensity of the peak at lowest energy, with respect to the other components. This intensity difference of the lowest energy peak was sufficient enough to have a knock on effect upon the peak fitting process (see section 3.2.8), thus altering the calculated positions of the components. The reason behind the decrease in intensity of the lowest energy signal may be down to the process of cooling used. As was mentioned above, a flow of liquid nitrogen through the probe on the system was used for the cold temperature experiments, with a period of at least 30 minutes needed for the sample to reach its lowest temperature. It has been shown above, while considering the UPS of clean thorium, that the amount of residual oxygen in the vacuum chamber is significant enough to contaminate the surface during, and after, the cooling process. The contamination may have been sufficient enough to result in the drop in intensity seen. The reason that only the lower energy of the two signals dropped in intensity may be that the unoccupied states responsible for it were the ones that became occupied upon reaction with the residual oxygen in the chamber.

An additional difference between the spectra acquired at the two different temperatures is that of the total intensity. The total intensity of the signal seen at the lower temperature was considerably less than that seen at the higher temperature, as could be seen in the non-normalised results. While variation in intensity can sometimes be down to the actual electronic environment of the sample, in this particular example however, where the environment stayed the same, that clearly cannot be the case, and there was another cause for what was observed.

It is in fact a very significant feature of the experimental setup used to carry out the inverse photoemission studies; that it often leads to a wide variation in the intensity of spectra acquired. The setup has demonstrated itself to be extremely sensitive to even very small changes in the positioning of the sample, electron gun, or detector, which can be explained by the extremely small signals being detected (the detected signal is routinely below 20 counts per second). Additionally, the electron gun is extremely variable in its output, the results of which are easily seen with the picoammeter attached to record the sample current. The maximum sample current seen for a specific filament current varied, along with the relationship between electron energy

and detected sample current. While the effect of the electron gun upon the actual shape of the spectra acquired was nullified by means of the modification method explained in section 2.4.3, this does not account or compensate for general changes in total intensity. This is why the spectra, particular those taken on different days, could vary so significantly with their intensities.

4.3 Adsorption of water (H_2O) on clean thorium

4.3.1 Introduction - the thorium and water system

The reaction of water with the radioactive actinide elements is of particular interest as water is one of the most likely contaminates that could come into contact with them whilst in storage. The risk of general corrosion, and the more important specific risk that the radioactive emission could exacerbate the problem of dissociative adsorption upon the surface, and lead to the release of considerable quantities of O_2 and H_2, has led to a considerable quantity of research being undertaken, especially on uranium [7,9,23,24]. The thorium/water reaction on the other hand has not been studied anywhere near as much, but with the likelihood that its use as a nuclear fuel will expand in the future, possibly dramatically, the need to fully understand the reaction will intensify on the grounds of safety [25-27].

The effect of exposure of thorium to water has been previously investigated, for instance by Nornes and Meisenheimer [9] who studied it at 120 K. However it is important to note that the research by Nornes and Meisenheimer, and others of the period, was undertaken before the large satellite in the XPS spectra of Th(4f) had been properly identified, and was thus mistakenly attributed to a thorium oxide.

In addition to the corrosion reasons noted above, and the more general investigation of the 5f electrons, it is also of interest to study the reaction of water upon the surface of thorium as the results can be compared against those from thorium exposed to oxygen, providing an insight into the oxidation process.

4.3.2 Experimental results – XPS and UPS

The effects of gradual exposure of clean thorium metal to increasing quantities of background dosed H_2O at approximately 298 K can be seen in figures 4.5 to 4.8. In the Th(4f) region (see figure 4.5) the H_2O oxidised the thorium surface resulting in the appearance of the thorium oxide peak at 335.2 eV. When compared to the work carried out by Nevitt [11] (which is backed up by McLean *et al* [10]) on the oxidation of thorium with O_2 (the thorium and oxygen system), there was a pronounced difference in the magnitude of exposure necessary to generate similar looking oxide peaks in the Th(4f) region. To generate the same intensity oxide signal the exposure needed to be approximately 20 times greater, so 100 Langmuirs of H_2O was needed to match the effect of 5 Langmuirs of O_2 [11]. While it may simply be due to differing reaction probabilities of the two reagents for the thorium surface, additional factors related to the reagents may potentially be involved. One important factor is the ratio of oxygen atoms in H_2O and O_2, which is 1:2 respectively, and also the availability of oxygen atoms formed by the splitting of O_2 on the surface. An additional factor that possibly contributes to the discrepancy is the nature of the reactions taking place on the surface between the hydrogen and thorium atoms. After the water adsorbs and dissociates upon the surface, the resulting hydrogen atoms could end up occupying the vacant sites, preventing further H_2O molecules from reacting with the surface. With few free sites the additional H_2O molecules could instead hydrogen bond to the oxide and hydroxide species already present on the surface, thereby preventing and eliminating the chance of them then adsorbing directly to the thorium and dissociating to provide the oxygen atoms needed to form ThO_2.

It was noted above that the thorium oxide peak is located very close in binding energy to the large thorium satellite. As the exposure to H_2O increased, the signal due to the satellite became obscured by the growing oxide peak. By 100 Langmuirs exposure the oxide peak was the dominant feature, with the thorium metal peak only making up 18.6 % of the total signal. Clearly the continuing presence of the unoxidised metal signal in the Th(4f) region indicates that metallic thorium is still in the near surface region, as the technique of XPS is only capable of analysing down to ~50 Å. The signal was most likely to be from thorium metal that was completely submerged by the oxide and hydroxide layers above, as the explanations offered for the relatively

slow oxidation of the surface with H_2O as opposed to O_2 rely upon the blocking of surface sites, and the unavailability of the pure thorium metal. Based upon the idea of distinct layers, the depth of the oxide/hydroxide layer was calculated to be approximately 25 Å thick. The concept of surface layers, and their thickness, is explored in greater detail later (see page 102), with the support of coverage calculations.

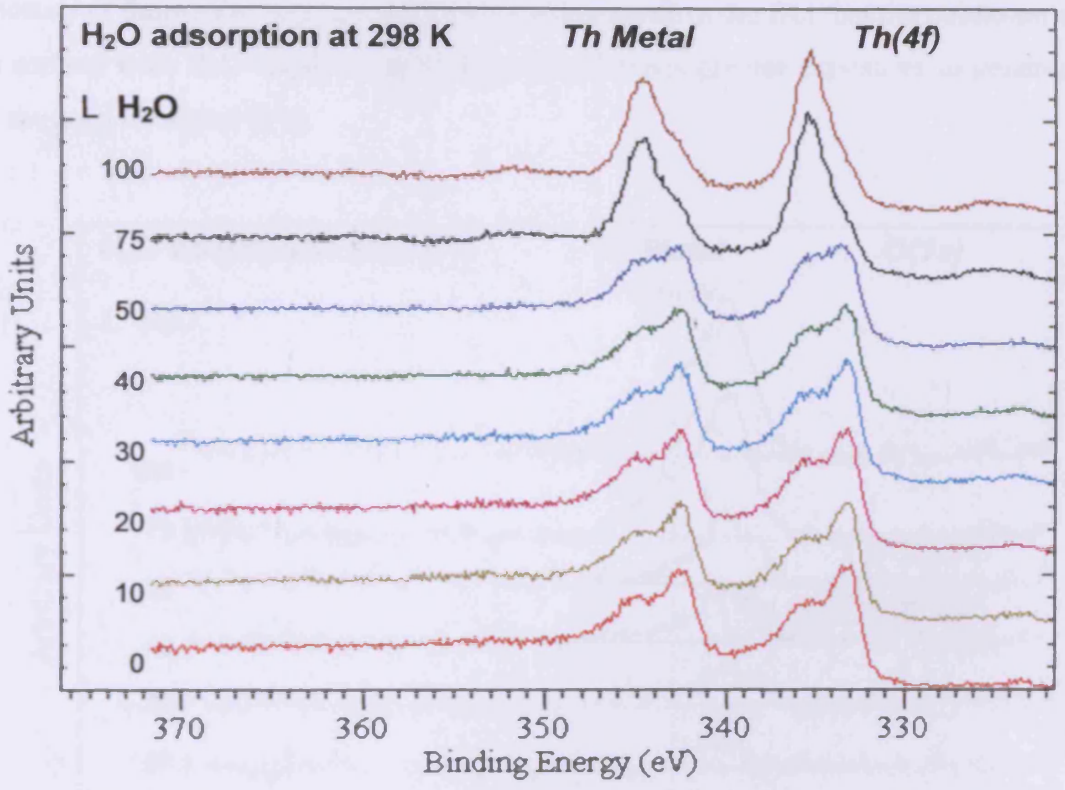

Figure 4.5: Th(4f) spectra for clean thorium exposed to increasing quantities of H_2O at 298 K

After 100 Langmuirs of H_2O exposure the signal from the clean thorium metal at 342.4 appeared noticeably larger than that of the one at 333.1 eV. This was due to the presence of a shake-up satellite situated at 343 eV which contributed to the lower binding energy side of the Th($4f_{5/2}$) peak. The existence of this satellite was confirmed by the visible presence of the second shake-up satellite, at approximately 352 eV, which was expected because of spin-orbit coupling. Satellites at these energies are characteristic of bulk ThO_2 [28].

It can be seen in figure 4.6 that there were two distinct components in the corresponding O(1s) spectra, as opposed to one which was seen in the thorium and oxygen system [10,11]. The smaller peak at 532.6 eV, which made up 40 % of the total signal, was due to OH^- species, as opposed to the O^{2-} species that form ThO_2, which were responsible for the larger peak at 531.0 eV [10]. 531.0 eV is the same binding energy for the O^{2-} species as has been reported for exposure of thorium to pure oxygen [10,11]. Again, when compared to the work carried out by Nevitt on the exposure of thorium to oxygen, the O(1s) spectra confirm the fact that the oxidation of the surface with H_2O requires approximately 20 times greater exposures to generate the same O(1s) signal [11].

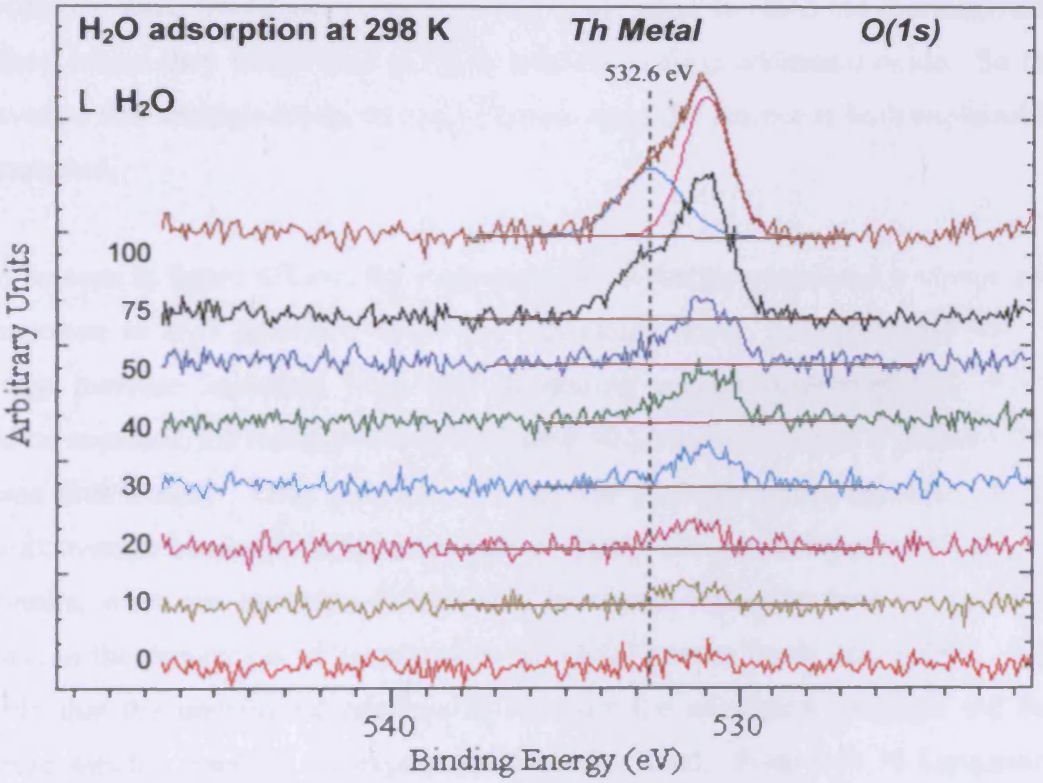

Figure 4.6: O(1s) spectra for clean thorium exposed to increasing quantities of H_2O at 298 K

By plotting the coverage of surface oxygen species, calculated from the O(1s) spectra using the Carley-Roberts equation [29] (see section 3.3 for details), against exposure to H_2O, it is possible to note any trends in surface coverage. Figure 4.7 shows the coverage versus exposure graph for the reaction of H_2O with thorium. The calculations carried out suggest the presence of multiple layers of adsorbate. Based

on the theoretical value for the number of active sites on the surface, 1 x 10^{15} sites per cm^2, after 100 Langmuirs the coverage was approaching the equivalent of 13 layers. Calculation of the thickness of the adsorbed layer, utilising the equation given in section 3.3.1, returned a value of 25 Å, which supports and agrees with the high multilayer coverage displayed in the figure.

The multilayer formation is possible due to the mechanism for the oxidation of thorium with water. Initially the incoming H_2O molecules adsorbed and dissociated directly on the thorium metal surface to form the oxide. After the formation of the first layer of oxide on the surface, additional oxidation relied upon the process of diffusion. The oxygen atoms supplied by the incoming water molecules, in the form of hydroxide ions, would diffuse through the oxide layer to reach the thorium/oxide interface, where they would then undergo reaction to form additional oxide. So the observation that multiple layers of oxide formed upon the surface is both explainable and expected.

It can be seen in figure 4.7 that the relationship between the calculated coverage and the exposure to H_2O does not follow the "standard" form. Instead of the rate of coverage increase beginning high, and decreasing upon further exposure, which would be expected, the rate remained stable until 50 Langmuirs, where it proceeded to increase dramatically. Only after this did the rate then proceed to decrease, as the surface coverage headed towards a saturation value. The period between 50 and 75 Langmuirs, when the coverage dramatically increased, coincided with a significant increase in the proportion of the signal in the O(1s) spectra being due to OH^-. It is possible that the unexpected relationship between the calculated coverage and the exposure was the result of the experimental method used. From 0 to 50 Langmuirs the exposures were carried out in 10 Langmuir intervals, with each exposure being undertaken at 10^{-7} mbar and lasting a duration of 100 seconds. From 50 to 100 Langmuirs the exposures were carried out in 25 Langmuir intervals, with each exposure again being undertaken at 10^{-7} mbar, but this time lasting a duration of 250 seconds. As the mechanism for the formation of the oxide relies upon the adsorption and dissociation of H_2O to form OH^-, which then diffuses through the adsorbate, it is possible that the equilibrium at the surface is influenced by the duration of the exposures. If the equilibrium on the surface between the adsorption and desorption

processes only adjusts slowly to changes in the system, it is possible that the extended duration under which the surface was exposed to incoming H_2O molecules could have driven the equilibrium further to the side of adsorption, thus facilitating an increase in dissociation, and therefore a significant increase in surface coverage. That there was not a similar significant increase when the total exposure increased from 75 to 100 Langmuirs was most likely due to the surface approaching saturation. The oxidation of thorium with O_2 has previously been shown to be diffusion limited, as the growing layer of oxide retards the diffusion of oxygen ions [11], so it is probable that the oxidation of thorium with H_2O is also diffusion limited, in this case reaching saturation after the adsorbate had grown to a thickness of 25 Å.

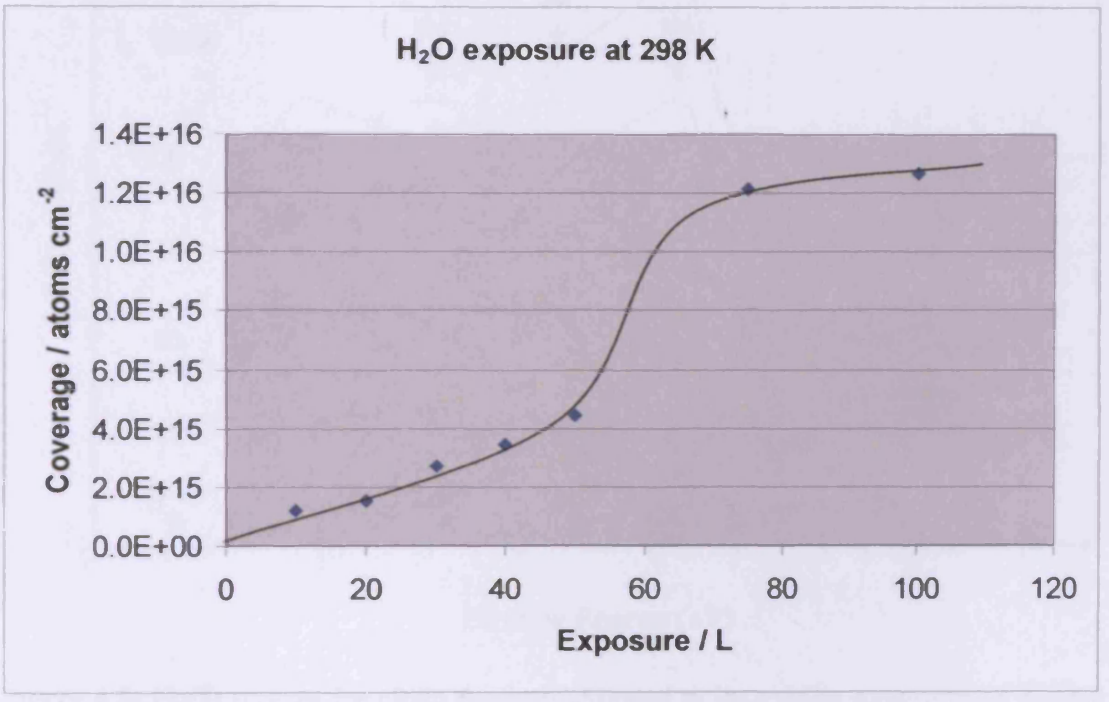

Figure 4.7: Adsorption of water on thorium at 298 K: calculated surface concentration of oxygen species plotted against exposure to H_2O

Figure 4.8 shows the corresponding He(I) UPS spectra acquired during the H_2O exposure experiments. With increasing exposure to H_2O a number of different peaks became visible in the region. Comparisons of the peak positions against reference values acquired for gaseous H_2O were used to help assign the observed signals [30-33]. The peak at approximately 5.5 eV corresponds to the $1b_1$ molecular orbital (overall non bonding [30]), while the partially hidden smaller peak at approximately

8.0 eV relates to the $3a_1$ molecular orbital (overall bonding [30], H-H bonding character [31,34]). An intense peak at approximately 5.5 eV has also been reported in the valence band of thorium after exposure to pure oxygen [10,11]. The final peak at approximately 11.1 eV corresponds to the $1b_2$ molecular orbital (overall bonding [30], O-H bonding character, H-H antibonding character [31]), of the gaseous molecule [32-34]. Figure 4.9, taken and adapted from "The Organic Chemist's Book of Orbitals" by W. L. Jorgensen and L. Salem [30], provides a visual representation of the various orbitals of gaseous water just described.

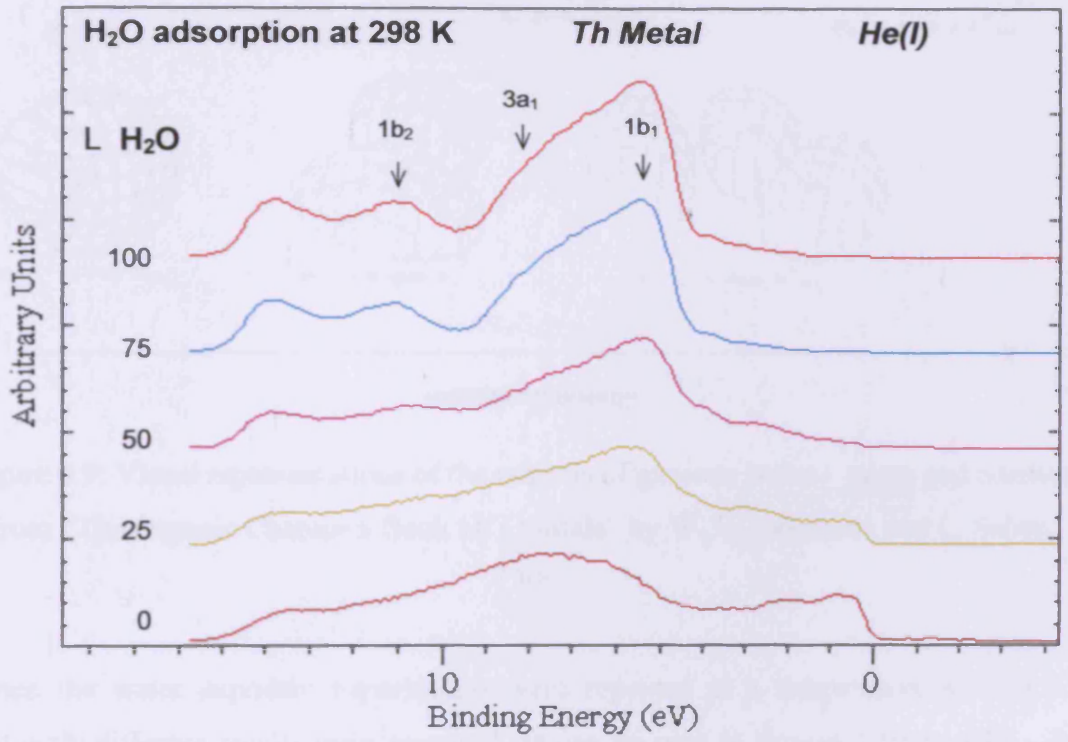

Figure 4.8: He(I) spectra for clean thorium exposed to increasing quantities of H_2O at 298 K

Between 50 and 75 Langmuirs of H_2O exposure the signal at the Fermi edge largely disappeared. This loss of the metallic 6d7s states close to the Fermi edge is understandable and agrees with the fact that thorium metal, like most actinides, has a high density of states (DOS) located at the Fermi edge, while thorium dioxide, which is an insulator, does not. Again, as with the XPS results and the calculated surface coverages, there was a noticeable increase in the signal recorded in the spectra between 50 and 75 Langmuirs. As well as an overall increase in intensity, the peaks

corresponding to the $1b_1$ and $3a_1$ orbitals increased in size compared to that of the $1b_2$ orbital. The increase is likely connected to the proportion of hydroxide making up the total oxygen signal, which was also seen to increase between 50 and 75 Langmuirs H_2O exposure.

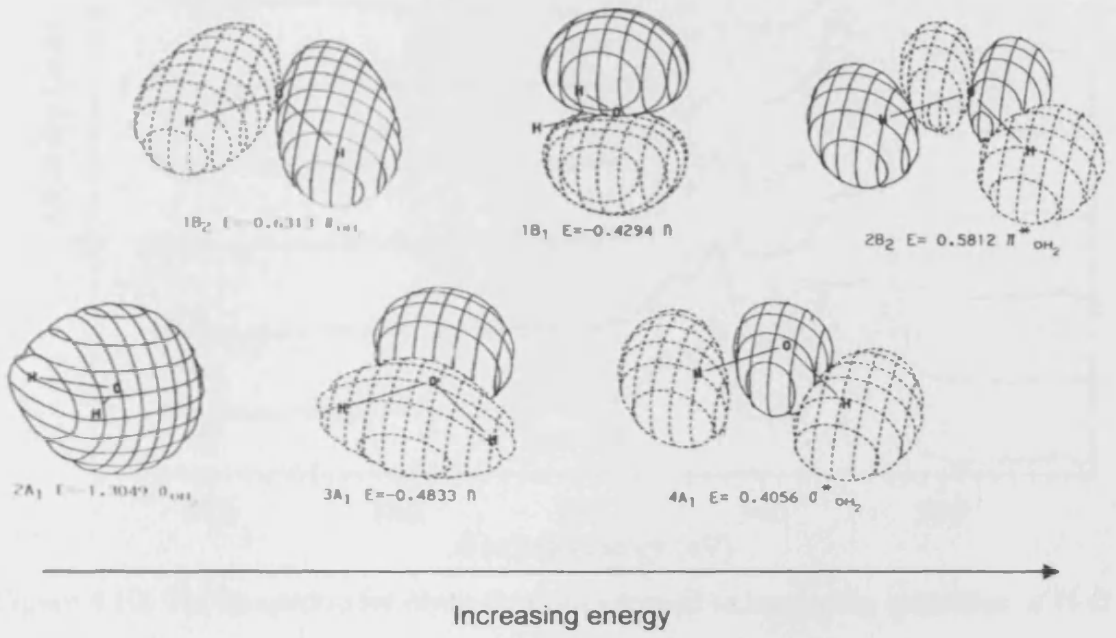

Figure 4.9: Visual representations of the orbitals of gaseous water – taken and adapted from "The Organic Chemist's Book Of Orbitals" by W. L. Jorgensen and L. Salem [30]

When the water exposure experiments were repeated at a temperature of 100 K, distinctly different results were acquired, as can be seen in figures 4.10 to 4.14. As before the addition of H_2O resulted in the oxidation of the thorium; however the two experiments deviated between 50 and 75 Langmuir exposure. Unlike the experiment run at ambient temperature, where the thorium oxide signal seen in the Th(4f) region continued to increase, the move from 50 to 75 Langmuirs at 100 K resulted in the disappearance of the Th(4f) signal in its entirety (see figure 4.10). This can be attributed to the formation of a layer of solid H_2O on the surface of the thorium that attenuated the signal from the thorium to the point where it could no longer be seen.

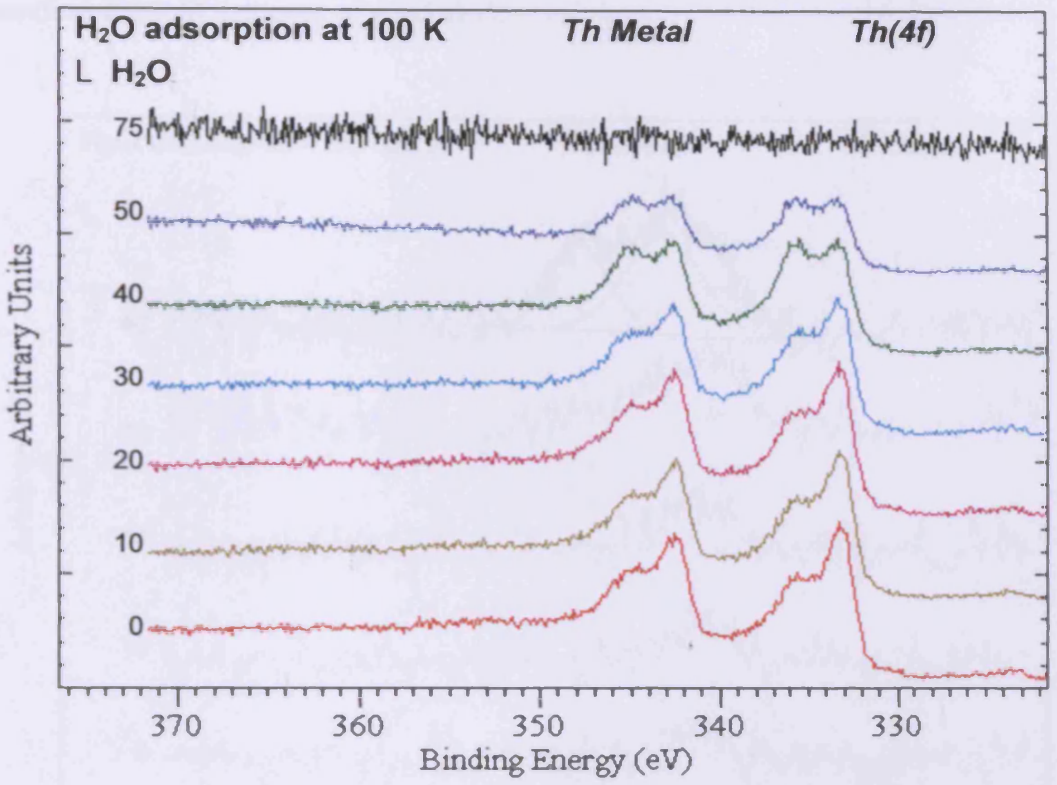

Figure 4.10: Th(4f) spectra for clean thorium exposed to increasing quantities of H_2O at 100 K

The differences between the two temperatures was also clearly visible in the O(1s) region (see figure 4.11). The results remained the same up until the increase from 30 to 40 Langmuirs exposure. After 40 Langmuirs exposure at 100 K a third distinct component became visible. This new component which made up 30 % of the total signal, and was centred at 534.9 eV, can be attributed to physisorbed H_2O on the surface of the sample. The three component spectrum seen after 40 Langmuirs matched up very well to the results seen by Nornes and Meisenheimer [9] in their own studies, after they exposed their thorium sample to 40 Langmuirs.

Further exposure to H_2O caused the newly formed third component at 534.9 eV to dramatically increase in intensity. Figure 4.12 shows the results acquired upon continuation of the dosing up to 50, and then 75 Langmuirs. The component resulting from the physisorbed H_2O increased both in size, and binding energy, as the exposure was increased. At 40 Langmuirs it was centred at 534.9 eV, at 50 it had increased to 535.3 eV, and finally at 75 Langmuirs it had shifted to 535.6 eV. The shift in energy

is possibly due to increases in the strength of the hydrogen bonding, due to the expanding depth of the layer of solid H_2O.

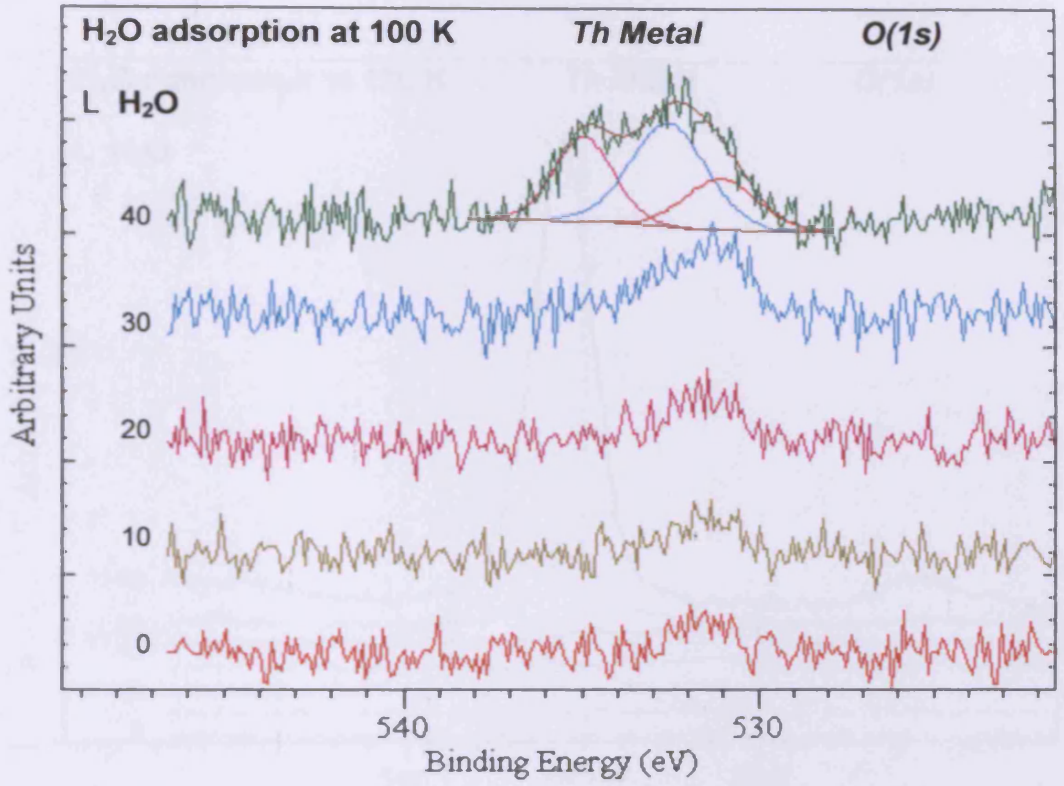

Figure 4.11: O(1s) spectra for clean thorium exposed to increasing quantities of H_2O at 100 K

The increases seen in the O(1s) region upon increasing exposure up to 75 Langmuirs coincided with the disappearance of the Th(4f) signal mentioned previously, as the layer of solid H_2O became the dominant factor and source of all detected photoelectrons, thus blocking off the signal in the thorium region. The growing layer of physisorbed ice predictably also led to the attenuation of the signals due to OH^- and O^{2-} species, which were completely lacking in the 75 Langmuir spectra.

Figure 4.13 shows the coverage versus exposure graph acquired when the H_2O exposure experiment was repeated at a temperature of 100 K. As with the results acquired at 298 K (see figure 4.7), the relationship between the two variables again deviated from the "standard" form. The rate of coverage increase remained relatively stable until 30 Langmuirs exposure, where it proceeded to accelerate rapidly up until 50 Langmuirs exposure, upon which it then proceeded to decrease again. Upon

reaching 75 Langmuirs exposure the coverage values appeared to be beginning to saturate; however it cannot be concluded for certain whether the surface species would have reached equilibrium without additional results being acquired.

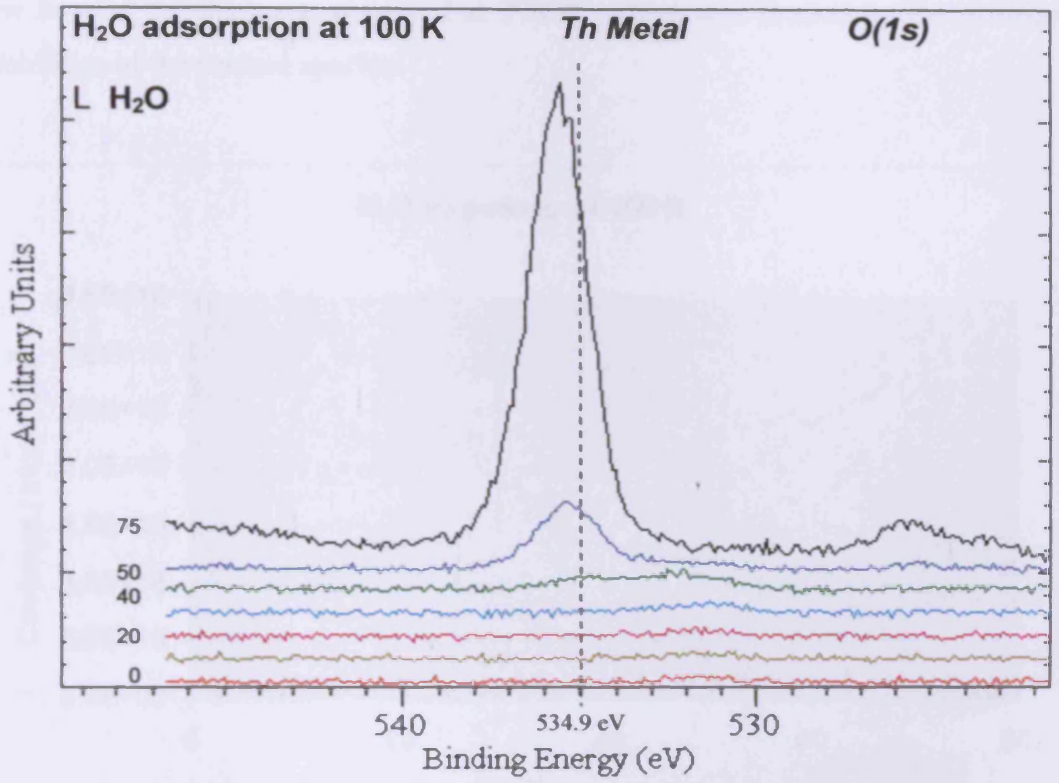

Figure 4.12: O(1s) spectra for clean thorium exposed to increasing quantities of H_2O at 100 K.

The sudden increase in the rate of growth of the adsorbate on the surface, upon the exposure rising above 30 Langmuirs, coincided with the appearance of a signal from physisorbed H_2O, and an increase in the OH^- signal, in the O(1s) spectra. It is possible that the probability of incoming H_2O molecules physisorbing onto the surface was enhanced through the presence of oxide, and more importantly hydroxide species, on the surface. So as the proportion of the hydroxide signal in the O(1s) spectra increased and became more prominent upon the exposure rising above 30 Langmuirs, a dramatic increase in the physisorption of H_2O molecules also occurred, leading to the observed sudden increase in the rate at which the adsorbate grew on the surface.

The total surface coverage after exposure to 75 Langmuirs of H_2O was 3.0 x 10^{16} atoms per cm^2, more than double the value calculated for the reaction at 298 K. This can be attributed to the fact that at 100 K the incoming H_2O was capable of physisorbing to form layers of solid water. It is because of this that the adsorbate grew beyond the thickness observed at 298 K, which was limited by the diffusion capabilities of the surface species.

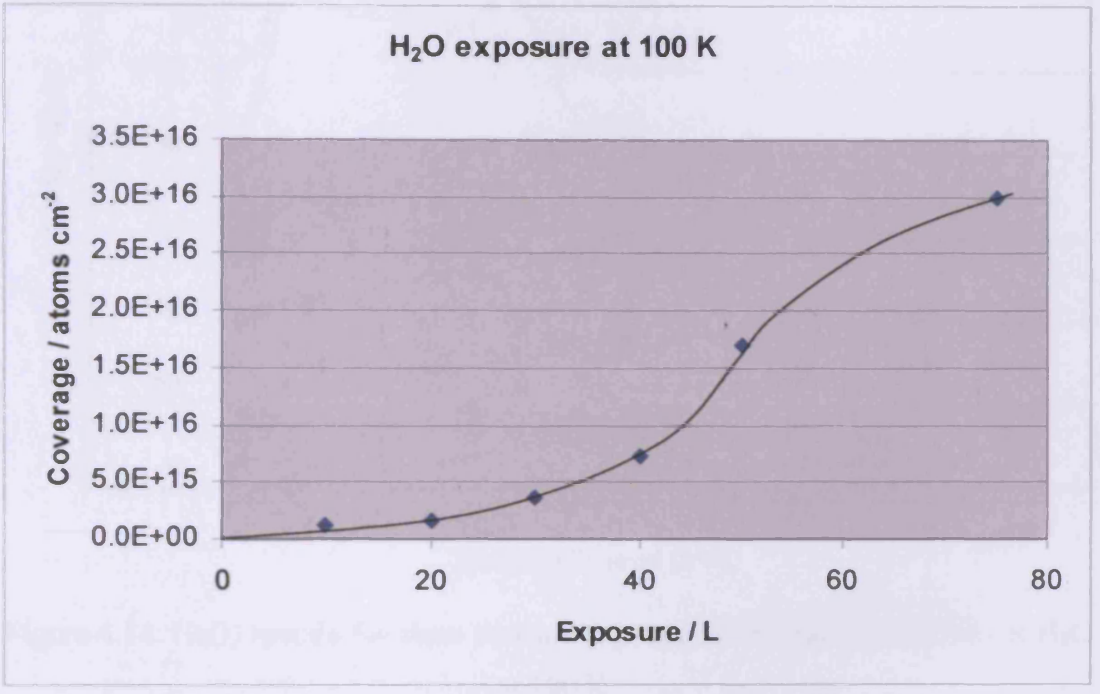

Figure 4.13: Adsorption of water on thorium at 100 K: calculated surface concentration of oxygen species plotted against exposure to H_2O

Figure 4.14 shows the corresponding He(I) UPS spectra acquired during the H_2O exposure experiments at cryogenic temperature. As in figure 4.8, exposure to H_2O resulted in a number of different peaks becoming visible in the region. Up to 60 Langmuirs exposure, the results were relatively similar to those seen at ambient temperature. The $1b_2$ molecular orbital peak at 11.1 eV was present; however the large peak at approximately 7.0 eV could not be as easily resolved into the separate components that correspond to the $1b_1$ and $3a_1$ molecular orbitals. This may be due to the thick layers of physisorbed H_2O which were shown to be forming by 60 Langmuirs exposure in figures 4.10 and 4.12. The spectra acquired at 80 and 100 Langmuirs exposure showed the effects of the growing layer of ice on the surface.

Hydrogen bonding, when in the solid state of ice, severely affects the $3a_1$ molecular orbital, causing it to appear significantly broadened and dominate the spectra, leading to the results seen [35].

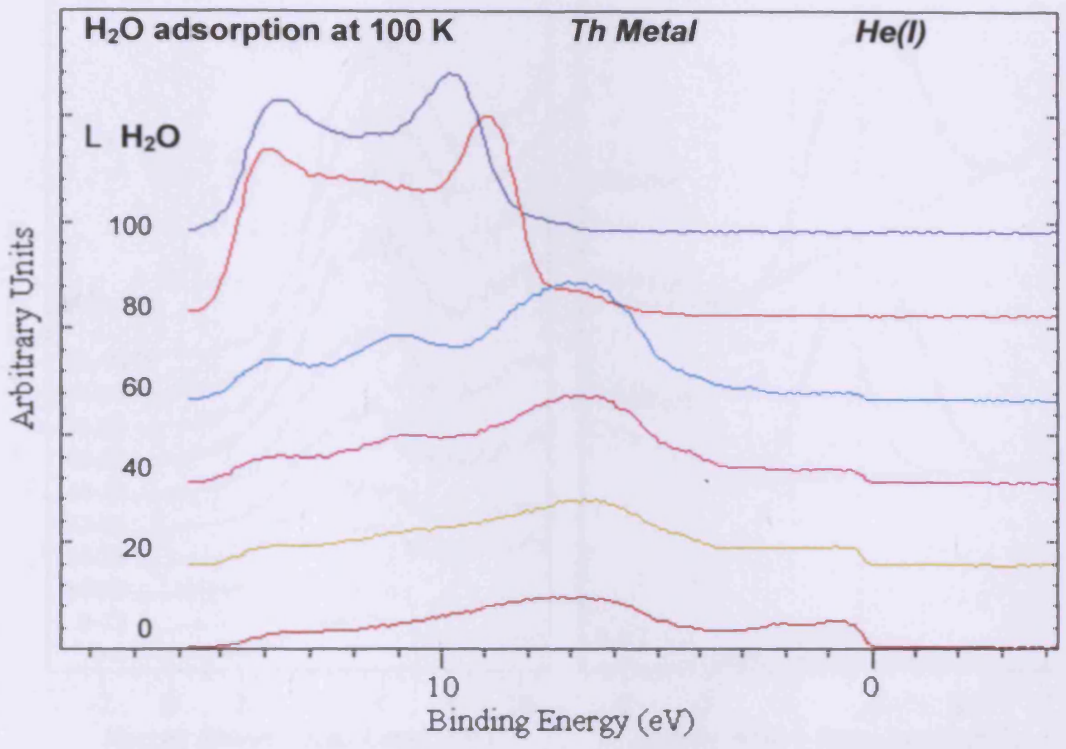

Figure 4.14: He(I) spectra for clean thorium exposed to increasing quantities of H_2O at 100 K

4.3.3 Experimental results – IPES

Inverse photoemission experiments examining the exposure of thorium to water were carried out separately from the forward photoemission experiments; however, the same two temperatures were investigated, and similar comparisons were made against the thorium and oxygen system.

The IPE spectra of thorium after exposure to H_2O at 298 K can be seen in figure 4.15. This system was the first to demonstrate the instability that can be caused by the low energy electron beam incident upon the surface. The left side of figure 4.15 features the raw data taken over a period of 80 minutes displayed in chronological order. After the first 4 minute scan a single broad peak was visible centred at 5.0 eV. This in

itself was composed of two separate components located at 4.1 and 5.7 eV that contributed 47 % and 53 % of the total peak respectively.

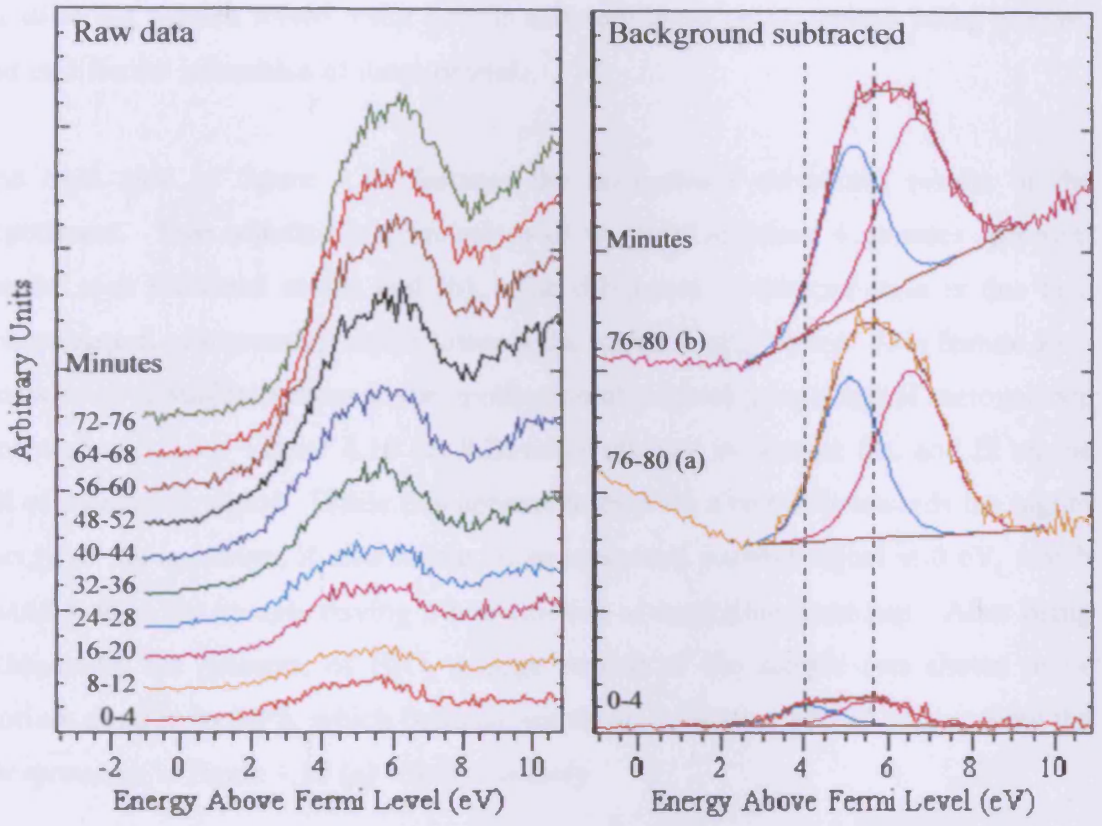

Figure 4.15: IPE spectra for thorium exposed to 500 L of H_2O at 298 K. The left features the raw data taken over a period of 80 minutes chronologically ordered. The right features the background subtracted data taken between 0-4 minutes and 76-80 minutes, with lines to highlight the shift in position

During the course of the next 76 minutes the sample was scanned 19 more times, detailing the gradual effect of the electron beam on the sample. By the end of the 80 minute experiment the observed broad peak had shifted 1.0 eV up in energy, so that it was centred at 6.0 eV. The two separate components had not only shifted upwards in energy, to 5.1 and 6.6 eV, but also shifted their relative contributions to a 50 % to 50 % split. In addition to the shift in energy, the intensity of the acquired signals also increased significantly over the course of the experiment. While a small part of this may be caused by the inherently variable nature of the low energy electron gun, the main cause will again be the instability of the surface under the electron beam. It is

possible the low energy electrons stimulated desorption of the more loosely held hydroxyl species from the surface, or led to their rearrangement into the oxide. This could lead to a noticeable change in intensity of the spectra, as the bonds formed with the differing species would result both in different unoccupied orbitals being present, and in different intensities of those orbitals.

The right side of figure 4.15 features the background subtracted results of the experiment. Two separate interpretations of the final acquired 4 minutes spectrum can be seen indicated as (a) and (b). The difference in interpretation is due to a noticeable tail of increasing signal towards the higher energy range. This feature adds a new level of subjectiveness in the application of the background signal removal step (see section 3.2.3.) Figure 4.15 (a) follows an attempt to account for, and fit to, the tail of increasing signal. While this appears to provide a better fit towards the higher energy of the spectrum, it also results in an unwanted positive signal at 0 eV, which would lead to the sample having a non existent or negligible band gap. After being oxidised by the presence of H_2O, a large portion of the sample was shown to be thorium dioxide by XPS, which being an insulator, does have a band gap, making the interpretation in figure 4.15 (a) wholly unlikely.

The alternative interpretation detailed in figure 4.15 (b) makes no attempt to account for the tail of increasing energy, treating it as part of an additional unoccupied state, the majority of which is located outside of the range of energies scanned. By acknowledging the existence of the additional unoccupied states, the removal of the background no longer results in an unwanted positive signal at 0 eV, which is more in keeping with the insulating properties of the sample.

IPES measurements of H_2O adsorption were repeated at 100 K, with the results split into two parts owing to the two distinct phases of surface coverage. The initial coverage of the surface up until 40 Langmuirs is shown in figure 4.16; while the secondary ice dominated coverage of the surface above 40 Langmuirs is shown in figure 4.17. For the first phase there was a significant difference between the 298 K experiment (500 Langmuirs) and the 100 K experiment (40 Langmuirs). 40 Langmuirs was chosen as the three different components in the O(1s) region were most visible after this exposure. Any greater exposure would lead to the quick

formation of multiple layers of ice on the surface. As there is no danger of ice formation at 298 K regardless of exposure, the 500 Langmuirs used is acceptable for comparison against the 40 Langmuirs used at 100 K.

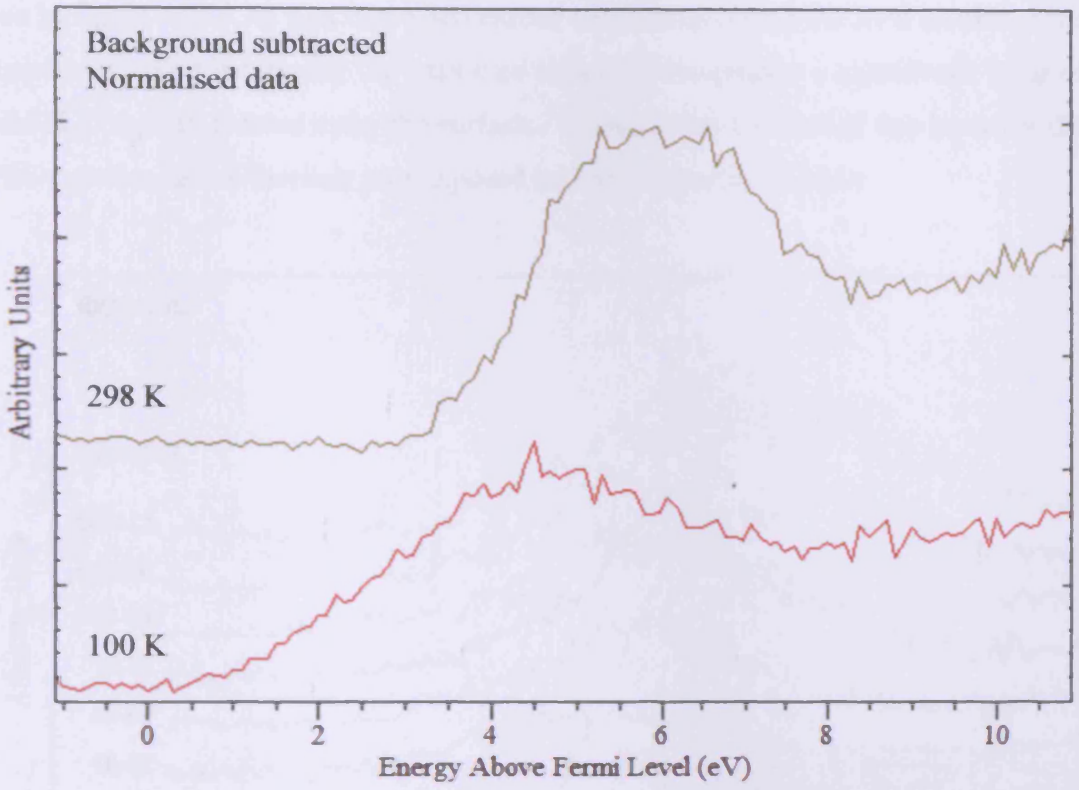

Figure 4.16: IPE spectra for thorium exposed to 500 L of H_2O at 298 K and 40 L at 100 K

To aid with comparison, figure 4.16 features the final spectrum taken at 298 K as well as that taken at 100 K. In contrast to the experiment carried out at 298 K, at 100 K the surface species were entirely stable under the electron beam, with no noticeable changes observed throughout the entire experiment. The extremely broad nature (~9 eV wide) of the single signal, centred at 4.5 eV, can be attributed to the presence of three distinct and largely similar sized signals in the O(1s) region as was shown in figure 4.11. Of particular note is the definite presence of a signal all the way down to the Fermi level itself, which when combined with the small signal present at the Fermi edge in the matching UPS spectra of figure 4.14, seems to suggest a negligible band-gap, and that the thorium is in a form that is still a conductor, or semi-conductor at the very least. The various thorium hydrides are known to display metallic conduction and semi conduction properties [27,36], so it is possible that a sufficient

quantity of the hydride has formed upon the surface, thus leading to the appearance of the small or negligible band-gap at this temperature.

The second part of the results for the exposure of thorium to H_2O at 100 K can be seen in figure 4.17. As was discussed earlier while considering the XPS results of the experiment, upon increasing the exposure above 40 Langmuirs a significant layer of solid H_2O rapidly formed upon the surface. To maximise the size of this layer for the IPES experiment the thorium was exposed to 500 Langmuirs of H_2O.

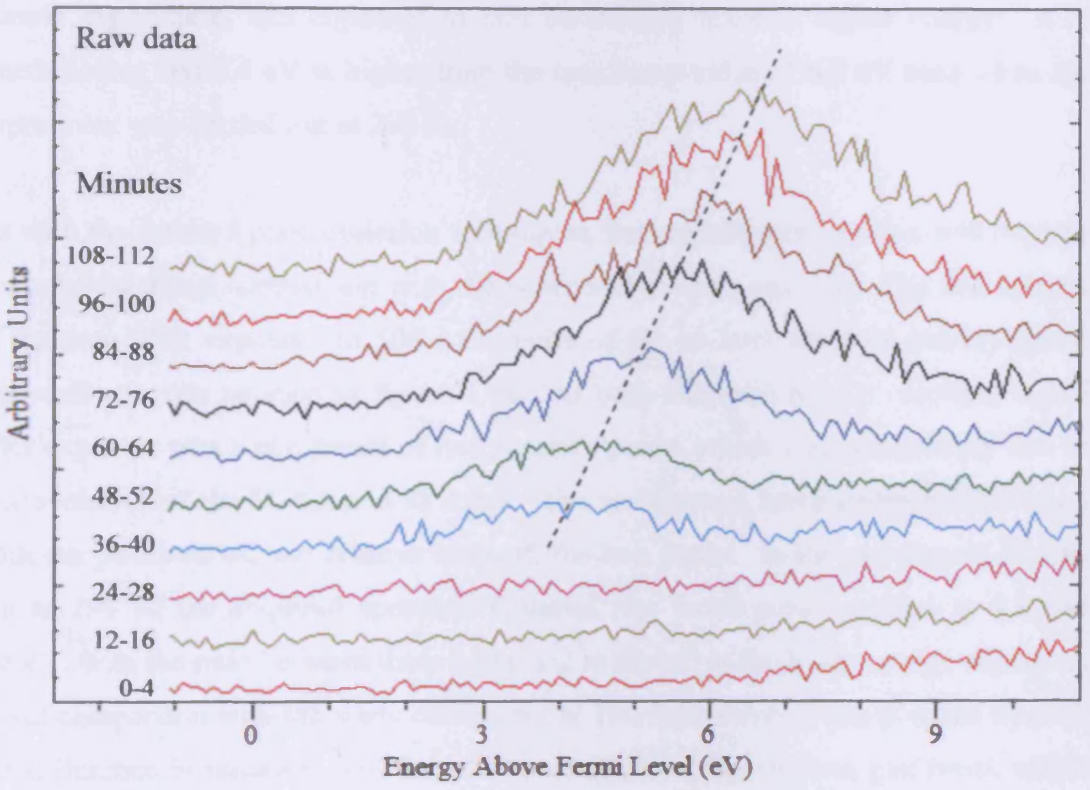

Figure 4.17: Chronologically ordered IPE spectra for thorium exposed to 500 L of H_2O at 100 K, taken over a period of 112 minutes

The acquired spectra in figure 4.17 provide another example of the unstable nature the surface can sometimes have whilst under bombardment from the low energy electron gun. Initially no signal was seen at all which indicated that there were no DOS within the first 10 eV above the Fermi level. This was due both to the thick layer of ice that prevented incoming electrons from reaching the thorium, and also to the fact that the 3s unoccupied orbitals of the oxygen atoms themselves were either not within the energy range studied, or the photoionisation cross-section towards them was

extremely low or negligible [21,22]. Therefore for a signal to be seen the layer of ice has to be thin enough to allow the low energy electrons to reach the proximity of the thorium, and trigger emission of photons from the 6d and 7s orbitals which the detector is known to be sensitive to. The surface had to undergo 32 minutes exposure towards the low energy electron beam before a signal first appeared. This indicates that the low energy electron beam is sufficiently powerful to stimulate desorption of the frozen layer of solid water. Over the course of the next 80 minutes the detected signal gradually increased in intensity and shifted upwards in energy. Beginning at approximately 4.0 eV the single peak had shifted to 6.4 eV by the end of the 120 minute experiment, and appeared to still be moving towards higher energy. It is worth noting that 6.4 eV is higher than the maximum value of 6.0 eV seen when the experiment was carried out at 298 K.

As with the forward photoemission techniques, the oxidation of thorium with oxygen is useful for direct comparison with the water and thorium reaction. The IPE spectra of thorium after exposure to 500 Langmuirs of O_2, at both ambient and cryogenic temperatures, can be seen in figure 4.18. At both temperatures the resulting signal after exposure was a composite of two separate peaks, which were most likely due to a convolution of the 5f, 6d, and 7s states. The temperature had a distinct effect upon both the positions of, and relative sizes of, the two peaks. In the experiment carried out at 298 K, the acquired spectrum featured two broad peaks centred at 4.8 and 6.6 eV, with the ratio between them being 3:2 in favour of the lower energy signal. A direct comparison with the study carried out at 100 K however is complicated by both the difference in intensity, and the additional effect of the electron gun itself, which again has shown the surface species to be only weakly bound.

Figure 4.19 shows the spectra acquired at 100 K every 20 minutes over a total period of 80 minutes. The damaging nature of the electron gun can be observed in the observation that the acquired signal subtly altered as time went on. While the two broad peaks began centred at 4.4 and 6.2 eV, after 100 minutes they had shifted to 4.2 and 6.1 eV respectively. Additionally the ratio between the two signals had also shifted, from 1:1 after 20 minutes, to 3:2 after 100 minutes (the 3:2 ratio matching that seen at 298 K).

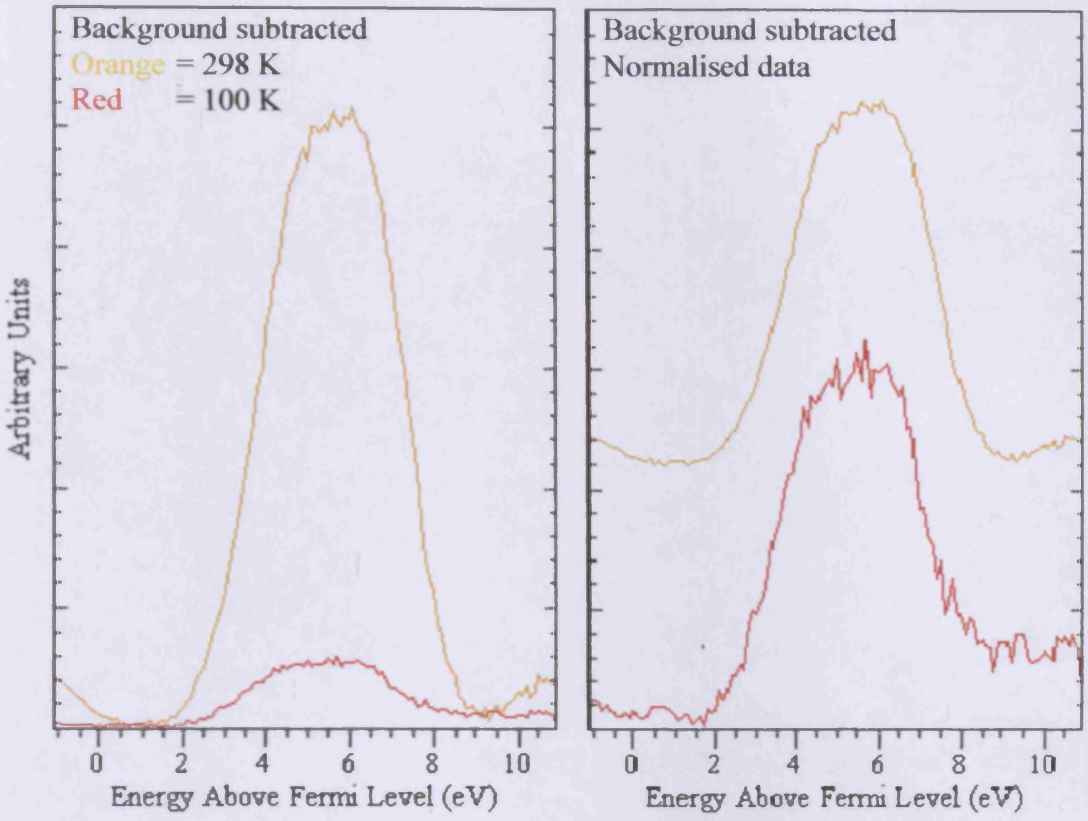

Figure 4.18: IPE spectra for thorium exposed to O_2 at 298 K and 100 K. The left spectra are before normalisation while the right ones after normalisation

When comparing the results of the exposure to oxygen against the exposure to water, the first notable difference was their stabilities under the low energy electron beam. The surface during the oxygen experiment was stable at 298 K but unstable at 100 K, while the surface during the water experiment was unstable at 298 K but stable, up to 40 Langmuirs, at 100 K. The second big difference was that while exposure to either reagent resulted in the formation of one broad peak, in the spectra from the oxygen experiment the peak was the only signal that was visible. This was in contrast to the results of the water experiment where there was a prominent tail of increasing energy leading from the high energy side of the single peak, suggesting the presence of additional unoccupied states centred outside the range of the scanned region. A third difference between the two experiments was the form that the single broad peak took. In the oxygen exposure experiments the peak could clearly be seen to be made up of two distinct components, with the greatest intensity on the higher energy side, which when peak fitted showed that the lower energy component made up 60 % of the total

signal. This was in contrast to the results of the 298 K water exposure experiment where, although the peak was also made up of two distinct components, the greatest intensity was on the lower energy side, and when peak fitted showed that both peaks provided approximately 50 % of the total signal. The water exposure experiment carried out at 100 K stood out from all the others in that the detected signal was symmetric in shape and could be fitted with a single broad peak shape.

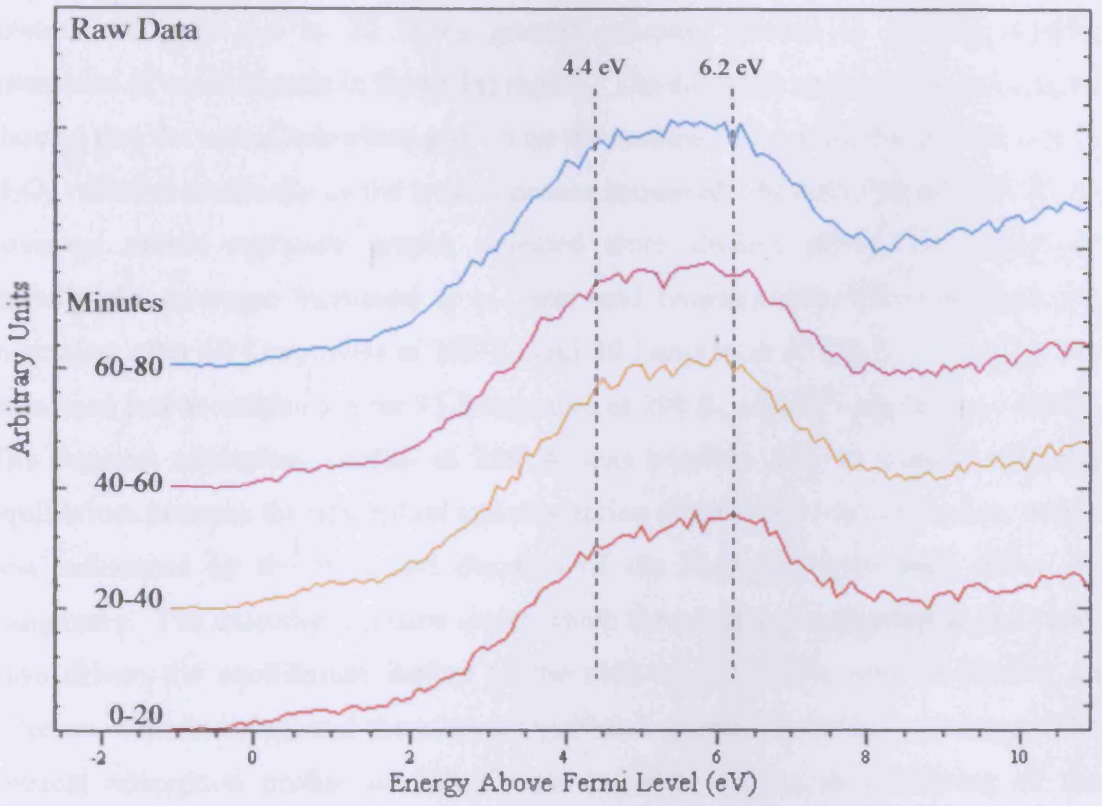

Figure 4.19: Chronologically ordered IPE spectra for thorium exposed to 500 L of O_2 at 100 K, taken over a period of 80 minutes

4.3.4 Additional discussion

At both 298 K and 100 K the exposure of clean thorium to H_2O led to the formation of multiple oxygen species. The binding energies for the Th(4f) and O(1s) regions indicated the presence of hydroxide and oxide species, with an additional component due to physisorbed H_2O at 100 K. Additional evidence for the formation of the oxide species was provided by the presence of shake-up satellites at 343 and 352 eV in the Th(4f) region, that are known to indicate the formation of bulk ThO_2 [28]. The shake-up satellites were only visible at 298 K, as at 100 K proportionally less oxide was

formed, especially at exposures greater than 50 Langmuirs. The three component O(1s) spectrum after 40 Langmuirs exposure at 100 K emulated and agreed with that seen in the literature [9]. The signal from the physisorbed H_2O at 100 K increased in size and dominated the O(1s) region after 50 Langmuirs exposure, resulting in the complete attenuation of the signal in the Th(4f) region.

The reactivity of the surface towards H_2O was shown to be considerably lower than towards O_2, with up to 20 times greater exposure needed to generate similar intensities of oxide signals in the O(1s) region. The coverage against exposure graphs showed that the rate of adsorbate growth on the surface of thorium, due to exposure to H_2O, varied dramatically as the total exposure increased. At both 298 and 100 K the coverage versus exposure graphs revealed three distinct phases of adsorption. Initially the coverage increased at a linear and constant rate before dramatically increasing after 50 Langmuirs at 298 K, and 30 Langmuirs at 100 K. The rate then decreased just as suddenly after 75 Langmuirs at 298 K, and 50 Langmuirs at 100 K. The unusual adsorption profile at 298 K was possibly due to a slow adjusting equilibrium between the adsorption and desorption of molecules on the surface, which was influenced by the increased duration of the H_2O exposures used above 50 Langmuirs. The extended duration under which the surface was exposed to H_2O may have driven the equilibrium further to the side of adsorption, thus facilitating an increase in dissociation, and therefore a significant increase in surface coverage. The unusual adsorption profile at 100 K was possibly due to an enhancing of the probability of incoming H_2O molecules physisorbing onto the surface, caused by the growing presence of hydroxide species on the surface, which became more prominent after 30 Langmuirs exposure. The increased probability led to the sudden and pronounced growth of multilayers of physisorbed H_2O on the surface.

The total surface coverage upon saturation at 298 K was calculated to be the equivalent of almost 13 layers, which was supported by depth calculations of the total layer thickness, that showed it be 25 Å thick. The total surface coverage after 75 Langmuirs at 100 K, calculated *via* the Carley-Roberts equation [29], equated to 30 layers, which was greater than the probing depth of XPS, meaning the total thickness was greater than 50 Å, but was too thick to calculate accurately using the methods described in chapter 3.

The low energy electron gun employed in the IPES experiments had a definite destructive effect upon the surface species at 298 K, and also upon large exposures carried out at 100 K. The single signals shifted upwards in energy away from the Fermi level as the experiments continued. Even with the loosely bound physisorbed H_2O present on the surface after 40 Langmuirs at 100 K, the general lack of energy in the system at that temperature was sufficient to cause the lack of susceptibility to the electron gun. After exposure to 500 Langmuirs at 100 K no signal was detected in the acquired IPE spectra until the surface had been under the effect of the low energy electron gun for 32 minutes. After 32 minutes a signal emerged that increased linearly in both intensity and energy above the Fermi level as the experiment continued.

The signals seen in the He(I) UPS and IPES results, acquired at 100 K, around the Fermi level show the conductive metallic nature of the surface up until 40 Langmuirs exposure, which was due to a combination of unreacted metallic thorium and thorium hydride. The hydrides of thorium, formed in this case due to the presence of hydrogen in H_2O, have been shown previously to display conductive and semi-conductive properties [27,36].

The relative stabilities of the 298 and 100 K surfaces towards the electron beam are the reverse of those seen for the O_2 on thorium system, where the surface was stable at 298 K and unstable at 100 K. Exposure to H_2O resulted in single peaks in the IPE spectra with additional tails of increasing energy that indicated additional intensity centred outside the range of the scan. This was in contrast to the single peak with no background intensity seen for the O_2 on thorium system at both 298 and 100 K.

4.4 Adsorption of ammonia (NH_3) on clean thorium

4.4.1 Introduction – the thorium and ammonia system

The reaction of ammonia with thorium has not been investigated before at any temperature, but it is suspected that it will lead to the formation of ThN. ThN, unlike the analogous and promising nuclear fuel UN [37], has proven highly unstable in air, even more so than pure thorium metal, which has hampered research into its

electronic structure [18]. Efforts made in the past to stabilise the ThN, to allow investigation of its electronic properties, by forming it through a process of reactive sputtering in a nitrogen environment, have proven somewhat successful [18]. Following on from this it is hoped that the exposure of clean thorium metal to ammonia will also result in a more stable example of ThN being formed, allowing a more complete investigation of its electronic structure, particularly that of the unoccupied orbitals.

4.4.2 Experimental results – XPS and UPS

The effect of gradual exposure of clean thorium metal to increasing quantities of background dosed NH_3 (up to 500 Langmuirs) at 298 K can be seen in figures 4.20 to 4.23. Additional exposure above 500 Langmuirs produced negligible differences in the photoemission spectra. The reaction of NH_3 with the thorium surface resulted in the satellite component of the Th(4f) spectra decreasing in intensity and shifting in binding energy by 0.5 eV, down to 335.1 eV for the $4f_{7/2}$ signal (see figure 4.20). This is possibly due to a nitride species bound to the surface through the 6d electrons. The bonding to the thorium would alter the energy of the 6d electrons, and the energy of the unoccupied orbitals (6d and 5f), which would in turn lead to a change in the energy of the shake-up satellites they generate in combination with the 4f electrons [16,17]. The changes observed in the satellite peak are in complete contrast to the main peak which did not alter in binding energy or intensity, which agrees with previous work carried out [17,18]. The decrease in intensity of the satellite combined with the shift in its binding energy towards the main peak resulted in the total $4f_{5/2}$ and $4f_{7/2}$ signals gradually taking the appearance of single asymmetric peaks. These observations agree with those seen when producing pure ThN *via* sputter deposition of a thorium surface in a partial pressure of nitrogen [18].

It can be seen in figure 4.21 that exposure of thorium to NH_3 resulted in the appearance of two distinct components in the N(1s) photoemission region. The position of the more intense peak at 396.6 eV most likely corresponds to nitrogen in the form of a nitride. This assignment is based both on the work of Gouder *et al* [18], and on the relative nitride positions of a number of other metal elements such as aluminium, chromium and titanium. The comparison with chromium and titanium is

particularly valid as it was explained previously in section 1.1 that the early actinide elements have many properties in common with the transition metals. The second peak at 398.8 eV corresponds to nitrogen in the form of NH_2 chemically bound to the surface [38]. It is worth noting that unlike the results seen upon exposure to H_2O, where there were noticeable differences in the spectra over the entire 100 Langmuir range studied, the spectra produced upon exposure to NH_3 remained largely identical over the range of 10-500 Langmuirs.

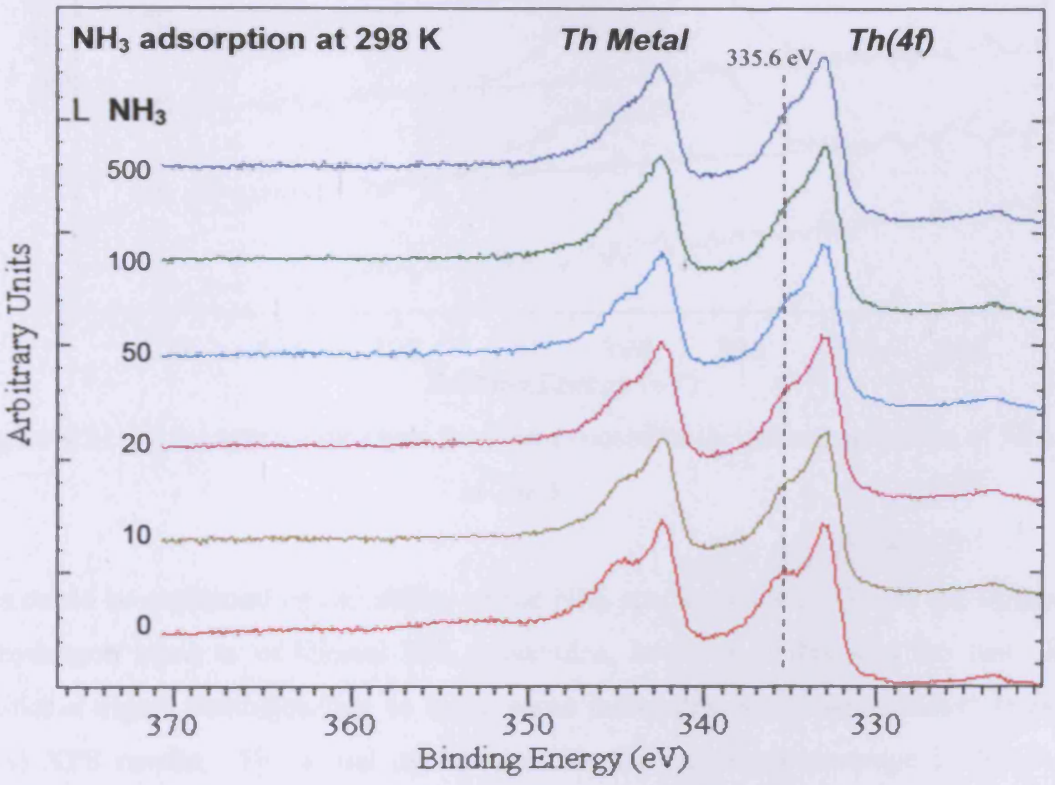

Figure 4.20: Th(4f) spectra for clean thorium exposed to increasing quantities of NH_3 at 298 K

Figure 4.22 shows a plot of the surface coverage of nitrogen species calculated using the Carley-Roberts equation against the exposure to NH_3. It can be seen that the plot follows a version of the so called "standard" relationship, where the rate of coverage increase begins high and decreases as the total exposure increases. As with the calculations carried out upon exposure to H_2O, the calculations for exposure to NH_3 also showed evidence for multilayer coverage. Based on the theoretical value for the number of active sites on the surface, 1×10^{15} sites per cm^2, after 500 Langmuirs the coverage was approaching the equivalent of 3.5 layers.

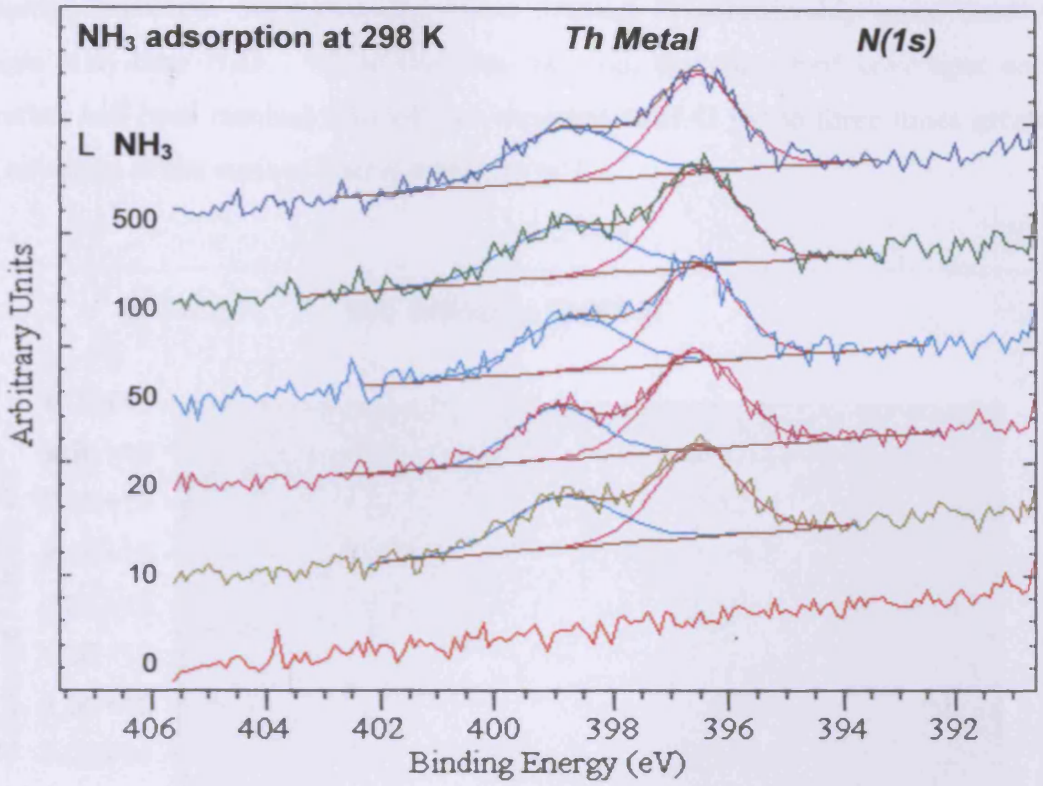

Figure 4.21: N(1s) spectra for clean thorium exposed to increasing quantities of NH_3 at 298 K

This could be explained by the ability of the NH_2 species shown to be on the surface to hydrogen bond to additional NH_3 molecules; however if this was the case an additional signal corresponding to those same molecules would be expected in the N(1s) XPS results. The actual explanation for the multilayer coverage is that the mechanism for nitride formation is similar to that of oxide formation, in that diffusion through the surface layers is possible. Upon formation of the first layer, additional ammonia molecules adsorb to the surface nitride whereby they dissociate to form NH_2. The adsorbed species then diffuse through the surface layer to reach the thorium/nitride interface, whereby they react to form additional nitride, thus increasing the coverage beyond that of a single layer.

The coverage against exposure graph of figure 4.22 also highlighted how little the acquired spectra varied over the entire range of exposures studied. After 10 Langmuirs the coverage was already 3.2×10^{15} atoms per cm^2, which was considerably higher than the 1.2×10^{15} atoms per cm^2 seen upon exposure to 10

Langmuirs of H_2O. This fact combined with the relative stability of the spectra upon increasing exposures suggested that clean thorium is considerably more reactive towards NH_3 than H_2O. While this may be true, the calculated coverages once saturation had been reached showed that exposure to H_2O led to three times greater total coverage of the surface than exposure to NH_3.

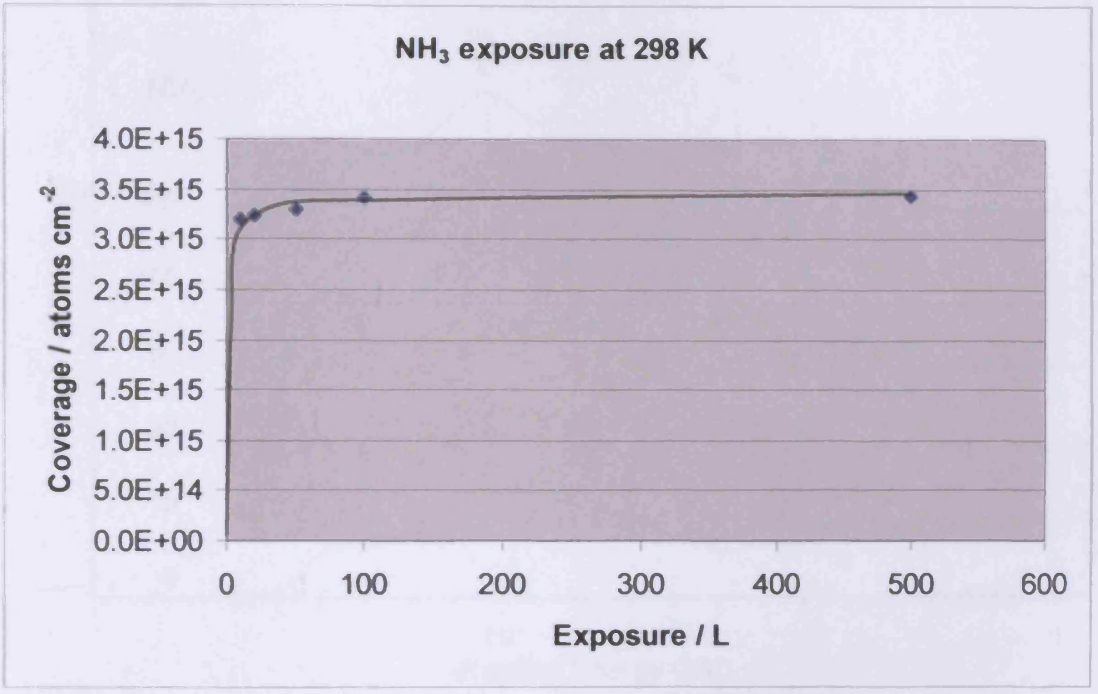

Figure 4.22: Adsorption of ammonia on thorium at 298 K: calculated surface concentration of nitrogen species plotted against exposure to NH_3

Figure 4.23 shows the corresponding He(I) UPS spectra acquired during the NH_3 exposure experiments. The addition of NH_3 into the system resulted in the appearance of a number of peaks which related to the nitrogen containing species adsorbed onto the surface. Comparisons of the peak positions against reference values acquired for gaseous NH_3 were used to help assign the observed signals [33,39-41]. The peak at approximately 4.5 eV corresponds to the $3a_1$ molecular orbital (overall non-bonding [39], H-H bonding character [40]) of gaseous NH_3, while the peak at 10.3 eV relates to the 1e degenerate molecular orbitals (overall bonding [39], strongly N-H bonding [40]) [33,34,41]. The peak at 7.6 eV was probably due to residual oxygen contamination upon the surface, as there was a signal visible at that same energy before the surface had been exposed to any NH_3, and a small signal was

seen in the O(1s) spectra that was taken before the experiment to check the cleanliness of the surface. Figure 4.24, taken and adapted from "The Organic Chemist's Book of Orbitals" by W. L. Jorgensen and L. Salem [39], provides a visual representation of the various orbitals of gaseous ammonia just described.

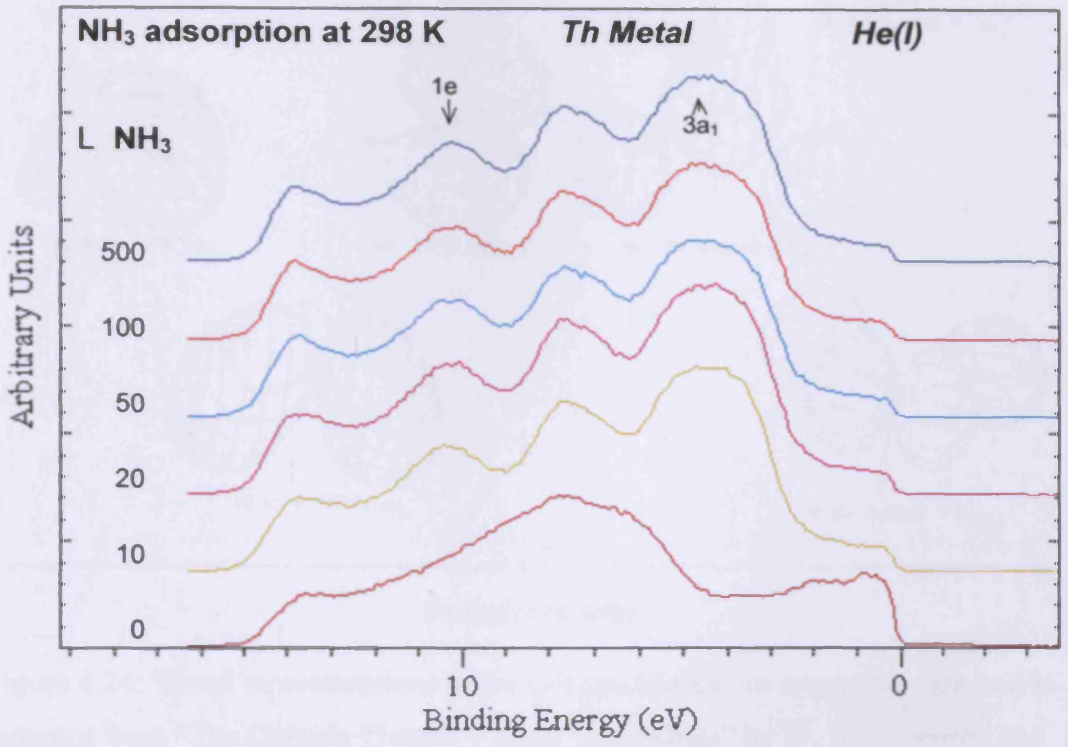

Figure 4.23: He(I) spectra for clean thorium exposed to increasing quantities of NH_3 at 298 K

The continuing presence of intensity at the Fermi edge, indicating a metallic nature to the surface, suggested the presence of metallic thorium. This agrees with the work carried out by Gouder *et al* [18], where they showed that thorium remains metallic, with a distinct intensity at the Fermi level, when in the form of ThN. Their results, like our own, disagree with those carried out by Norton *et al* [17], who concluded that ThN was non-metallic. The formation of a nitride *can* lead to the loss of a signal at the Fermi level, and any metallic nature, but only when Th_3N_4 is formed [18]. The continuing presence of both the intensity at the Fermi level, and the prominent satellite in the Th(4f) region, indicate that the formation of Th_3N_4 through exposure of thorium to ammonia at 298 K is not possible.

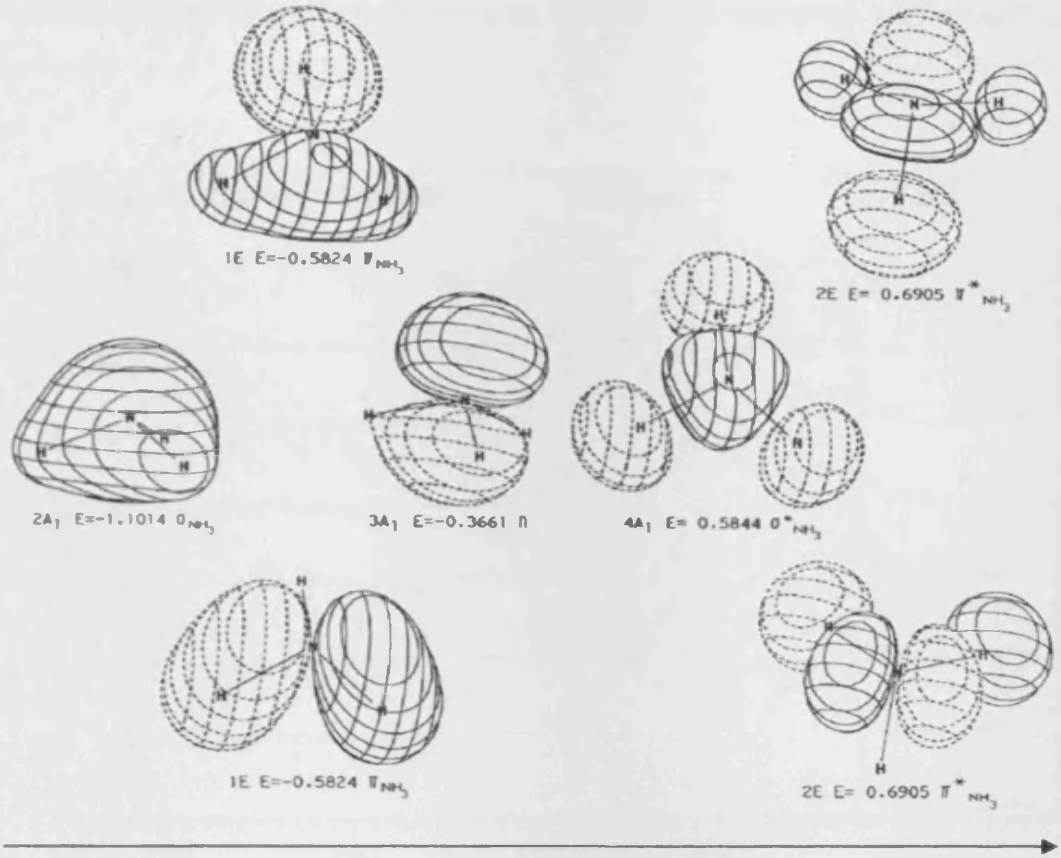

Figure 4.24: Visual representations of the orbitals of gaseous ammonia – taken and adapted from "The Organic Chemist's Book Of Orbitals" by W. L. Jorgensen and L. Salem [39]

As with the H_2O studies, distinctly different results were acquired when the NH_3 exposure experiments were repeated at 100 K, as can be seen in figures 4.25 to 4.28. As before, the addition of NH_3 resulted in the formation of different nitrogen containing species on the surface; however the number of different species, and the relative ratios between them, was markedly different at this lower temperature.

The Th(4f) results featured in figure 4.25 showed that as the NH_3 exposure was increased, the effect on the thorium signals was almost negligible. This coincides with the observance of a significantly smaller nitride peak in the N(1s) region than at 298 K (see figure 4.26). As there was less nitride being formed at this lower temperature, the screening process of the 4f electrons by the 6d electrons, which is

responsible for the large thorium satellite, was far less disrupted than at ambient temperature.

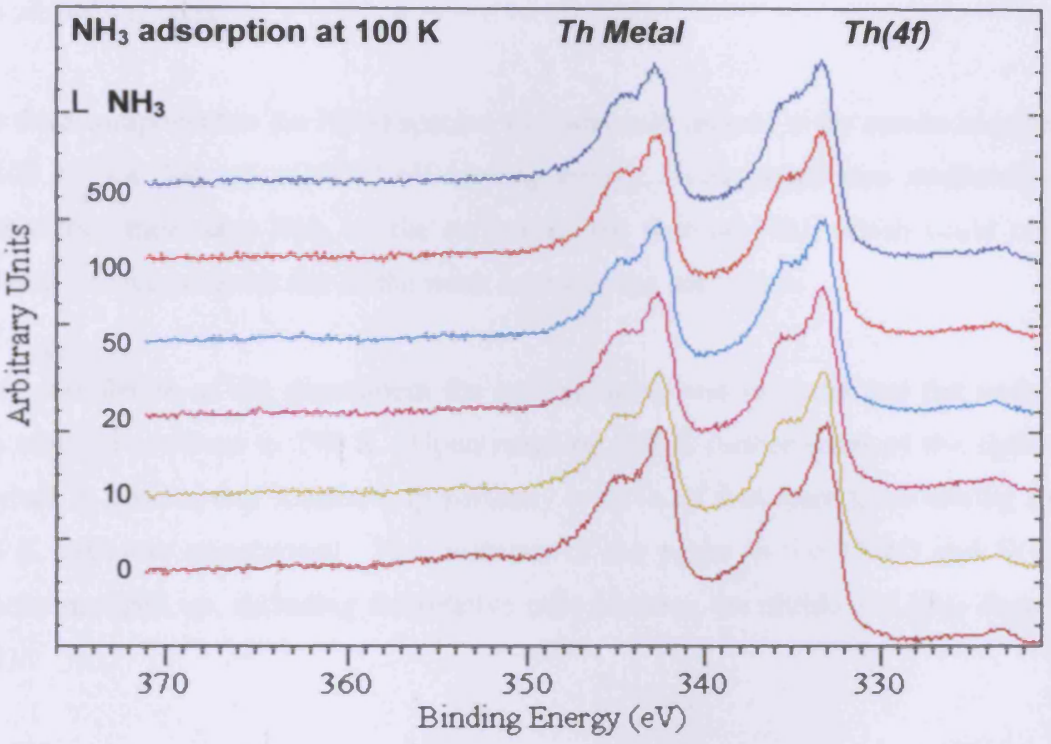

Figure 4.25: Th(4f) spectra for clean thorium exposed to increasing quantities of NH_3 at 100 K

The greatest differences stemming from the different temperatures were seen in the N(1s) region (see figure 4.26). As opposed to the two species seen in the 298 K experiment, immediately upon exposure at 100 K three different signals, corresponding to three different species, were observable in the N(1s) region. The two lowest binding energy peaks, at 396.7 and 398.9 eV, were located at approximately the same energies as those observed during the ambient temperature experiment. Again they were due to the formation of nitride and NH_2 species respectively. While they may have been positioned at the same energy, the relative intensity of the two signals was markedly different at this lower temperature. At ambient temperature the ratio between the signals at 396.5 and 398.8 eV was approximately 3:2 respectively. The results taken from the exposure carried out at 100 K show the ratio to be approximately 5:6, as there was proportionally more NH_2 on the surface than at 298 K. This was most likely due to the energy required to fully

split the NH_3 to form the nitride. At the colder temperature there was likely less energy available, and thus less of a driving force to split the adsorbed NH_2 into its component atoms, which resulted in the observed swing in abundance between the two nitrogen species.

The third component in the N(1s) spectra, that was only present in the results acquired at 100 K, was located at 401.2 eV binding energy. This signal was attributed to physisorbed molecular NH_3 on the surface of the thorium [42], which could only occur at low temperature due to the weak nature of the adsorption.

After completion of the experiment the cooling setup was removed and the surface was allowed to return to 298 K. Upon reaching 298 K further scans of the surface resulted in spectra that matched up perfectly with those that were taken during the 298 K exposure experiment. The positions of the peaks in the Th(4f) and N(1s) regions matched up, including the relative ratio between the nitride and NH_2 signals (3:2).

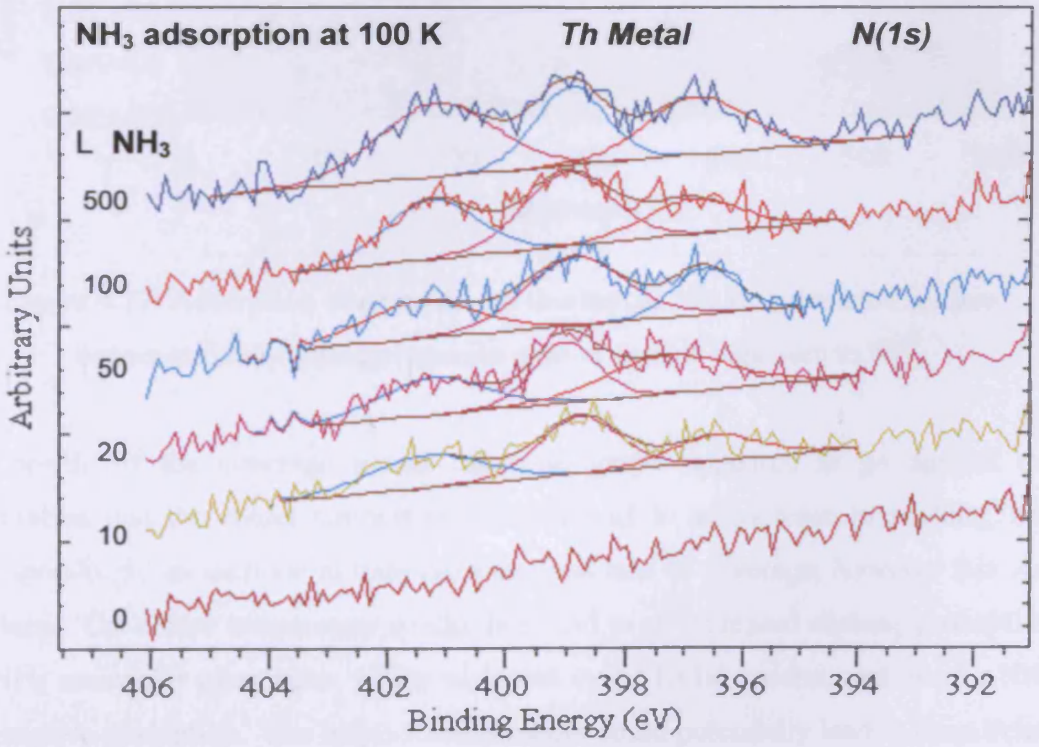

Figure 4.26: N(1s) spectra for clean thorium exposed to increasing quantities of NH_3 at 100 K

Figure 4.27 shows the coverage versus exposure graph acquired when the NH_3 exposure experiment was repeated at a temperature of 100 K. As in the case of the experiment undertaken at ambient temperature, the results acquired at this colder temperature also showed the same "standard" relationship between the two variables. When compared to the experiment at 298 K, the results featured in figure 4.27 were notable for showing both a considerably slower uptake of nitrogen containing species, and a total coverage value after 500 Langmuirs that matched that of the other experiment.

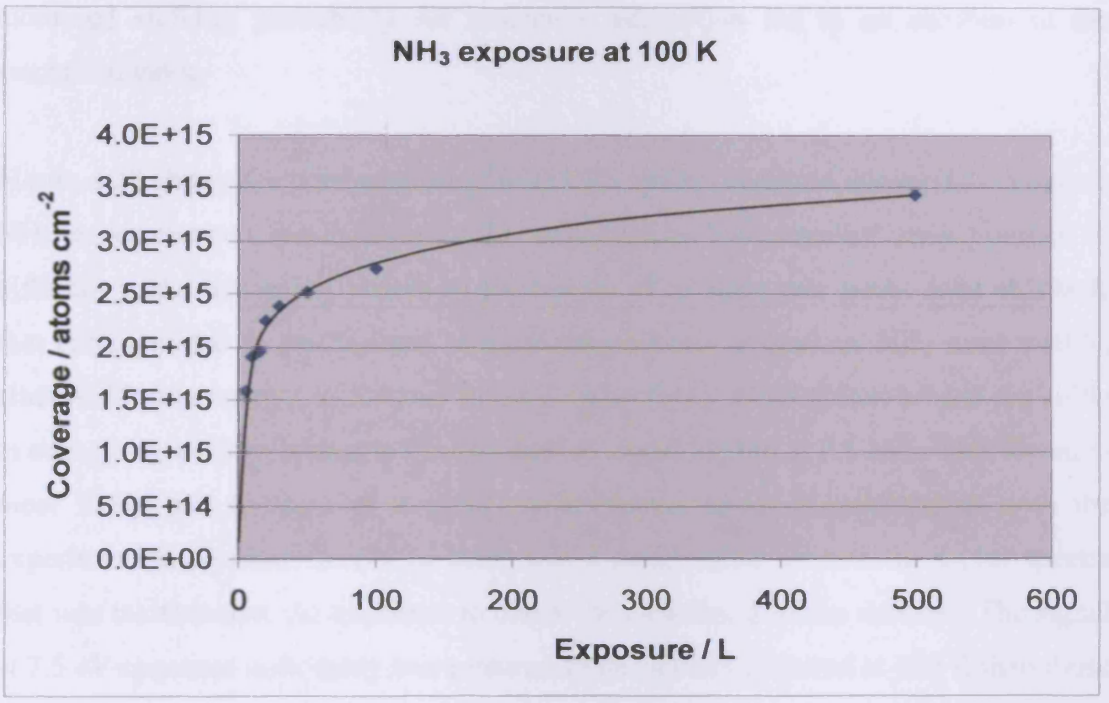

Figure 4.27: Adsorption of ammonia on thorium at 100 K: calculated surface concentration of nitrogen species plotted against exposure to NH_3

The profile of the coverage versus exposure graph appeared to go against the expectation that the colder temperature should lead to an increase in sticking, and correspondingly an increase in total coverage and rate of coverage; however this was a fallacy. The colder temperature would only lead to an increased sticking probability for NH_3 molecular adsorption, which was seen in the N(1s) spectra, and not for NH_3 dissociative adsorption. The reduced temperature could potentially lead to there being a decrease in both the dissociation of NH_3 molecules upon the surface, and in the diffusion towards the thorium/nitride boundary, due to the lack of available energy.

This could explain the apparent reduction in the proportion of nitride seen in the N(1s) spectra taken at 100 K, and could also explain the relatively slow rate at which the coverage increased when compared to the experiment at 298 K.

It is worth noting that while the total calculated coverage after exposure to 500 Langmuirs of NH_3 was the same for both the experiments, the surface at 100 K did not appear to be saturated, unlike that at 298 K. Figure 4.27 indicated that the total coverage was still increasing after 500 Langmuirs, and that while the colder temperature reduced the rate at which the layers of nitride, NH_2, and NH_3 formed, the increased sticking probability for molecular adsorption led to an increase in the saturation value.

Figure 4.28 shows the corresponding He(I) UPS spectra acquired during the cryogenic NH_3 experiments. As in figure 4.23, exposure to NH_3 resulted in a number of different peaks becoming visible in the region. The same two peaks seen at 298 K that corresponded to the $3a_1$ and 1e molecular orbitals of gaseous NH_3 were visible, albeit shifted in energy, at 5.1 and 10.4 eV respectively. The reason behind the shifts in energy is possibly connected to the intense signal visible at 7.5 eV. This signal is most likely due to residual oxygen contamination upon the surface, as with the experiment undertaken at 298 K, there was a small signal seen in the O(1s) spectra that was taken before the exposure to check the cleanliness of the surface. The signal at 7.5 eV appeared noticeably more intense in the spectra acquired at 100 K than those acquired at 298 K; however this may be due to what appears to be a relative decrease in intensity of the peak at 5.1 eV. An increase in the signal at 7.5 eV would actually be expected, as it has already been noted that the extent of oxygen contamination upon the thorium surface increases during the 30 minutes needed to cool down the sample to 100 K.

The decrease in intensity and increase in binding energy of the peak due to the $3a_1$ molecular orbital, combined with the slight alterations in the positions and appearances of the other peaks when compared to the 298 K experiments, is likely due to a combination of factors. The oxygen contamination upon the surface noted above, in combination with the presence of physisorbed NH_3, and the change in proportion of the nitride and NH_2 components, could lead to the resulting spectra. As evidence that

the differing nitrogen containing species played a large part in the spectra taken, upon returning the surface to 298 K it was discovered, as with the XPS above, that further UV photoemission spectra taken of the surface at this temperature matched up perfectly with those acquired during the exposure at 298 K experiments.

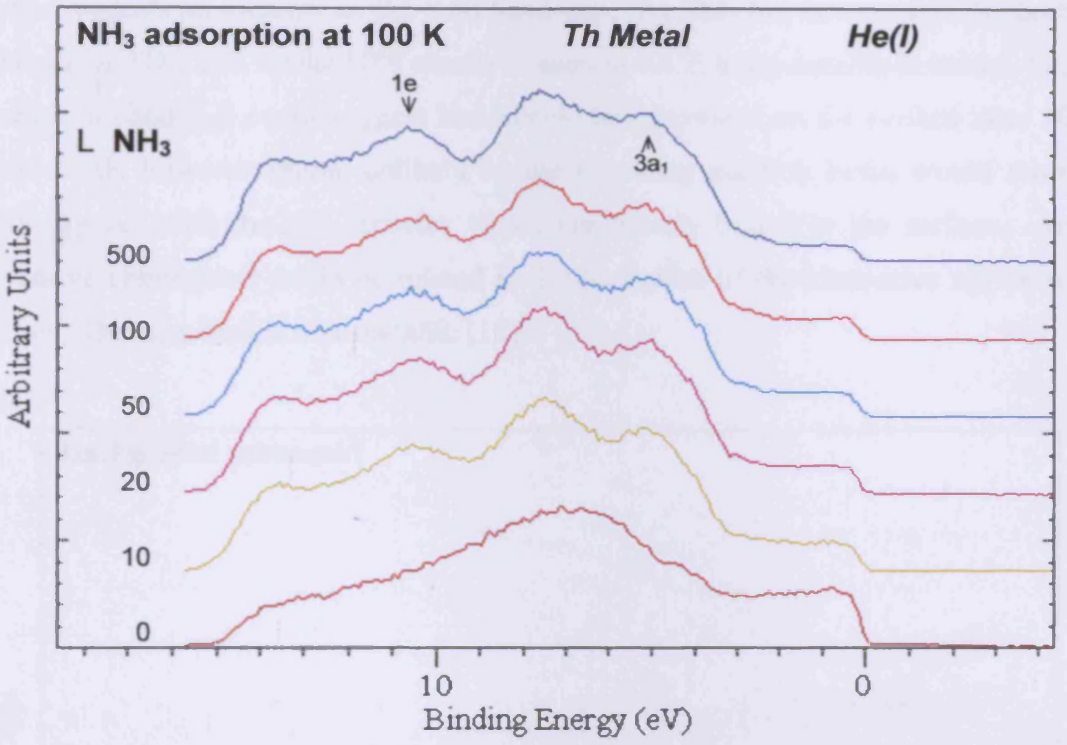

Figure 4.28: He(I) spectra for clean thorium exposed to increasing quantities of NH_3 at 100 K

4.4.3 Experimental results – IPES

Inverse photoemission experiments involving the exposure of thorium to ammonia were carried out separately from the forward photoemission experiments; however, the same two temperatures were investigated, and all other variables were kept the same.

The IPE spectra of thorium after exposure to NH_3, at 298 K can be seen in figure 4.29. The thorium/NH_3 system also demonstrated the damaging nature of the low energy electron gun towards the 'fragile' species on the surface. The detected signal was centred at approximately 5.0 eV during the first hour, but this had shifted upwards in

energy to 5.7 eV by the end of the tenth hour. Of particular note was the additional effect the shift in energy had on the relative position of the Fermi level. During the first hour the gap to the Fermi level was 0.85 eV; however after 10 hours this had increased to 1.7 eV. While there is unfortunately no matching UPS data from after the 10 hour exposure to the electron gun, the shift in energy observed in the IPE spectra suggests an increase in the total band-gap. As ThN has been proven by both Gouder *et al* [18], and by the UPS results in section 4.4.2, to be metallic in nature, this increase in band-gap could suggest less nitride being present on the surface after 10 hours. This however seems unlikely as the incoming electron beam would more likely interact with the NH_2 species which are loosely bound to the surface. An alternative explanation could be related to the formation of the alternative nitride of thorium, Th_3N_4, which is non-metallic [18].

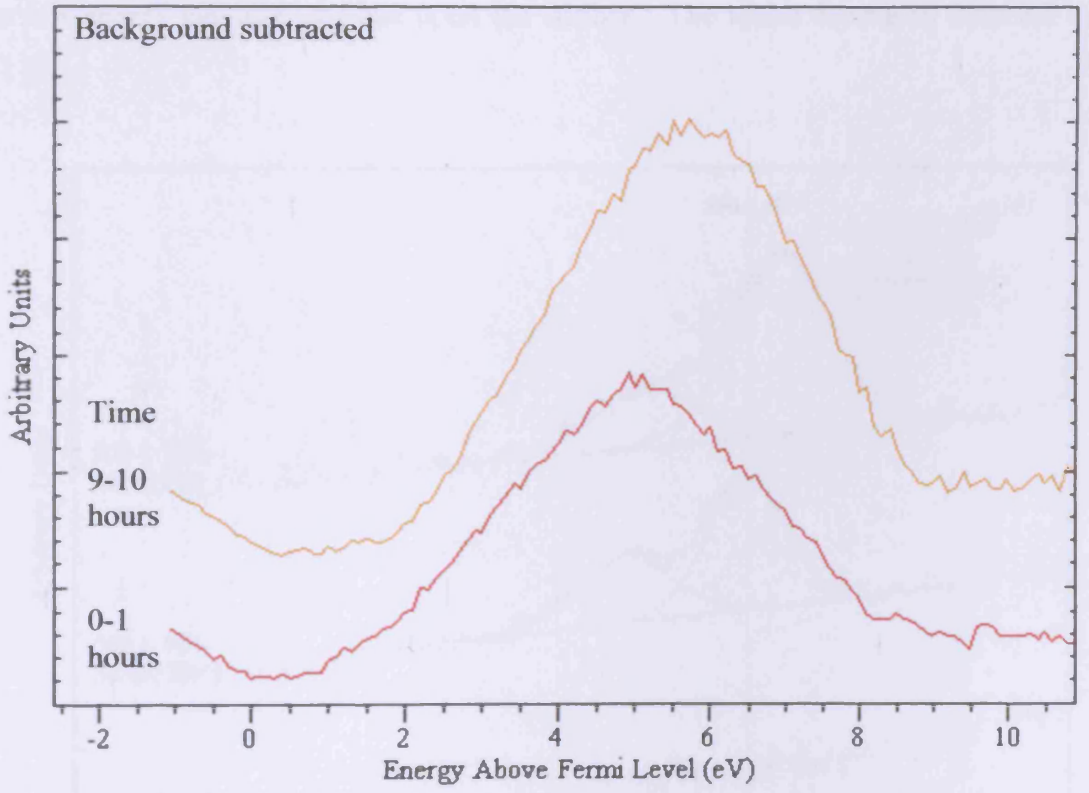

Figure 4.29: IPE spectra for thorium exposed to 500 L NH_3 at 298 K

Support for the idea of Th_3N_4 being formed on the surface can be seen in figure 4.30, which features N(1s) XPS data taken both before and after the 10 hour IPES experiment. It can clearly be seen that after the IPES experiment the peak due to nitride had shifted down in energy from 396.5 to 395.9 eV, which agrees very well

with the literature value for Th_3N_4 which is 395.8 eV [18]. Additionally the atomic ratio between thorium and nitrogen in the surface region had shifted from 3:1 to 2:1 respectively, which was partly due to the increased ratio between the two elements in the alternative nitride formed, and partly due to an apparent increase in the total coverage of the surface by nitrogen species.

All the spectra acquired during the 10 hour period of the experiment showed a single broad peak. Again, as with the H_2O experiments, the signal was from the 6d and 7s orbitals that were shifted upwards in energy away from the Fermi level due to interactions with the adsorbed molecules on the surface. The broad nature of the observed signals was attributed to the presence of multiple distinct species upon the surface (NH_2, nitride(s), possible hydride), which were revealed by the previous XPS results. It is worth noting that a change in the width of the signals was another effect the low energy electron gun had upon the surface. The width decreased from 8.2 to 7.1 eV.

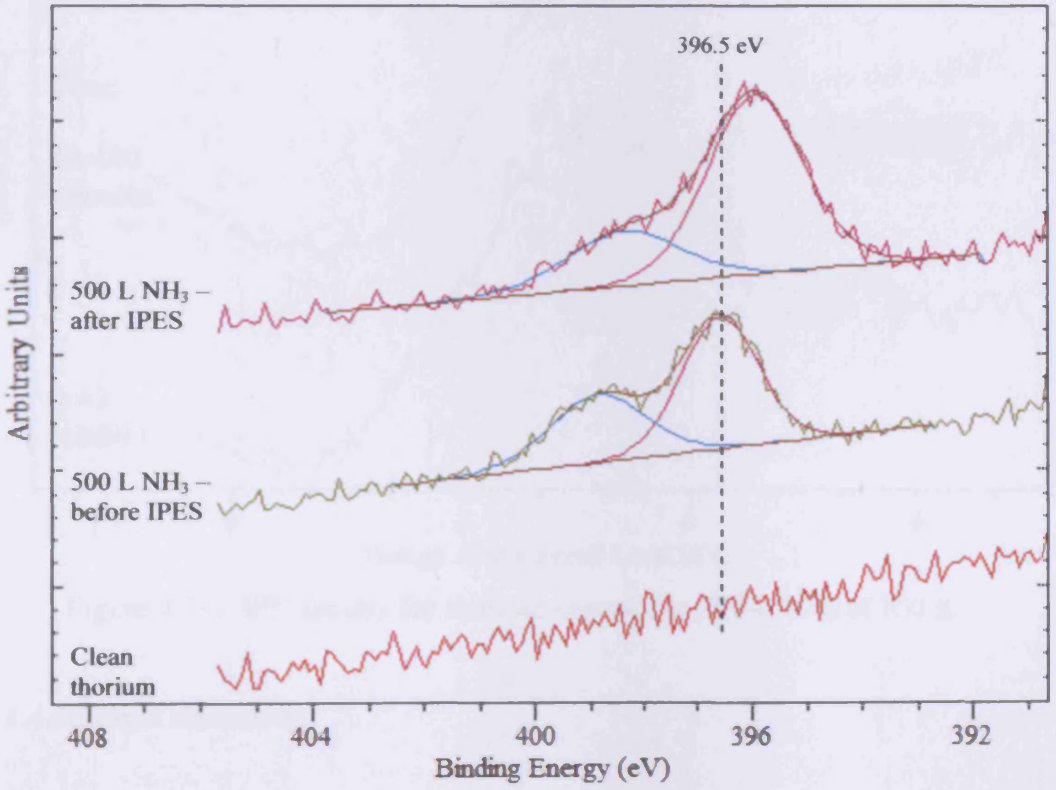

Figure 4.30: N(1s) spectra for a) clean thorium, b) clean thorium after exposure to 500 L of NH_3, and c) clean thorium exposed to 500 L of NH_3 and then bombarded with low energy electrons for 10 hours

IPES measurements of NH_3 adsorption were repeated at 100 K, with the results shown in figure 4.31. As with the experiment carried out at 298 K the low energy electron gun had a pronounced effect upon the surface of the thorium. The detected signal was centred at approximately 4.5 eV during the first 40 minutes, but this had shifted to approximately 5.2 eV by the end of the experiment. In contrast to the experiment at 298 K, where the signal was only just becoming stable after 10 hours under the electron beam, at 100 K the signal had stabilised after less than one hour. However, like the 298 K experiment, the low energy electron gun also had the effect of increasing the energy gap to the Fermi level, in this case from approximately 1.0 to 1.6 eV. It is probable that the reason for this increase is the same as that seen at 298 K, the formation of Th_3N_4.

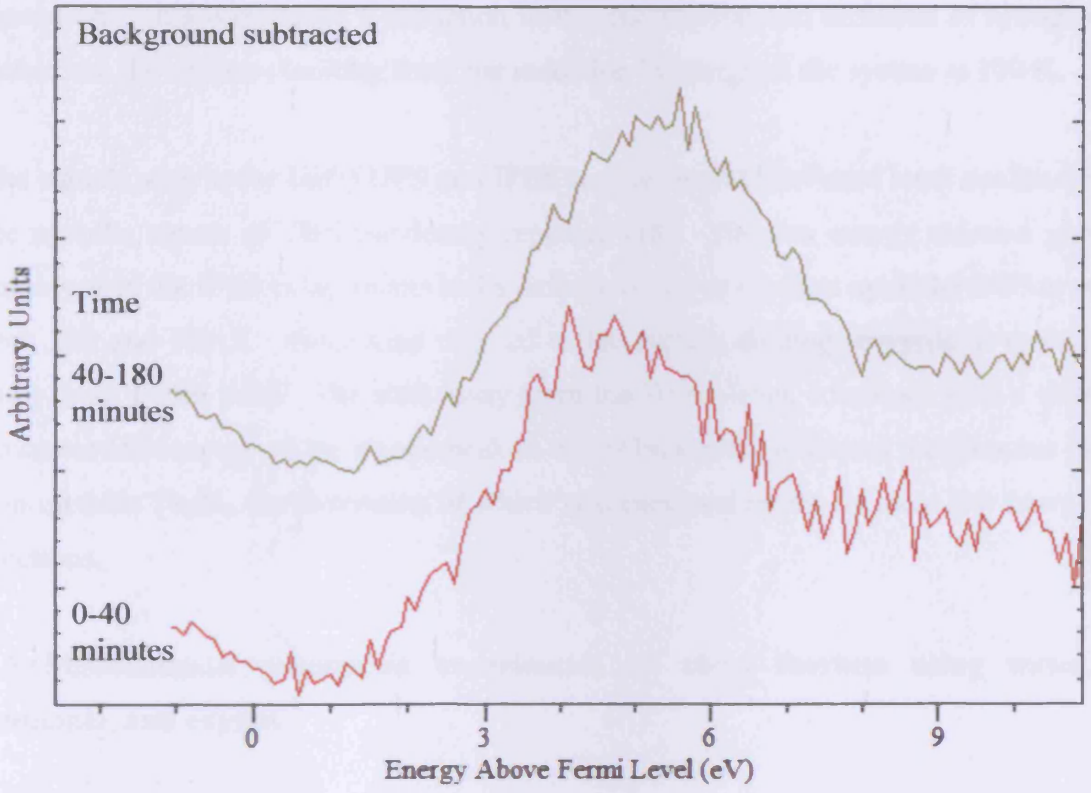

Figure 4.31: IPE spectra for thorium exposed to 500 L NH_3 at 100 K

4.4.4 Additional discussion

At both 298 K and 100 K the exposure of clean thorium to NH_3 led to the formation of multiple nitrogen species. The binding energies for the Th(4f) and N(1s) regions indicated the presence of NH_2 and nitride in the form of ThN, with an additional

component due to physisorbed NH_3 at 100 K. The proportion of nitride in the N(1s) region was lower at 100 K due to the reduced energy available to split the incoming NH_3. Upon increasing the temperature to 298 K, the surface previously reacted at 100 K transformed so that any further XPS and UPS data acquired matched perfectly with that acquired from the sample reacted directly at 298 K.

The coverage against exposure graphs showed the expected multilayer coverage, and a "standard" relationship between the two variables for the experiments, at both 298 and 100 K. The total surface coverage upon saturation at 298 K was calculated to be equivalent to 3.5 layers, with the majority of that already adsorbed after just 10 Langmuirs. At 100 K the surface was also covered by 3.5 layers after 500 Langmuirs; however the coverage increased more gradually, and the surface did not reach saturation. This was due to a reduction in the dissociation and diffusion of nitrogen species on the surface resulting from the reduction in energy of the system at 100 K.

The signals seen in the He(I) UPS and IPES results around the Fermi level confirmed the metallic nature of ThN previously reported [18]. The low energy electron gun employed in the IPES experiments had a definite destructive effect upon the surface at both 298 and 100 K. Over time this led to the signals shifting upwards in energy away from Fermi level. The shift away from the Fermi level, combined with a shift downwards in energy of the nitride peak in the N(1s) region, indicated the presence of non-metallic Th_3N_4, the formation of which was catalysed by the incident low energy electrons.

4.5 Miscellaneous adsorption experiments on clean thorium using water, ammonia, and oxygen

4.5.1 Sequential adsorption of ammonia and oxygen on clean thorium

The sequential adsorption of NH_3 and O_2 at a clean thorium surface was carried out in an effort to understand the oxidation processes occurring. As was mentioned above, exposure to O_2 has been shown many times to quickly oxidise the clean surface of thorium metal, and it was shown in section 4.4 that NH_3 is readily adsorbed onto the surface in the form of nitride and NH_2. If added sequentially the expectation would

be that the O_2 would oxidise and remove some or all of the nitrogen containing species from the surface.

The results of exposure of clean thorium to 500 Langmuirs of NH_3 followed by increasing exposures of O_2 can be seen in figures 4.32 to 4.34. The N(1s) region featured in figure 4.32 firstly showed that NH_3 adsorbs, as previously noted, to form a large nitride peak at 396.5 eV, and a smaller peak at 398.8 eV that corresponds to NH_2. The exposures towards O_2 carried out after this were seen to have the distinct effect of decreasing the signals seen in the region. After exposure to 200 Langmuirs of O_2 the area beneath the two signals had decreased by almost 25 % due to oxidation. The loss increased to 50 % upon exposure to 1000 Langmuirs. Unusually the exposure of the sample towards further quantities of O_2 had negligible effect upon the signals seen in the N(1s) region, indicating a difficulty associated with further oxidation.

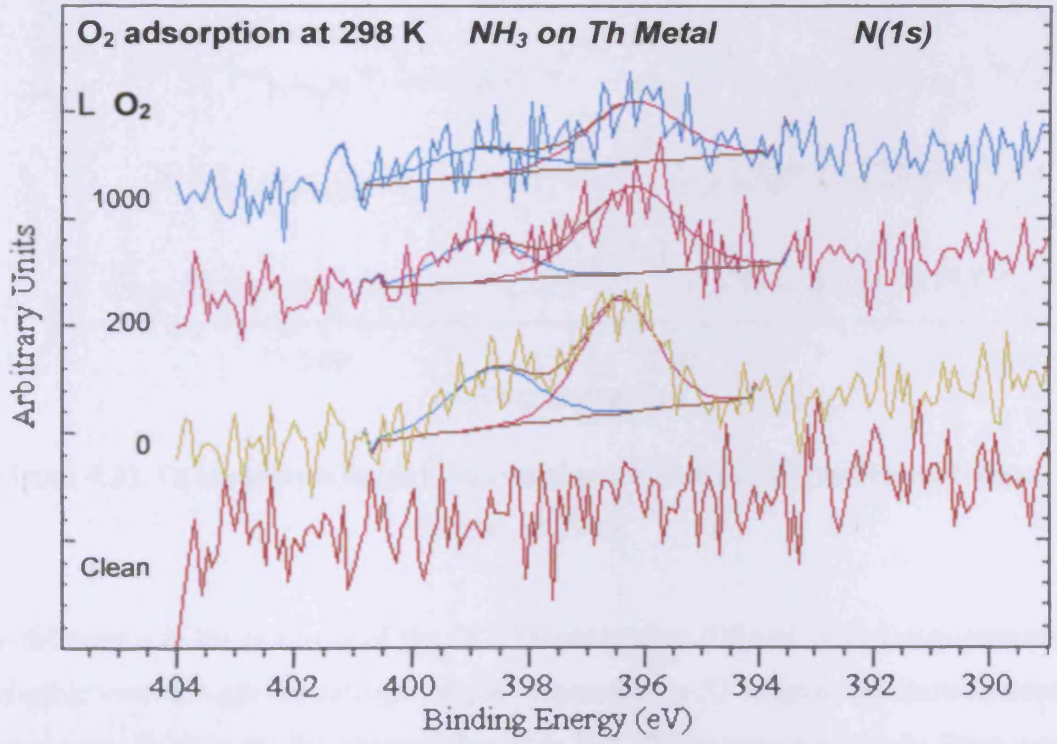

Figure 4.32: N(1s) spectra for the sequential adsorption of NH_3 and O_2 onto clean thorium at 298 K

The corresponding O(1s) spectra are seen in figure 4.33. The exposure towards oxygen led to the appearance of an intense signal at 530.5 eV corresponding to an oxide, and a smaller shoulder at 532.6 eV. The energy of the smaller peak was extremely close to that of molecularly adsorbed NO (532.7 eV), suggesting the possible formation of oxygen-nitrogen species that remain upon the surface [11]. Unfortunately due to the poor signal to noise ratio it was not possible to accurately confirm the presence of a signal at 399.5 eV in the N(1s) region, which would correspond to, and support, the presence of molecularly adsorbed NO on the surface.

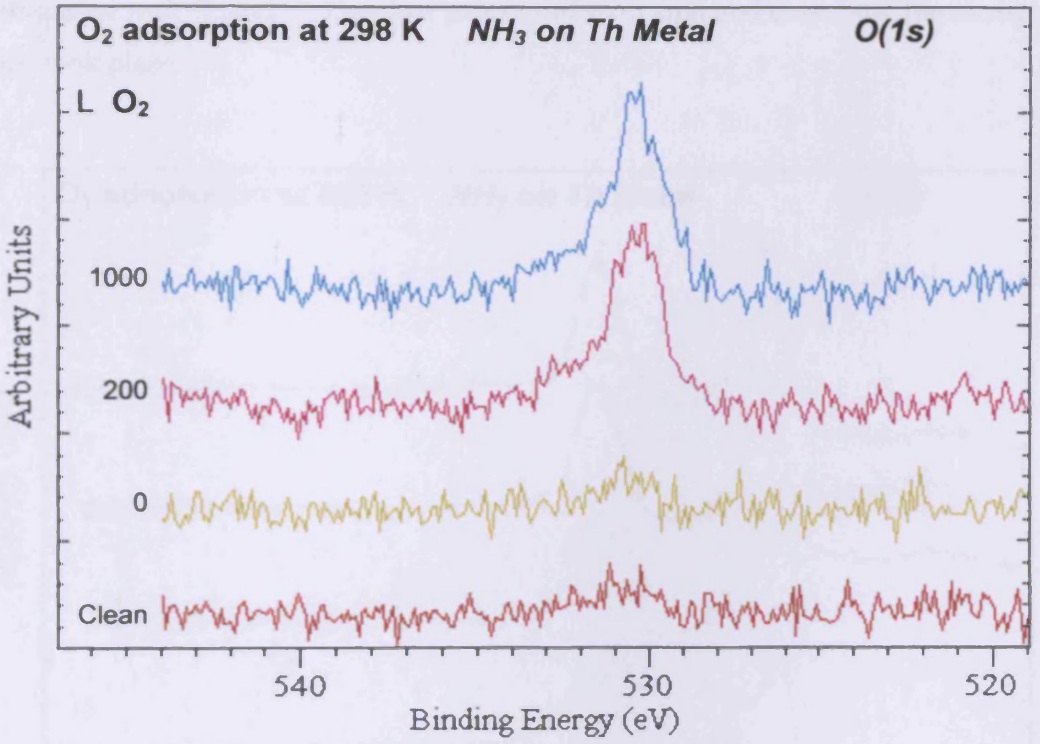

Figure 4.33: O(1s) spectra for the sequential adsorption of NH_3 and O_2 onto clean thorium at 298 K

The difference in the intensity of the O(1s) signals after 200 and 1000 Langmuirs was negligible even though the nitrogen signal decreased by 33 % upon the same increase in exposure. Further studies showed that after just 10 Langmuirs exposure there were negligible increases in the O(1s) signals, which actually agreed with previous work examining the high reactivity of thorium towards pure O_2 [10,11]. The results appear to suggest that incident oxygen molecules first bond to and occupy available spaces upon the surface, maximising the total quantity of oxygen species upon the surface at

this time. After this point any additional O_2 exposure leads to the very slow oxidation and desorption of the nitrogen species through both displacement upon the surface, and the formation of oxygen-nitrogen molecules such as NO.

The trends visible in the Th(4f) region for the experiment (see figure 4.34) matched those already noted for the O(1s) region. The exposure towards NH_3 produced the same resulting shift in energy of the satellite peaks already noted in section 4.4. The intense oxide signal visible upon exposure to O_2 underwent negligible change upon increasing from 200 to 1000 Langmuirs. This supports the suggestion that the surface was saturated with O_2 before the slow process of oxidising and desorbing the nitrogen species took place.

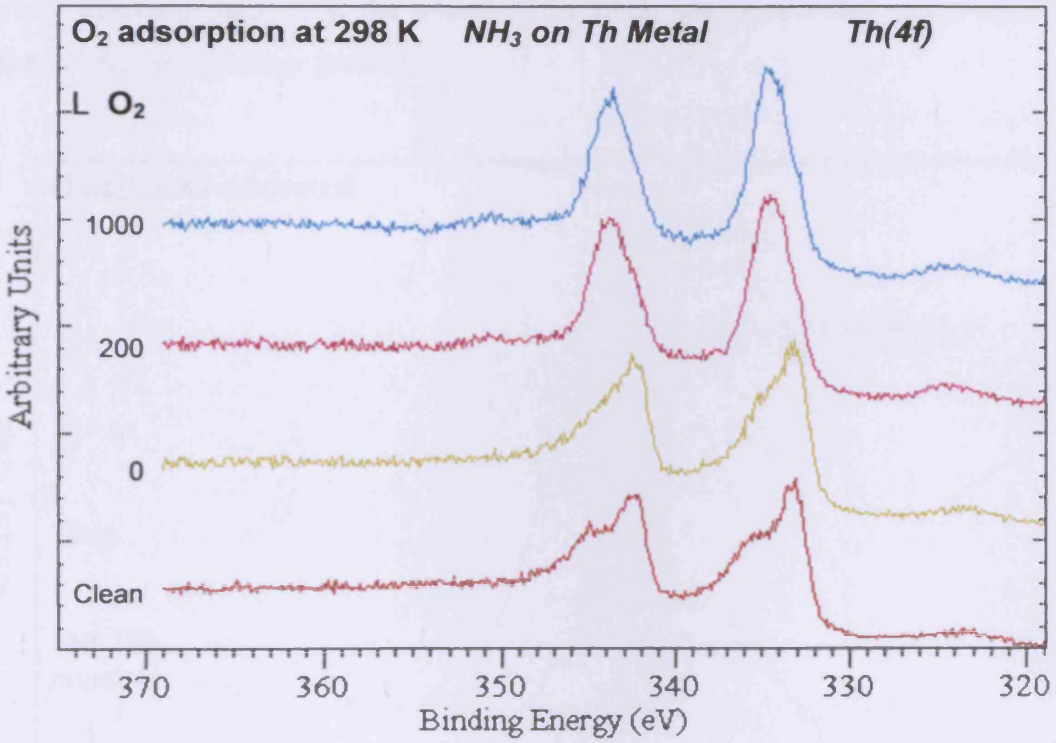

Figure 4.34: Th(4f) spectra for the sequential adsorption of NH_3 and O_2 onto clean thorium at 298 K

An additional IPES experiment examining the sequential adsorption of 1000 Langmuirs of NH_3 and 1000 Langmuirs of O_2 was also carried out, with the results visible in figure 4.35. As with the IPES results acquired after exposure to only NH_3 (see section 4.4.3), the surface upon sequential exposure to NH_3 and O_2 was also

unstable under the low energy electron beam used. The signal moved very gradually upwards in energy during the first 140 minutes before a sudden increase occurred between 140 and 160 minutes. After this the acquired signals remained stable for the remainder of the experiment. The distinct and sudden change is highlighted in the results shown in figure 4.35 through the splitting of the spectra taken before and after it occurred. During the first phase of the results the signal, with a maximum intensity at 5.0 eV, appeared to be made up of three distinct components corresponding to the two seen after pure O_2 adsorption (figure 4.18) and the one seen after pure NH_3 adsorption (figure 4.29). This agreed with the XPS results that showed the presence of both species on the surface even after the 1000 Langmuir O_2 exposure. After the transition the signal was still composed of 3 distinct components; however the energy of maximum intensity had shifted upwards to 6.0 eV. Additionally a tail of increasing intensity emerged, indicating the existence of additional unoccupied states centred outside of the energy range probed.

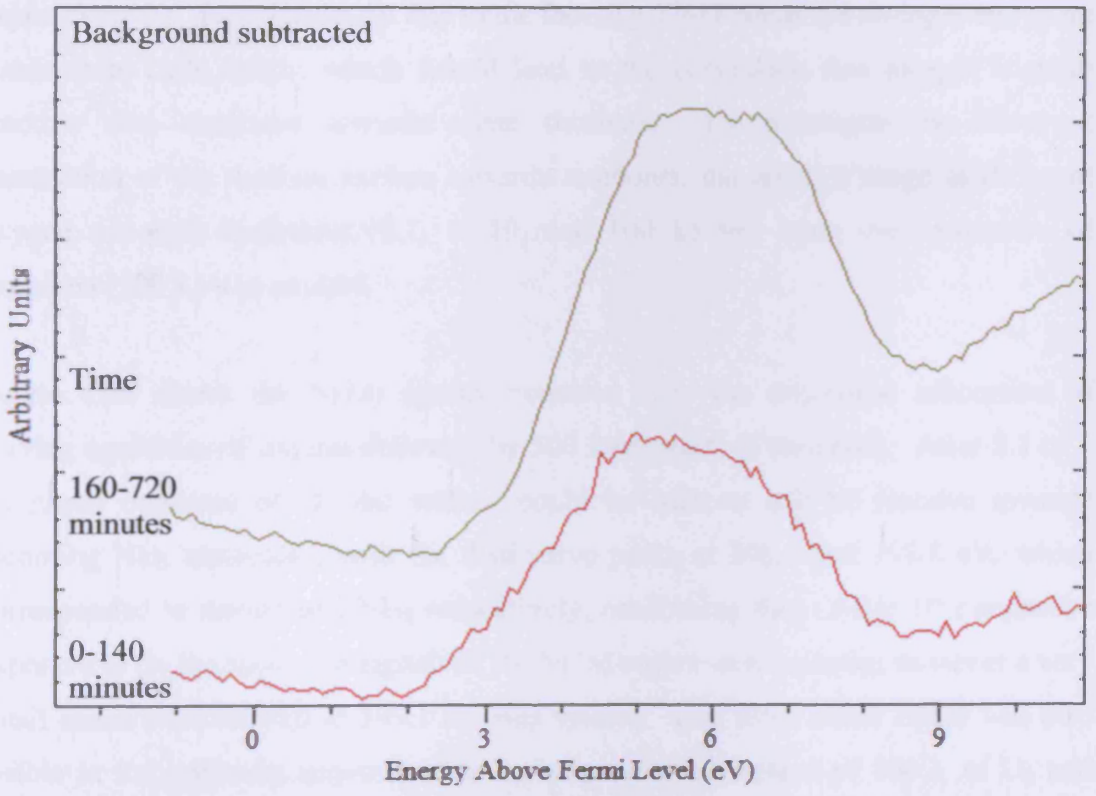

Figure 4.35: IPE spectra for the sequential adsorption of 1000 L NH_3 and 1000 L O_2 onto clean thorium at 298 K

The results acquired from the sequential exposure of thorium to NH_3 and O_2 suggests both that the nitrogen species were difficult to oxidise and remove, and also that their presence had little effect upon the appearance of the Th(4f) region when compared to oxygen containing species.

4.5.2 Sequential adsorption of oxygen and ammonia on clean thorium

It was shown above that saturation of the thorium surface with nitride and NH_2 species does not prohibit the reaction with background dosed oxygen. The incoming oxygen molecules not only oxidised the nitrogen species present, but also adsorbed directly onto the surface. The reverse reaction, where oxygen then ammonia were sequentially adsorbed onto the thorium surface, was also looked at.

Preliminary results showed that, unlike in the reverse reaction covered in section 4.5.1, exposure to NH_3 had no effect on a thorium surface already saturated through exposure to O_2. This was likely due to the fact that Th-O bonds are stronger and more stable than Th-N bonds, which would lead to the conclusion that oxygen is more reactive than ammonia towards clean thorium. To investigate the observed passivation of the thorium surface towards ammonia, the effect a range of different oxygen exposure quantities (0.1, 1, 10, and 100 L) had upon the adsorption of ammonia (500 L) was studied.

Figure 4.36 shows the N(1s) spectra acquired after the sequential adsorption of varying quantities of oxygen followed by 500 Langmuirs of ammonia. After 0.1 or 1 Langmuir exposure of O_2 the surface could be seen to still be reactive towards incoming NH_3 molecules, with the distinctive peaks at 396.5 and 398.8 eV, which corresponded to nitride and NH_2 respectively, confirming this. After 10 Langmuirs exposure to O_2 the same two signals in the N(1s) region were missing; however a very small broad peak located at 399.1 eV was visible. This same small signal was also visible in the spectrum acquired after the sequential adsorption of 100 L of O_2 and 500 L of NH_3. The results suggest that while the thorium surface is passivated towards the vast majority of reactions with NH_3 molecules, after being exposed to 10 or more Langmuirs of oxygen, a very small quantity of nitrogen containing species can still be formed upon the surface.

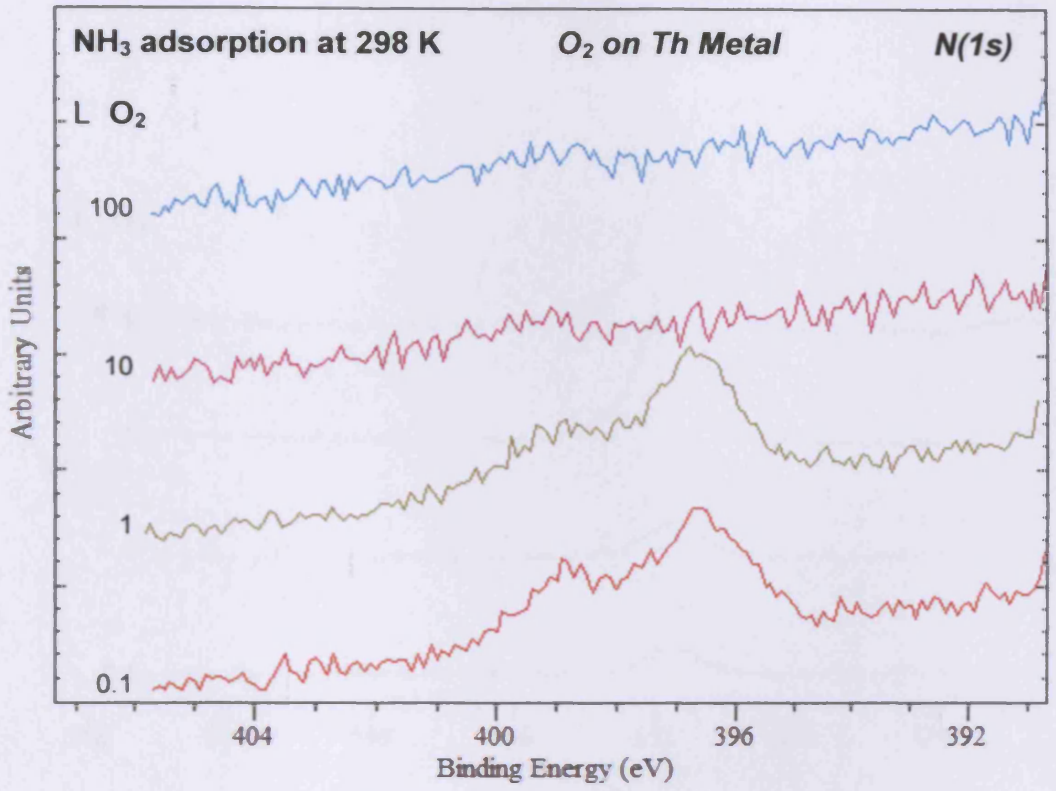

Figure 4.36: N(1s) spectra for the sequential adsorption of O_2 (varying quantities) and NH_3 (500 L) onto clean thorium at 298 K

The nitrogen species formed are possibly mixed nitrogen-oxygen species bound to the thorium, as opposed to being nitride or NH_x species. Evidence for this can be seen in the O(1s) spectra featured in figure 4.37. As with the spectra in figure 4.36, the spectra acquired in the O(1s) XPS region were also of the sequential adsorption of varying quantities of oxygen followed by 500 Langmuirs of ammonia. Resolution of the signals seen in the 10 and 100 L oxygen exposure spectra revealed a possible signal at approximately 532.7 eV. As was noted in section 4.5.1, the binding energy 532.7 eV corresponds to molecularly adsorbed NO. This provides support for the idea that a thorium surface largely composed of the oxide, when exposed to NH_3, will form small quantities of nitrogen-oxygen containing species.

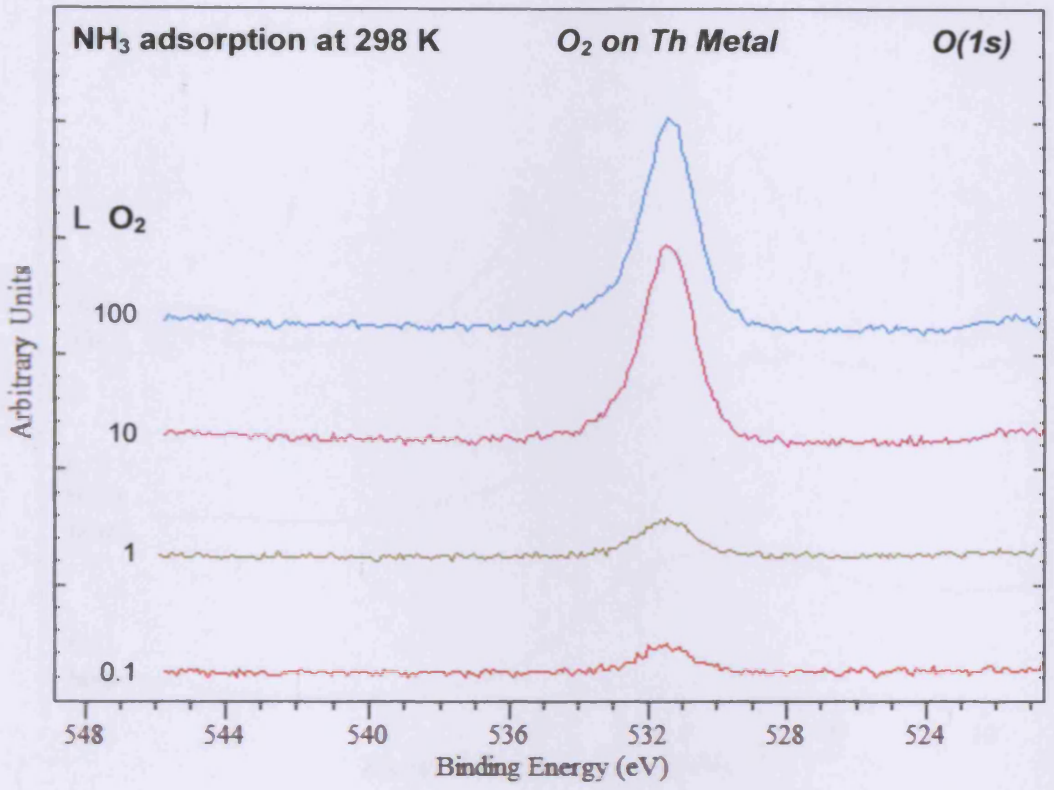

Figure 4.37: O(1s) spectra for the sequential adsorption of O_2 (varying quantities) and NH_3 (500 L) onto clean thorium at 298 K

4.5.3 Additional adsorption of oxygen on clean thorium: IPES studies

Besides the basic adsorption of oxygen on clean thorium IPES experiments, already carried out in section 4.3.3, a number of additional IPES experiments involving thorium and oxygen were studied. The first of these involved exposing clean thorium to the ambient atmosphere at 298 K and allowing it to oxidise naturally. The resulting inverse photoemission spectra of the sample can be seen in figure 4.38 along with one spectrum acquired from pure thorium dioxide for comparison. One important thing to note about the results was the difficulty encountered when trying to apply a background to the spectra. The backgrounds fitted to, and subtracted from, the signals were chosen with the implicit aim of avoiding an unrealistic positive signal towards the Fermi level.

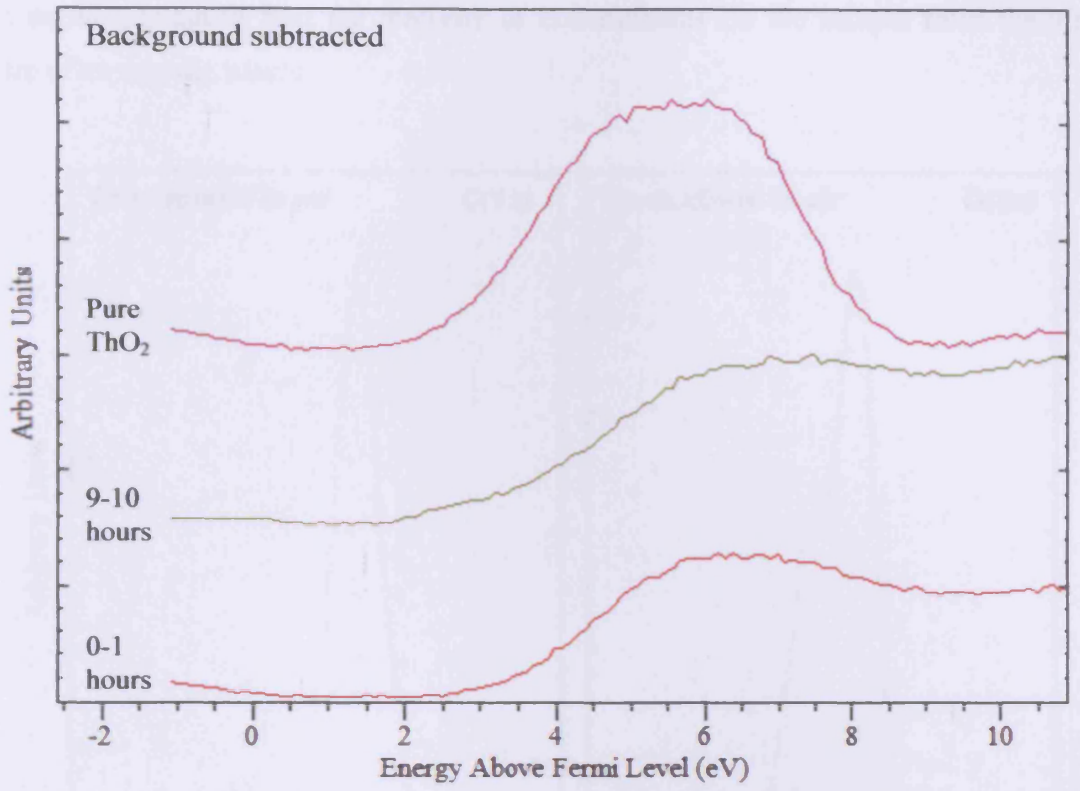

Figure 4.38: IPE spectra for thorium after exposure to air at 298 K. The spectrum of pure thorium dioxide is present as an aid to comparison

The first thing noted from the spectra was the instability of the naturally oxidised surface under the low energy electron beam used in the technique. This was in contrast to the results seen for pure ThO_2, which was shown to be stable under the electron beam at 298 K. In addition to the instability, the intensity and positions of the signals seen with the naturally oxidised thorium also distinguished the sample from pure thorium dioxide. After one hour under the electron beam the acquired signals, which were made up of three overlapping peaks, were centred at 7.1, 5.7, and 4.7 eV, and were all due to the convolution of the 5f, 6d, and 7s states. This was significantly different to the 6.6 and 4.4 eV values seen with pure thorium dioxide. After 10 hours under the electron beam the peaks from the naturally oxidised sample had shifted even further away from those seen for the pure dioxide, to 7.4, 5.8, and 4.7 eV respectively. The differences seen between the thorium oxidised in air, and the thorium oxidised in pure oxygen, could be put down to contaminants present in the atmosphere. XPS taken of the air oxidised sample (see figure 4.39) showed the presence of large quantities of carbon, of more than one oxidation state, upon the

surface. This, in addition to the presence of multiple oxidation states of oxygen on the surface, suggests that the majority of contaminants on the sample from the air were of an organic nature.

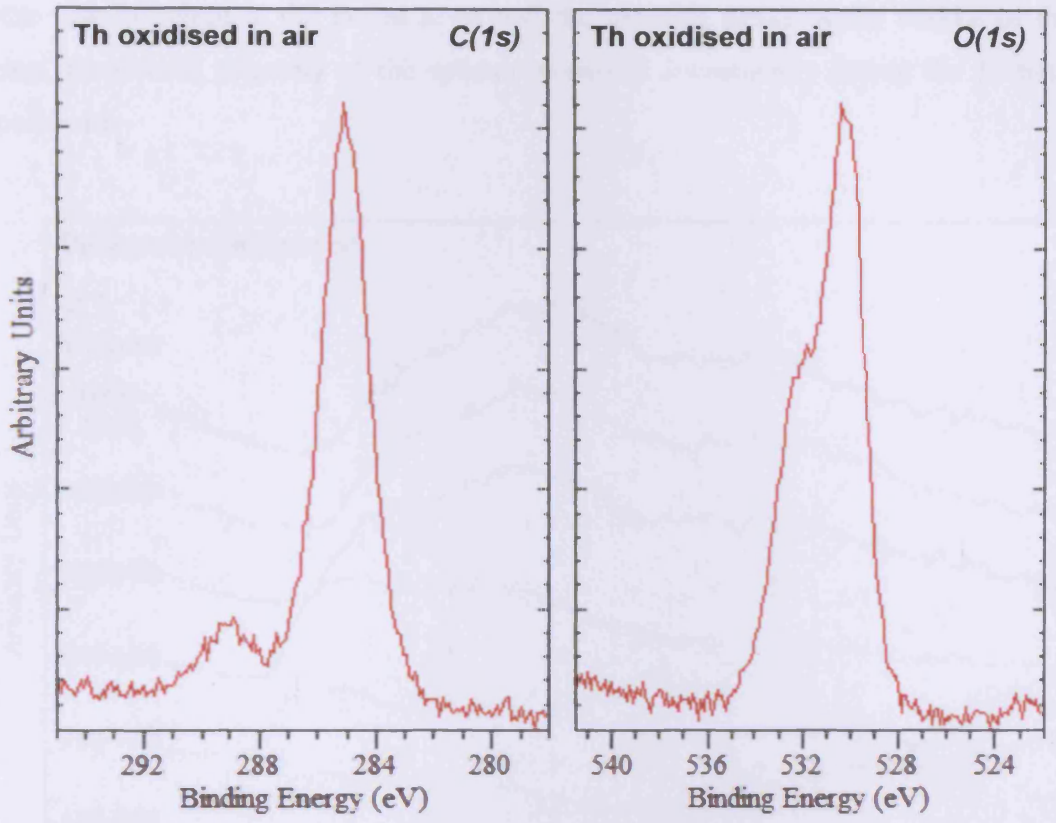

Figure 4.39: C(1s) and O(1s) spectra for clean thorium exposed to the ambient atmosphere

Following on from the experiment above where the thorium was allowed to oxidise in air at atmospheric pressure, the process was repeated in UHV conditions, with the clean thorium being left to oxidise in the 'clean' environment of the system with progress followed by IPES. It is important to note now that it is unknown what effect the continual presence of the low energy electron beam used in the technique will have had on the species being formed upon the surface.

Figure 4.40 shows the chronologically ordered IPE spectra taken during the 18 hours the sample was left to oxidise in the system. During this period the spectra taken gradually transformed in appearance from those of clean thorium (already covered in section 4.2), to those of a partially oxidised surface. It is important to note that on

comparison with the results acquired after exposure to pure O_2, it was clear that even after 18 hours the surface was far from being completely oxidised to ThO_2. A loss of signal near the Fermi level signified the gradual loss of thorium metal as time went on, with the loss accompanied by growing signals at both 4.0 and 7.0 eV. In addition to the loss of signal at the Fermi level and the growing peaks in the middle of the region, the overall intensity of the spectra increased dramatically during the 18 hour experiment.

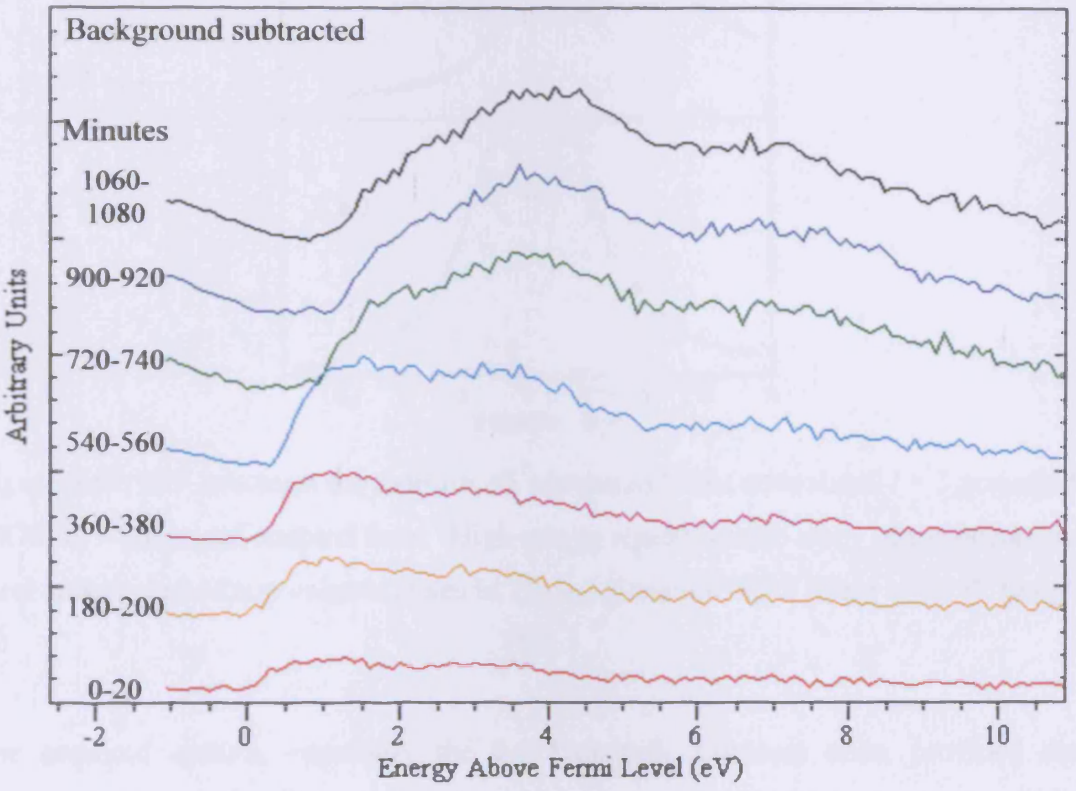

Figure 4.40: Chronologically ordered IPE spectra following the contamination of clean thorium at base pressure and 298 K by the UHV system, taken over a period of 18 hours

A comparison against the Bremsstrahlung Isochromat Spectroscopy (BIS) spectrum of clean thorium reported in the literature (see figure 4.41) highlighted some similarities between the two [43]. It is possible that the BIS spectrum of 'clean' thorium was in fact of a partially oxidised surface, as thorium has been known to be very difficult to clean [9]. If this was in fact the case it would be possible that at some fixed level of contamination the sample would match up with the one that produced the BIS spectrum, resulting in a matching of the two spectra. As 18 hours exposed to

the background gases in the UHV system did not oxidise the sample sufficiently to match the BIS spectrum, the experiment was repeated but with the addition of small exposures of O_2 to accelerate the process. The results of the gradual addition of 0.5 and 1.0 Langmuir exposures to clean thorium can be seen in figure 4.42.

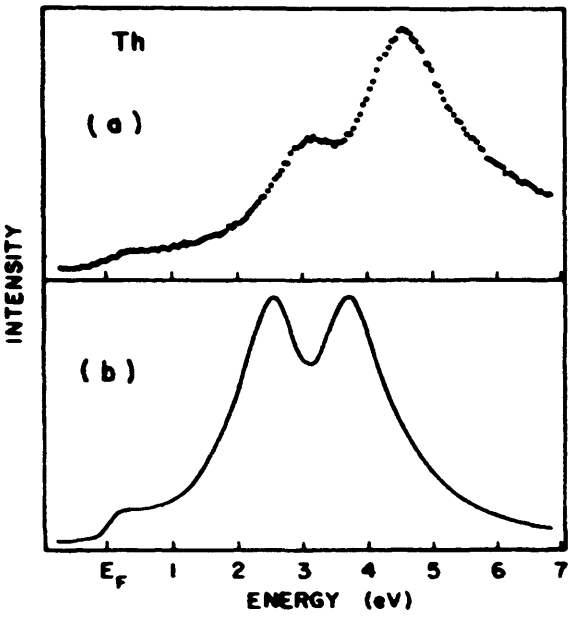

Figure 4.41: BIS spectrum for thorium, a), compared to the convoluted $l = 3$ projected DOS, b) – taken and adapted from "High-energy spectroscopic study of the occupied and unoccupied 5f and valence states in Th and U metals" by Y. Baer and J.K. Lang [43]

The acquired spectra, especially the 0.5 Langmuir exposure ones, provided the opportunity to see the slow and gradual formation of the signals seen previously in figure 4.18. The spectrum that most closely matched the BIS results was seen after 5 x 0.5 Langmuir exposures. At this point the spectrum featured multiple components, but the largest one, centred at 4.2 eV matched up reasonably well with the value of 4.51 eV seen in the BIS spectrum. Upon resolution of the signal an additional component at 2.9 eV was established, which matched up reasonably well with the value of 3.15 eV seen in the BIS spectrum. Thus the results acquired suggest that the BIS spectrum was indeed of a partially oxidised surface, and not the clean thorium reported [43].

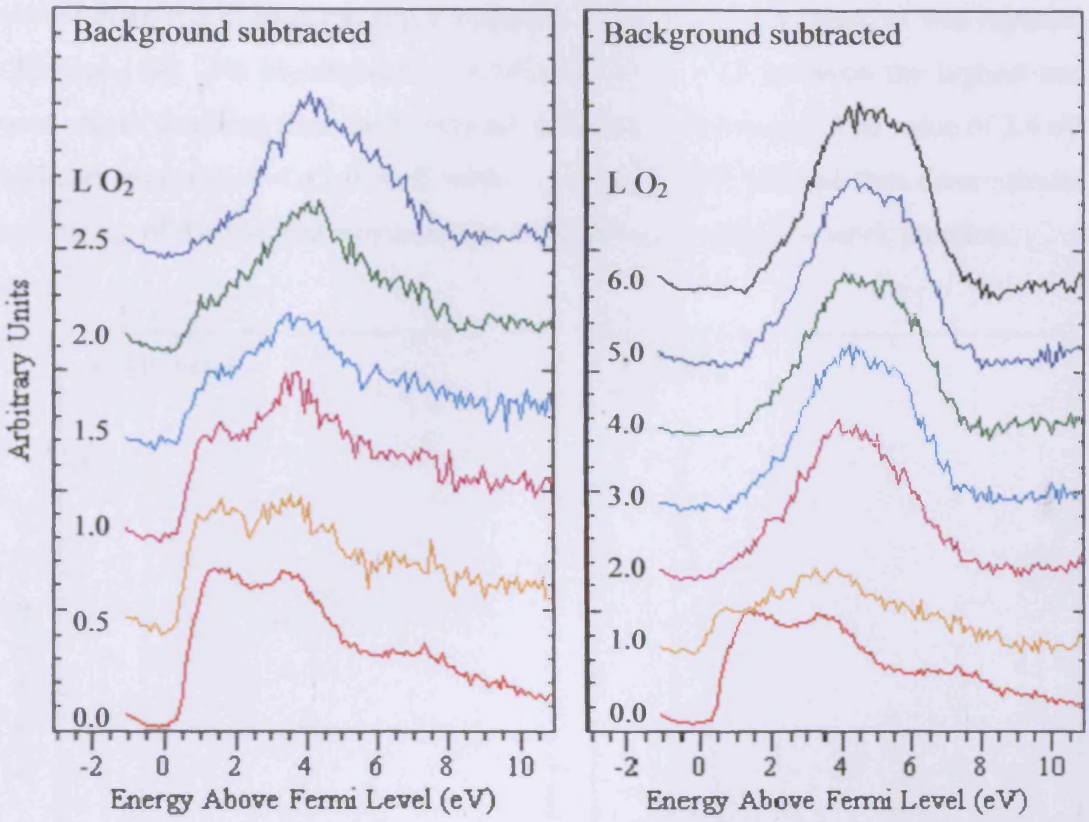

Figure 4.42: IPE spectra following the 'artificial' contamination of clean thorium at 298 K *via* exposure to increasing quantities (0.5 or 1.0 L) of oxygen

4.5.4 Calculations of the thorium work function and thorium dioxide band-gap

An additional ability of the ultraviolet photoemission setup is the ability to measure and report values for the work function of metals and the band-gap of semi-conductors and insulators. These are both achieved through the application of a bias to the sample, 18 volts in this case, followed by a scan intended to capture the entire spectral width. Subtraction of the entire spectral width from the photon energy used (21.2 eV) results in the work function of a metal or the band-gap of an insulator, depending on what is being scanned.

Figure 4.43 features two UPS spectra that show the entire spectral width of a) thorium metal, and b) thorium dioxide. Using the spectral subtraction method described above an estimate for the work function of thorium metal of approximately 3.4 eV was calculated. The work function of thorium has been calculated many times with

photoemission, thermionic, and contact potential difference methods being used; however there has been some slight variation in the values obtained, as was reported by Rivière [44]. He highlighted a variation of ca. 0.3 eV between the highest and lowest values resulting from more than ten different calculations. The value of 3.4 eV calculated from figure 4.43 is well within the range reported, and thus demonstrates the accuracy of the spectral subtraction method for estimating the work function.

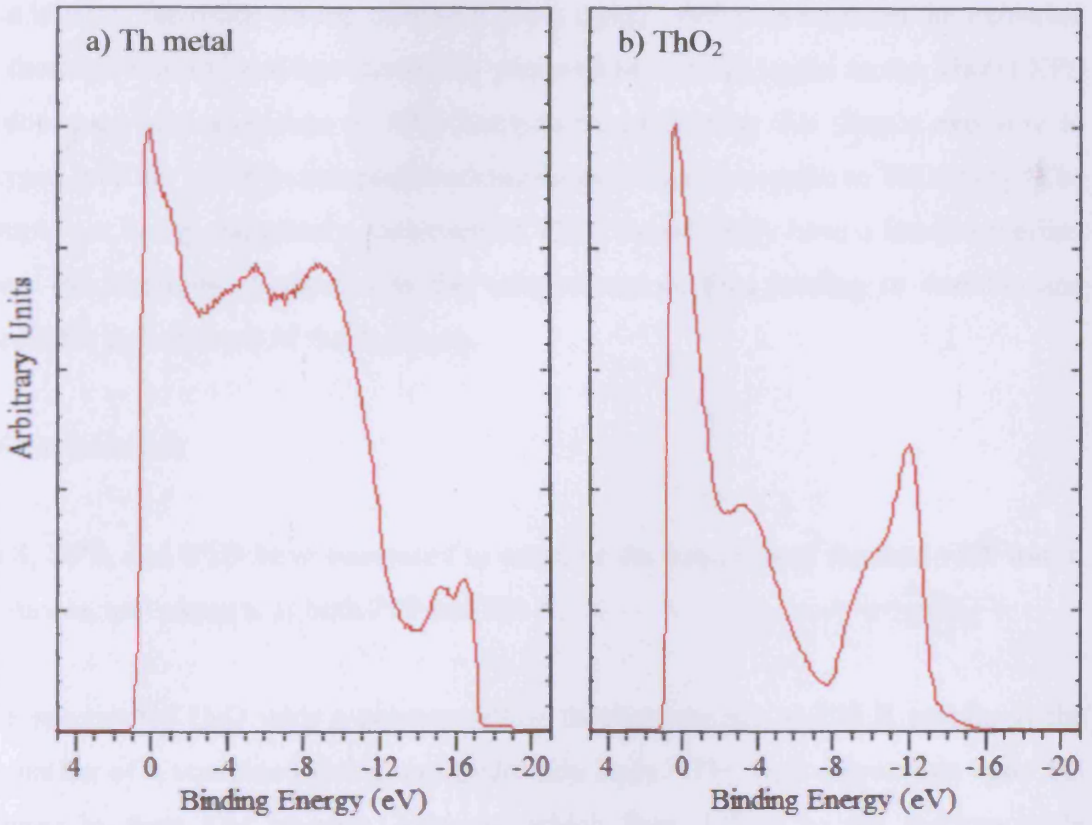

Figure 4.43: UPS spectra taken over the entire spectral width of a) thorium metal and b) thorium dioxide at 298 K

Using the spectral subtraction method again, the band-gap of thorium dioxide was calculated to be approximately 5.0 eV. There is quite a large degree of variation in the calculated band-gap values given in the literature. Values vary from 3.82 eV [45] all the way to 6.0 eV [6], so the 5.0 eV band-gap calculated here is certainly reasonable. The accuracy of the value acquired using the spectral subtraction method can be examined through the use of an alternative method to calculate it, utilising the UPS and IPES results. By combining the distance to the Fermi edge of the UPS signal (2.0 eV) with the distance to the Fermi edge of the IPES signal (1.75 eV) a

value for the total band-gap of 3.75 eV was calculated. One possible reason for the large discrepancy between the different calculations is the difficulty in accurately determining the edge of the detected signals in the UPS and IPES results. This difficulty means the potential error involved in the second calculation of the band-gap is likely to be greater that ± 1 eV. An alternative explanation for the wide variation between the two calculated values, and the values acquired from the literature, is that the sample was not entirely composed of thorium dioxide, and instead only featured a thin layer of the oxide on top of mostly clean metal. Previous work on the oxidation of thorium with oxygen has shown the presence of a metal signal in the Th(4f) XPS region even after exposure to 3000 Langmuirs, suggesting that simple exposure to oxygen will not result in complete conversion of the entire sample to ThO_2 [11]. The sample not being completely composed of ThO_2 would likely have a knock-on effect upon the electronic properties in the valance region, thus leading to variable and unreliable calculations of the band-gap.

4.6 Conclusions

XPS, UPS, and IPES have been used to examine the reactions of thorium with water, ammonia, and oxygen, at both 298 and 100 K.

The reaction of H_2O with a polycrystalline thorium surface at 298 K results in the formation of a combined oxide and hydroxide layer. The H_2O dissociates upon the surface to form OH^- species, some of which then diffuse to the thorium/oxide interface to react and form the oxide. The reaction appears to be self limiting, and had almost reached saturation after 100 Langmuirs exposure, by which time the layer formed had reached a depth of 25 Å. The extent of oxidation seen upon exposure to H_2O was 5 % of that seen for the reaction with O_2. This was due to a combination of the differing reaction probabilities, the oxygen content of the reagents, and the blocking of sites due to formation of the hydride.

At 100 K the reaction results in an oxide and hydroxide layer that is subsequently quickly covered by one consisting of physisorbed water molecules. In contrast to the reaction at 298 K that was observed to have almost reached saturation, the surface coverage at the end of the 100 K experiment was still increasing at a significant rate.

Additional experimentation would be needed to determine the point of saturation, and what exposure this corresponds to.

The unoccupied orbitals of thorium move upwards and away from the Fermi edge upon reaction with H_2O at 298 and 100 K. The distance to the Fermi edge, when combined with the results of the UPS, confirm the insulating nature of the surface formed. At both temperatures the surface species formed after exposure to 500 Langmuirs of H_2O were unstable under the low energy electron gun of the IPES technique. The low energy electrons gradually caused the signals to shift further and further away from the Fermi edge. Only the surface formed after exposure to 40 Langmuirs of H_2O at 100 K was entirely stable when exposed to the electron gun. After exposure to 500 Langmuirs of H_2O at 100 K no signal was detected in the IPE spectra due to the thick layer of physisorbed H_2O. After a period of 32 minutes the low energy electrons had stimulated the desorption of sufficient water molecules for the signal from the ThO_2 below to become visible in the spectra.

The reaction of NH_3 with a polycrystalline thorium surface at 298 K results in the formation of a combined nitride and NH_2 layer. The NH_3 dissociates upon the surface to form NH_2 species, some of which then diffuse to the thorium/nitride interface to react and form nitride. The reaction is self limiting, and after 500 Langmuirs had formed 3.5 layers of nitrogen containing species upon the surface. The reaction appears to proceed at a far faster rate than that of thorium with H_2O, and reached saturation after less than 100 Langmuirs exposure.

At 100 K the reaction with NH_3 results in the formation of a significant physisorbed NH_3 component in addition to those of nitride and NH_2. The proportion of the adsorbed nitrogen present in the form of the nitride was less than that seen at 298 K, with the nitride component the smallest seen in the N(1s) spectra. The coverage increased at a slower rate than was seen at 298 K, due to a lack of available energy for dissociation and diffusion that led to the blocking of active sites. As a result of this, after 500 Langmuirs exposure, saturation had not yet been reached.

The unoccupied orbitals of thorium expand upwards in energy from the Fermi edge upon reaction with NH_3 at both 298 and 100 K. At both temperatures the surface

species were unstable under the low energy electron gun of the IPES technique used to study them. Initially there was a signal present at the Fermi edge, which when combined with the prominent signal at that energy in the occupied valence region, shows the metallic conductive nature of the surface formed upon exposure to NH_3. The addition of the NH_2 species on the surface does not interfere significantly with the conductive properties of pure ThN. The low energy electrons gradually caused the signals to shift further and further away from the Fermi edge, which when combined with a downwards shift in energy in the N(1s) region, showed that non-metallic Th_3N_4 was being formed upon the surface.

The surface formed upon exposure to NH_3 at 298 K is highly vulnerable to the effects of O_2. Exposure to O_2 (100 Langmuirs) oxidises the nitride and NH_2 species, resulting in approximately 50 % of them being removed from the surface. The remaining nitrogen species cannot be removed regardless of the magnitude of the exposure. The incoming oxygen molecules appear to dissociatively adsorb to the surface, and only once the surface becomes saturated does the process of oxidising and desorbing the nitrogen species begin take place. The presence of the nitrogen species upon the surface does not effect the formation of the oxide; however there is evidence that it leads to the formation of molecularly adsorbed NO, as opposed to the hydroxide.

The reaction of NH_3 with thorium is highly dependent on the cleanliness of the surface, especially the presence of any adsorbed oxygen. Sequential adsorption of O_2 and NH_3 revealed that 10 Langmuirs of O_2 is sufficient to completely inhibit the formation of nitride and NH_2 on the surface. While the formation of nitride and NH_2 was inhibited, a very small signal did emerge after exposing the oxidised thorium surface to NH_3, which suggested the presence of molecularly adsorbed NO.

4.7 References

1 I. Hore-Lacy. *2009.* "Thorium" In: Encyclopedia of Earth. Eds. Cutler J. [WWW] <URL:http://www.eoearth.org/article/Thorium> [Accessed 20 August 2010]

2 D. L. Clark, *Los Alamos Science*, 2000, **26**, 364-381.

3 R. C. Albers, *Nature*, 2001, **410**, 759-761.

4 P. Nevitt, *Discovery: The Science & Technology Journal of AWE*, 2005, **11**, 16-25.

5 S. Cotton, Lanthanide and Actinide Chemistry, **2006**, John Wiley & Sons, Ltd: Chichester, p. 1-263.

6 B. W. Veal and D. J. Lam, *Physical Review B*, 1974, **10**, 4902-4908.

7 C. A. Colmenares, *Progress in Solid State Chemistry*, 1975, **9**, 139-239.

8 B. W. Veal, D. J. Lam, H. Diamond and H. R. Hoekstra, *Physical Review B*, 1977, **15**, 2929-2942.

9 S. B. Nornes and R. G. Meisenheimer, *Surface Science*, 1979, **88**, 191-203.

10 W. McLean, C. A. Colmenares, R. L. Smith and G. A. Somorjai, *Physical Review B*, 1982, **25**, 8-24.

11 P. Nevitt, "Photoemission Studies of The Light Actinides", *Ph.D. Thesis*, University of Cardiff, **2006**.

12 A. Yahia and L. Maron, *Organometallics*, 2009, **28**, 672-679.

13 K. T. Moore and G. van der Laan, *Reviews of Modern Physics*, 2009, **81**, 235-298.

14 SPECTRA; R. Unwin,

15 CasaXPS; N. Fairley, Version 2.3.15, 2009

16 J. C. Fuggle, A. F. Burr, L. M. Watson, D. J. Fabian and W. Lang, *Journal of Physics F-Metal Physics*, 1974, **4**, 335-342.

17 P. R. Norton, R. L. Tapping, D. K. Creber and W. J. L. Buyers, *Physical Review B*, 1980, **21**, 2572-2577.

18 T. Gouder, L. Havela, L. Black, F. Wastin, J. Rebizant, P. Boulet, D. Bouexiere, S. Heathman and M. Idiri, *Journal of Alloys and Compounds*, 2002, **336**, 73-76.

19 T. Gouder, J. Naegele, C. A. Colmenares and J. J. Verbist, *Inorganica Chimica Acta*, 1987, **140**, 35-36.

20 S. Tull, *Ph.D. Thesis*, University of Cardiff, **2002**.

21 J. J. Yeh and I. Lindau, *Atomic Data and Nuclear Data Tables*, 1985, **32**, 1-155.

22 T. Fauster and F. J. Himpsel, *Physical Review B*, 1984, **30**, 1874.

23 P. H. Holloway and E. B. Evans, *Oxidation of Metals*, 1972, **4**, 27.

24 T. Kondo, F. H. Beck and M. G. Fontana, *Corrosion*, 1974, **30**, 330-339.

25 C. D. Bowman, E. D. Arthur, P. W. Lisowski, G. P. Lawrence, R. J. Jensen, J. L. Anderson, B. Blind, M. Cappiello, J. W. Davidson, T. R. England, L. N. Engel, R. C. Haight, H. G. Hughes, J. R. Ireland, R. A. Krakowski, R. J. Labauve, B. C. Letellier, R. T. Perry, G. J. Russell, K. P. Staudhammer, G. Versamis and W. B. Wison, *Nuclear Instruments & Methods in Physics Research Section A-Accelerators Spectrometers Detectors and Associated Equipment*, 1992, **320**, 336-367.

26 R. K. Sinha and A. Kakodkar, *Nuclear Engineering and Design*, 2006, **236**, 683-700.

27 I. R. Shein, K. I. Shein, N. I. Medvedeva and A. L. Ivanovskii, *Physica B-Condensed Matter*, 2007, **389**, 296-301.

28 G. M. Bancroft, T. K. Sham, J. L. Esquivel and S. Larsson, *Chemical Physics Letters*, 1977, **51**, 105-110.

29 A. F. Carley and M. W. Roberts, *Proceedings of the Royal Society of London Series a-Mathematical Physical and Engineering Sciences*, 1978, **363**, 403-424.

30 W. L. Jorgensen and L. Salem, The Organic Chemist's Book Of Orbitals, **1973**, Academic Press, p. 70.

31 D. W. Turner, Molecular Photoelectron Spectroscopy, **1970**, Wiley-Interscience, p. 77-81.

32 K. Kimura, S. Katsumata, Y. Achiba, T. Yamazaki and S. Iwata, Handbook of HeI Photoelectron Spectra of Fundamental Organic Molecules, **1981**, Japan Scientific Societies Press, p. 33.

33 M. H. Matloob, *Ph.D. Thesis*, University of Bradford, **1978**.

34 M. J. Campbell, J. Liesegang, J. D. Riley and J. G. Jenkin, *Journal of Physics C-Solid State Physics*, 1982, **15**, 2549-2558.

35 M. J. Campbell, J. Liesegang, J. D. Riley, R. C. G. Leckey, J. G. Jenkin and R. T. Poole, *Journal of Electron Spectroscopy and Related Phenomena*, 1979, **15**, 83-90.

36 X. F. Wang, L. Andrews and L. Gagliardi, *Journal of Physical Chemistry A*, 2008, **112**, 1754-1761.

37 T. Nakagawa, H. Matsuoka, M. Sawa, M. Hirota, M. Miyake and M. Katsura, *Journal of Nuclear Materials*, 1997, **247**, 127-130.

38 J. L. Bischoff, F. Lutz, D. Bolmont and L. Kubler, *Surface Science*, 1991, **248**, L240-L244.

39 W. L. Jorgensen and L. Salem, The Organic Chemist's Book Of Orbitals, **1973**, Academic Press, p. 69.

40 D. W. Turner, Molecular Photoelectron Spectroscopy, **1970**, Wiley-Interscience, p. 356-359.

41 K. Kimura, S. Katsumata, Y. Achiba, T. Yamazaki and S. Iwata, Handbook of HeI Photoelectron Spectra of Fundamental Organic Molecules, **1981**, Japan Scientific Societies Press, p. 42.

42 J. A. Schreifels, J. E. Deffeyes, L. D. Neff and J. M. White, *Journal of Electron Spectroscopy and Related Phenomena*, 1982, **25**, 191-209.

43 Y. Baer and J. K. Lang, *Physical Review B*, 1980, **21**, 2060-2062.

44 J. C. Riviere, *Proceedings of the Physical Society of London*, 1962, **80**, 124-129.

45 S. A. Mahmoud, *Solid State Sciences*, 2002, **4**, 221-228.

Chapter 5 – The interaction of uranium with water and ammonia

5.1 Introduction

This chapter focuses on the interactions between ammonia, water, oxygen and the surface of uranium metal.

Uranium, arguably the most important of the actinide elements, has an electronic structure of $[Rn]5f^{3}6d^{1}7s^{2}$. Being the most abundant of the light actinides that possess valence f electrons, uranium is an especially useful element for investigating their effect upon surface reactions. As was explained in section 1.1, both the physical and chemical properties of the light actinides are influenced heavily by the 5f electrons, with research into their behaviour being of fundamental interest [1-4]. Through comparison of uranium with thorium, which lacks any valence f electrons, or the heavier actinides (or lanthanides), whose f electrons are localised, researchers have in the past attempted to distil the effect that the delocalised electrons have on surface bonding [5-16]. However the research is far from complete, as it has been noted that there are still many unanswered questions relating to the 5f valence electrons and the actinides in general [16].

Uranium metal will allow us to investigate a $5f^{3}$ system and see the behaviour of the delocalised valence f electrons of a light actinide alongside those of the 6d and 7s orbitals.

5.2 Clean uranium

Before examining the results of any reactions upon the surface, it is important to understand some key points about photoelectron spectroscopy of uranium.

Photoelectron spectroscopy studies of uranium, as with all other actinide elements, are hazardous and difficult to undertake. While the issue of radiation was more significant than when looking at thorium [17], the acquired spectra were more easily analysed as the distinctive satellite commented on in section 4.2 was not seen with uranium. The lack of the satellite was due to the presence of only one 6d electron, as opposed to the two that thorium possesses, which are required to screen the 4f hole and generate the distinct loss features of the satellites [10,18,19]. The lack of

additional 6d electrons was accompanied by the presence of three 5f electrons that also distinguish uranium from thorium, as thorium possesses none.

As with the other actinide elements, uranium has an open f shell with two degenerative states. The effect of spin-orbit coupling (see section 2.3.3.4 d) results in the splitting of the degenerate states into two peaks. The two peaks, shown in figure 5.1, correspond to $f_{5/2}$ and $f_{7/2}$ final states with the ratio between the peak areas being 3:4. The signals seen with uranium were considerably more asymmetric than those seen for thorium, because of the increased density of states (DOS) at the Fermi level brought about by the three 5f electrons that the element has [10,20].

As was explained in section 2.3.2.1, the binding energies observed by XPS are characteristic for each element. In the case of uranium the two primary signals in the U(4f) region, the $f_{5/2}$ and $f_{7/2}$, have known values for the pure metal. Figure 5.1 shows the U(4f) spectra of clean uranium at both "ambient" (298 K), and "cryogenic" (100 K) temperatures. For all the cryogenic experiments carried out the sample was cooled down *via* a continuous flow of liquid nitrogen through internal pipes running the length of the sample probe. The peak positions of 388.2 and 377.4 eV corresponded to U $4f_{5/2}$ and U $4f_{7/2}$ respectively, and are typical of the values for uranium metal seen in the literature [13,18,21-23]. As can be seen in the figure, there were no significant differences between the spectra acquired at the two different temperatures, which was to be expected as the uranium is in the α (orthorhombic) allotrope at both temperatures. The transition to the β (tetragonal) allotrope only occurs upon heating to approximately 933 K. As the process of cooling down the sample to cryogenic temperatures takes upwards of 30 minutes, it could be expected that any residual water or other molecules in the vacuum would contaminate the clean surface. Therefore the fact that the U(4f), C(1s), and O(1s) spectra (see figures 5.1 and 5.2) appear largely the same at both temperatures is a strong indicator of the clean condition of the vacuum system.

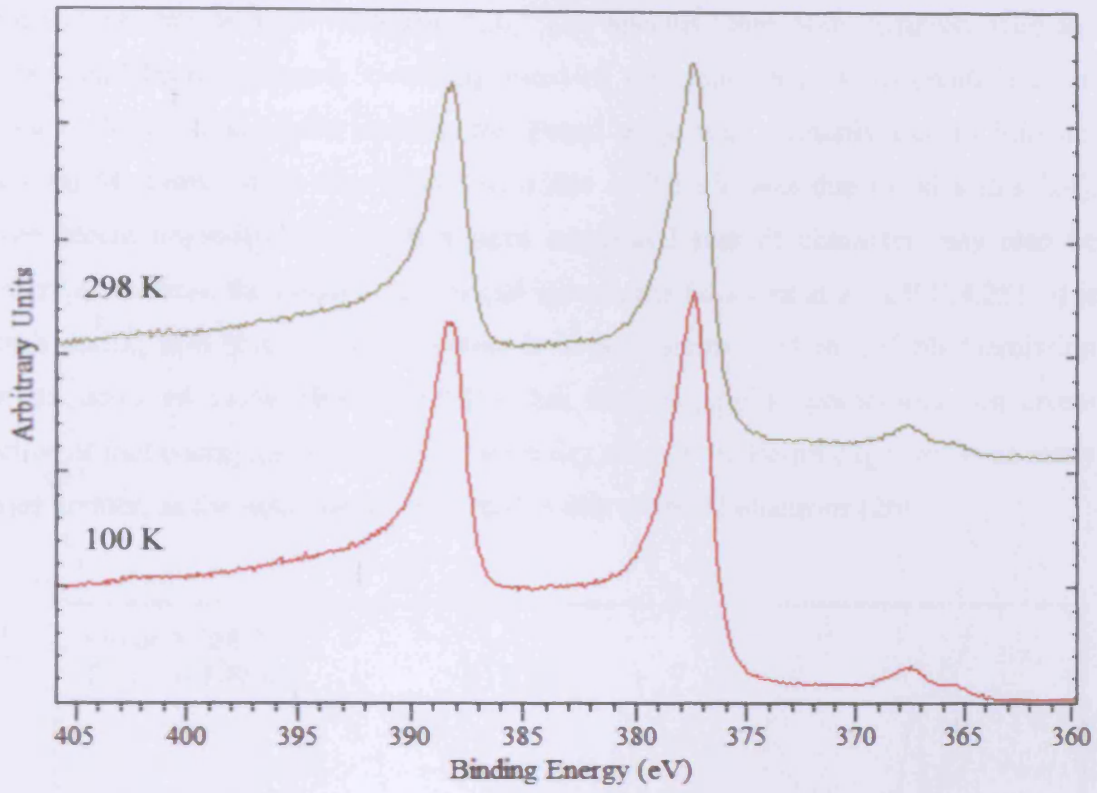

Figure 5.1: U(4f) spectra for clean uranium acquired at 298 K and at 100 K

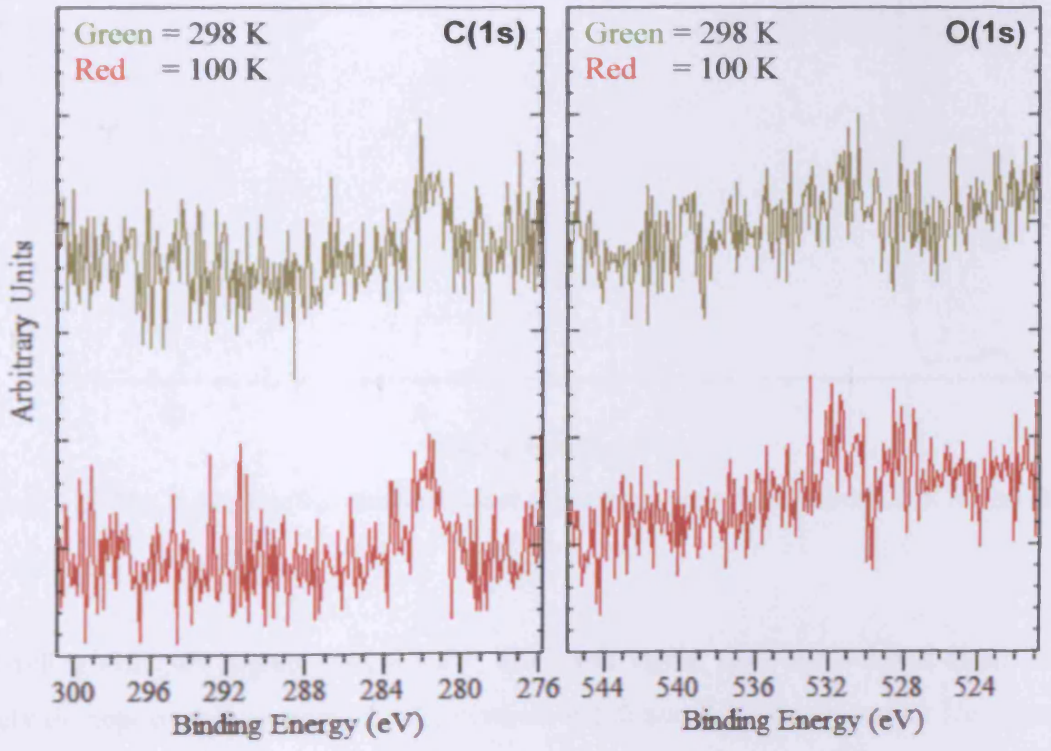

Figure 5.2: C(1s) and O(1s) spectra for clean uranium acquired at 298 K and at 100 K

The ultra-violet photoelectron spectra of uranium, at both ambient and cryogenic temperature, can be seen in figure 5.3. The spectra were both acquired after the surface had been sputtered, removing most of the contaminants, to create a clean surface. The strong signal seen at the Fermi edge was primarily due to itinerant uranium 5f states, while the smaller shoulder at 2.3 eV was due to 6d states [24]. More recent angle-resolved studies have suggested that 5f character may also be present away from the Fermi edge, mixed in with the 6d states at 2.3 eV [24,25]. It is worth noting now that the 5f emission is largely suppressed in UV photoemission spectra acquired using He(I) radiation due to a negligible photoionisation cross-section at that energy, so in reality the intensity seen at the Fermi edge would be many times greater, as the majority of the signal is due to the 5f electrons [26].

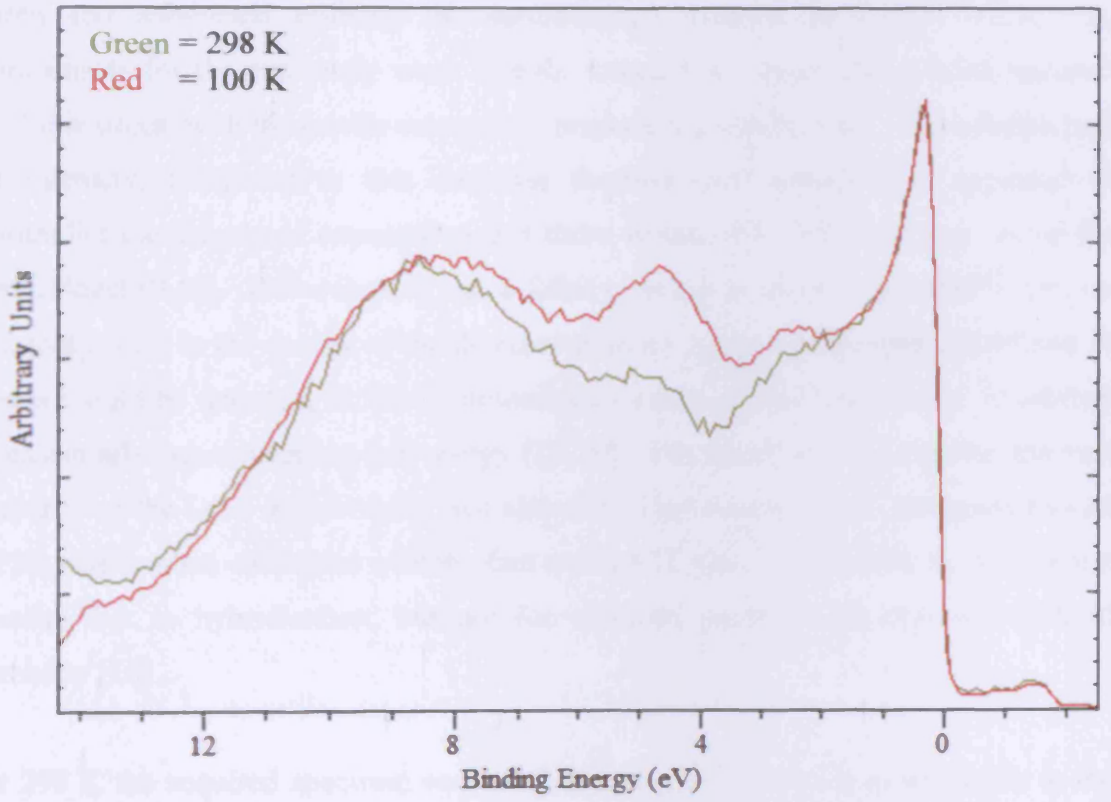

Figure 5.3: He(I) spectra for uranium after sputtering, acquired at both 298 K and at 100 K

At binding energies higher than 4.0 eV, when the signal from the valence states has largely disappeared, two new signals, centred at 5.0 and 8.5 eV appeared. The signal located at 5.0 eV could be attributed to either the 7s states [25], or to residual contamination upon the surface, either in the form of bulk oxide, or adsorbed O_2 and

H_2O based species. The fact that the signal was more prominent in the spectra taken at 100 K indicated that the residual oxygen species explanation was more likely, as the additional time taken to cool down the sample would possibly result in an increase in the contamination seen. While this would seem to go against the suggestion made upon examination of the XPS results, that the vacuum system appeared very clean, the increased surface sensitivity of UPS renders it a far more accurate and reliable measure of the quality of the vacuum. The final peak, located at 8.5 eV, potentially corresponds to that of a shifted oxygen species, which again could be due to contamination from the vacuum chamber, or from oxide located in the bulk [21,27].

The inverse photoelectron (IPE) spectra of clean uranium, at both ambient and cryogenic temperatures, can be seen in figure 5.4. The background has already been fitted and subtracted utilising the methodology detailed in section 3.2.3. To compensate for the extremely weak signals detected, the experiments were repeated multiple times, with the results summed to produce the spectra seen. The relative lack of intensity, compared to that seen for thorium (see section 4.2), appeared to contradict the calculated expectation that there would be a high DOS just above the Fermi level [9,10]. However this was a fallacy, as it was previously noted in section 4.2 that owing to the energy of the detected photons being 9.5 eV, only the 6d and 7s states would be detected, as the photoionisation cross-section towards the 5f orbitals is essentially non-existent at this energy [28,29]. This therefore suggests that the vast majority of the DOS in the region just above the Fermi level are 5f, as opposed to 6d or 7s, which when combined with the fact that the 5f states were visible in the thorium spectra due to hybridisation, but not for uranium, explains the observed lack of intensity [16].

At 298 K the acquired spectrum consisted of a single broad peak which began at the Fermi edge and stretched to approximately 6 eV, which was attributed to 6d and 7s states. The spectrum taken at 100 K, also shown in figure 5.4, which featured the highest intensity at approximately 2 eV instead of the Fermi edge, suggested that the single signal seen at 298 K was actually formed of multiple superimposed signals. If the spectrum acquired at 298 K did indeed feature multiple separate signals, then the one centred at 0 eV decreased in intensity upon repeating the scan at 100 K. This decrease in intensity of the lowest energy signal may be down to the cooling process

used. As was mentioned above, a flow of liquid nitrogen through the probe on the system was used for the cold temperature experiments, with a period of at least 30 minutes needed for the sample to reach its lowest temperature. The UPS results above provided evidence for an increase in the surface contamination upon cooling the sample, so it is feasible that the time-reversed version of that technique would also show similar signs, such as the observed drop in intensity by the Fermi level.

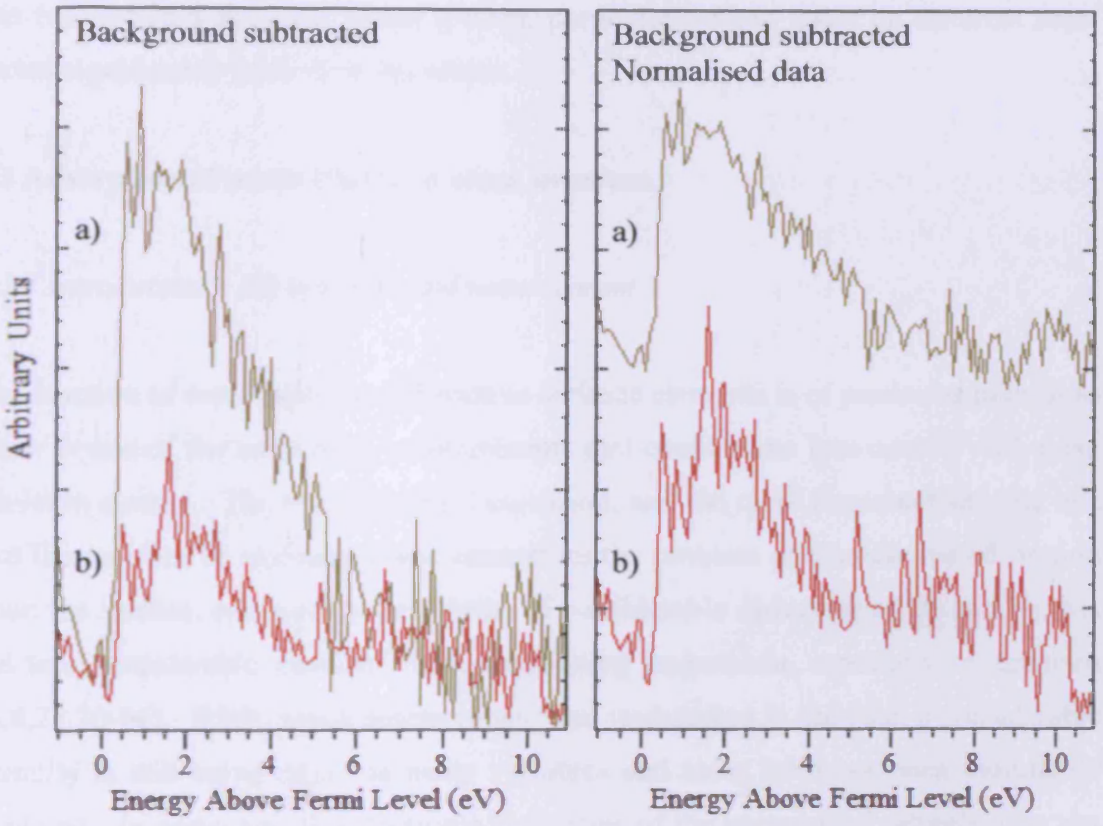

Figure 5.4: Inverse photoemission (IPE) spectra for clean uranium metal at a) 298 K and b) 100 K. The data is presented both before and after normalisation to aid comparison

An additional difference between the spectra acquired at the two different temperatures was that of the total intensity. The total intensity of the signal seen at the colder temperature was considerably less than that seen at the higher temperature, as could be seen in the non-normalised results. While variation in intensity can sometimes be down to the actual electronic environment of the sample, in this

particular example however, where the environment stayed largely the same, that clearly cannot be the case, and there was another cause for what is observed.

As was explained in section 4.2, the experimental setup used to carry out the inverse photoemission studies was extremely sensitive to even very minor changes in the positioning of the sample, electron gun, or detector, because of the extremely small signals being detected. This combined with the highly variable output of the electron gun resulted in a situation where spectra, particularly those taken on different days, varied significantly with their intensities.

5.3 Adsorption of water (H_2O) on clean uranium

5.3.1 Introduction - the uranium and water system

The reaction of water with the radioactive actinide elements is of particular interest as water is one of the most likely contaminants that could come into contact with them whilst in storage. The risk of general corrosion, and the more important specific risk that the radioactive emission could exacerbate the problem of dissociative adsorption upon the surface, and lead to the release of considerable quantities of O_2 and H_2, has led to a considerable quantity of research being undertaken, especially on uranium [6,8,23,30-36]. While much research has been undertaken in the past, a considerable quantity is still being done, as many variables and areas have not been thoroughly explored. In particular, the electronic properties of the unoccupied orbitals have not yet been thoroughly examined. As the unoccupied orbitals dictate and control the reactive properties of the sample, they are one of the features that will be investigated in this work.

In addition to the corrosion reasons noted above, and the more general investigation of the 5f electrons, it is also of interest to study the reaction of water upon the surface of uranium as the results can be compared against those from uranium exposed to oxygen, providing an insight into the oxidation process.

5.3.2 Experimental results – XPS and UPS

The effects of gradual exposure of clean uranium metal to increasing quantities of background dosed H_2O at approximately 298 K can be seen in figures 5.5 to 5.8. In the U(4f) region (see figure 5.5) the H_2O oxidised the surface resulting in the appearance of a uranium oxide peak at approximately 380.9 eV. This energy value agreed with that reported by Winer *et al* [23] for the oxidation of uranium with water, but disagreed with that reported by Nornes and Meisenheimer [8]. Additionally the value agreed with the work carried out by Tull on both the water and uranium, and oxygen and uranium systems [21], and that reported by Fuggle *et al* [18] and McLean *et al* [11] for the *in situ* oxidation of uranium with oxygen. The binding energy of 380.9 eV corresponded to an oxide with a stoichiometry below that of the standard dioxide; UO_{2-X} [37]. The sub-stoichiometric characterisation provided an explanation for the disagreement between the oxide value observed in this work, and some of the values reported for UO_2 in the literature [22].

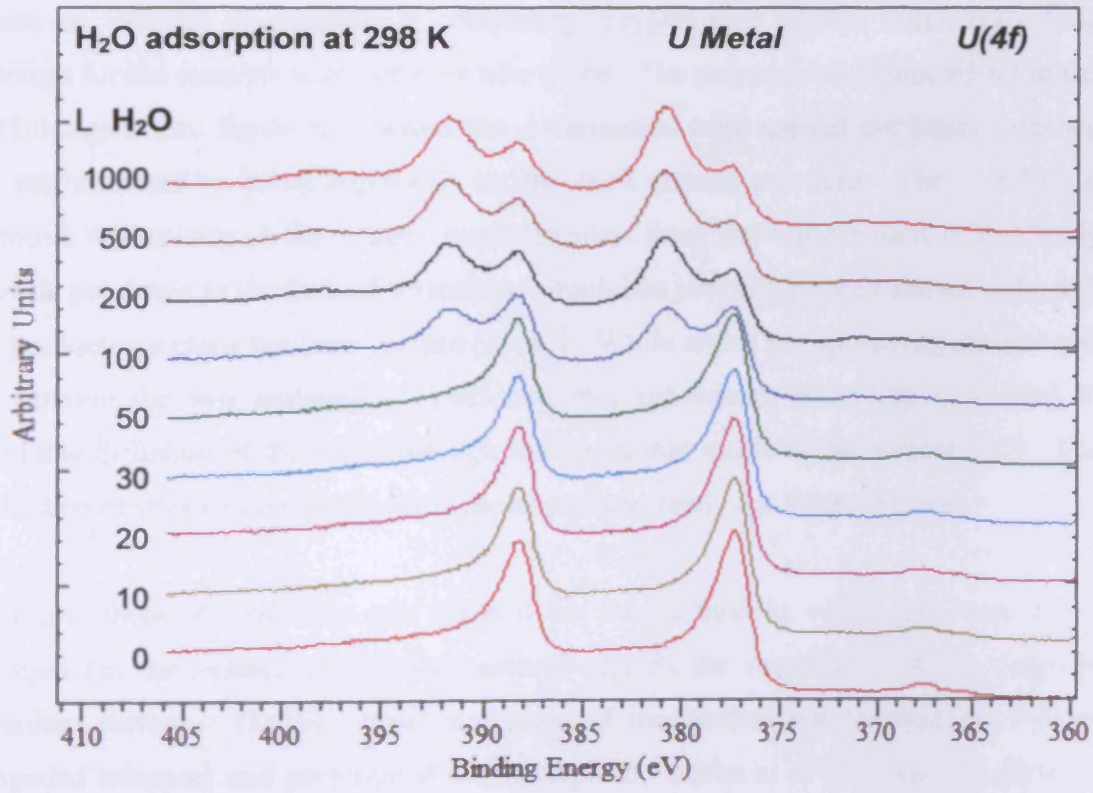

Figure 5.5: U(4f) spectra for clean uranium exposed to increasing quantities of H_2O at 298 K

When compared to the multitude of studies examining the oxidation of uranium with oxygen, there was a pronounced difference in the magnitude of exposure to water vapour necessary to generate similar looking oxide peaks in the U(4f) region. To generate the same intensity oxide signal the exposure of water needed to be considerably greater than that needed with pure oxygen. The difference ranged from needing approximately 20 times the quantity of oxygen [8], to needing 100 times the quantity of oxygen [21]. While this would seem to indicate that oxygen is considerably more reactive towards uranium than water is, a review by Winer *et al* [23] has shown otherwise, and explained why the previous false observations have been made.

Winer *et al* noted that there have been a number of reports indicating not only that water has a similar reactivity as oxygen (when taking into account oxygen content of reagents), but also that the presence of any oxygen, either in the gas phase or adsorbed to the surface, severely retards the reaction between water and uranium [23,32,33,38]. The suggestion was then made that reports of water being less reactive can be blamed upon an inability to maintain a completely oxygen free surface sufficiently long enough for the reaction with water to take place. The presence of a faint signal in the O(1s) region (see figure 5.6) before the experiments were carried out lends credence to this explanation being applicable to the work carried out here. The inability to remove the entirety of the oxygen contamination from the sample used in this study can be put down to the lack of annealing, which has previously been shown to be key to producing a clean uranium surface [39,40]. While argon ion sputtering can be used to remove the vast majority of surface oxide, subsequent annealing is needed to promote diffusion of the metal through the remaining oxide to the surface [40]. The diffusion creates an essentially clean metal surface, ready for future reaction.

Multiple theories have been put forward for the method in which the presence of oxygen (in the system and on the surface) retards the reaction of water with the uranium surface. The two main categories of mechanism put forward are that of impeded transport and preferential chemisorption. Allen *et al* [32], one of those in favour of the impeded transport mechanism, suggested that the effect of the oxygen was not apparent until it had formed a thick (> 3 nm) oxide layer, as then the oxygen could control the transport of newly formed OH^- through the oxide layer, by impeding

the diffusion of the OH^- interstitials. They postulated that this was done through the formation of defect complexes that would diffuse more slowly through the oxide, and would act as a barrier to the OH^-. Winer *et al* [23] simplified the idea by suggesting that O^{2-} and O^-, which are also transported *via* an interstitial mechanism, would cause a "traffic jam" as they migrate more slowly than the OH^- ions, which would thus have to wait for the slower oxygen ions to migrate out of the way before being able to proceed on towards the uranium metal.

The alternative idea of preferential chemisorption, which was put forward by Colmenares [38], suggests that the oxygen is preferentially chemisorbed to the surface, and in turn blocks adsorption sites normally available to water molecules. This blocking action would thus interfere with the dissociation of the water molecules, and thus impact upon the formation of OH^- in the oxide layer. Supporting evidence that oxygen can prevent the dissociation of water at the surface [41], and potentially reduce the adsorption of the water vapour in the first place [42] has also been published in the literature.

The preferential chemisorption explanation fits the results acquired in this study better than the impeded transport mechanism, as the quantity of oxide detected on the surface before reaction was considerably less than a monolayer, so the requirement of a thick oxide layer having been formed, for the transport to be impeded, would not have been met [23].

An additional feature visible in figure 5.5 after exposure to water was that of a shake-up satellite centred at 6.7 eV higher binding energy than the $4f_{5/2}$ oxide peak. The satellite from the $4f_{7/2}$ peak was also present; however it was partly obscured as it fell upon the low energy side of the $4f_{5/2}$ uranium metal signal. It has been suggested that the satellites can be attributed to the shake-up of an electron from the O(2p) valence band into the unoccupied U(5f) level that accompanies the photoionisation process [43-46]. As the occupation and character of the 5f-electron level depends strongly on the O/U ratio of the formed uranium compound, it can be expected that as the satellite is the result of a shake-up into that level, its position will strongly depend on the stoichiometry of the sample [22]. The relative position of the satellite reported was approximately characteristic of stoichiometric $UO_{2.0}$ [22,38].

The corresponding O(1s) spectra produced by exposing uranium to increasing quantities of H_2O can be seen in figure 5.6. At all exposures two distinct components were visible upon curve fitting the data. The first signal, located at 530.8 eV after 10 Langmuirs exposure shifted steadily upwards in energy, reaching 531.3 eV after 1000 Langmuirs. Both energies corresponded to the formation of an oxide (O^{2-}); however the value of 531.3 eV corresponded specifically to the formation of an oxide upon exposure to H_2O [21,23]. The shifts in the binding energy observed upon changing the adsorbate were attributed to changes in the surface dipole caused by the O_2 and H_2O molecules, which changed the work function of the surface. It is thought that the binding energies are generally 0.5 eV higher in energy for water than for pure oxygen because of the presence of hydrogen on the surface [21]. The second less intense peak located at 532.8 eV, which after 1000 Langmuirs contributed 30 % of the final signal, has been characterised as being due to surface bound hydroxide (OH^-) as opposed to strongly chemisorbed or interstitial O^- [21,23].

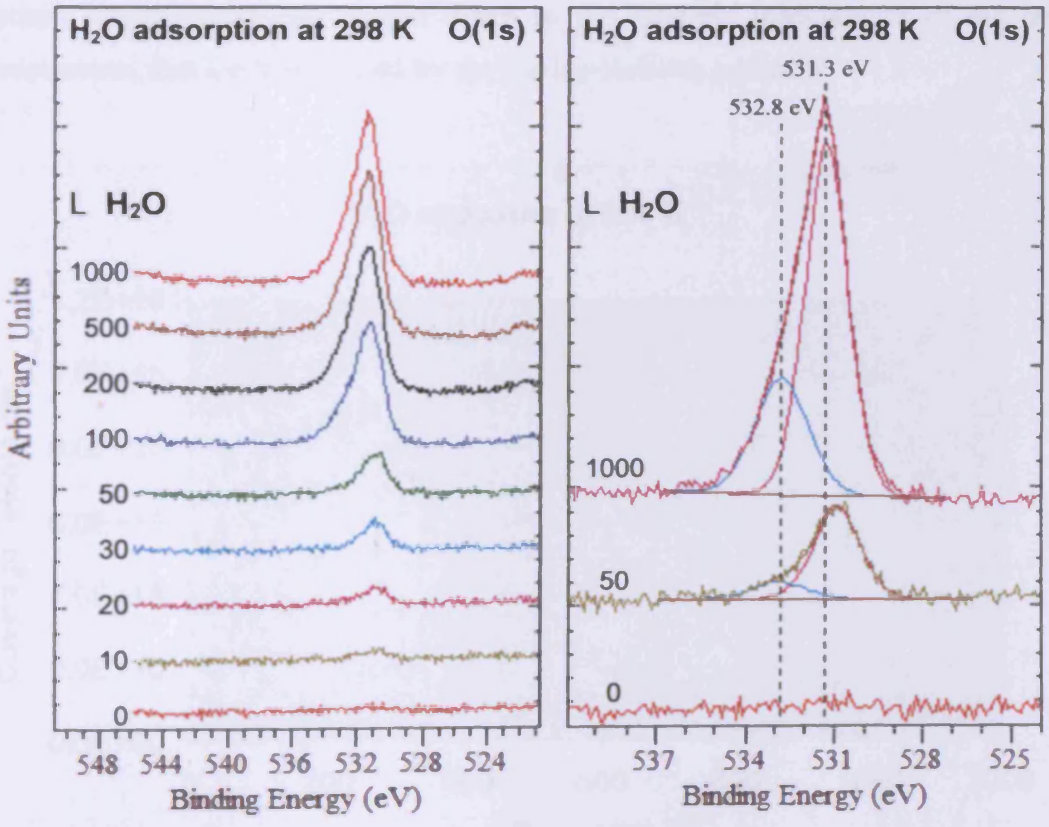

Figure 5.6: O(1s) spectra for clean uranium exposed to increasing quantities of H_2O at 298 K

The relative rate of signal increase in the O(1s) region upon exposure to H_2O compared to that seen with O_2, again made it appear as though O_2 is considerably more reactive than H_2O [8,21]. As explained above this was the result of residual oxygen present on the surface that severely retarded any reaction between incoming H_2O molecules and the uranium surface.

By plotting the coverage of surface oxygen species, calculated from the O(1s) spectra using the Carley-Roberts equation [47] (see section 3.3 for details), against exposure to H_2O, it is possible to note any trends in surface coverage. Figure 5.7 shows the coverage versus exposure graph for the reaction of H_2O with uranium. It can be seen that the relationship between the two variables somewhat follows the "standard" form, where the rate of coverage increase begins high and decreases as the total exposure gradually approaches a saturation value, where no more can be adsorbed on the surface. While the results of figure 5.7 do follow this well there is an anomalous period between 0 and 50 Langmuirs where the reaction proceeds at a slower rate than expected, however this can be put down to the inherent inaccuracies of the area measurements, that are highlighted by the Carley-Roberts equation.

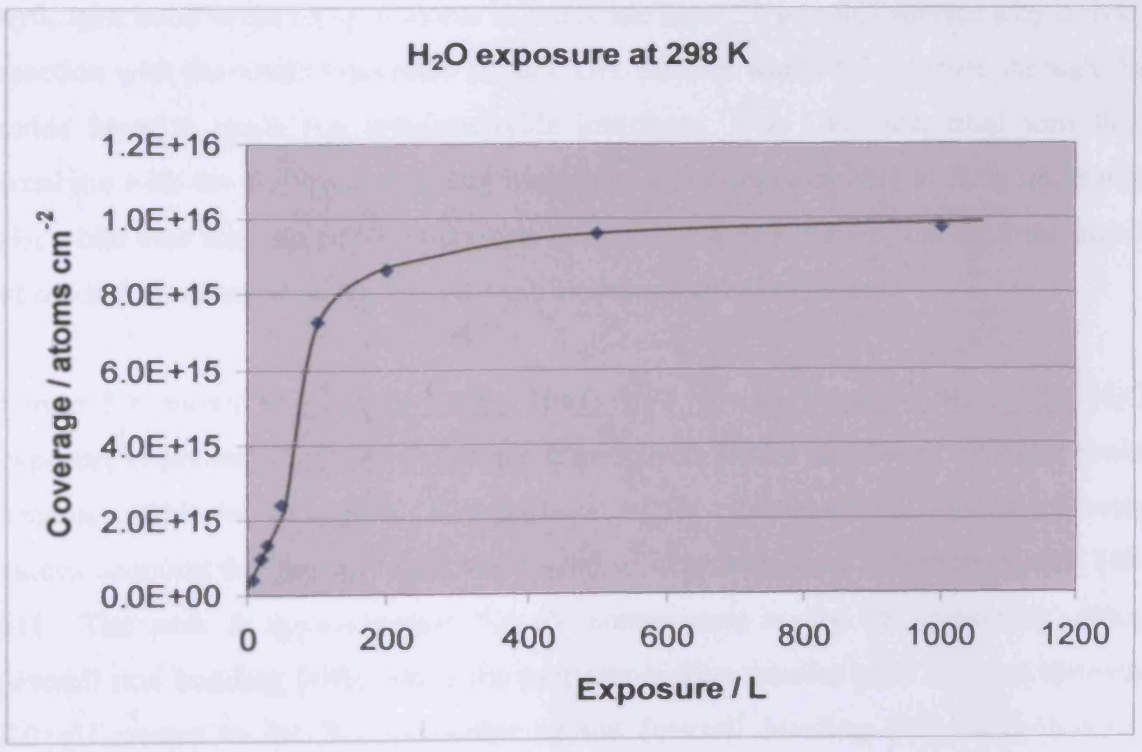

Figure 5.7: Adsorption of water on uranium at 298 K: calculated surface concentration of oxygen species plotted against exposure to H_2O

As with the graphs generated for thorium in chapter 4, the calculations carried out here also suggest the presence of multiple layers of adsorbate. Based on the theoretical value for the number of active sites on the surface, 1 x 10^{15} sites per cm^2, after 1000 Langmuirs the coverage was approaching the equivalent of ten layers. Calculation of the thickness of the adsorbed layer, utilising the equation given in section 3.3.1, returned a value of 24 Å, which supports and agrees with the high multilayer coverage displayed in the figure.

While the mechanism for the oxidation of uranium with water is less well understood than the associated oxidation of uranium with oxygen, some key aspects are still known [38]. The initial step involves the incoming water molecules chemisorbing onto the surface through a metal-oxygen bond. Chemisorption then breaks one of the O-H bonds in a dissociation reaction that leaves a strongly bound OH^- and a weakly held H that is bound to the surface hydroxyl group. The H species then recombine to form molecular H_2, that most likely escapes into the gas phase, leaving behind an oxide. This then continues until a single layer of the oxide has been formed, which when in place, alters the mechanism by which additional water molecules react. Without the benefit of a metal surface to promote dissociation, the water molecules hydrogen bond to the oxygen atoms in the oxide layer. Upon this surface a hydrolysis reaction with the oxide can create surface OH^- species which then diffuse through the oxide layer to reach the uranium/oxide interface. The OH^- interstitial ions then combine with the uranium, releasing hydrogen atoms that combine to form molecular H_2, while also forming additional oxide [23]. So the observation that multiple layers of oxide formed upon the surface is both explainable and expected.

Figure 5.8 shows the corresponding He(I) UPS spectra acquired during the H_2O exposure experiments. With increasing exposure to H_2O a number of different peaks became visible in the region. Comparisons of the peak positions against reference values acquired for gaseous H_2O were used to help assign the observed signals [48-51]. The peak at approximately 5.6 eV corresponds to the $1b_1$ molecular orbital (overall non bonding [48]), while the partially hidden smaller peak at approximately 8.0 eV relates to the $3a_1$ molecular orbital (overall bonding [48], H-H bonding character [49,52]). Intense peaks at approximately 5.6 eV have also been reported in the valence band of uranium after exposure to pure oxygen [21,24,27,53], and after

exposure to water [21]. The final peak at approximately 10.5 eV corresponds to the $1b_2$ molecular orbital (overall bonding [48], O-H bonding character, H-H antibonding character [49]), of the gaseous molecule [50-52]. Figure 5.9, taken and adapted from "The Organic Chemist's Book of Orbitals" by W. L. Jorgensen and L. Salem [48], provides a visual representation of the various orbitals of gaseous water just described.

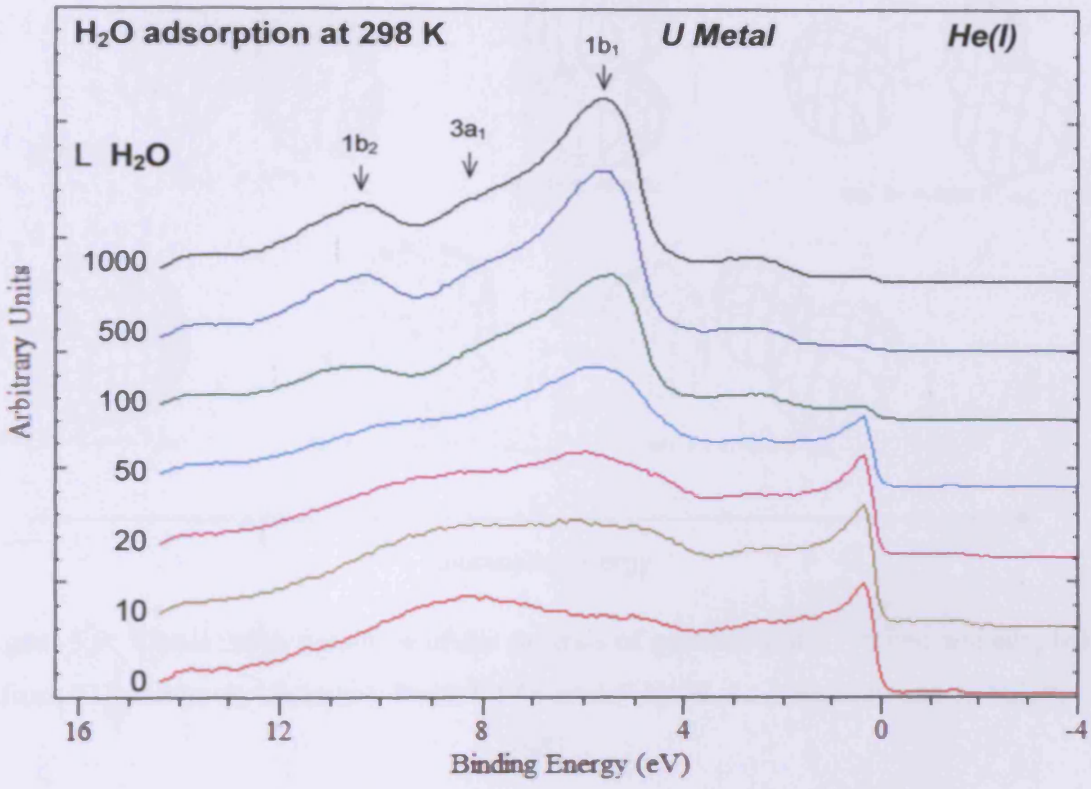

Figure 5.8: He(I) spectra for clean uranium exposed to increasing quantities of H_2O at 298 K

As with the XPS results above, there was a noticeable increase in the intensity of the signals recorded in the spectra after 50 Langmuirs exposure. Upon increasing the exposure from 50 to 100 Langmuirs of H_2O the signal at the Fermi edge largely disappeared. This loss of the metallic 6d7s states close to the Fermi edge is understandable and agrees with the fact that uranium metal, like most actinides, has a high density of states located at the Fermi edge, while uranium dioxide, which is a semiconductor, does not [5,6,23,24]. With the loss of intensity at the Fermi edge, the lowest energy signal remaining was centred at approximately 2.3 eV. This was noticeably higher than the value of ~1 eV reported from the reaction of uranium with

pure O_2, indicating the likelihood that the surface formed upon exposure to H_2O is a worse semiconductor than pure UO_2 [11,23,24]. To investigate this perceived difference the uranium sample used in this work was also exposed to pure O_2 to provide a comparison, with the UPS results shown in figure 5.10, alongside those acquired after exposure to H_2O.

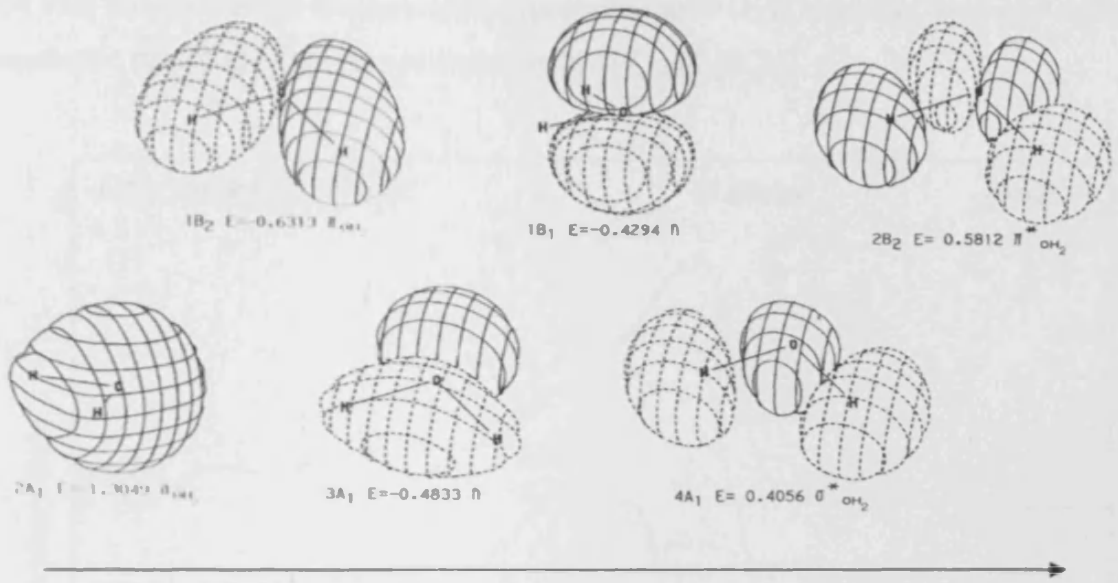

Figure 5.9: Visual representations of the orbitals of gaseous water – taken and adapted from "The Organic Chemist's Book Of Orbitals" by W. L. Jorgensen and L. Salem [48]

The UV photoemission spectra acquired after exposure to pure O_2 matched those seen in the literature for pure UO_2 [54]. The spectra largely matched the one acquired upon exposure to H_2O except for the fact they were shifted by 1.3 eV towards the Fermi edge, and also lacked the signal associated with the $1b_2$ molecular orbital of water. The largest signal at 4.3 eV was due to the O(2p) level of uranium oxide. The position of the lowest energy signal after exposure to O_2 was centred at 1.4 eV, rather than the 2.3 eV value seen after exposure to H_2O. A value of approximately 1.4 eV was expected as the bonding in UO_2 is mostly ionic in nature, with the f-electrons fully localised, and as such a signal at that energy in the valence band has been reported previously [55]. While the 5f electrons often behave in a delocalised manner (see section 1.1), in UO_2 they are localised, which is likely because of the oxidation

state of the uranium. It is possible that the high oxidation state (+4) results in less shielding and an increase in the effectiveness of the core, which in turn leads to the contraction and localisation of the 5f electrons [26].

The smaller gap between the Fermi edge and the lowest energy signal, when compared to the results acquired upon exposure of uranium to H_2O, also reinforces the idea that the surface formed upon exposure to pure O_2 is a smaller band-gap semi-conductor than that formed upon exposure to H_2O [11,23,24].

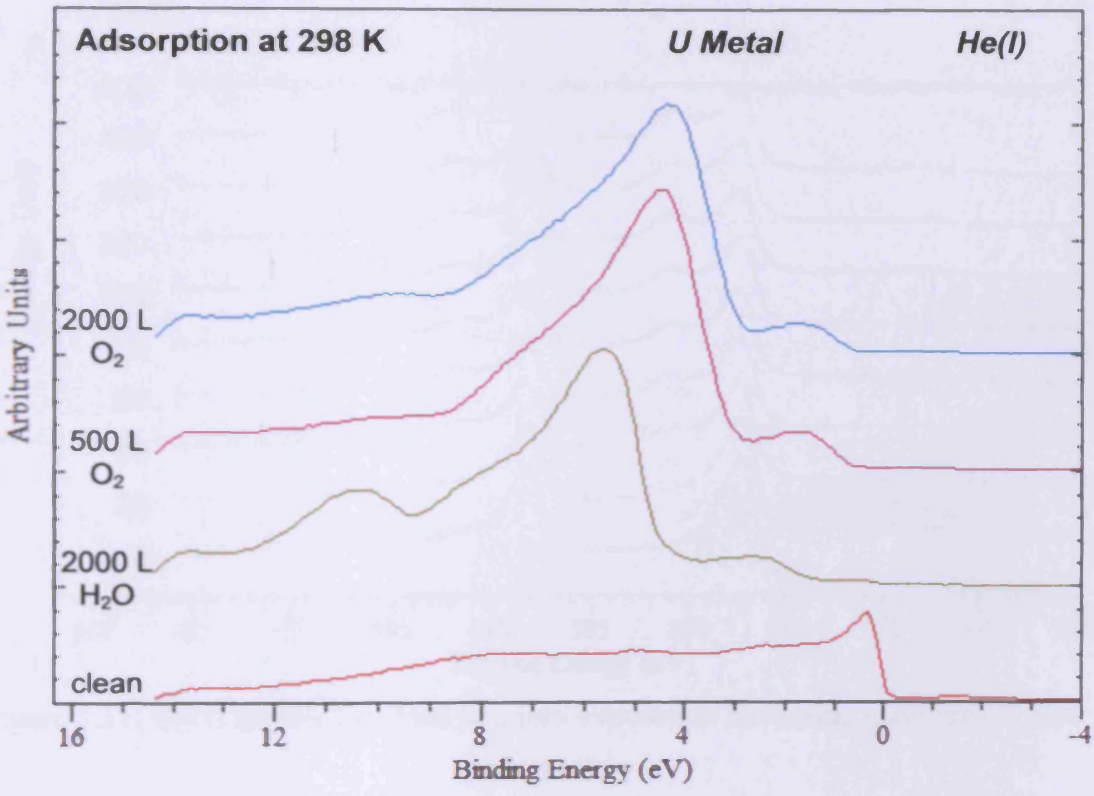

Figure 5.10: He(I) spectra for clean uranium exposed to O_2 (500 and 2000 L) or H_2O (2000 L) at 298 K

When the water exposure experiments were repeated at a temperature of 100 K, distinctly different results were acquired, as can be seen in figures 5.11 to 5.15. As before, the addition of H_2O resulted in the oxidation of the uranium; however the apparent rate at which it occurred differed dramatically. Quite unexpectedly the signal corresponding to uranium oxide in the U(4f) region (see figure 5.11) appeared and increased in intensity at a considerably slower rate than seen at 298 K. This appeared to contradict the expectation that the colder temperature should lead to an

increase in sticking, and thus surface coverage; however this was a fallacy. The colder temperature only leads to an increased sticking probability for H_2O molecular adsorption, which is seen in the O(1s) spectra, and not for H_2O dissociative adsorption. It is actually possible for the reduced temperature to lead to a decrease in the dissociation of the H_2O molecules, due to the unavailability of energy needed to break the bonds.

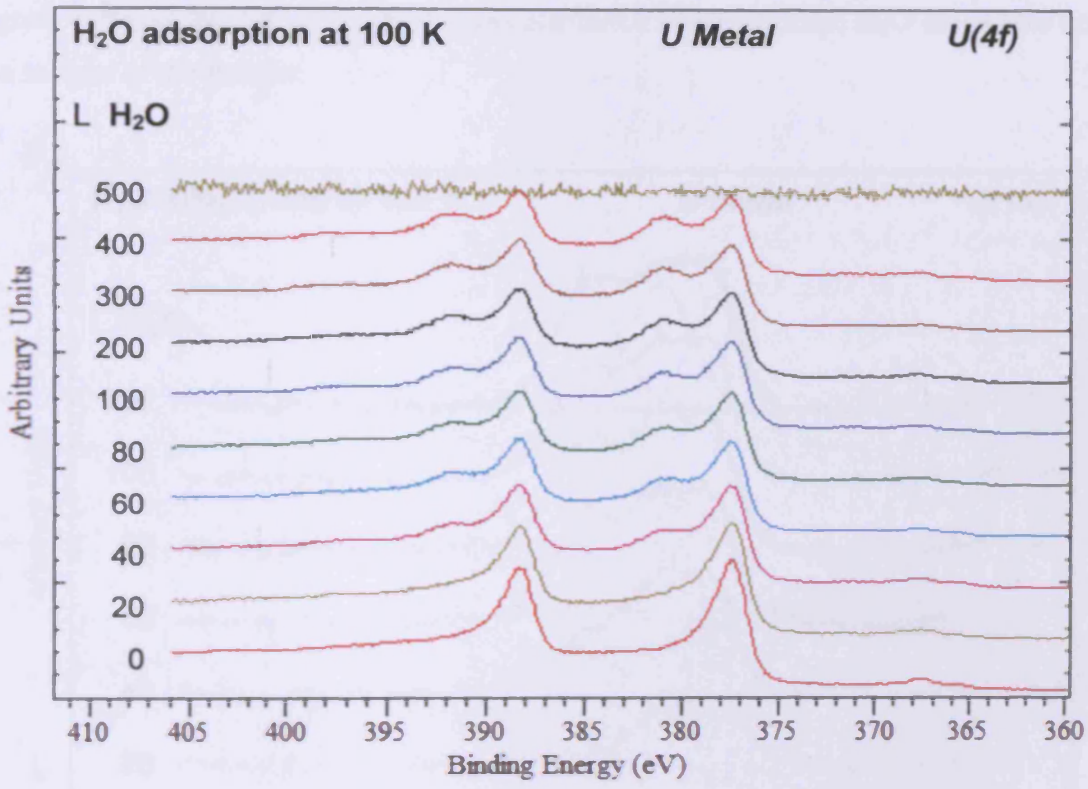

Figure 5.11: U(4f) spectra for clean uranium exposed to increasing quantities of H_2O at 100 K

After 500 Langmuirs exposure the spectra for the two adsorption temperatures diverged from each other even further as the signal in the U(4f) region at 100 K disappeared entirely. This can be attributed to the formation of a layer of solid H_2O on the surface that attenuated the signal from the uranium to the point where it could no longer be seen. The formation of the solid H_2O may also provide the explanation for the apparent lack of oxidation that occurred between 0 and 500 Langmuirs exposure. If the majority of the incoming H_2O molecules were hydrogen bonding to each other, and to the OH^- and O^{2-} species on the surface, as opposed to the surface itself, the results acquired from the U(4f) region would appear to indicate a relatively

clean surface that did not accurately reflect the effect of the exposure upon the surface.

Evidence of the real effect of the exposure to H_2O at 100 K can be seen in the O(1s) region shown in figure 5.12. After just 20 Langmuirs exposure the results deviated from those seen at 298 K, as three distinct components were visible, as opposed to two. This third signal which, after 200 Langmuirs, contributed 37 % of the total signal, and was located at 534.6 eV, was attributed to physisorbed H_2O molecules on the surface of the sample.

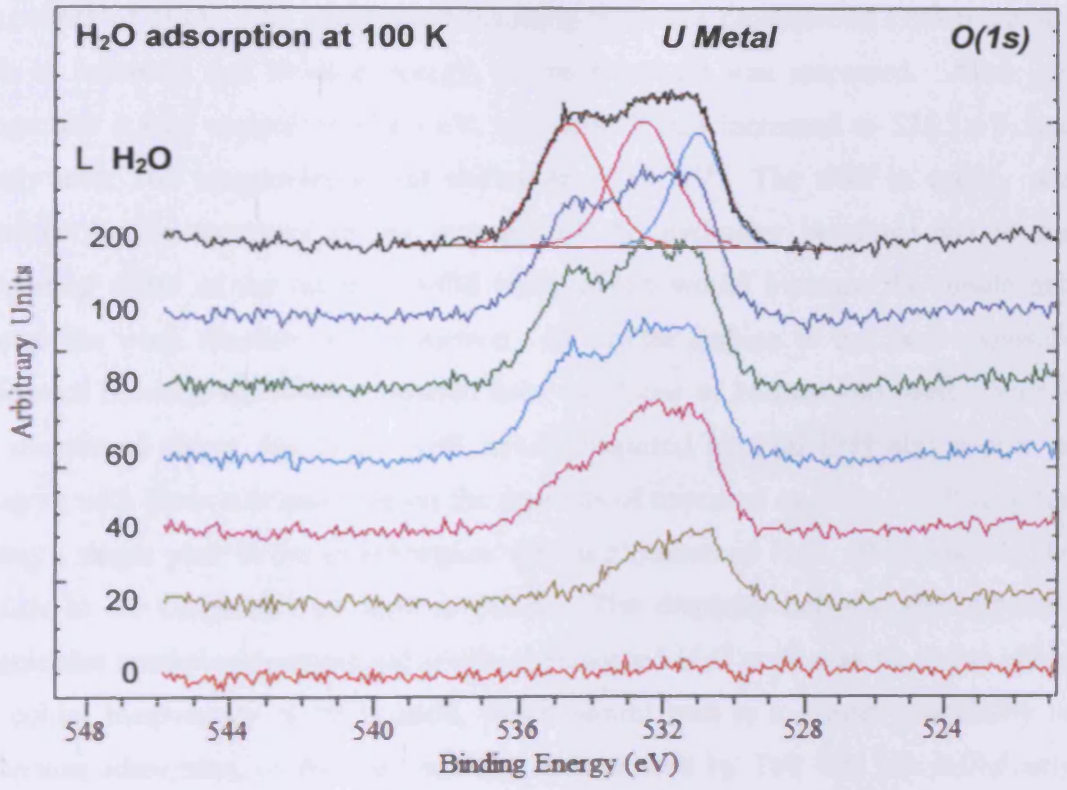

Figure 5.12: O(1s) spectra for clean uranium exposed to increasing quantities of H_2O at 100 K

The signals from the three components grew separately and at different rates from each other. The oxide signal was the first to dominate, appearing at 531.2 eV, followed by the OH^- signal, which had matched the intensity of the oxide by 40 Langmuirs exposure, at 532.5 eV. Finally the signal due to the physisorbed H_2O, which began 534.4 eV, increased, approximately equalling the intensity of the other two signals after 200 Langmuirs exposure. After 200 Langmuirs exposure the three

signals were all of comparable intensity, and matched up with the spectrum reported by Nornes and Meisenheimer [8] for the exposure of 80 K uranium to 36 Langmuirs of H_2O. The disparity between the exposures needed to generate the results may be down to the presence of a greater quantity of oxygen contamination on the surface of the sample, which has been shown previously to reduce the reactivity of uranium towards H_2O [23,32,38].

Further exposure to H_2O, over and above 200 Langmuirs, caused the physisorbed H_2O component at 534.6 eV to dramatically increase in intensity. Figure 5.13 shows the results acquired upon continuation of the dosing up to 300, 400, and finally 500 Langmuirs of H_2O. The component resulting from the physisorbed H_2O increased both in intensity, and binding energy, as the exposure was increased. After 200 Langmuirs it was centred at 534.6 eV, after 300 it had increased to 535.3 eV, and finally after 500 Langmuirs it had shifted to 535.5 eV. The shift in energy was possibly due to increases in the strength of the hydrogen bonding, due to the expanding depth of the layer of solid H_2O, which would increase the dipole and change the work function of the surface. In similar fashion to the large exposure difference between the results reported here and those of Nornes and Meisenheimer [8] mentioned above, the O(1s) XPS results acquired by Tull [21] also appear to disagree with those reported here on the grounds of exposure quantity. Tull reported seeing a single peak in the O(1s) region, due to physisorbed H_2O, after exposing the surface to 30 Langmuirs of H_2O at 80 K. The disparity between the exposure magnitudes needed to generate the single physisorbed H_2O peak may be due to either the colder temperature of 80 K used, which would lead to a greater probability of molecular adsorption, or the fact that the surface used by Tull was not sufficiently clean. It could be seen in the results reported by Tull that a large signal was present in the O(1s) region of the 'clean' uranium before the exposure to H_2O was carried out [21]. The signal visible in the clean spectrum, composed of two different components at energies that corresponded to the oxide and the hydroxide, was large enough in intensity to suggest significant contamination of the surface before the experiment, leading any conclusions based on specific Langmuir exposures to be unreliable [21].

The extremely large increase seen in the O(1s) region upon increasing the exposure from 400 to 500 Langmuirs coincided with the disappearance of the U(4f) signal

mentioned previously, as the layer of solid H_2O became the dominant factor and source of all detected photoelectrons, thus attenuating the signal in the uranium region. The growing layer of physisorbed ice predictably also led to the attenuation of the signals due to OH^- and O^{2-} species, which were completely lacking in the 500 Langmuir spectra.

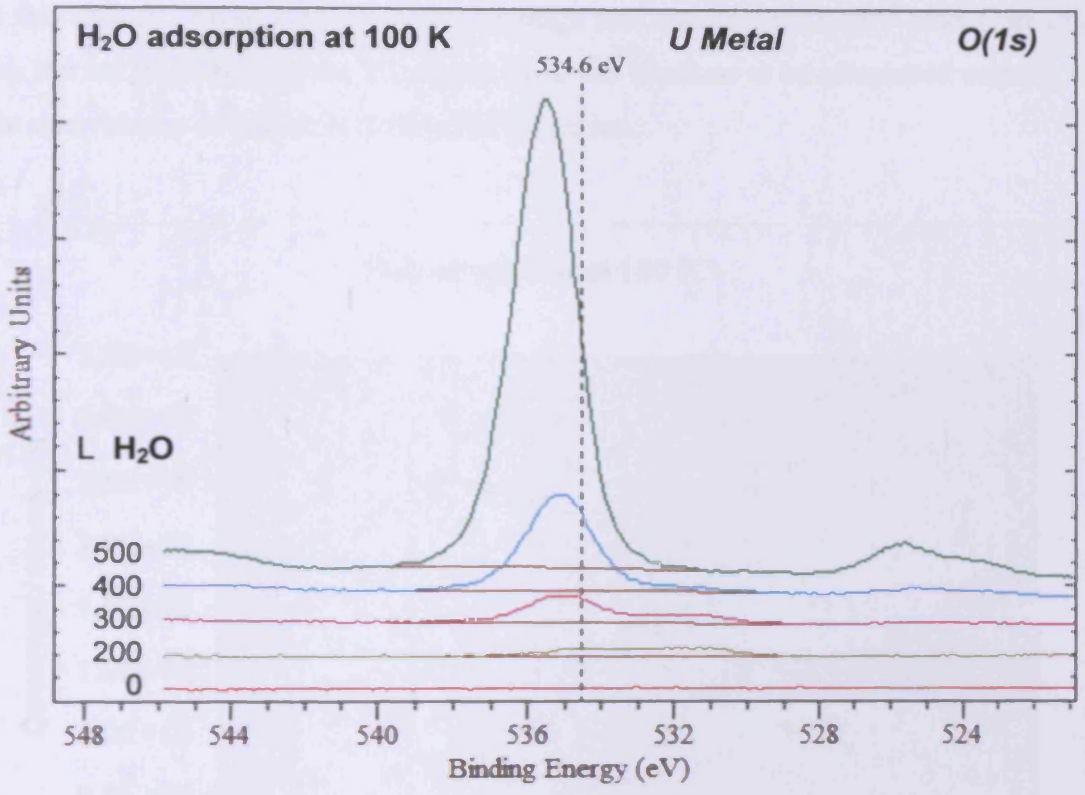

Figure 5.13: O(1s) spectra for clean uranium exposed to increasing quantities of H_2O at 100 K

Figure 5.14 shows the coverage versus exposure graph acquired when the H_2O exposure experiment was repeated at a temperature of 100 K. Unlike the results acquired at 298 K, the results of the 100 K experiments did not follow the "standard" form. Instead the coverage versus exposure graph was composed of three distinct phases, with the first stretching from 0 to 60 Langmuirs. Up until 60 Langmuirs the coverage increased linearly with respect to the exposure. The second phase, between 60 and 200 Langmuirs, featured negligible increases in the calculated coverage, as the system appeared essentially stable. The final phase, from 200 to 500 Langmuirs, featured a dramatic increase in the coverage from 9.3×10^{15} to 3.2×10^{16} atoms per cm^2. Upon reaching 500 Langmuirs exposure the coverage values appeared to be

beginning to saturate; however it cannot be concluded for certain whether the surface species would have reached equilibrium without additional results being acquired.

The sudden increase in the surface coverage upon the exposure rising above 200 Langmuirs coincided with the dramatic increase in the physisorbed H_2O peak in the O(1s) region, suggesting that from 200 Langmuirs onward ice was exclusively formed on the surface. Only after the total coverage had reached 3.2 x 10^{16} atoms per cm^2 was the ice thick enough for the signal from the uranium to be attenuated entirely so that no evidence of it was seen in the U(4f) region.

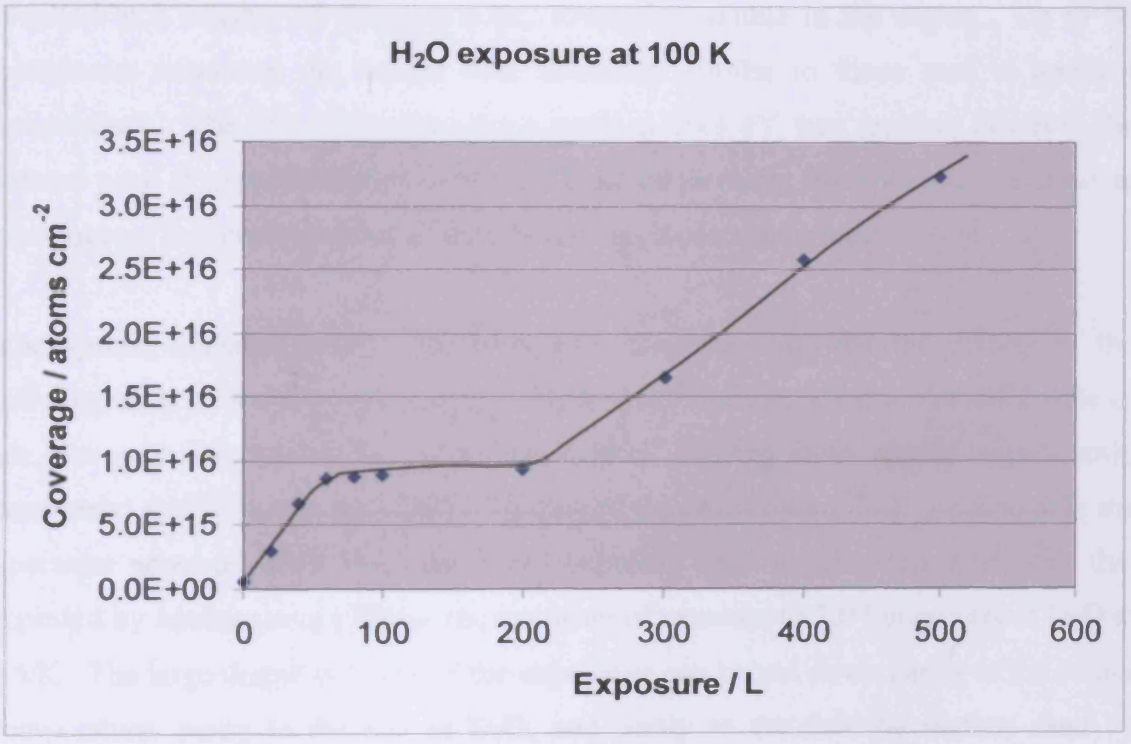

Figure 5.14: Adsorption of water on uranium at 100 K: calculated surface concentration of oxygen species plotted against exposure to H_2O

The average coverage value calculated for the period of negligible change from 60 to 200 Langmuirs, of 9 x 10^{15} atoms per cm^2, approximately matched that seen upon saturation of the surface at 298 K. Saturation was reached at 298 K due to the inability of further OH^- species to be formed upon the surface and diffuse to the uranium/oxide interface. Based on the understanding of the reaction mechanism, this was because after 500 Langmuirs exposure the surface consisted of entirely OH^- species, and not the oxide that was necessary for the binding and hydrolysing of

incoming water molecules [23]. It is conceivable that the surface at 100 K also formed a surface of purely OH^- species, which was only completed after exposure to a total of 200 Langmuirs of water. It is possible that it was only after the surface had been completely saturated with OH^- that any additional water molecules began to hydrogen bond to them, and led to the formation of multiple layers of solid H_2O. This would explain the sudden and dramatic increase in coverage seen from 200 Langmuirs exposure onwards.

Figure 5.15 shows the corresponding He(I) UPS spectra acquired during the H_2O exposure experiments at cryogenic temperature. As in figure 5.8, exposure to H_2O resulted in a number of different peaks becoming visible in the region. Up to 80 Langmuirs exposure, the results were relatively similar to those seen at ambient temperature. The $1b_2$ molecular orbital peak at 10.4 eV was present; however the intense peak at approximately 6.7 eV could not be as easily resolved into the separate components that corresponded to the $1b_1$ and $3a_1$ molecular orbitals.

The spectra acquired after >100 Langmuirs exposure showed the effects of the growing layer of ice upon the surface. Hydrogen bonding, when in the solid state of ice, severely affects the $3a_1$ molecular orbital, causing it to appear significantly broadened and dominate the spectra, leading to the results seen [56]. Additionally the spectrum acquired after 100 Langmuirs exposure also matched up well with that reported by Manner *et al* [34] for the exposure of uranium to 2.0 Langmuirs of D_2O at 85 K. The large disparity between the exposures can be put down partly to the colder temperature, partly to the use of D_2O, and partly to the fact the surface used by Manner *et al* may have contained less residual oxygen which, as noted before, slows the reaction with H_2O [23,32,33,38].

In contrast to the results acquired at 298 K, where there was a small residual signal near the Fermi edge even after exposure to 1000 Langmuirs, at 100 K the signal had been completely lost after 200 Langmuirs. This was to be expected as the layers of ice would behave like an insulator and inhibit the semiconductor nature of UO_2, thus leading to the loss of signal near the Fermi edge.

It is worth noting that the UPS results shown in figure 5.15 appeared to suggest the formation of substantial quantities of physisorbed H_2O upon the surface after just 100 Langmuirs, as opposed to the 300 Langmuir exposure needed to generate similar evidence in the XPS results. This may be due either to the increased surface sensitivity of the UPS technique, which would highlight proportionally more of the physisorbed H_2O on the surface, or be due to differences in the relative cleanliness of the sample before each of the experiments. If the surface used for the XPS experiment was contaminated with a greater quantity of residual oxygen species, which were noted above to interfere with the reaction of H_2O upon uranium, then the formation of the thick layers of physisorbed H_2O would have occurred after a greater exposure value, as in the results reported.

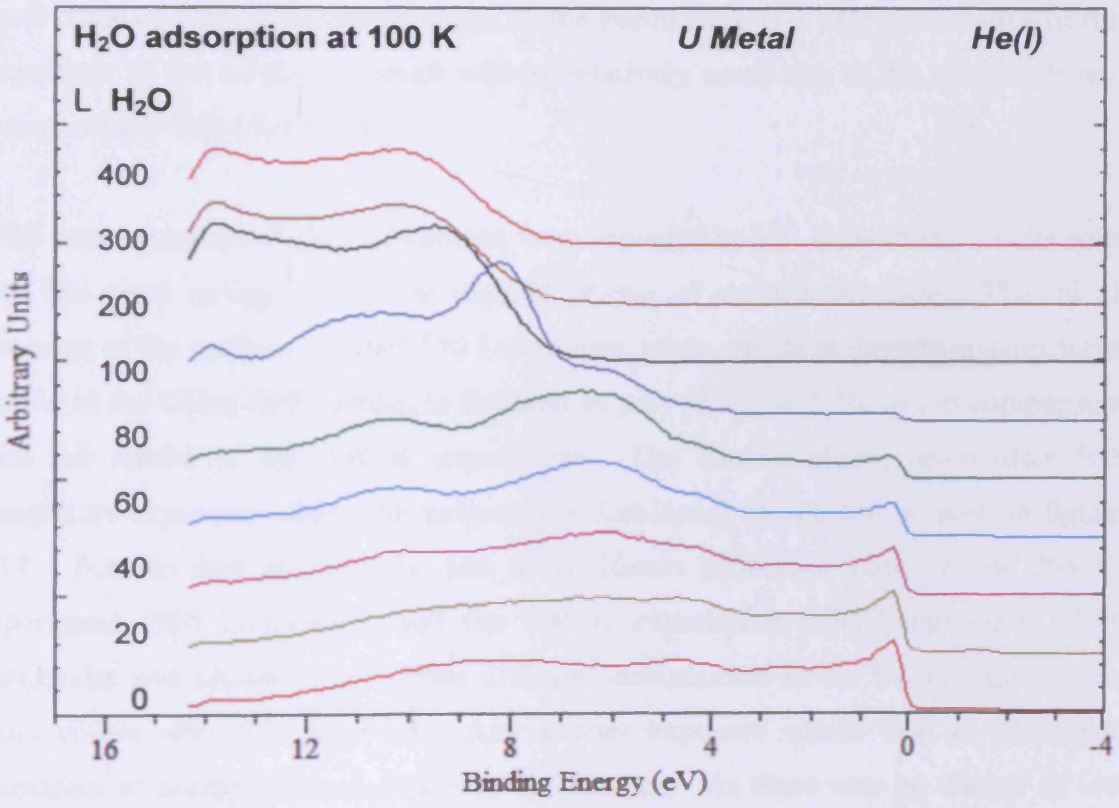

Figure 5.15: He(I) spectra for clean uranium exposed to increasing quantities of H_2O at 100 K

5.3.3 Experimental results – IPES

Inverse photoemission experiments examining the exposure of uranium to water were carried out separately from the forward photoemission experiments; however, the

same two temperatures were investigated, and similar comparisons were made against the uranium and oxygen system.

The IPE spectra of uranium after exposure to H_2O at 298 K can be seen in figure 5.16. The uranium surface was stable under the low energy electron beam for the entire 18 hours the experiment was carried out over, which was in contrast to some of the IPES experiments reported previously (see chapter 4). The single broad signal detected was made up of two distinct components at 3.1 and 4.8 eV that contributed 18.9 % and 81.1 % of the intensity respectively. The signal detected will have been due to the 6d and 7s states, not only because the 5f states are largely not detected at the photon energy used, but also because in UO_2 the entire 5f band is moved below the Fermi level into the realm of the forward photoemission techniques [10]. The relatively small distance from the detected signal to the Fermi edge (1.4 eV) is indicative of the magnitude of the band-gap, which will be relatively small due to the semiconductor nature of pure UO_2 [5,6,23,24].

IPES measurements of H_2O adsorption were repeated at 100 K, with the results split into two parts owing to the two distinct phases of surface coverage. The initial coverage of the surface up until 150 Langmuirs, when the three oxygen species were visible in the O(1s) XPS results, is featured as part of figure 5.16, to aid comparison with the results of the 298 K experiment. The second phase, taken after 500 Langmuirs exposure, where the surface was dominated by ice can be seen in figure 5.17. For the first phase there was a significant difference between the 298 K experiment (500 Langmuirs) and the 100 K experiment (150 Langmuirs). 150 Langmuirs was chosen as the three different components in the O(1s) region were most visible after this exposure. Any greater exposure would lead to the quick formation of multiple layers of ice on the surface. As there was no danger of ice formation at 298 K regardless of exposure, the 500 Langmuirs used is acceptable for comparison against the 150 Langmuirs used at 100 K.

As with the experiment carried out at 298 K, after 150 Langmuirs at 100 K the surface also remained completely stable under the low energy electron beam utilised in the technique. The spectra featured two distinct signals, with the first being a broad peak, centred at 6.1 eV, that was superimposed onto the steadily rising background that

made up the second distinct signal. As with the results of the 298 K experiment, both detected signals were due to the 6d and 7s states, with particular emphasis on the 6d states. In contrast to the spectra acquired at 298 K, where the signal began 1.4 eV above the Fermi edge, the signal at 100 K was further away from the edge, at 3.2 eV. This was due to the physisorbed H_2O component upon on the surface, which after 150 Langmuirs was approximately equal in intensity to that of the hydroxide and oxide signals, which partially insulated the surface, increasing the band-gap of what would normally be a semiconductor.

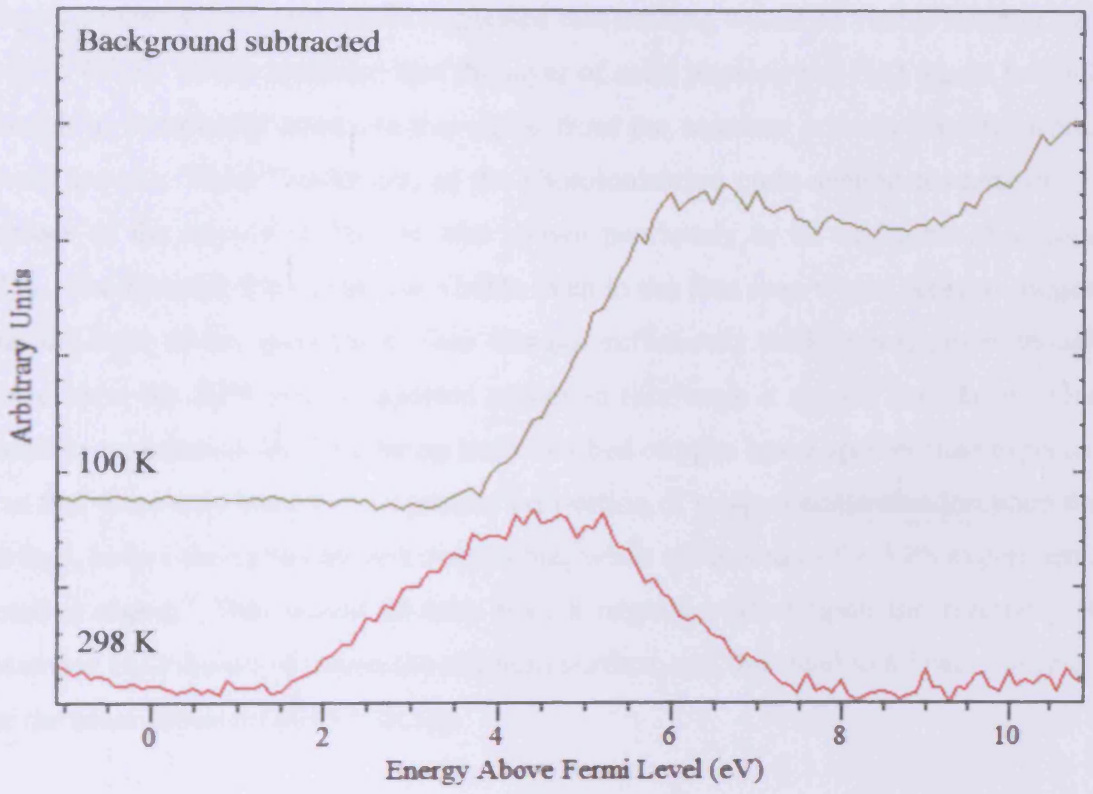

Figure 5.16: IPE spectra for uranium exposed to 500 L of H_2O at 298 K and 150 L at 100 K

The second part of the results for uranium exposed to H_2O at 100 K are seen in figure 5.17. As was discussed earlier while considering the XPS results of the experiment, upon increasing the exposure above approximately 200 Langmuirs a significant layer of solid H_2O rapidly formed upon the surface. To maximise the depth of this layer for the IPES experiment the uranium was exposed to 500 Langmuirs of H_2O.

The acquired spectra in figure 5.17 provided the first example of a uranium surface that was unstable whilst under bombardment from the low energy electron gun. The signals recorded gradually shifted upwards in energy away from the Fermi edge as time progressed. The low energy limit of the signal was approximately 2 eV during the first scan, but had increased to 4 eV by the seventh and final scan, while the approximate centre point of the slopes (highlighted in the figure) increased from 5 to 6.2 eV.

The presence of the detected signal from the very first scan was unexpected, as previous experiments carried out suggested that nothing would be visible initially (see section 4.3.3). It was expected that the layer of solid physisorbed H_2O would be thick enough to completely attenuate the signal from the uranium orbitals beneath, which would leave a "blank" spectrum, as the photoionisation cross-section towards the 3s orbitals of the oxygen in the ice was shown previously to be negligible (See page 115). The fact that the signal was visible even in the first scan would seem to suggest that the layer of ice upon the surface was not sufficiently thick enough, even though based upon the XPS results reported earlier in this work it should have been. One possible explanation for there being less adsorbed oxygen based species than expected was that there may have been a greater proportion of oxygen contamination upon the surface, before the exposure was carried out, when compared to the XPS experiments detailed above. This would in turn have a negative effect upon the reactivity of incoming H_2O molecules upon the uranium surface, and thus lead to a lower coverage for the same exposure [23,32,33,38].

An alternative explanation for the signal being visible from the very first scan relates to how the experiment was undertaken. The surface was exposed to 150 Langmuirs of H_2O, and scanned for a total of 80 minutes, to produce the spectra seen in figure 5.16. After this an additional exposure of 350 Langmuirs of H_2O was carried out, and the surface was scanned for an additional 28 minutes. While no changes were visible in the spectra during the 80 minutes the sample was initially scanned for, after exposure to 150 Langmuirs, it is still possible that some form of rearrangement occurred due to the incident low energy electron beam. The proposed rearrangement could have then either limited the adsorption of further H_2O, or altered the chemical

form in which it took upon the surface, thus leading to the observance of a signal in the acquired IPE spectra right from the very first scan.

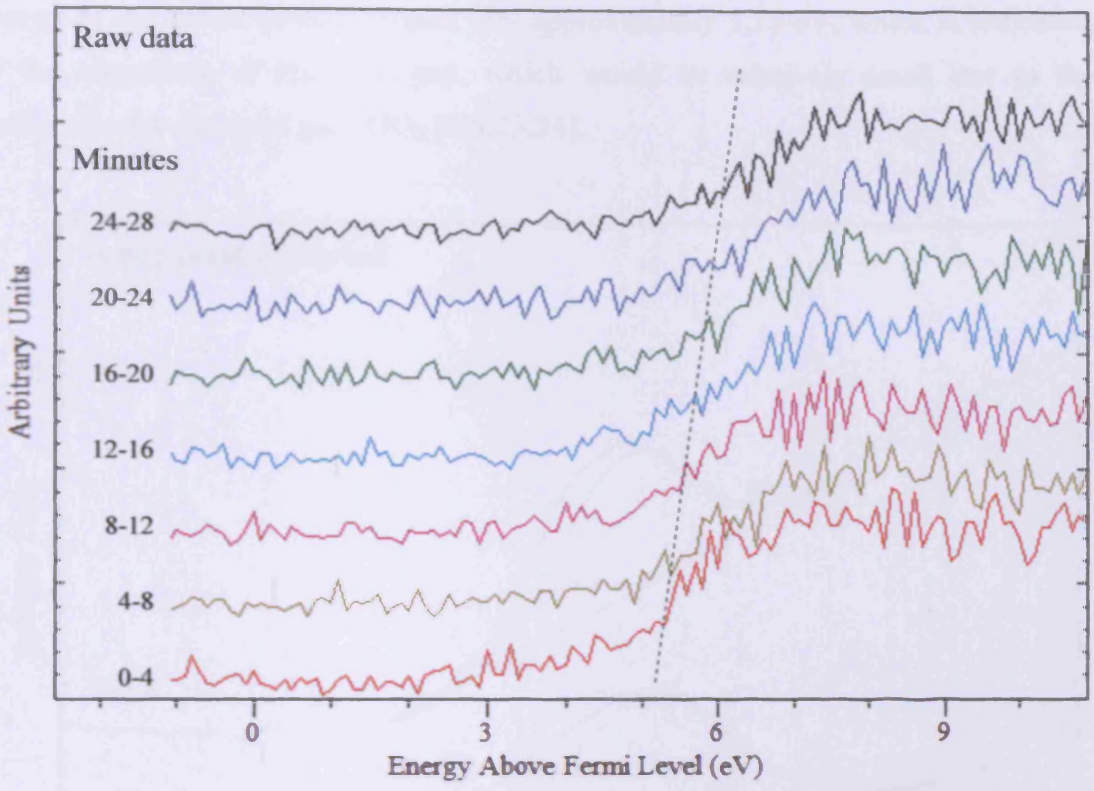

Figure 5.17: Chronologically ordered IPE spectra for uranium exposed to 500 L of H_2O at 100 K, taken over a period of 28 minutes

As with the forward photoemission techniques, the oxidation of uranium with oxygen was useful for direct comparison with the water and uranium reaction. The IPE spectra of uranium after exposure to 500 Langmuirs of O_2, at both ambient and cryogenic temperatures, can be seen in figure 5.18. It is worth noting that the spectrum acquired at 298 K largely matched the IPES results reported by Roussel *et al* [57] for pure $UO_{2.0}$.

At both temperatures the resulting signal after exposure was a composite of two separate peaks, which were due to the 6d and 7s states, as the 5f states would all be below the Fermi level [10]. The temperature had a distinct effect upon both the positions of, and relative intensities of, the two peaks. In the experiment carried out at 298 K, the acquired spectrum featured two broad peaks centred at 3.9 and 5.7 eV, which made up 23 % and 77 % of the total signal respectively. The signal at 3.9 eV

has been attributed to the $6d^1$ states [57], while the signal at 5.7 eV has been attributed to the $5f^3$ final state [58], which disagrees with the suggestion that the 5f states would all be below the Fermi level [10]. The distance between the Fermi edge and the energy of the lowest detected signal was approximately 1.75 eV, which is indicative of the magnitude of the band-gap, which would be relatively small due to the semiconductor nature of pure UO_2 [5,6,23,24].

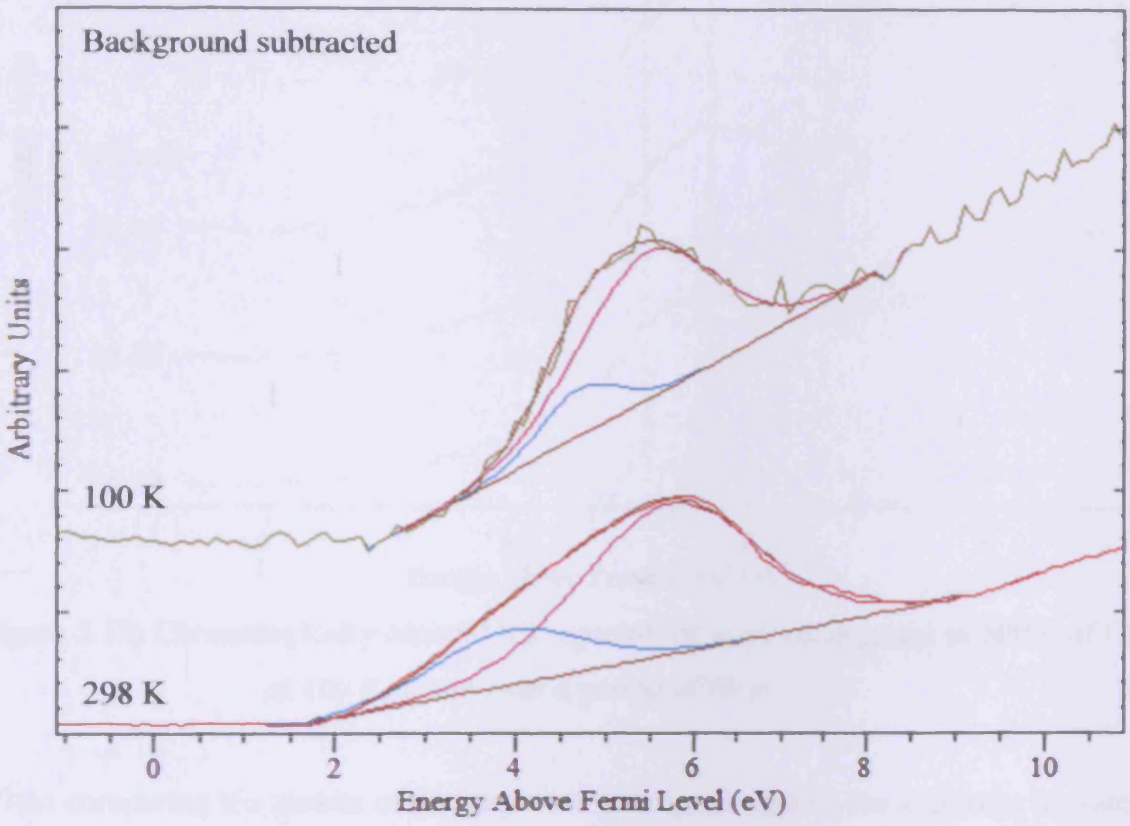

Figure 5.18: IPE spectra for uranium exposed to 500 L O_2 at 298 K and 100 K

A direct comparison with the results of the experiment carried out at 100 K was complicated however by the fact that the surface was not stable under the electron beam, suggesting the surface species were only weakly bound. Figure 5.19 shows the spectra acquired at 100 K every 20 minutes over a total period of 60 minutes. While the effects of the electron gun were not as pronounced as in some of the other results reported in this work, it can still be seen that there was a subtle broadening of the peak as time went on, combined with a loss of intensity of the peak when compared to the steadily increasing background signal. The background subtracted spectrum shown in figure 5.18 was of the first 0 to 20 minutes scan period, and was made up of two

distinct broad peaks centred at 4.7 and 5.5 eV, which made up 16 % and 84 % of the total signal respectively.

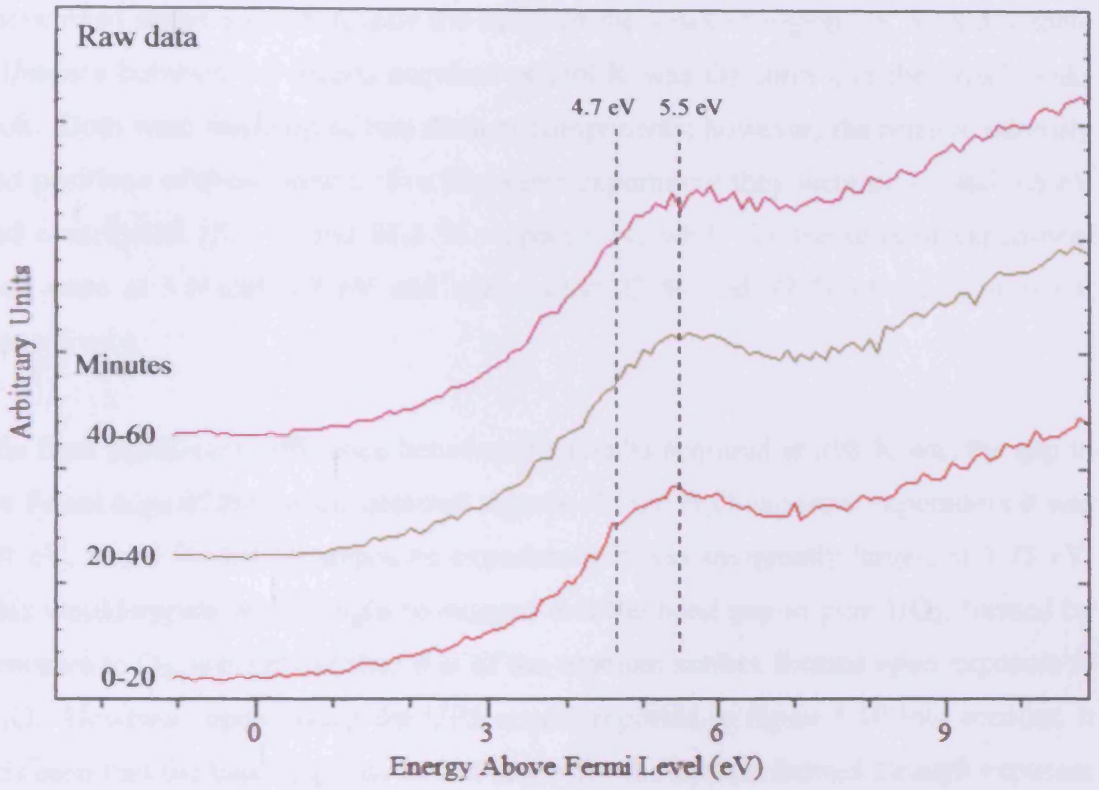

Figure 5.19: Chronologically ordered IPE spectra for uranium exposed to 500 L of O_2 at 100 K, taken over a period of 60 minutes

When comparing the results of the exposure to oxygen against the exposure to water the first notable similarity was that both surfaces resulting from exposure at 298 K were entirely stable under the low energy electron gun. This was in contrast however to the results acquired at 100 K, where the surface after exposure to oxygen was unstable, while the surface after exposure to water (150 Langmuirs) was stable. While it is true that after 500 Langmuirs of H_2O the surface *was* unstable under the electron beam, this is not however comparable to the O_2 exposure results, as the total coverage was many times greater due to the presence of physisorbed species, in addition to those chemisorbed, which were only formed through exposure to H_2O and not O_2.

A notable difference between the results acquired at 298 K was that while exposure to either reagent resulted in the formation of one broad peak, in the spectra from the

water experiment the peak was the only signal visible. This was in contrast to the results of the oxygen experiment, where there was a prominent tail of increasing energy on the high energy side of the peak, suggesting the presence of additional unoccupied states centred outside the range of the scanned region. A second notable difference between the results acquired at 298 K was the form that the broad peaks took. Both were made up of two distinct components; however, the relative intensity and positions of these varied. For the water experiment they were at 3.1 and 4.8 eV and contributed 18.9 % and 81.1 % respectively, while for the oxygen experiment they were at 3.9 and 5.7 eV and contributed 23 % and 77 % of the total signal respectively.

The final significant difference between the results acquired at 298 K was the gap to the Fermi edge of the lowest detected signals. In the H_2O exposure experiment it was 1.4 eV, while for the O_2 exposure experiment it was marginally larger, at 1.75 eV. This would appear at first sight to suggest that the band gap in pure UO_2, formed by exposure to O_2, was greater than that of the uranium surface formed upon exposure to H_2O. However, upon taking the UPS results reported in figure 5.10 into account, it was seen that the band gap was in fact larger for the surface formed through exposure to H_2O (3.25 eV for H_2O exposure against 2.56 eV for O_2 exposure).

5.3.4 Additional discussion

At both 298 K and 100 K the exposure of clean uranium to H_2O led to the formation of multiple oxygen species. The binding energies for the U(4f) and O(1s) regions indicated the presence of hydroxide and oxide species, with an additional component due to physisorbed H_2O at 100 K. Additional evidence for the formation of the oxide species was provided by the presence of shake-up satellites at 384.1 and 394.9 eV in the U(4f) region that are known to indicate the formation of uranium oxide, specifically the $UO_{2.0}$ stoichiometry [22,38]. The three component O(1s) spectrum after 200 Langmuirs exposure at 100 K emulated that seen in the literature after 36 Langmuirs at 80 K [8]. The signal from the physisorbed H_2O at 100 K increased in size and dominated the O(1s) region after 300 Langmuirs exposure, resulting in the complete attenuation of the signal in the U(4f) region.

The reactivity of the surface towards H_2O was shown to be considerably lower than towards O_2, with up to 100 times greater exposure needed to generate similar intensities of oxide signals in the U(4f) region. The low reactivity towards H_2O was explained to be due to the presence of residual oxygen upon the surface, which blocked adsorption sites.

The coverage against exposure graphs showed the expected multilayer coverage at both temperatures, and a "standard" relationship between the two variables for the experiment at 298 K, but not at 100 K. At 100 K a sudden and rapid increase in surface coverage was observed between 200 and 500 Langmuirs exposure that was shown to be due to the formation of purely physisorbed water upon the surface. The total surface coverage upon saturation at 298 K was calculated to be the equivalent of 10 layers, which was supported by depth calculations of the total layer thickness, that showed it be 24 Å thick. The total surface coverage after 500 Langmuirs at 100 K, calculated *via* the Carley-Roberts equation [47], equated to 32 layers, which was greater than the probing depth of XPS, meaning the total thickness was greater than 50 Å, but was too thick to calculate accurately using the methods described in chapter 3.

The 5f, 6d, and 7s unoccupied orbitals shifted upwards in energy away from the Fermi edge upon reaction with H_2O. The unoccupied orbitals at 298 K were located at a lower energy that those seen after 150 Langmuirs at 100 K due to the presence of considerable physisorbed H_2O at the colder temperature. The unoccupied orbitals at 298 K were located at a lower energy than those seen upon reaction with pure O_2, due to the formation of hydroxide groups when exposed to H_2O. The surface after 500 Langmuirs at 298 K, and 150 Langmuirs at 100 K, proved to be entirely stable under low energy electron gun utilised in the IPES technique. The surface after 500 Langmuirs exposure at 100 K, when a thick layer of physisorbed H_2O had been formed, proved to be unstable under the beam, with the signal shifting upwards in energy as time went on.

The signals seen in the He(I) UPS and IPES results, acquired at 298 K, around the Fermi level exposed the relatively small band-gap of the sample after exposure to H_2O that is characteristic of the semi-conductor nature of UO_2.

5.4 Adsorption of ammonia (NH_3) on clean uranium

5.4.1 Introduction - the uranium and ammonia system

UN is an important compound being considered for use as one of the fuel types for the future advanced nuclear reactors [26,59,60]. A number of different reaction mechanisms used to form it have been investigated, many of which involve the use of ammonia as the source of the nitrogen [59,60]. While the reactions themselves have been studied, very little work has been done on the direct reaction between clean uranium and ammonia, and what species the reaction forms. It is not yet fully known what affect the presence of additional NH_x species, expected to form upon reaction with ammonia, could have on the overall stability and electronic properties of the UN surface. Additionally, as with all the work undertaken throughout this study, the unusual technique of IPES offers the chance to investigate the rarely looked at, yet vitally important, unoccupied orbitals.

5.4.2 Experimental results – XPS and UPS

The effect of gradual exposure of clean uranium metal to increasing quantities of background dosed NH_3 (up to 1000 Langmuirs) at 298 K can be seen in figures 5.20 to 5.24. Additional exposure above 1000 Langmuirs produced negligible differences in the photoemission spectra. In the U(4f) region (see figure 5.20) the reaction of NH_3 with the surface was seen to have resulted in only subtle changes to the uranium metal peaks. The positions of the $4f_{5/2}$ and $4f_{7/2}$ peaks had shifted 0.2 eV upwards in energy, which agreed with the spectra of pure UN published in the literature [10,26]. Additionally the maximum intensity of the peaks decreased upon reaction with the incoming NH_3 molecules, while the FWHM increased (from 2.0 to 2.6 eV for the $4f_{7/2}$ peak).

The peaks recorded after exposure to NH_3 retained the asymmetric nature of the clean uranium spectrum. The asymmetric nature for clean uranium was explained, both generally in section 3.2.2, and more specifically in section 5.2, to be caused by the high density of states situated at the Fermi edge. This suggested that a significant proportion of those density of states remained at the Fermi edge upon formation of

UN. This observation agreed with the results published by Black *et al* [26], and based upon their work, also provided evidence that UN was formed as opposed to U_2N_3, which would have generated symmetric peaks in the U(4f) region. The asymmetric properties of the peaks additionally resulted in a visible broadening of the signals; however this alone did not explain the significant increase in the FWHM reported above, upon formation of UN. A comprehensive examination of the reason for this broadening was carried out by Norton *et al* [10]. By a process of elimination they determined it was due to configuration interactions, in particular the possibility of mixed valency of the uranium. The chemical shift due to mixed valency would be in the order of 1 eV; however due to the already broad nature of the peaks and the resolution of the system it would not be possible to resolve the separate components, thus resulting in the increased broadness observed in the acquired spectra.

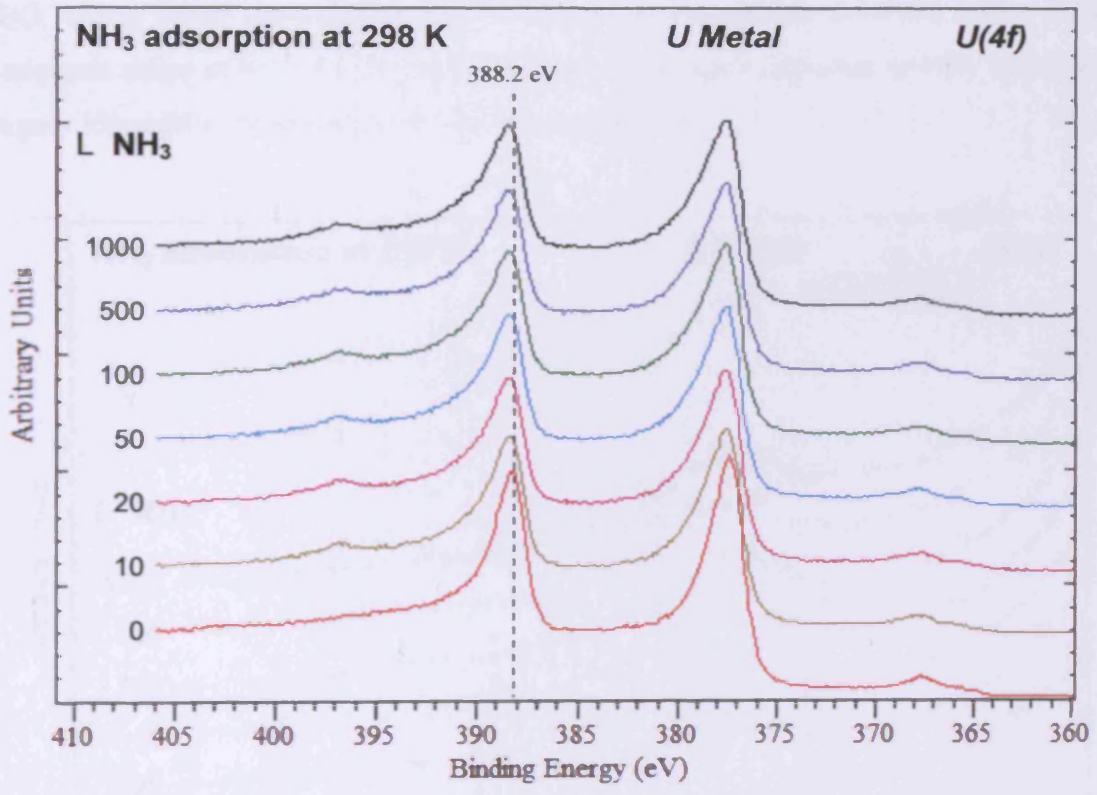

Figure 5.20: U(4f) spectra for clean uranium exposed to increasing quantities of NH_3 at 298 K

In addition to the alterations to the $4f_{5/2}$ and $4f_{7/2}$ peaks, exposure to NH_3 also resulted in the appearance of a peak towards higher binding energy. This photoemission

signal was from the nitrogen itself, as the U(4f) and N(1s) XPS regions overlapped. Close-up spectra of the N(1s) region for the experiment can be seen in figure 5.21.

The signal visible in the N(1s) region was made up of two distinct components, with the larger of the two, located at 396.8 eV, due to the formation of the nitride. The position of this peak matched up well with that reported in the literature for pure UN [10,26,61]. The second peak, located at 398.6 eV, which contributed approximately 15 % of the total signal, was assigned to nitrogen in the form of NH_2 chemically bound to the surface [62]. The lack of any signal relating to NH would appear to suggest that it was not a stable species upon the surface, and underwent sudden and immediate loss of the final hydrogen to form the nitride instead.

It is worth noting that unlike the results seen in the O(1s) region upon exposure to H_2O, where there were noticeable differences in the spectra over the entire 1000 Langmuir range studied, the N(1s) spectra produced upon exposure to NH_3 remained largely identical over the range of 10-1000 Langmuirs.

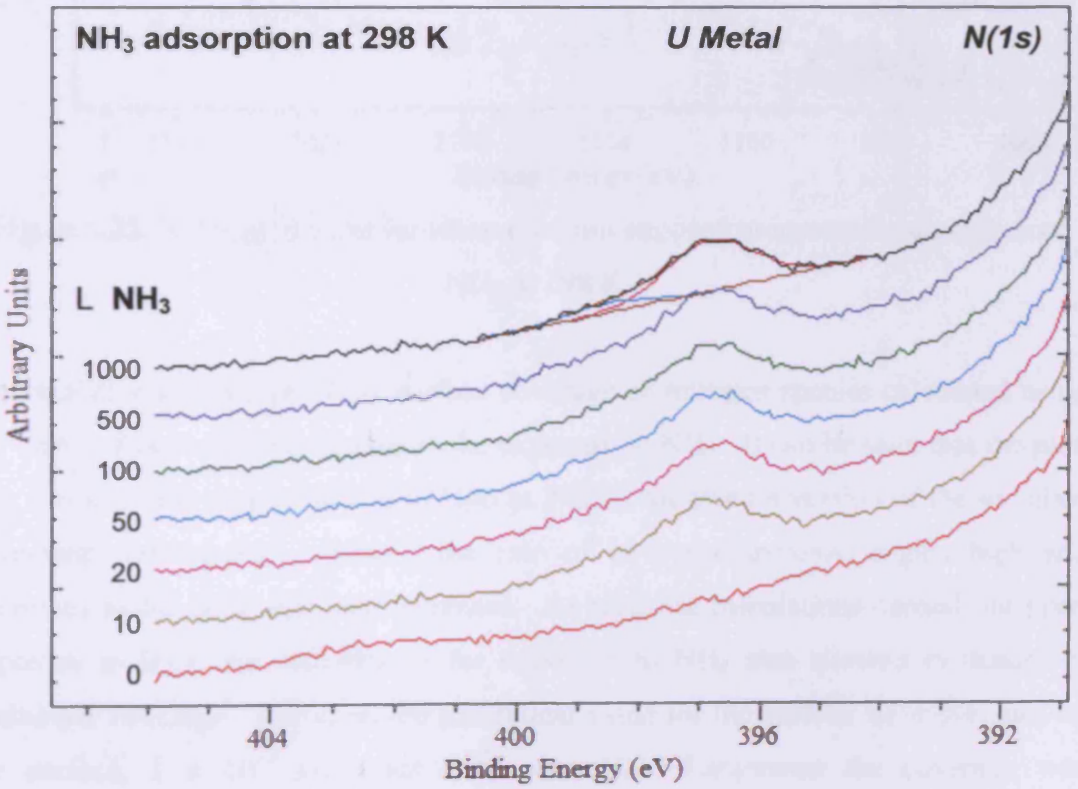

Figure 5.21: N(1s) spectra for clean uranium exposed to increasing quantities of NH_3 at 298 K

In addition to the N(1s) region, the N(KLL) Auger signal was monitored, with the results shown in figure 5.22. The exposure to NH_3 resulted in the immediate appearance of a signal at 1102.5 eV equivalent binding energy. After the initial 10 Langmuir exposure the signal remained stable, in both position and intensity, while the surface was exposed to a total of 1000 Langmuirs.

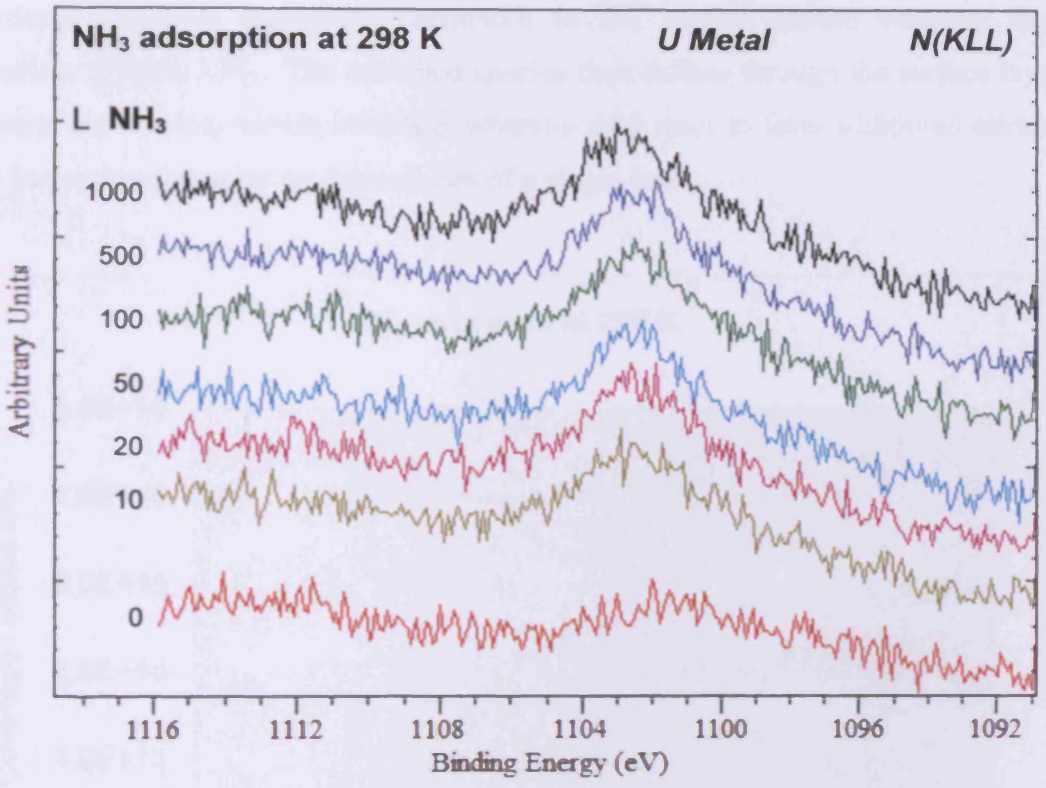

Figure 5.22: N Auger spectra for clean uranium exposed to increasing quantities of NH_3 at 298 K

Figure 5.23 shows a plot of the surface coverage of nitrogen species calculated using the Carley-Roberts equation against the exposure to NH_3. It can be seen that the plot, like that acquired after exposure to H_2O at 298 K, followed a version of the so called "standard" relationship, whereby the rate of coverage increase begins high and decreases as the total exposure increases. As with the calculations carried out upon exposure to H_2O, the calculations for exposure to NH_3 also showed evidence for multilayer coverage. Based on the theoretical value for the number of active sites on the surface, 1 x 10^{15} sites per cm^2, after 1000 Langmuirs the coverage was approaching the equivalent of 4.4 layers.

This could be explained by the ability of the NH_2 species shown to be on the surface to hydrogen bond to additional NH_3 molecules; however if this was the case an additional signal corresponding to those same molecules would be expected in the N(1s) XPS results. The actual explanation for the multilayer coverage is that the mechanism for the nitride formation is similar to that of the oxide formation, in that diffusion through the surface layers is possible. Upon formation of the first layer, additional ammonia molecules chemisorb to the surface nitride whereby they dissociate to form NH_2. The adsorbed species then diffuse through the surface layer to reach the uranium/nitride interface, whereby they react to form additional nitride, thus increasing the coverage beyond that of a single layer.

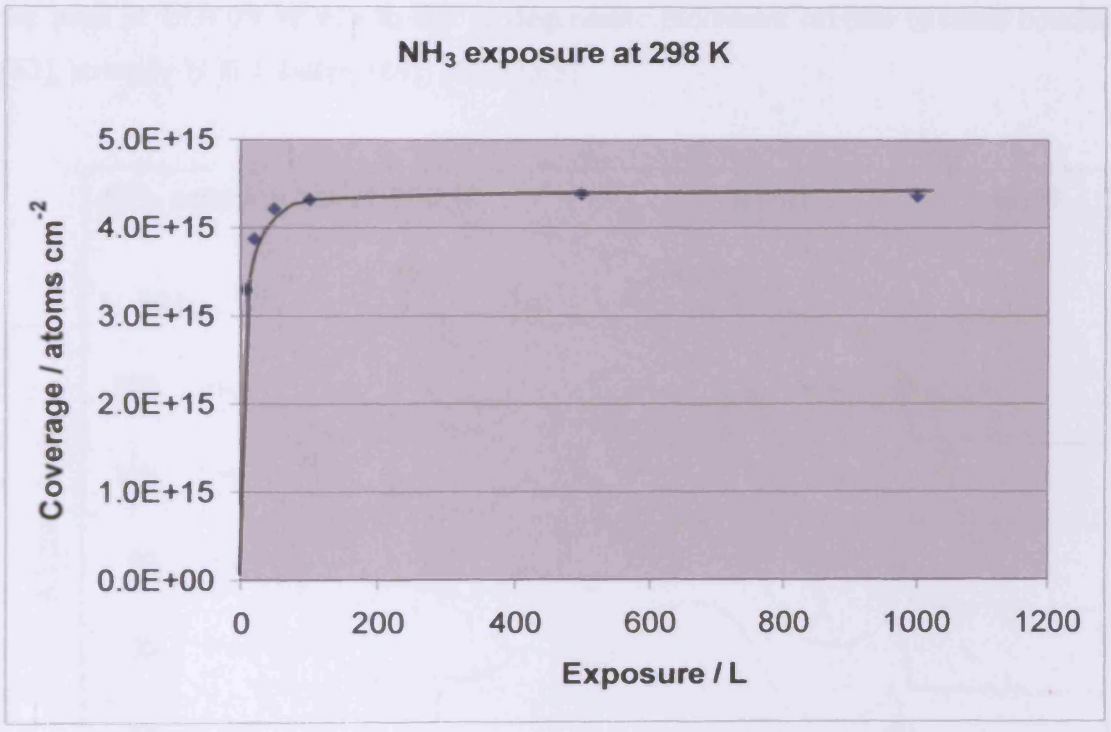

Figure 5.23: Adsorption of ammonia on uranium at 298 K: calculated surface concentration of nitrogen species plotted against exposure to NH_3

The coverage against exposure graph of figure 5.23 also highlighted how little the acquired spectra varied over the entire range of exposures studied. After 10 Langmuirs the coverage was already 3.3 x 10^{15} atoms per cm^2, which was considerably higher than the 4.2 x 10^{14} atoms per cm^2 seen upon exposure to 10 Langmuirs of H_2O. This fact combined with the relative stability of the spectra upon increasing exposures suggested that clean uranium was initially considerably more

reactive towards NH_3 than H_2O. While this may be true, the calculated coverages once saturation had been reached showed that exposure to H_2O led to more than double the total coverage of the surface than exposure to NH_3.

Figure 5.24 shows the corresponding He(I) UPS spectra acquired during the NH_3 exposure experiments. The addition of NH_3 into the system resulted in the appearance of a number of peaks which related to the nitrogen containing species adsorbed onto the surface. Comparisons of the peak positions against reference values acquired for gaseous NH_3 were used to help assign the observed signals [51,63-65]. The peak at approximately 4.4 eV corresponds to the $3a_1$ molecular orbital (overall non-bonding [63], H-H bonding character [64]) of gaseous NH_3, while the peak at 10.0 eV relates to the 1e degenerate molecular orbitals (overall bonding [63], strongly N-H bonding [64]) [51,52,65].

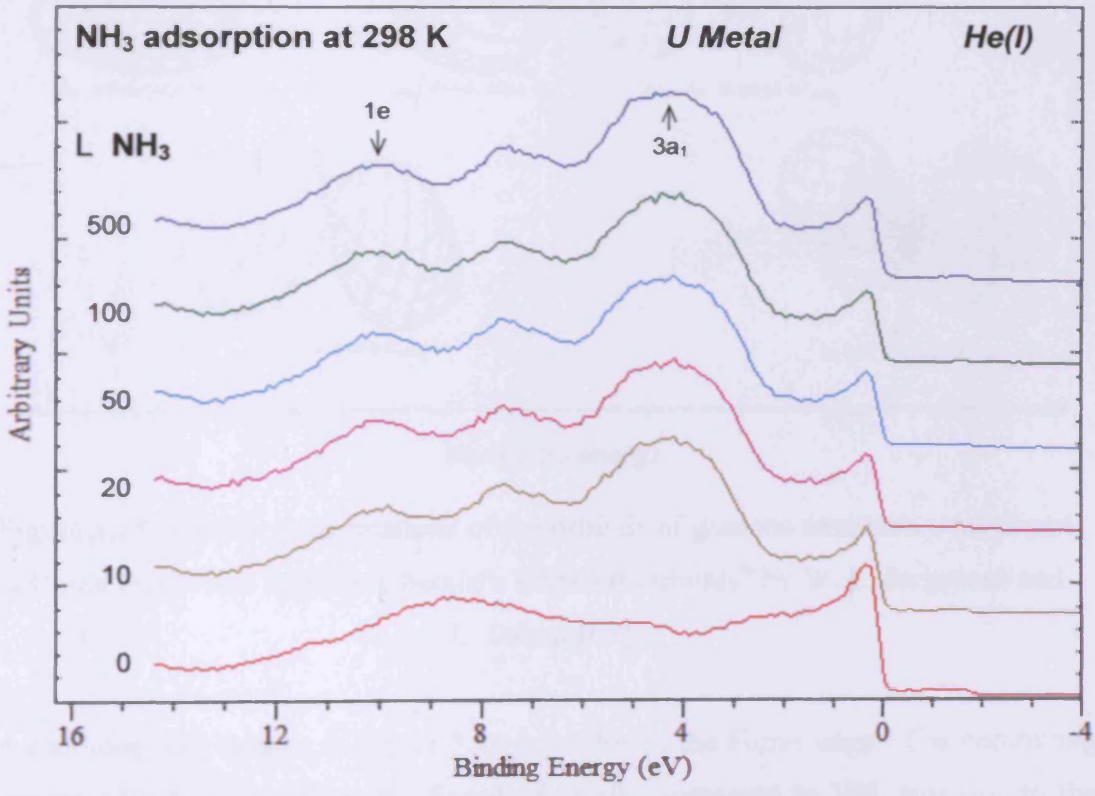

Figure 5.24: He(I) spectra for clean uranium exposed to increasing quantities of NH_3 at 298 K

The peak at 7.6 eV was probably due to residual oxygen contamination upon the surface, as there was a signal visible near that same energy before the surface had

been exposed to any NH_3, and a small signal was seen in the O(1s) spectra that was taken before the experiment to check the cleanliness of the surface. Figure 5.25, taken and adapted from "The Organic Chemist's Book of Orbitals" by W. L. Jorgensen and L. Salem [63], provides a visual representation of the various orbitals of gaseous ammonia just described.

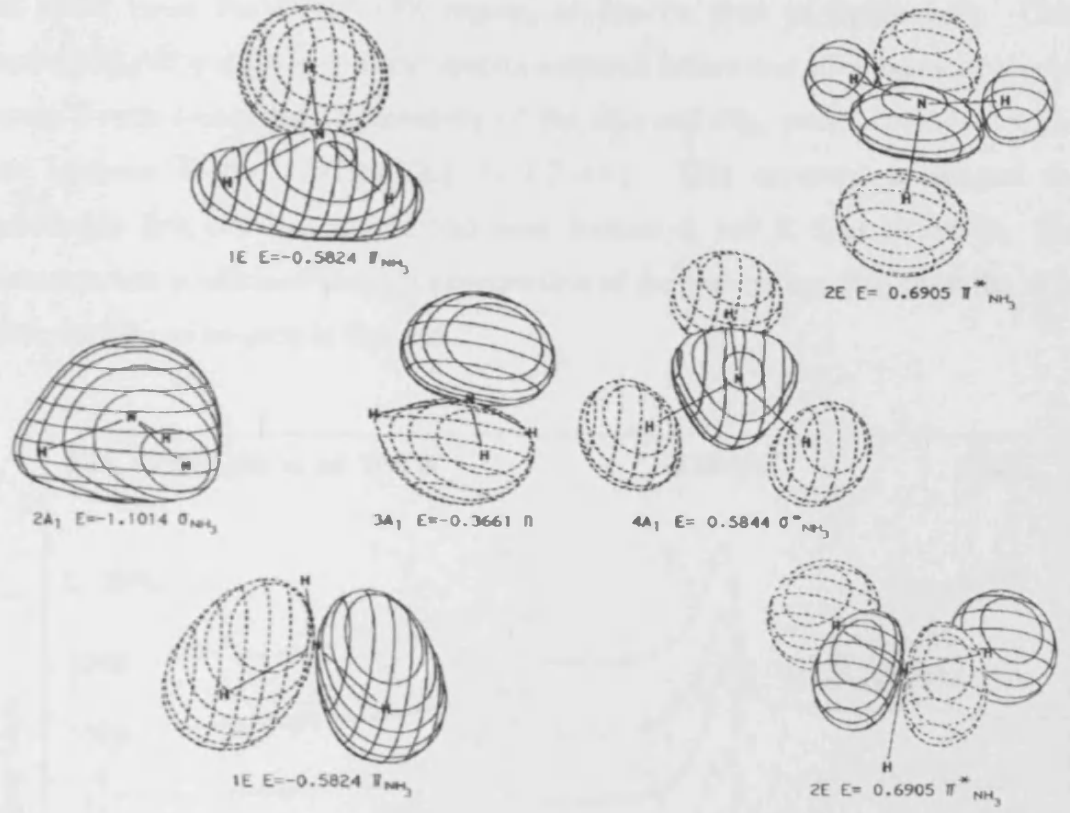

Figure 5.25: Visual representations of the orbitals of gaseous ammonia – taken and adapted from "The Organic Chemist's Book Of Orbitals" by W. L. Jorgensen and L. Salem [63]

An additional key feature in figure 5.24 is visible at the Fermi edge. The continuing presence of a large signal at the Fermi edge after exposure to NH_3 was due to the delocalised nature of the 5f electrons in classic UX based compounds, such as UN, where the U-U spacing is below 3.5 Å (which is the Hill limit) [26]. The intensity recorded at the Fermi edge also explains the observation that the $4f_{5/2}$ and $4f_{7/2}$ peaks seen in figure 5.20 remained asymmetric in appearance even after exposure to NH_3.

The observed intensity at the Fermi edge also agreed well with that observed in the UPS spectra of pure UN reported in the literature [10,26,61].

As with the H_2O studies, distinctly different results were acquired when the NH_3 exposure experiments were repeated at 100 K, as can be seen in figures 5.26 to 5.30. Unlike the experiments carried out at 298 K, the exposure to NH_3 at 100 K had very little effect upon the U(4f) XPS region, as can be seen in figure 5.26. Close examination and comparison of the spectra acquired before and after exposure showed up only a very minor drop in intensity of the $4f_{5/2}$ and $4f_{7/2}$ peaks, combined with a small increase in the FWHM (2.1 to 2.2 eV). This appeared to suggest that considerably less uranium nitride had been formed at 100 K than at 298 K. This conclusion was confirmed through examination of the spectra acquired from the N(1s) region, which can be seen in figure 5.27.

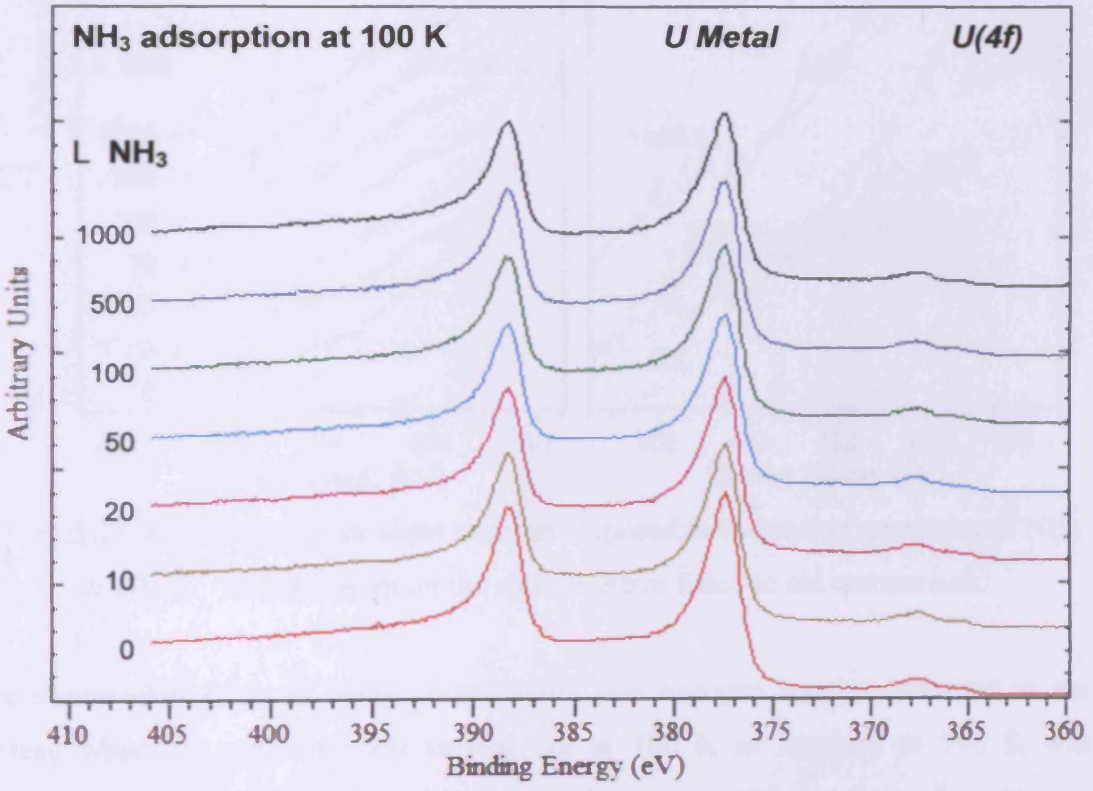

Figure 5.26: U(4f) spectra for clean uranium exposed to increasing quantities of NH_3 at 100 K

Upon exposure to NH_3 only a very minor increase in the N(1s) region was recorded, although it was still possible to identify two separate components. Observation of the

actual specific intensities and positions of the signals was hampered by the poor signal to noise ratio which, whilst not a problem at 298 K, made any accurate quantification difficult at 100 K. The more intense of the components, which was estimated to make up 2/3 of the total signal, was centred at approximately 396.9 eV, and corresponded to the presence of nitride. The less intense of the two components, at approximately 398.7 eV, was due to the presence of NH_2 bound to the uranium surface, as was the case in the experiment carried out at 298 K.

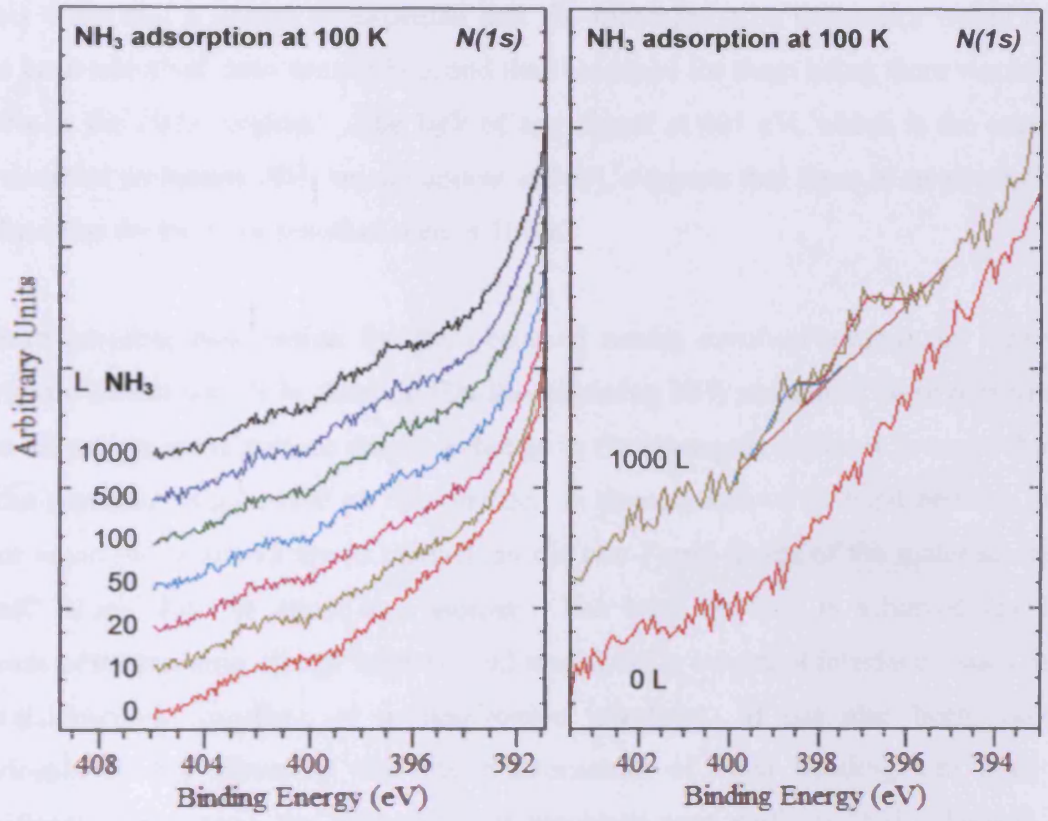

Figure 5.27: N(1s) spectra for clean uranium exposed to increasing quantities of NH_3 at 100 K. The spectrum on the right is curve fitted to aid comparison

The observation of there being considerably less nitrogen species adsorbed at the surface when the exposure was carried out at 100 K as opposed to 298 K was unexpected. The colder temperature would be expected to cause the sticking probability for NH_3 molecular adsorption to increase, resulting in an overall increase in the total number of nitrogen based species upon the surface. One possible explanation for this observation related to the process used to cool down the sample. As it took 30 minutes to fully cool down the sample it is possible that residual O_2 and

H_2O in the vacuum system adsorbed to the surface during this time, thus reducing available sites for the incoming NH_3 molecules. However examination of the O(1s) XPS region (see figure 5.28) revealed only very minor and altogether insignificant increases in the detected signal over the course of the experiment.

A second possible explanation was that it was possible that the colder temperature may have had the unforeseen effect of limiting the dissociation of the incoming NH_3 molecules due to there being a lack of available energy to break the bonds. However if this were true it would be expected that the incoming NH_3 molecules would still have been adsorbed onto the surface, and thus evidence for them being there would be visible in the N(1s) region. The lack of any signal at 401 eV, which is the energy physisorbed molecular NH_3 would appear at [66], suggests that there is an alternative explanation for the poor reaction seen at 100 K.

A third possible explanation for the observed results revolves around the idea of electronic hindrance. It is possible that the incoming NH_3 molecules were prevented from adsorbing at the surface due to a change in the electronic structure brought about by the presence of an oxide on the surface. A process known as band bending can occur when two surfaces are in contact, as the two Fermi levels of the materials will "bend" in an effort to equal one another. The band bending is achieved *via* the process of exchanging charge carriers, and traditionally occurs at interfaces, such as a material/vacuum interface, or a metal/oxide interface. It has also been shown previously in the literature that the phenomenon of band bending can have a significant effect upon the adsorption of reactants onto surfaces [67]. Thus it is indeed possible that on the uranium surface studied band bending took place due to the presence of an oxide on the surface, which in turn led to a decrease in the total quantity of NH_3 based species adsorbed.

However, as the effect only occurred at low temperature it seemed to suggest that a change in the surface species was possibly involved as well. To test this idea the surface was cooled down to 100 K then immediately allowed to naturally warm back up to 298 K. A repeat of the 298 K NH_3 exposure experiment then undertaken produced identical results to those acquired when the exposure was carried out at

100 K. This suggests that a permanent rearrangement of the surface and surface species occurs upon cooling down the surface to 100 K.

So the poor adsorption of NH_3 at 100 K was likely due to the combination of there being residual oxygen on the surface which underwent rearrangement at the cryogenic temperature, and the phenomenon of band bending which also occurred due to the presence of oxygen on the surface.

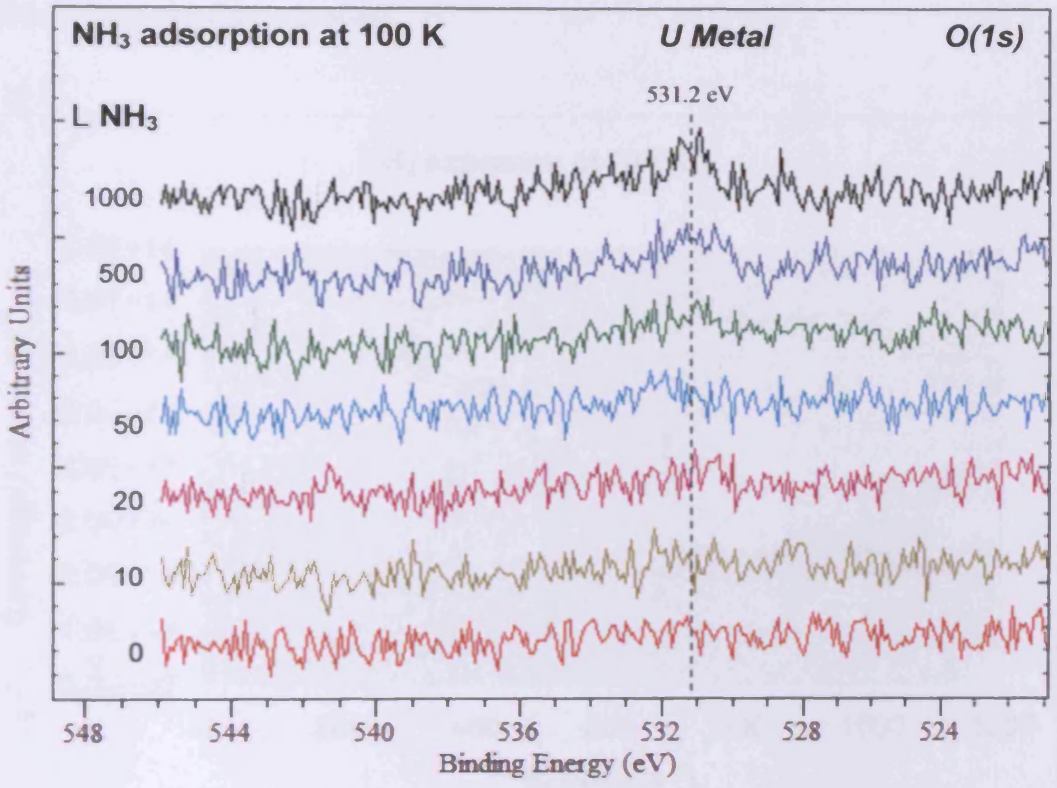

Figure 5.28: O(1s) spectra for clean uranium exposed to increasing quantities of NH_3 at 100 K

Figure 5.29 shows the exposure versus coverage graph acquired for when the NH_3 exposure experiment was repeated at a temperature of 100 K. As in the case of the experiment undertaken at ambient temperature, the results acquired at this colder temperature also showed the same approximate "standard" relationship between the two variables. It is worth noting now that owing to the poor signal to noise ratio in the N(1s) spectra, the accuracy of the area measurements used in the Carley-Roberts equation was potentially low, which resulted in there being a significant potential error associated with the calculated coverage values. This potential error explains

why the calculated values did not follow the "standard" relationship quite as strictly as those calculated from the results acquired at 298 K.

When compared to the XPS results reported above, the graph shows more clearly just how little nitride was actually formed upon the surface when the experiment was repeated at 100 K. After 1000 Langmuirs the calculated coverage was just 7.0 x 10^{14} atoms per cm^2 at 100 K, as opposed to 4.4 x 10^{15} atoms per cm^2 at 298 K. That the surface reached saturation after less than a monolayer had been formed highlights the unusually low coverage observed.

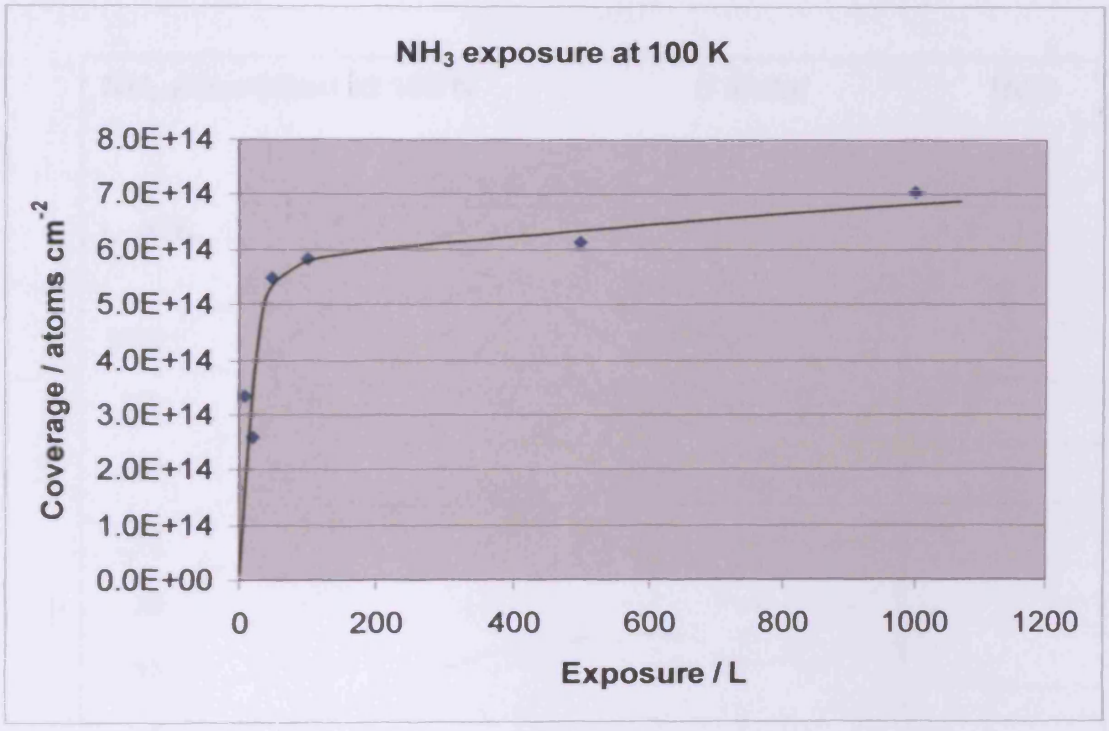

Figure 5.29: Adsorption of ammonia on uranium at 100 K: calculated surface concentration of nitrogen species plotted against exposure to NH_3

Figure 5.30 shows the corresponding He(I) UPS spectra acquired during the cryogenic temperature NH_3 experiments. As UPS is a more surface sensitive technique than XPS, the spectra revealed more visually the effect of the exposure upon the uranium surface.

As in figure 5.24, exposure to NH_3 resulted in a number of different peaks becoming visible in the region. The same two peaks seen at 298 K that corresponded to the $3a_1$

and 1e molecular orbitals of gaseous NH_3 were visible, albeit considerably less intense, and shifted in energy to 4.5 and 10.2 eV respectively. The reason behind the two peaks being shifted in energy, and less intense, was possibly connected to the large signal, visible at 7.3 eV, which also appeared upon exposure to NH_3.

The peak at 7.3 eV was considerably more intense than the corresponding peak at 7.6 eV seen in the spectra acquired at 298 K (see figure 5.24). As this signal was thought to originate from residual oxygen upon the surface, the difference in energy and intensity may be evidence for the surface rearrangement and band bending, proposed above, that contributed to the poor adsorption.

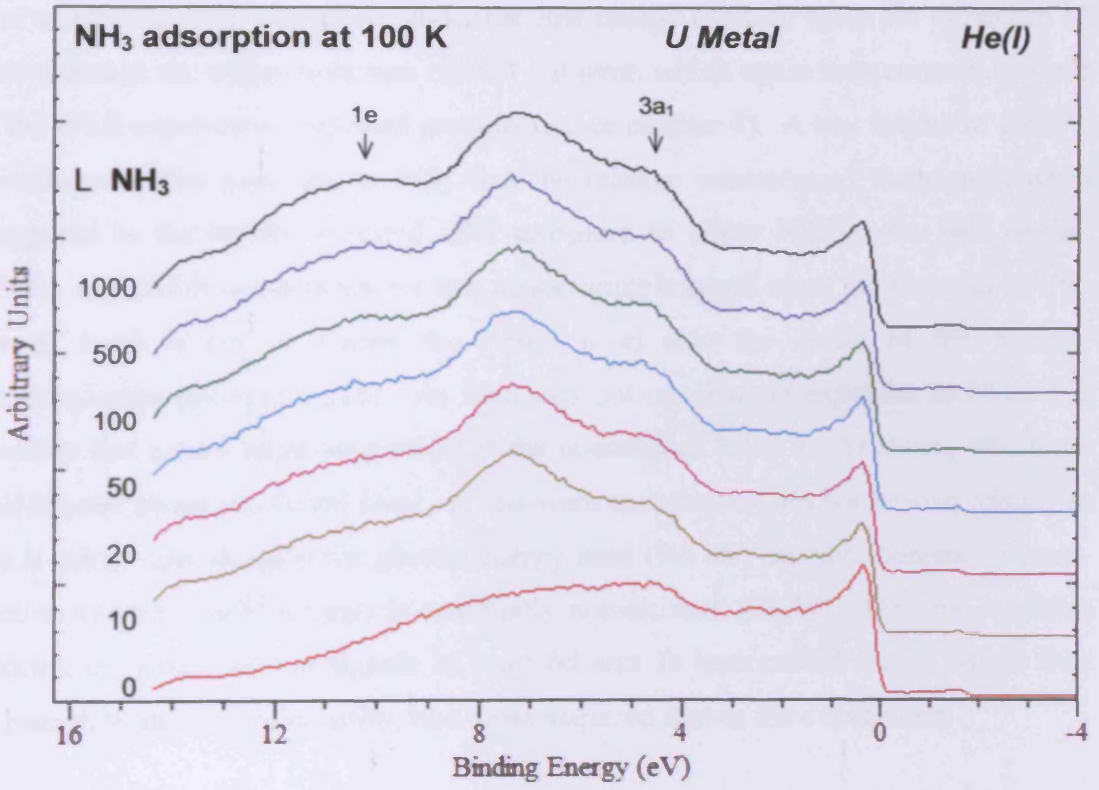

Figure 5.30: He(I) spectra for clean uranium exposed to increasing quantities of NH_3 at 100 K

In addition to the primary features noted above, exposure to NH_3 also led to a noticeable decrease in the intensity seen at the Fermi edge. The decrease was comparable to that seen when the exposure was carried out at 298 K, even though considerably less nitride and NH_2 was adsorbed on the surface. This could be considered more evidence for the ideas of surface rearrangement and band bending, as

these two processes both involve electronic alterations which could alter the observed valence spectra.

5.4.3 Experimental results – IPES

Inverse photoemission experiments examining the exposure of uranium to ammonia were carried out separately from the forward photoemission experiments; however, the same two temperatures were investigated, and all other variables were kept the same.

The IPE spectra of uranium after exposure to NH_3 at 298 K can be seen in figure 5.31. The uranium surface was stable under the low energy electron beam for the entire 12 hour duration the experiment was carried out over, which again is in contrast to some of the IPES experiments reported previously (see chapter 4). A key feature of the IPE spectra seen after exposure to NH_3 was the relative weakness of the signals when compared to the results acquired after exposure to either H_2O or O_2 (see section 5.3.3). A possible explanation for this observation is based upon the fact that in UO_2 the 5f band is moved below the Fermi level into the realm of the forward photoemission techniques [10]. As this does not occur upon exposure to NH_3, it is possible that a very large proportion of the unoccupied DOS are 5f states, which are still located above the Fermi level. If this were true they would not be very visible in the acquired spectra, as at the photon energy used (9.5 eV) the photoionisation cross-section towards the 5f orbitals is essentially non-existent [28,29]. Thus the resulting spectra, composed of the signals of only 6d and 7s unoccupied states, would thus appear to be lacking in intensity, like those acquired during the experiment.

The exposure to NH_3 resulted in there being four distinct signals in the spectra. The largest and broadest signal, that dominated the spectrum, was centred at approximately 5.4 eV. The other definitive signals were all visible as shoulders of the largest peak, at 0.8, 1.7, and 9.1 eV. As stated above, all four signals were largely due to the 6d and 7s unoccupied states.

The final key feature of the spectra to note is that the signal was present all the way to the Fermi edge. This combined with the similar presence of a signal all the way to the

Fermi edge in the UPS spectra (see figure 5.24) confirms and supports the DFT calculations carried out for UN, that suggest it to be a metallic based conductor [68].

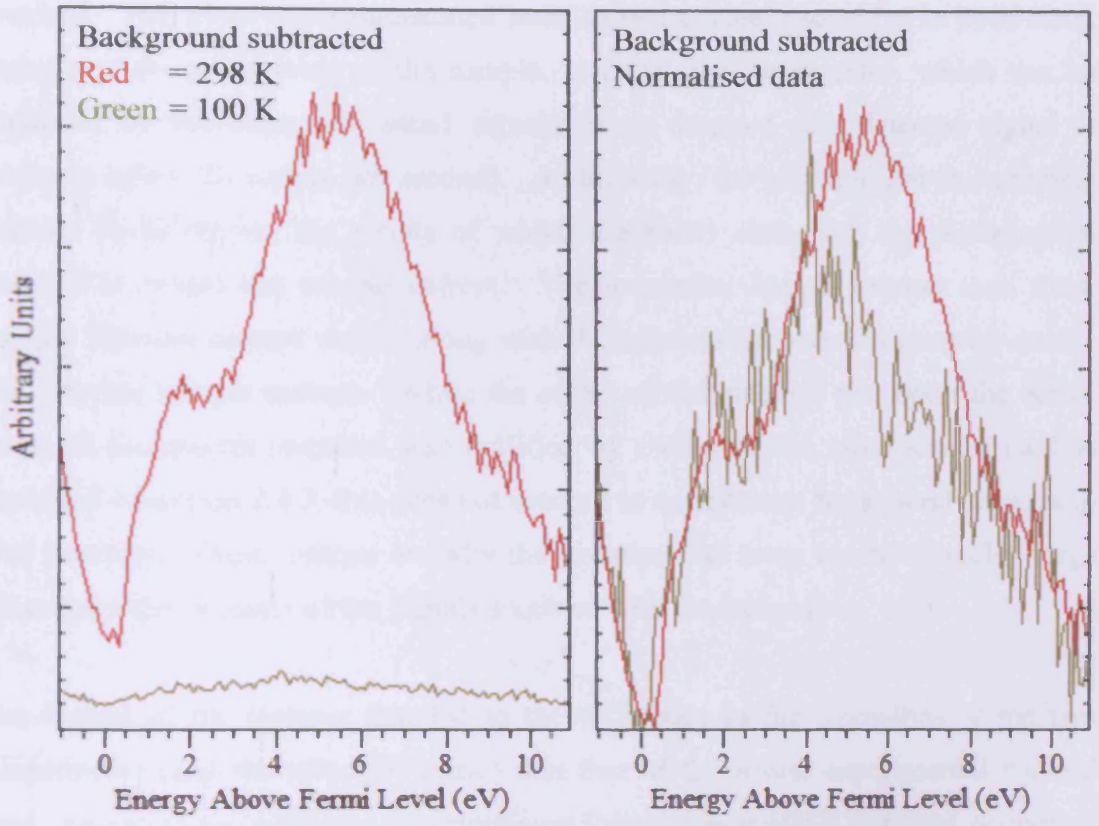

Figure 5.31: IPE spectra for uranium exposed to 500 L of NH_3 at 298 K and 100 K. The left spectra are before normalisation while the right ones after normalisation

IPES measurements of NH_3 adsorption were repeated at 100 K, with the results shown in figure 5.31, along with those acquired at 298 K, for ease of comparison. As with the experiment carried out at 298 K, the low energy electron beam had no effect upon the surface, suggesting the surface species were strongly bound. Even though the XPS results showed that exposure to NH_3 at 100 K had had very little effect upon the surface the IPES technique, like the UPS technique, is more surface sensitive, and thus evidence of the exposure was clearly seen in the acquired spectra.

The first thing noted was the relative lack of intensity of the signal acquired at 100 K compared to at 298 K. The spectra on the left of figure 5.31 are as recorded, while those on the right were subject to normalisation for ease of comparison. The

difference in intensity was due to two distinct features of the experiment, working in tandem. Firstly there was the actual nature of the experimental setup itself, which has previously been noted to often lead to a wide variation in the intensity of the signals acquired. The setup has demonstrated itself to be extremely sensitive to even small changes in the positioning of the sample, electron gun, or detector, which can be explained by the extremely small signals being detected (the detected signal is routinely below 20 counts per second). Additionally, the electron gun is extremely variable in its output, the results of which are easily seen with the picoammeter attached to record the sample current. The maximum sample current seen for a specific filament current varied, along with the relationship between electron energy and detected sample current. While the effect of the electron gun upon the actual shape of the spectra acquired was nullified by means of the modification method explained in section 2.4.3, this does not account or compensate for general changes in total intensity. These reasons are why the experimental setup can have such a large effect upon the intensity of the signals acquired with the technique.

The second of the features that led to the difference in the intensities at the two temperatures (and the principle cause) was that of the actual experimental method used. Owing to the difficulty in maintaining the sample at 100 K for long periods of time the experiment at the colder temperature was conducted for a shorter period of 3 hours, with each separate scan recorded separately. This was in contrast to the experiment at 298 K that was conducted over 12 hours, where groups of five scans were recorded together, with the signals summed together to help compensate for anomalous spikes in the signal which have occasionally been observed. This in turn resulted in the final processed data from the experiment at 298 K, observable in the spectra of figure 5.31, appearing approximately five times more intense than that acquired at 100 K.

The poor signal to noise ratio of the results acquired at 100 K meant it was difficult to accurately define the total number, and position of, the various components visible in the spectrum. The same two peaks at 0.8 and 1.7 eV that were visible in the results of the experiment at 298 K were also present at 100 K, as was the highest energy peak at 9.1 eV. The peak that dominated the spectrum acquired at 298 K, which was located at 5.4 eV, appeared considerably less intense in the results of the 100 K experiment,

and was centred at the lower energy of approximately 4.1 eV. The reason for the difference in this particular signal between the two temperatures is likely connected to the reason given for the poor adsorption of NH_3 species at 100 K. The surface rearrangement of the residual oxide components and the associated band bending would almost certainly have an effect upon the unoccupied DOS.

It is worth noting that as with the results acquired at 298 K, a signal was visible all the way down to the Fermi edge at 100 K, indicating the surface of the sample was still in a metallic conductive form. This indicates that the surface rearrangement and band bending, while powerful effects, did not interfere with the metallic nature of the surface.

5.4.4 Additional discussion

At both 298 K and 100 K the exposure of clean uranium to NH_3 led to the formation of multiple nitrogen species. The binding energies for the U(4f) and N(1s) regions indicated the presence of NH_2 and nitride, in the form of UN, at both temperatures. The lack of any signal relating to NH suggested that it was not a stable species upon the surface, and underwent sudden and immediate loss of the final hydrogen to form the nitride. The proportion of nitride in the N(1s) region was lower at 100 K due to the reduced energy available to split the incoming NH_3.

The coverage against exposure graphs showed the expected multilayer coverage at 298 K, and a "standard" relationship between the two variables for the experiments at both 298 and 100 K. Exposure to NH_3 at 100 K led to a total coverage of only 16 % of that seen at 298 K. The poor coverage was due to residual oxygen upon the surface that underwent rearrangement at 100 K, combined with the electronic hindrance brought about by "band bending". The total surface coverage upon saturation at 298 K was calculated to be equivalent to 4.4 layers, with the majority of that already adsorbed after just 10 Langmuirs, while at 100 K the total coverage seen equated to only 70 % of a single layer.

The surface after 500 Langmuirs at both 298 and 100 K was entirely stable under the low energy electron gun utilised in the IPES technique. The 5f, 6d, and 7s

unoccupied orbitals expanded upwards in energy from the Fermi edge upon reaction with NH_3. The observed spectra at both temperatures lacked overall intensity, indicative that the 5f orbitals were large contributors, as they were not detected well by the technique. A signal remained at the Fermi edge, in both the IPES and He(I) results, which confirmed the conclusion that UN, which is a metallic conductor, was formed upon the surface at both temperatures.

5.5 Miscellaneous adsorption experiments on clean uranium using ammonia, and oxygen

5.5.1 Sequential adsorption of ammonia and oxygen on clean uranium

The sequential adsorption of NH_3 and O_2 at a clean uranium surface was carried out in an effort to understand the oxidation processes occurring. As was mentioned above, exposure to O_2 has been shown many times to quickly oxidise the clean surface of uranium metal, and it was shown in section 5.4 that NH_3 is readily adsorbed onto the surface in the form of nitride and NH_2. If added sequentially the expectation would be that the O_2 would oxidise and remove some or all of the nitrogen containing species from the surface.

The result of exposure of clean uranium to 1000 Langmuirs of NH_3 followed by increasing exposures of O_2 can be seen in figures 5.32 to 5.36. The N(1s) region featured in figure 5.32 firstly showed that NH_3 adsorbed, as previously noted, to form a large nitride peak at 396.8 eV, and a less intense peak at 398.6 eV that corresponded to NH_2. The exposures towards O_2 carried out after this were seen to have a distinct effect upon the signal in the region; however this was complicated by the proximity of the N(1s) region to that of the U(4f). The primary signal visible after exposure to O_2 was a shake-up satellite of the $4f_{5/2}$ oxide peak, and not evidence of nitrogen still being present upon the surface. Through careful peak fitting of the spectra acquired after oxygen exposure a small shoulder at 396.2 eV was revealed, that corresponded to residual nitride on the surface. To confirm the apparent residual nitride species on the surface after exposure to oxygen, the nitrogen Auger peak was followed as well, with the acquired spectra shown in figure 5.33.

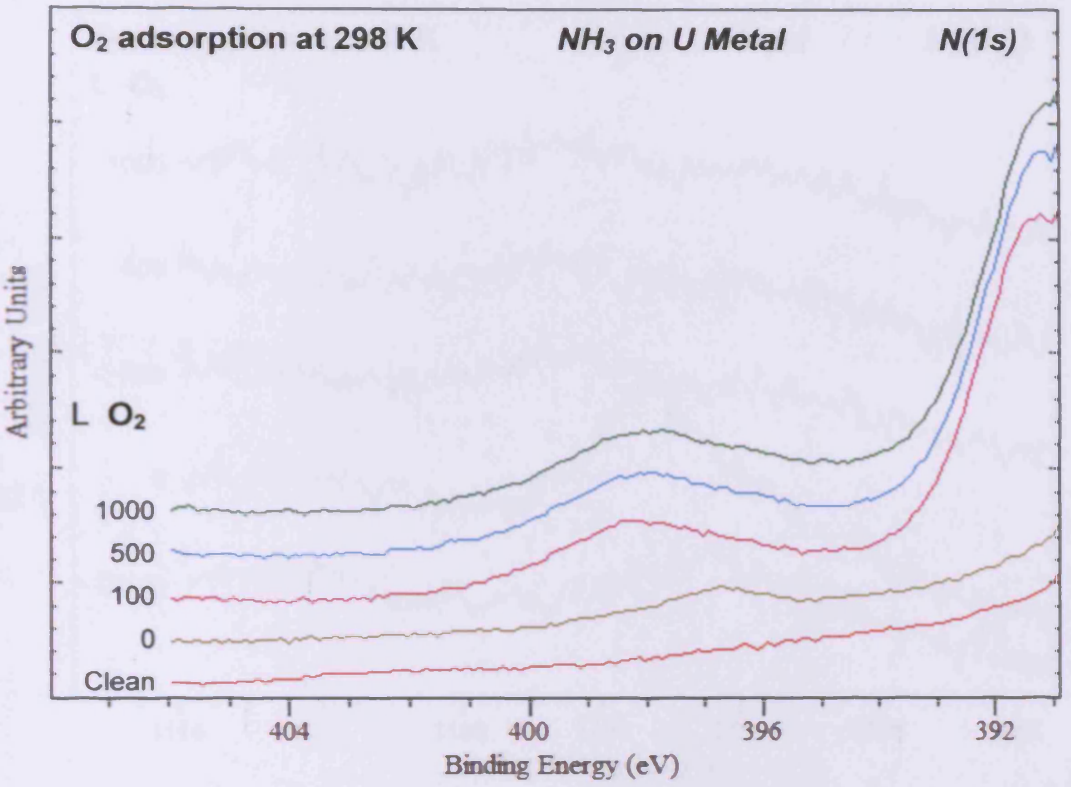

Figure 5.32: N(1s) spectra for the sequential adsorption of NH_3 and O_2 onto clean uranium at 298 K

The single peak at 1102.5 eV following exposure to NH_3 can clearly be seen in the N(KLL) Auger region, replicating the results reported in section 5.4.2. After exposure to oxygen the defined peak was no longer visible; however the spectra acquired did not match that of the clean uranium. This noticeable difference between the spectra appears to support the findings in the N(1s) region, that the oxygen was not capable of oxidising and removing all of the nitrogen species adsorbed to the surface, and that a small quantity of the nitride remained present.

The corresponding O(1s) region after the reaction can be seen in figure 5.34. The exposure towards oxygen led to the appearance of a large signal at 530.8 eV that corresponded to an oxide, and a smaller shoulder at 532.6 eV that corresponded to surface bound hydroxide, as opposed to strongly chemisorbed or interstitial O^- [21,23]. The difference in the intensity of the O(1s) signals after 100, 500 and 1000 Langmuirs was negligible, which agreed with the previous work that has shown the high reactivity of uranium towards pure O_2 [8,21].

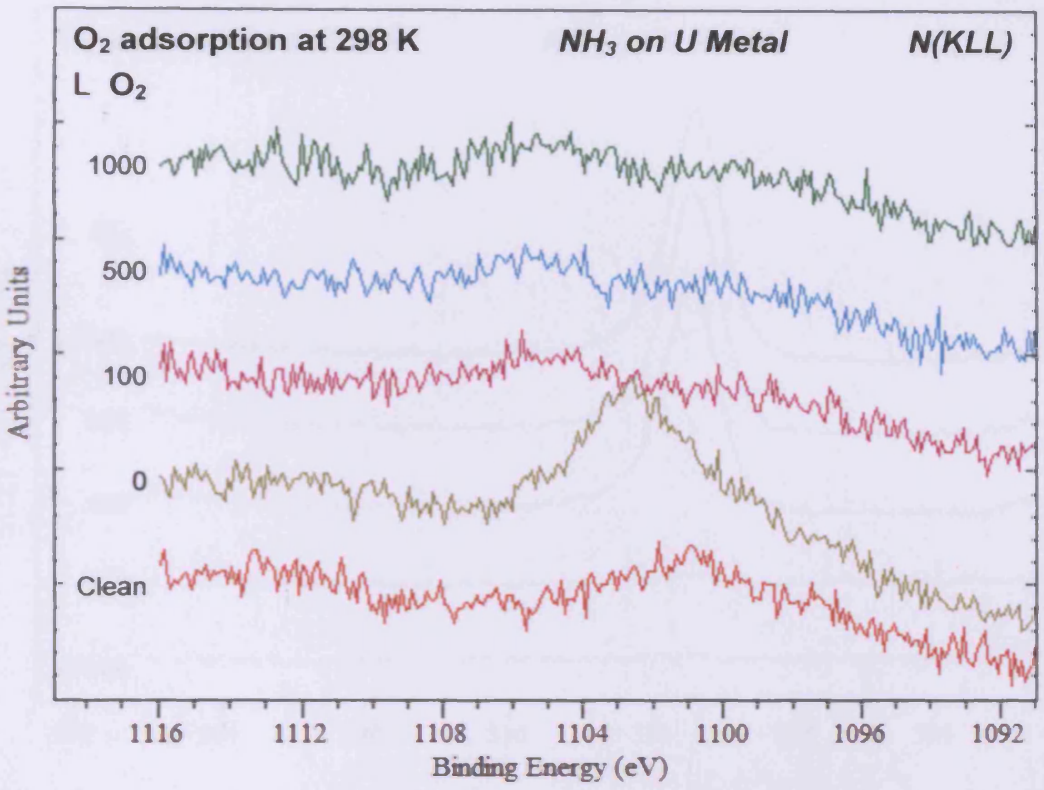

Figure 5.33: N Auger spectra for the sequential adsorption of NH_3 and O_2 onto clean uranium at 298 K

The trends visible in the U(4f) region for the experiment (see figure 5.35) matched those already noted for the N(1s) and O(1s) region. The exposure to NH_3 resulted in the same 0.2 eV increase in energy of the 4f peaks, and widening of the signals, already detailed in section 5.4.2. The large oxide signal visible upon exposure to O_2 underwent negligible change when the exposure was increased from 100 to 1000 Langmuirs. This supports the idea that very little oxygen was required to saturate the surface, and oxidise the maximum possible quantity of the nitride and NH_2 species previously adsorbed onto the surface.

Figure 5.36 features the UPS results acquired for the same sequential exposure experiment, with an additional spectrum from pure UO_2 added for ease of comparison. As expected the exposure to NH_3 led to the same spectrum as those observed in figure 5.24, and the exposure to O_2 oxidised the surface.

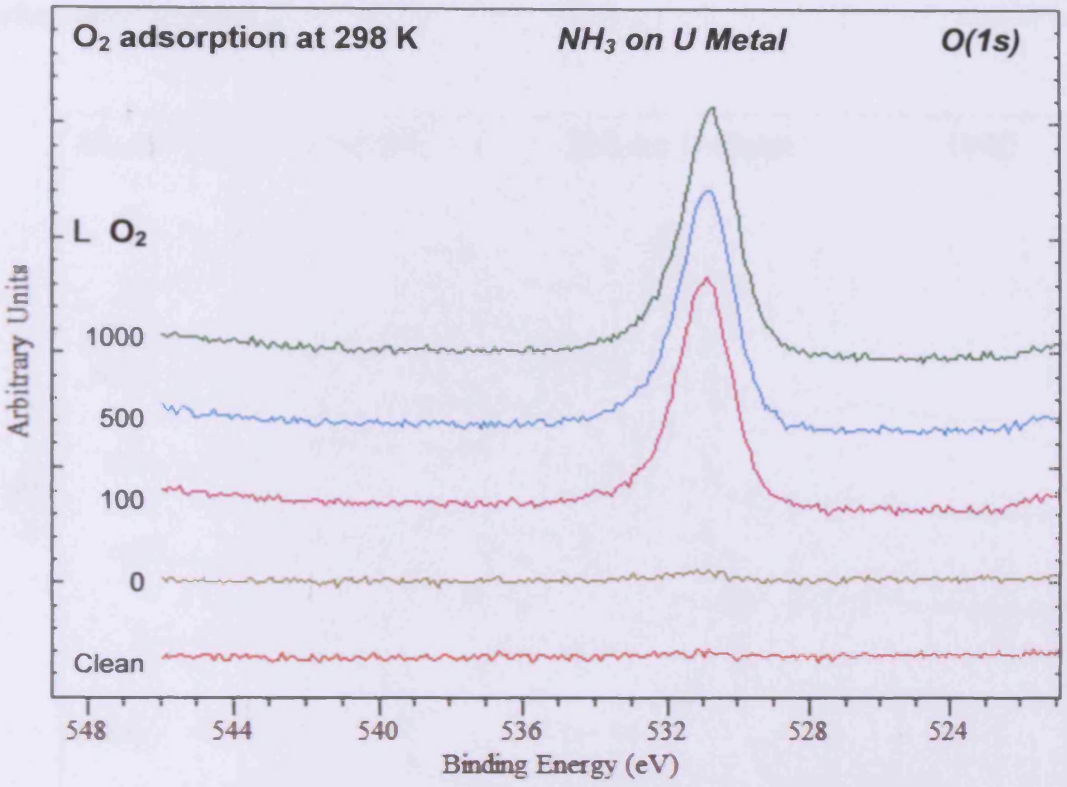

Figure 5.34: O(1s) spectra for the sequential adsorption of NH_3 and O_2 onto clean uranium at 298 K

The more surface sensitive technique of UPS confirmed that the surface was saturated with O_2 after 100 Langmuirs, and that increasing the exposure to 500 Langmuirs had no effect. There was a large disparity in the intensity of the spectra acquired after sequential exposure to both NH_3 and O_2, and that of UO_2 produced *via* exposure to purely O_2. As the experimental method was identical for the acquisition of both spectra, and the difference in intensity so large, it is probable that this was a real effect caused by the presence of the nitrogen species upon the surface. In addition to the variation in intensity, the acquired signals above 9 eV also varied. Upon normalisation of the different spectra at the point of greatest intensity it was seen that the spectra acquired after the sequential exposure featured a rising intensity profile from 9 eV upwards. This was in stark contrast to the spectrum acquired after exposure to purely O_2 which featured a decreasing intensity profile from 9 eV upwards. This distinct contrast again provided evidence of the different surface produced through the sequential adsorption of NH_3 and O_2 when compared to

adsorption of O_2 only, which was due to the continuing presence of nitride upon the surface after oxidation.

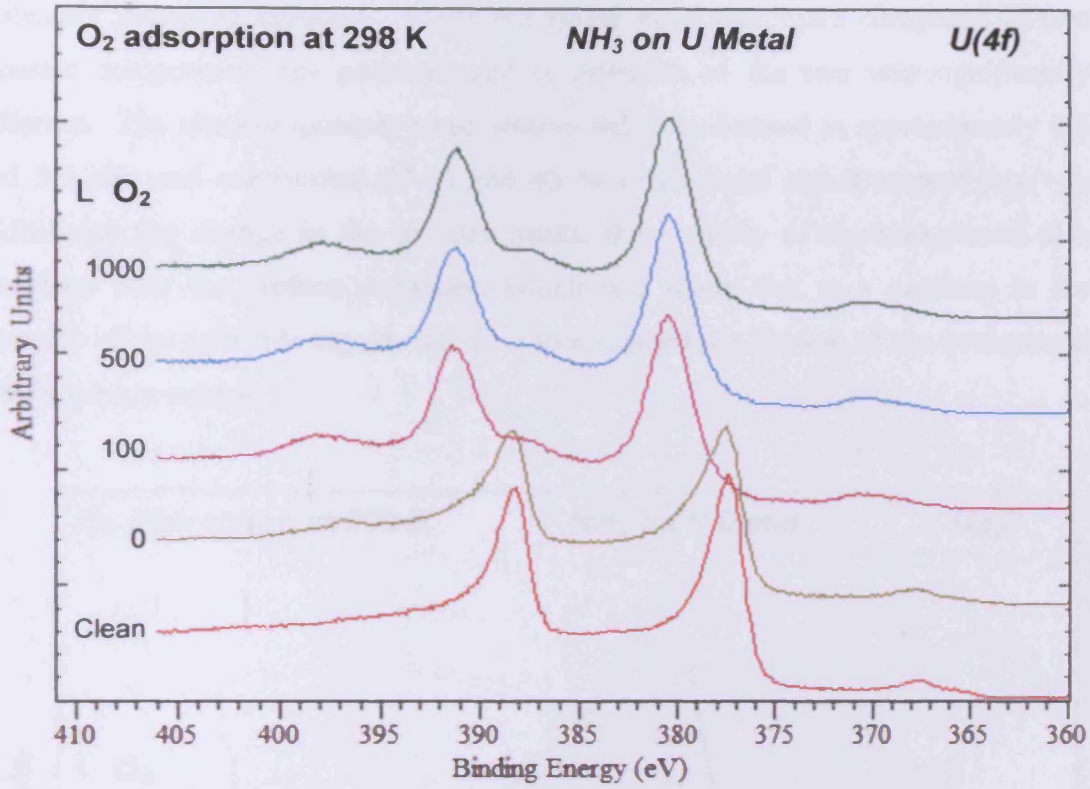

Figure 5.35: U(4f) spectra for the sequential adsorption of NH_3 and O_2 onto clean uranium at 298 K

An additional IPES experiment examining the sequential adsorption of 500 Langmuirs of NH_3 and 500 Langmuirs of O_2 was also carried out, with the results shown in figure 5.37. Unlike with the IPES results acquired after exposure to purely NH_3 or O_2 at 298 K, the surface upon sequential exposure to NH_3 and O_2 was unstable under the low energy electron beam used. The signal initially moved subtly, before stabilising after a total of 40 minutes under the electron beam. After this the surface remained entirely stable for the remainder of the experiment. The spectra acquired during the first 40 minutes, and those acquired during the remaining 680 minutes, are reported separately in figure 5.37, to emphasise the difference brought about by the unstable nature of the surface. The spectrum acquired over the course of the first 40 minutes featured one principle signal superimposed on a steadily increasing background that was likely due to additional unoccupied states that were centred outside the region scanned. The single peak was composed of two distinct

components situated at approximately 3.8 and 5.6 eV, which contributed 15 % and 85 % of the total signal respectively. The spectrum detailing the results acquired after the period of instability was also composed of one principle signal superimposed onto a steadily rising background. While the single peak was again composed of two separate components, the positions and contribution of the two was significantly different. The two components were determined to be located at approximately 4.8 and 5.9 eV, and contributed 57 % and 43 % of the total signal respectively. In addition to the change in the primary peaks, the intensity of the background also increased after the surface stabilised, which was likely due to a decrease in the intensity of the principle signal, which in turn created the illusion of the background growing more intense.

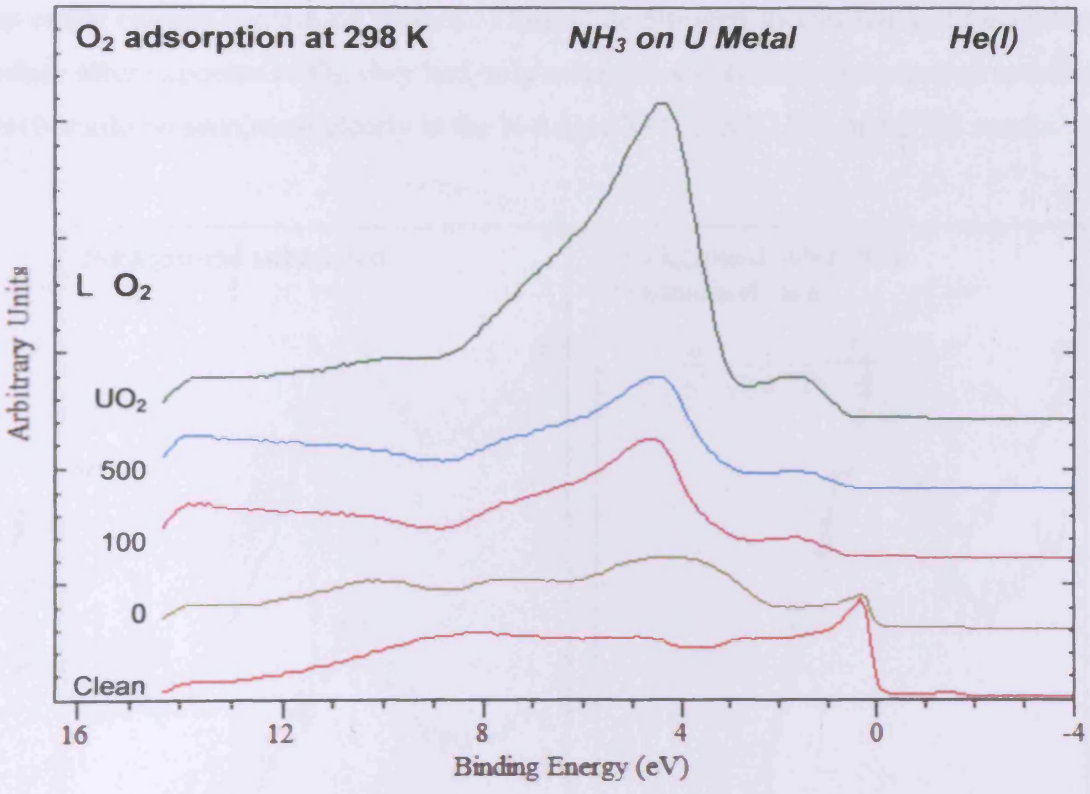

Figure 5.36: He(I) spectra for the sequential adsorption of NH_3 and O_2 onto clean uranium at 298 K

The acquired IPES spectra differed significantly from that acquired when uranium was exposed to purely O_2 (see figure 5.16). While they both contained a single principle signal, the position and relative intensities of the components differed. The components after exposure to purely O_2 were at 3.9 and 5.7 eV, contributing 23 % and

77 % of the total signal respectively. These values are loosely similar to those seen when the surface created from sequential exposure was first scanned (3.8 and 5.6 eV). However the changes brought about by the low energy electron gun caused the components to shift further away from those values (to 4.8 and 5.9 eV), in addition to increasing the intensity of the rising background signal. These two significant ways in which the observed spectra differed from that acquired from uranium exposed to pure O_2 provided evidence for the existence of a different surface environment, caused by the presence of residual nitrogen species which were not removed.

The results acquired from the sequential exposure of uranium to NH_3 and O_2 suggest both that the nitrogen species were difficult to oxidise and remove, and also that their presence had little effect upon the appearance of the U(4f) region when compared to that of the oxygen containing species. Thus while nitrogen species remained upon the surface after exposure to O_2, they had only a very small effect on the acquired spectra, which could be seen most clearly in the N Auger XPS, He(I) UPS, and IPES results.

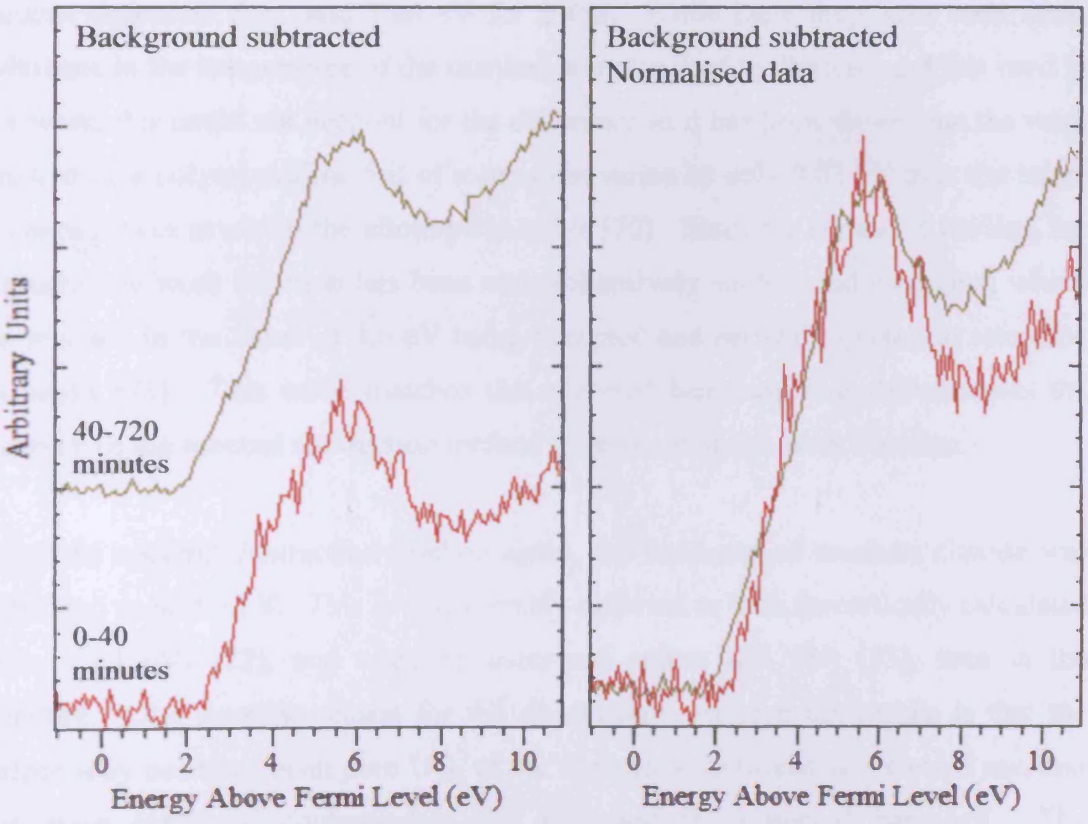

Figure 5.37: IPE spectra for the sequential adsorption of 500 L of NH_3 and 500 L of O_2 onto clean uranium at 298 K

5.5.2 Calculations of the uranium work function and uranium dioxide band-gap

An additional ability of the ultraviolet photoemission setup is the ability to measure and report values for the work function of metals and the band-gap of semi-conductors and insulators. These are both achieved through the application of a bias to the sample, 18 volts in this case, followed by a scan intended to capture the entire spectral width. Subtraction of the entire spectral width from the photon energy used (21.2 eV) results in the work function of a metal or the band-gap of an insulator, depending on what is being scanned.

Figure 5.38 features two UPS spectra that show the entire spectral width of a) uranium metal, and b) uranium dioxide. Using the spectral subtraction method described above, an estimate for the work function of uranium metal of approximately 3.6 eV was calculated. The work function of uranium has been calculated previously but the reliability of many of the measurements was bought into question in a review by Rivière in 1961 [69]. His own experiments produced the values of 3.20 eV for a vacuum deposited film, and 3.08 eV for a foil. While there may have been some difference in the temperature of the uranium samples used by Rivière, and that used in this work, this could not account for the difference as it has been shown that the work function of a polycrystalline foil of α-uranium varies by only 0.02 eV over the range of temperatures at which the allotrope is stable [70]. Since the review of Rivière, the photoelectric work function has been comprehensively studied and measured, which has resulted in the value of 3.6 eV being accepted and regularly quoted in reference textbooks [71]. This value matches that reported here, and thus demonstrates the accuracy of the spectral subtraction method for estimating the work function.

Using the spectral subtraction method again, the band-gap of uranium dioxide was calculated to be 5.6 eV. This is considerably different to both theoretically calculated values (2.3 eV) [72], and optically measured values (2.1 eV) [73], seen in the literature. One possible reason for the discrepancy between the results is that the surface may not have been pure UO_2 at the time the experiment was carried out, and may have contained contaminants that increased the observed band-gap. The accuracy of the value acquired using the spectral subtraction method can be examined through the use of an alternative method to calculate it, utilising the UPS and IPES

results. By combining the distance to the Fermi edge of the UPS signal (0.81 eV) with the distance to the Fermi edge of the IPES signal (1.75 eV) a value for the total band-gap of 2.56 eV was calculated. This value agrees far more with those reported in the literature, while also suggesting that the UO_2 sample used in the spectral subtraction calculation above was likely contaminated and not pure UO_2.

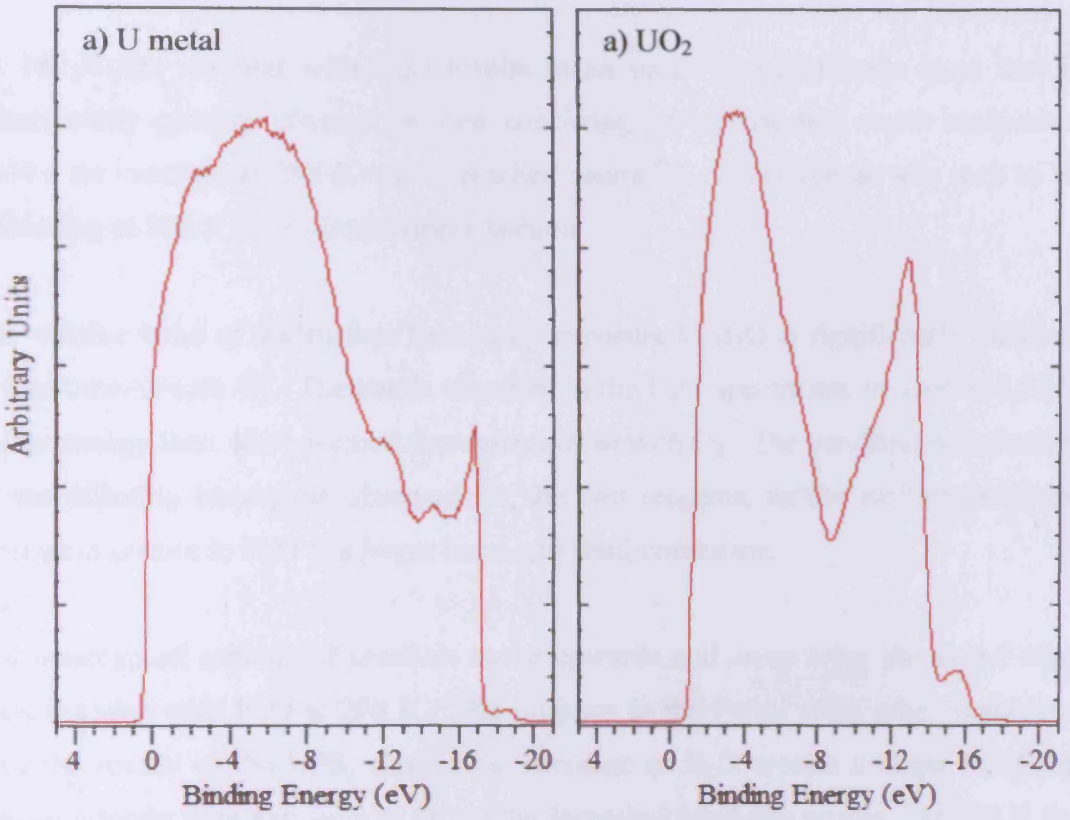

Figure 5.38: UPS spectra taken over the entire spectral width of a) uranium metal and b) uranium dioxide at 298 K

5.6 Conclusions

XPS, UPS, and IPES have been used to examine the reactions of uranium with water, ammonia, and oxygen, at both 298 and 100 K.

The reaction of H_2O with a polycrystalline uranium surface at 298 K results in the formation of a combined oxide and hydroxide layer. The H_2O dissociates upon the surface to form OH^- species, some of which then diffuse to the uranium/oxide interface to react and form the oxide. The reaction is self limiting, and reached

saturation after 1000 Langmuirs exposure, by which time the layer formed had reached a depth of 24 Å. The reaction with H_2O proceeds at a comparable rate to that with O_2, except when the surface is not completely free of contaminants. In the presence of small partial monolayer quantities of oxygen contamination the reaction with H_2O is heavily impaired, resulting in exposures of up to 100 times greater magnitude being needed to match the results seen with O_2.

At 100 K the reaction with H_2O results in an oxide and hydroxide layer that is subsequently quickly covered by one consisting of physisorbed water molecules. Unlike the reaction at 298 K which reached saturation, the coverage was seen to be increasing at 100 K in an almost linear fashion.

The valence band of the surface formed by exposure to H_2O is significantly different to that formed with O_2. The bands observed in the UPS spectra are situated at 1.3 eV higher energy than when formed through reaction with O_2. The variation is indicative of the differing band-gaps observed for the two reagents, as the surface produced through exposure to H_2O is a larger band-gap semi-conductor.

The unoccupied orbitals of uranium move upwards and away from the Fermi edge upon reaction with H_2O at 298 K. The distance to the Fermi edge, when combined with the results of the UPS, shows that exposure to H_2O creates a larger band-gap semi-conductor than exposure to O_2, as the increased band-gap proves. At 100 K the unoccupied orbitals move an additional 2 eV away from the Fermi edge, which can be explained by the presence of significant quantities of solid water on the surface that acts as an insulator, increasing the band-gap.

The reaction of NH_3 with a polycrystalline uranium surface at 298 K results in the formation of a combined nitride and NH_2 layer. The NH_3 dissociates upon the surface to form NH_2 species, some of which then diffuse to the uranium/nitride interface to react and form nitride. The reaction is self limiting, and reached saturation after less than 500 Langmuirs exposure. The reaction appears to proceed at a far faster rate than that of uranium and H_2O, which suggests that the presence of residual oxygen contamination does not impair the reaction, and may in fact increase it.

At 100 K the reaction with NH_3 is extremely impaired through a combination of the residual oxygen on the surface undergoing rearrangement, and electronic hindrance brought about by "band bending". The total impairment was so serious that the coverage was only 16 % of that seen at 298 K.

The unoccupied orbitals of uranium expand upwards in energy from the Fermi edge upon reaction with NH_3 at both 298 and 100 K. A signal always remains present at the Fermi edge, which when combined with the prominent signal at that energy in the occupied valence region, shows the metallic conductive nature of the surface formed upon exposure to NH_3. The addition of NH_2 species on the surface does not interfere with the conductive properties of pure UN.

The surface formed upon exposure to NH_3 is highly vulnerable to the effects of O_2. Exposure to O_2 oxidises the nitride and NH_2 species, resulting in 89 % of them being removed from the surface. The remaining nitrogen species cannot be removed, regardless of the magnitude of the exposure; however their presence does not effect the formation of oxide and hydroxide species upon the surface. The distance to the Fermi edge of the occupied and unoccupied orbitals shows that the surface formed upon sequential exposure to NH_3 then O_2 is a semi-conductor with a band-gap comparable to that produced through exposure to O_2 alone.

5.7 References

1 D. L. Clark, *Los Alamos Science*, 2000, **26**, 364-381.

2 R. C. Albers, *Nature*, 2001, **410**, 759-761.

3 P. Nevitt, *Discovery: The Science & Technology Journal of AWE*, 2005, **11**, 16-25.

4 S. Cotton, Lanthanide and Actinide Chemistry, **2006**, John Wiley & Sons, Ltd: Chichester, p. 1-263.

5 B. W. Veal and D. J. Lam, *Physical Review B*, 1974, **10**, 4902-4908.

6 C. A. Colmenares, *Progress in Solid State Chemistry*, 1975, **9**, 139-239.

7 B. W. Veal, D. J. Lam, H. Diamond and H. R. Hoekstra, *Physical Review B*, 1977, **15**, 2929-2942.

8 S. B. Nornes and R. G. Meisenheimer, *Surface Science*, 1979, **88**, 191-203.

9 Y. Baer and J. K. Lang, *Physical Review B*, 1980, **21**, 2060-2062.

10 P. R. Norton, R. L. Tapping, D. K. Creber and W. J. L. Buyers, *Physical Review B*, 1980, **21**, 2572-2577.

11 W. McLean, C. A. Colmenares, R. L. Smith and G. A. Somorjai, *Physical Review B*, 1982, **25**, 8-24.

12 F. Gerken and J. Schmidtmay, *Journal of Physics F-Metal Physics*, 1983, **13**, 1571-1580.

13 P. Nevitt, "Photoemission Studies of The Light Actinides", *Ph.D. Thesis*, University of Cardiff, **2006**.

14 K. T. Moore, G. van der Laan, M. A. Wall, A. J. Schwartz and R. G. Haire, *Physical Review B*, 2007, **76**, 073105.

15 A. Yahia and L. Maron, *Organometallics*, 2009, **28**, 672-679.

16 K. T. Moore and G. van der Laan, *Reviews of Modern Physics*, 2009, **81**, 235-298.

17 S. Cotton, Lanthanide and Actinide Chemistry, **2006**, John Wiley & Sons, Ltd: Chichester, p. 147.

18 J. C. Fuggle, A. F. Burr, L. M. Watson, D. J. Fabian and W. Lang, *Journal of Physics F-Metal Physics*, 1974, **4**, 335-342.

19 T. Gouder, L. Havela, L. Black, F. Wastin, J. Rebizant, P. Boulet, D. Bouexiere, S. Heathman and M. Idiri, *Journal of Alloys and Compounds*, 2002, **336**, 73-76.

20 A. Kotani and Y. Toyozawa, *Journal of the Physical Society of Japan*, 1974, **37**, 912-919.

21 S. Tull, *Ph.D. Thesis*, University of Cardiff, **2002**.

22 G. C. Allen, I. R. Trickle and P. M. Tucker, *Philosophical Magazine B-Physics of Condensed Matter Statistical Mechanics Electronic Optical and Magnetic Properties*, 1981, **43**, 689-703.

23 K. Winer, C. A. Colmenares, R. L. Smith and F. Wooten, *Surface Science*, 1987, **183**, 67-99.

24 T. Gouder, C. Colmenares, J. R. Naegele and J. Verbist, *Surface Science*, 1990, **235**, 280-286.

25 S. L. Molodtsov, J. Boysen, M. Richter, P. Segovia, C. Laubschat, S. A. Gorovikov, G. V. Prudnikova and V. K. Adamchuk, *Physical Review B*, 1998, **57**, 13241-13245.

26 L. Black, F. Miserque, T. Gouder, L. Havela, J. Rebizant and F. Wastin, *Journal of Alloys and Compounds*, 2001, **315**, 36-41.

27 T. Gouder, J. Naegele, C. A. Colmenares and J. J. Verbist, *Inorganica Chimica Acta*, 1987, **140**, 35-36.

28 J. J. Yeh and I. Lindau, *Atomic Data and Nuclear Data Tables*, 1985, **32**, 1-155.

29 T. Fauster and F. J. Himpsel, *Physical Review B*, 1984, **30**, 1874.

30 P. H. Holloway and E. B. Evans, *Oxidation of Metals*, 1972, **4**, 27.

31 T. Kondo, F. H. Beck and M. G. Fontana, *Corrosion*, 1974, **30**, 330-339.

32 G. C. Allen, P. M. Tucker and R. A. Lewis, *Journal of the Chemical Society-Faraday Transactions Ii*, 1984, **80**, 991-1000.

33 M. Balooch and A. V. Hamza, *Journal of Nuclear Materials*, 1996, **230**, 259-270.

34 W. L. Manner, J. A. Lloyd and M. T. Paffett, *Journal of Nuclear Materials*, 1999, **275**, 37-46.

35 N. Shamir, E. Tiferet, S. Zalkind and M. H. Mintz, *Surface Science*, 2006, **600**, 657-664.

36 E. Tiferet, S. Zalkind, M. H. Mintz, I. Jacob and N. Shamir, *Surface Science*, 2007, **601**, 936-940.

37 G. C. Allen, J. A. Crofts, M. T. Curtis, P. M. Tucker, D. Chadwick and P. J. Hampson, *Journal of the Chemical Society-Dalton Transactions*, 1974, 1296-1301.

38 C. A. Colmenares, *Progress in Solid State Chemistry*, 1984, **15**, 257-364.

39 G. C. Allen and R. K. Wild, *Chemical Physics Letters*, 1972, **15**, 279.

40 G. C. Allen and R. K. Wild, *Journal of the Chemical Society-Dalton Transactions*, 1974, **5**, 493-498.

41 J. Jupille, J. Fusy and P. Pareja, *Surface Science*, 1984, **143**, L433-L438.

42 E. M. Stuve, S. W. Jorgensen and R. J. Madix, *Surface Science*, 1984, **146**, 179-198.

43 G. C. Allen and P. M. Tucker, *Chemical Physics Letters*, 1976, **43**, 254-257.

44 J. J. Pireaux, N. Martensson, R. Didriksson, k. Siegbahn, J. Riga and J. Verbist, *Chemical Physics Letters*, 1977, **46**, 215-219.

45 J. J. Pireaux, E. Thibaut, J. Riga, C. Tenretnoel, R. Caudano and J. J. Verbist, *Chemical Physics*, 1977, **22**, 113-120.

46 N. Beatham, A. F. Orchard and G. Thornton, *Journal of Electron Spectroscopy and Related Phenomena*, 1980, **19**, 205-211.

47 A. F. Carley and M. W. Roberts, *Proceedings of the Royal Society of London Series a-Mathematical Physical and Engineering Sciences*, 1978, **363**, 403-424.

48 W. L. Jorgensen and L. Salem, The Organic Chemist's Book Of Orbitals, **1973**, Academic Press, p. 70.

49 D. W. Turner, Molecular Photoelectron Spectroscopy, **1970**, Wiley-Interscience, p. 77-81.

50 K. Kimura, S. Katsumata, Y. Achiba, T. Yamazaki and S. Iwata, Handbook of HeI Photoelectron Spectra of Fundamental Organic Molecules, **1981**, Japan Scientific Societies Press, p. 33.

51 M. H. Matloob, *Ph.D. Thesis*, University of Bradford, **1978**.

52 M. J. Campbell, J. Liesegang, J. D. Riley and J. G. Jenkin, *Journal of Physics C-Solid State Physics*, 1982, **15**, 2549-2558.

53 S. Van den Berghe, F. Miserque, T. Gouder, B. Gaudreau and M. Verwerft, *Journal of Nuclear Materials*, 2001, **294**, 168-174.

54 J. R. Naegele and J. Ghijsen, Actinides - Chemistry and Physical Properties, in *Structure and Bonding, Vol. 59/60* (Ed.: L. Manes), **1985**, Springer-Verlag: Berlin, p. 244.

55 J. R. Naegele and J. Ghijsen, Actinides - Chemistry and Physical Properties, in *Structure and Bonding, Vol. 59/60* (Ed.: L. Manes), **1985**, Springer-Verlag: Berlin, p. 240-241.

56 M. J. Campbell, J. Liesegang, J. D. Riley, R. C. G. Leckey, J. G. Jenkin and R. T. Poole, *Journal of Electron Spectroscopy and Related Phenomena*, 1979, **15**, 83-90.

57 P. Roussel, P. Morrall and S. J. Tull, *Journal of Nuclear Materials*, 2009, **385**, 53-56.

58 Y. Baer and J. Schoenes, *Solid State Communications*, 1980, **33**, 885-888.

59 T. Nakagawa, H. Matsuoka, M. Sawa, M. Hirota, M. Miyake and M. Katsura, *Journal of Nuclear Materials*, 1997, **247**, 127-130.

60 C. B. Yeamans, G. W. C. Silva, G. S. Cerefice, K. R. Czerwinski, T. Hartmann, A. K. Burrell and A. P. Sattelberger, *Journal of Nuclear Materials*, 2008, **374**, 75-78.

61 G. C. Allen and N. R. Holmes, *Journal of Nuclear Materials*, 1988, **152**, 187-193.

62 J. L. Bischoff, F. Lutz, D. Bolmont and L. Kubler, *Surface Science*, 1991, **248**, L240-L244.

63 W. L. Jorgensen and L. Salem, The Organic Chemist's Book Of Orbitals, **1973**, Academic Press, p. 69.

64 D. W. Turner, Molecular Photoelectron Spectroscopy, **1970**, Wiley-Interscience, p. 356-359.

65 K. Kimura, S. Katsumata, Y. Achiba, T. Yamazaki and S. Iwata, Handbook of HeI Photoelectron Spectra of Fundamental Organic Molecules, **1981**, Japan Scientific Societies Press, p. 42.

66 J. A. Schreifels, J. E. Deffeyes, L. D. Neff and J. M. White, *Journal of Electron Spectroscopy and Related Phenomena*, 1982, **25**, 191-209.

67 C. A. Colmenares and K. Terada, *Journal of Nuclear Materials*, 1975, **58**, 336-356.

68 R. A. Evarestov, M. V. Losev, A. I. Panin, N. S. Mosyagin and A. V. Titov, *Physica Status Solidi B-Basic Solid State Physics*, 2008, **245**, 114-122.

69 J. C. Riviere, *Proceedings of the Physical Society of London*, 1962, **80**, 116-123.

70 C. P. Opeil, R. C. Albers, K. B. Blagoev, M. Gulacsi, J. C. Lashley, P. B. Littlewood, M. E. Manley, B. Mihaila, P. S. Riseborough, R. K. Schulze, D. J. Thoma, H. M. Volz and J. L. Smith, *Journal of the Physical Society of Japan*, 2006, **75**, 56-57.

71 W. F. Gale, C. J. Smithells and T. C. Totemeier, Smithells Metals Reference Book, Eighth ed., **2004**, Elsevier: Bristol, p.

72 H. L. Shi, M. F. Chu and P. Zhang, *Journal of Nuclear Materials*, 2010, **400**, 151-156.

73 J. Schoenes, *Journal of Applied Physics*, 1978, **49**, 1463-1465.

Chapter 6 – Conclusion

6.1 Introduction

This chapter will centre on comparisons between the thorium and uranium results reported in chapters 4 and 5. The reactions with water and ammonia will be discussed, with particular focus on the reactivities of the two metals, and the differences due to the presence of valence 5f electrons in uranium. In addition, this chapter will also detail the preliminary success of inverse photoemission spectroscopy as a technique for the study of the actinides.

6.2 The reaction with water

The adsorption and dissociation of water on the surface of the actinides is a subject that has attracted much attention in the past; however the majority of this has focused upon uranium. While understandable given the technological relevance of the metal, and the complicated nature of the reaction, the difference, when compared to the quantity of work examining the reaction with thorium, is still startling. This study has allowed the re-examination of the thorium and water reaction, utilising both forward and inverse photoemission techniques, with the aim of investigating the influence of the 5f electrons. The effect of the 5f valence electrons will be deduced by comparison with the reaction between water and the surface of uranium.

The first observation from the two experiments is that the reaction with water occurs in a largely similar fashion for both actinide elements. The incoming water dissociates and forms an oxide surface, with additional hydroxide species also present. Figure 6.1 shows the O(1s) region for both elements after saturation had been reached, with the oxide and smaller hydroxide components both clearly visible. Both experiments resulted in the formation of multiple layers of oxide, and both were diffusion limited, with the calculated thickness of the layer being 25 Å for thorium and 24 Å for uranium at saturation.

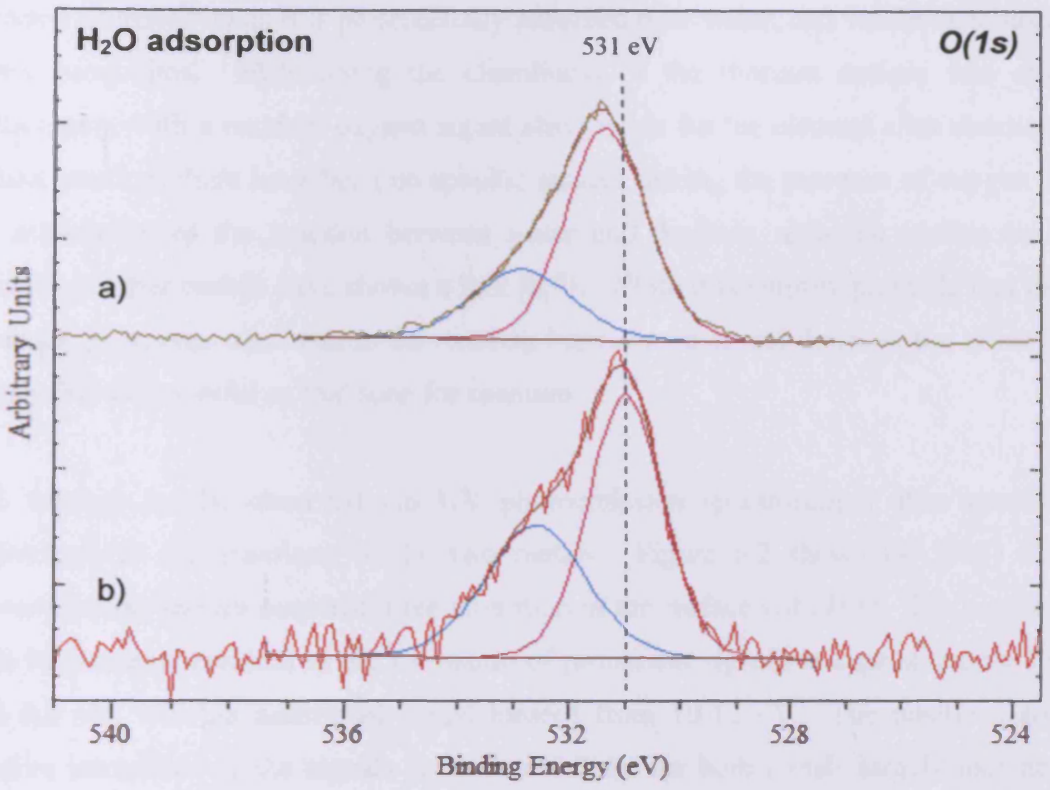

Figure 6.1: O(1s) spectra for a) clean uranium after exposure to 1000 Langmuirs of H_2O, and b) clean thorium after exposure to 100 Langmuirs of H_2O

While there were a great number of similarities between the reactions of thorium and uranium with water, one key way in which they differed was the rate at which the surfaces reached saturation, and how much exposure it required. Saturation of the uranium surface required exposure to approximately five times the quantity of water needed to saturate the thorium surface (500 as opposed to 100 Langmuirs). In addition, the total calculated coverage for the thorium sample was 20 % greater than that for the uranium sample (1.2×10^{16} atoms per cm^2 as opposed to 1.0×10^{16} atoms per cm^2). This feature of the results went against expectation, as it has been previously reported that uranium is more reactive than thorium for the largely analogous reaction with oxygen [1,2]. The most likely explanation for the difference in reaction rates is one related to residual oxygen on the surface of the metals. As explained in chapter 5, the reaction between water and uranium is severely retarded by the presence of any oxygen in the system, either adsorbed to the surface, or in the gas phase [3-7]. It proved extremely difficult to generate and maintain a clean uranium surface, with evidence of trace residual oxygen still present after ion

sputtering. While small, the oxygen component could potentially have led to the decrease in reactivity as it is preferentially adsorbed over water, and would thus block dissociation sites. Maintaining the cleanliness of the thorium surface was also challenging, with a residual oxygen signal also visible for the element after cleaning. Unlike uranium there have been no specific studies linking the presence of oxygen to the retardation of the reaction between water and thorium, although studies on a number of other metals have shown a link [8,9]. While it is entirely probable that the presence of oxygen also retards the reaction between water and thorium, the effect is clearly not as powerful as that seen for uranium.

The valence bands, observed *via* UV photoemission spectroscopy, also revealed differences in the reactions of the two metals. Figure 6.2 shows the He(I) UV photoemission spectra acquired after saturation of the surface with H_2O. The reaction with both metals resulted in the formation of prominent signals at approximately 5.6 and 8.0 eV, with an additional signal located from 10-12 eV. The positions and relative intensities of the signals at 5.6 and 8.0 eV for both metals largely matched those previously reported for the reaction of oxygen [2,10]. Of greatest interest in the valence region was the presence of a signal at 2.3 eV that was only visible in the uranium spectra. This signal was due to the presence of 5f valence electrons partially localised after reaction, and as such was only visible for uranium as thorium has no 5f electrons [11]. The signal was positioned at a significantly higher energy than the 1.4 eV value reported for UO_2 produced through reaction with oxygen [11]. The difference was either due to the large number of hydroxyl groups present after reaction with H_2O, or evidence that the surface formed was not precisely stoichiometric, and may have been substoichiometric UO_{2-x}. The weak nature of the signal itself was due to the use of He(I) as opposed to He(II) as the UV source. The 5f emission is largely suppressed in UV photoemission spectra acquired using He(I) radiation due to a negligible photoionisation cross-section at that energy. He(II) does not suffer from the same photoionisation cross-section issue, and as such UV photoemission spectra of UO_2 utilising that energy have been reported to feature intense sharp peaks at similar energies [11]. It is the presence of this intensity near the Fermi edge that leads to UO_2 being a semi-conductor, while ThO_2, which lacks it, is an insulator.

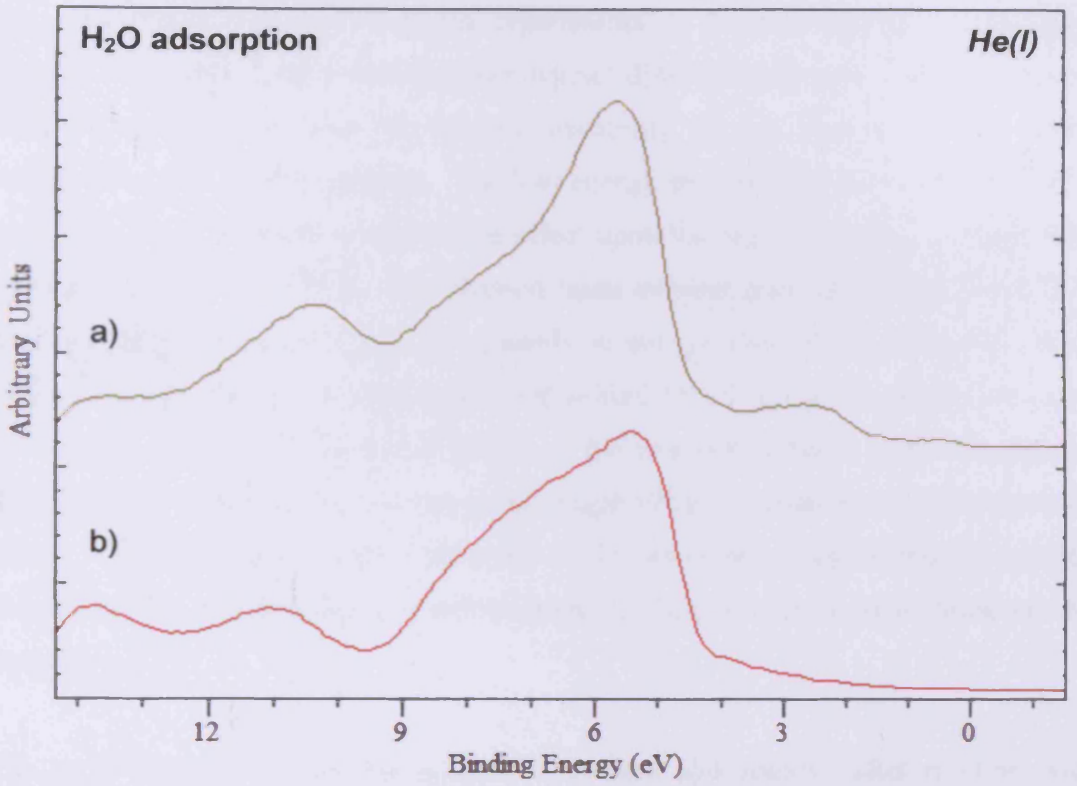

Figure 6.2: He(I) spectra for a) clean uranium after exposure to 1000 Langmuirs of H_2O, and b) clean thorium after exposure to 100 Langmuirs of H_2O

When the experiments were repeated at 100 K the results from the two metals largely matched once again. The O(1s) spectra revealed that the colder temperature led to the accumulation of oxide, hydroxide, and physisorbed water on the surfaces. The signal from the physisorbed water molecules quickly grew to dwarf those of the oxide and hydroxide, as a thick layer of solid ice formed upon the surfaces. The growing layer of ice eventually caused the complete attenuation of the signals from the thorium and uranium metals, indicating that it was at least 50 Å thick (the approximate analysis depth of XPS). As with the experiments undertaken at 298 K, at 100 K the rate of the thorium reaction was considerably faster than that of the uranium reaction. After 75 Langmuirs the coverage of the thorium surface was approximately 3.0×10^{16} atoms per cm^2, while to reach that same coverage of the uranium surface required an exposure of more than 450 Langmuirs. The difference between the reaction rates was smaller than that seen at 298 K; however it remained unexpected, as uranium should be more reactive towards water than thorium. As at 298 K, the difference can again be attributed to residual oxygen on the uranium surface blocking dissociation sites.

The results of the first IPES based experiments on the reactions of thorium and uranium with water also revealed some distinct differences between the two metals. Immediately apparent was the relative instability of the thorium surface when compared to that of the uranium. The low energy electron gun utilised in the IPES technique proved to have a destructive effect upon the thorium surface formed after reaction with water at 298 K. The electron beam incident upon the surface caused the detected signals to gradually shift upwards in energy away from the Fermi edge. After a period of 80 minutes the signals had shifted 1.0 eV to higher energy. This was in complete contrast to the stable nature of the uranium surface, where the signals remained at the same energy for the entire length of the experiment under the electron beam. The differing stabilities observed could potentially suggest that the species present on the oxidised thorium surface were not bound as strongly as those on the uranium surface.

The peaks detected in the IPE spectra of thorium and uranium after reaction with water also differed, however only subtly. Figure 6.3 shows a comparison between the spectra of the two metals, with the thorium result featured being the first acquired, before the low energy electron beam had altered the energy of the detected signal. The spectra from both metals featured a single prominent signal that was composed of two separate components. In both cases this was due to predominantly 6d and 7s unoccupied states, as the energy of the detected photons was 9.5 eV, and at that energy the photoionisation cross-section towards the 5f orbitals is essentially non-existent [12,13]. The signals observed for the two metals were centred at different energies, 5.0 eV for thorium and 4.5 eV for uranium. The lower energy for uranium may be due to the increased nuclear charge of the element when compared to thorium, which would result in the orbitals being held closer, and at lower energy. The uranium spectra also featured intensity that was closer to the Fermi edge than the thorium spectra. This is indicative of the smaller band-gap known to exist for the semi-conducting UO_2, when compared to the insulating ThO_2.

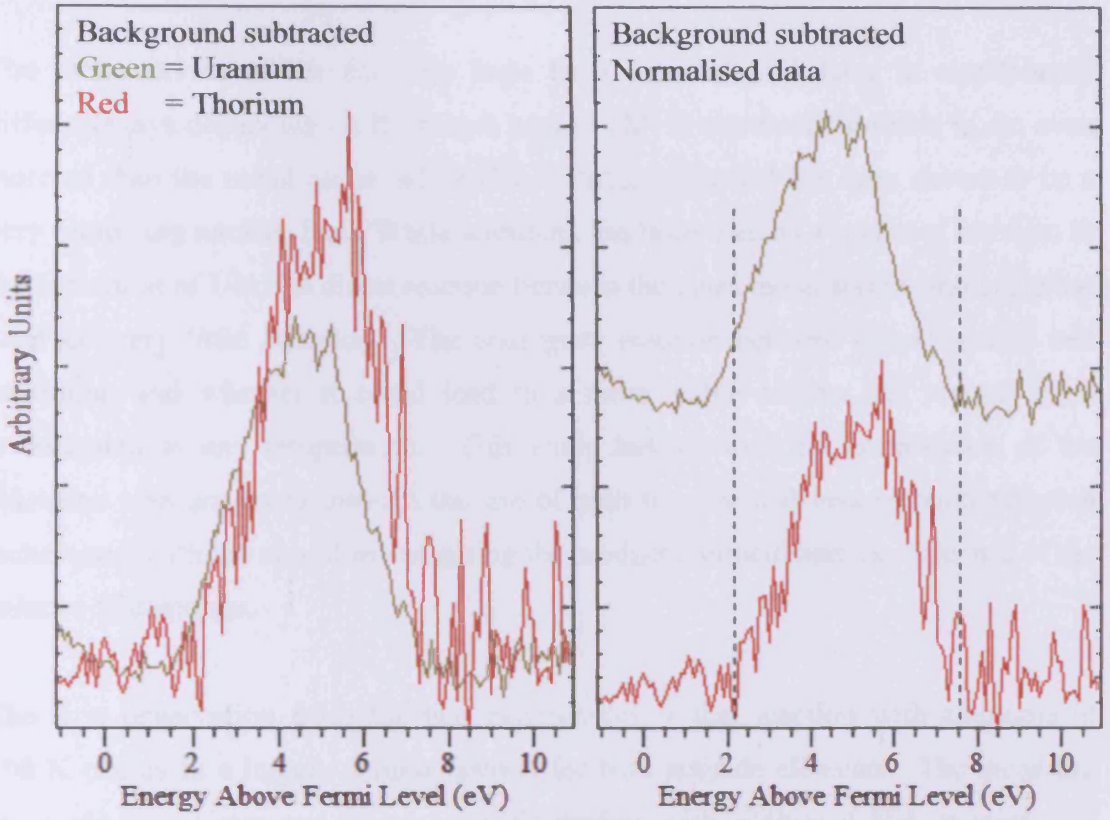

Figure 6.3: Inverse photoemission (IPE) spectra for clean uranium and thorium metal after exposure to 500 Langmuirs of H_2O. The data is presented both before and after normalisation to aid comparison, with vertical lines marking the width of the thorium signal

In summary, the reactions of water with thorium and with uranium occurred in a largely identical manner. Both oxide and hydroxide species were formed on the surface of both metals, with additional physisorbed water present at 100 K. The difference in reaction rates was due to oxygen contamination on the surface hindering dissociation. The most significant difference brought about by uranium possessing valence 5f electrons was the semi-conductor nature of the oxide, compared to the insulating oxide of thorium. Evidence for this was seen in the prominent signal near the Fermi edge in the UV photoemission spectra of uranium, which was lacking in the spectra for thorium.

6.3 The reaction with ammonia

The mononitrides of the actinides have been reported to behave in significantly different ways depending on the bound metal. ThN is extremely unstable in air, even more so than the metal alone, while UN is stable in air and has been shown to be a very promising nuclear fuel. While ammonia has been used as a source of nitrogen in the formation of UN, the direct reaction between the clean metal and the molecule has received very little attention. The analogous reaction between clean thorium and ammonia, and whether it could lead to a more stable nitride, has not yet been investigated at any temperature. This study has allowed the examination of the reactions with ammonia through the use of both forward and inverse photoemission techniques, with the aim of investigating the products formed, and the influence of the valance 5f electrons.

The first observation from the two experiments is that reaction with ammonia at 298 K occurs in a largely similar fashion for both actinide elements. The incoming ammonia dissociates and forms a nitride surface with additional NH_2 species also present. Figure 6.4 shows the background subtracted N(1s) region for both elements after saturation had been reached, with the nitride and smaller NH_2 components both clearly visible. The background was removed due to an overlap of the N(1s) and U(4f) regions, as the signals from the nitride and NH_2 species were both superimposed onto the high energy side of the uranium $4f_{5/2}$ peak. The proportion of the signal due to NH_2 species differed significantly for the two actinide elements, with it contributing 40 % of the signal in the thorium experiment, and 15 % of the signal in the uranium experiment. The difference in proportion was likely connected to the observation that the total calculated coverages of the two metals once saturation had occurred also differed. The coverage of the uranium was estimated to be 4.4×10^{16} atoms per cm^2, which was considerably greater than the 3.5×10^{16} atoms per cm^2 value calculated for thorium. As the mechanism for the multilayer formation of nitride relies upon the NH_2 species diffusing down to the metal/nitride boundary, the majority of the NH_2 present will be on the actual surface, with nitride forming the layers below. The greater coverage calculated for uranium compared to thorium would equate to a greater thickness of nitride below the NH_2 composed surface layer,

therefore a smaller proportion of the measured N(1s) signal would be due to NH_2 species.

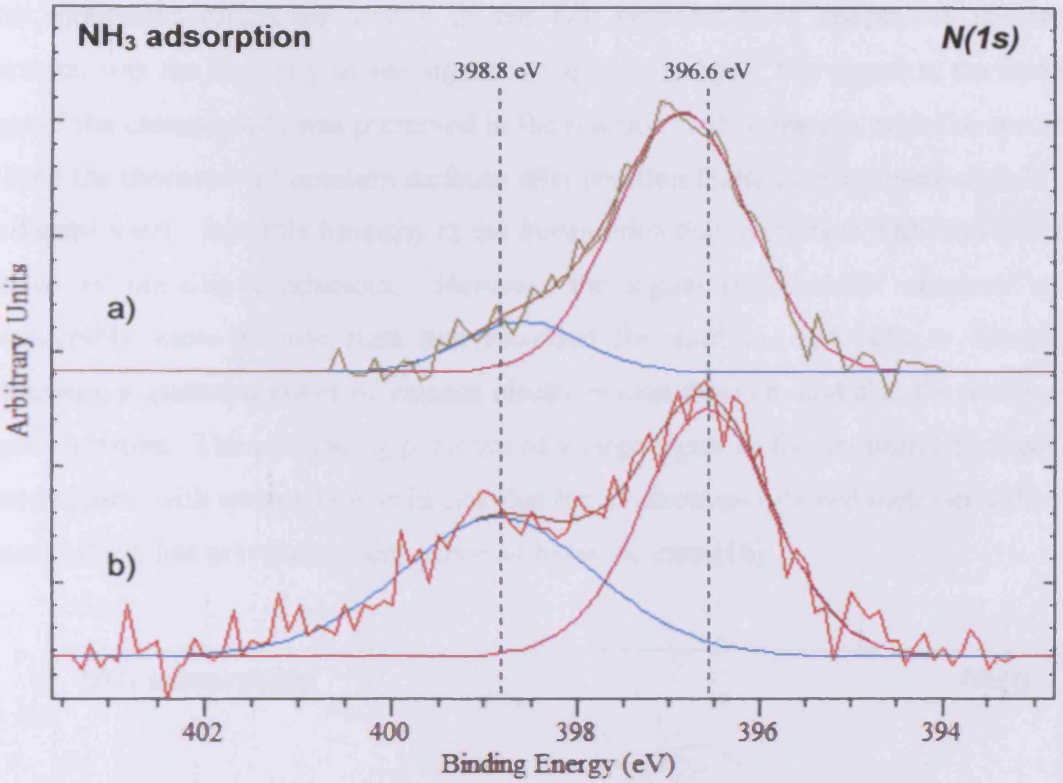

Figure 6.4: Background subtracted N(1s) spectra for a) clean uranium after exposure to 1000 Langmuirs of NH_3, and b) clean thorium after exposure to 500 Langmuirs of NH_3

The valence bands, observed *via* UV photoemission spectroscopy, also revealed differences in the behaviours of the two metals. Figure 6.5 shows the He(I) UV photoemission spectra acquired after saturation of the surfaces at 298 K with NH_3. The reaction with both metals resulted in the formation of prominent signals at approximately 4.5, 7.6, and 10.1 eV. The positions and relative intensities of the signals seen in the spectra of uranium failed to match those previously reported for UN to any significant extent [14-16]. The spectra acquired for thorium also failed to agree with those reported for the mononitride compound in the literature [14]. These disagreements are potentially evidence of the electronic effects of NH_2 species upon the surface, or that the formation of the mononitride, through exposure of the clean

metal to ammonia, has far reaching effects on the electronic structure of the resulting material.

One significant difference visible in the UV photoemission spectra of the two elements was the intensity of the signal at the Fermi edge. The signal at the Fermi edge of the clean metals was preserved in the reaction with ammonia, with the spectra of both the thorium and uranium surfaces after reaction featuring prominent signals at the Fermi level. It is this intensity at the Fermi edge that leads both ThN and UN to behave as metallic conductors. However the signal recorded for uranium was considerably more intense than that recorded for thorium, due both to uranium possessing a greater number of valence electrons than thorium, and also the nature of those electrons. The continuing presence of a large signal at the uranium Fermi edge after reaction with ammonia is evidence that the 5f electrons retained their delocalised nature, which has previously been reported to be the case [16].

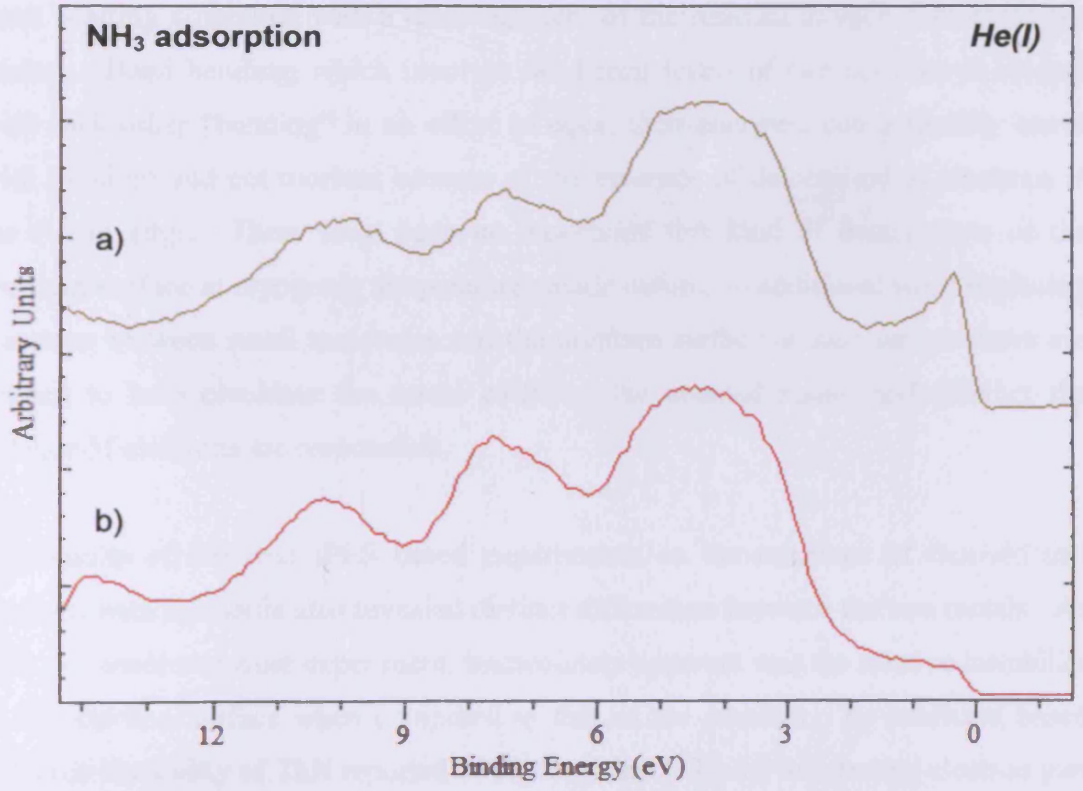

Figure 6.5: He(I) spectra for a) clean uranium after exposure to 1000 Langmuirs of NH_3, and b) clean thorium after exposure to 500 Langmuirs of NH_3

The results featured above demonstrate that both thorium and uranium react in largely identical ways when exposed to ammonia at 298 K. However, when the exposure experiments were repeated at 100 K there was a far more pronounced difference between the reactions of the two metals. The calculated surface coverage for the reaction of thorium with ammonia at 100 K was 3.5 x 10^{16} atoms per cm^2, the same value as that calculated for the experiment at 298 K. What did vary between the two temperatures was the species formed upon the surface. When undertaken at 100 K physisorbed NH_3 was present upon the surface in addition to the nitride and NH_2 already noted to form at 298 K. The reaction of uranium with ammonia at 100 K did not lead to a calculated surface coverage comparable to the value of 4.4 x 10^{16} atoms per cm^2 seen for the experiment at 298 K. The actual coverage was 7.0 x 10^{14} atoms per cm^2 at 100 K, the equivalent of less than 16 % of the coverage value reported at 298 K. Additionally, unlike the reaction with thorium, only nitride and NH_2 were formed, with no evidence for the presence of physisorbed NH_3. The explanation given in chapter 5 for the poor adsorption and dissociation seen at 100 K was one of band bending combined with a rearrangement of the residual oxygen present on the surface. Band bending, which involves the Fermi levels of two surfaces in contact with each other "bending" in an effort to equal their energies, could feasibly occur with uranium and not thorium because of the presence of delocalised 5f electrons at the Fermi edge. There have been no reports of this kind of deactivation of the uranium surface at cryogenic temperatures made before, so additional work exploring reactions between small molecules and the uranium surface at such temperatures are needed to help elucidate the actual cause of the unusual result, and whether the valence 5f electrons are responsible.

The results of the first IPES based experiments on the reactions of thorium and uranium with ammonia also revealed distinct differences between the two metals. As with the water exposure experiment, immediately apparent was the relative instability of the thorium surface when compared to that of the uranium. As predicted based upon the instability of ThN reported in the literature [17], the low energy electron gun proved to have a destructive effect upon the thorium surface formed after reaction with ammonia at 298 K. The electron beam incident upon the surface caused the detected signals to gradually shift upwards in energy away from the Fermi edge. After a period of 600 minutes the signals had shifted 0.7 eV to higher energy, and in

doing so increased their distance from the Fermi level. This was in complete contrast to the stable nature of the uranium surface, where the signals remained at the same energy for the entire length of the experiment under the electron beam. Analysis of the thorium surface after the IPES experiment revealed that exposure to the low energy electron beam also led the nitride signal in the N(1s) region to decrease in energy by 0.6 eV. The altered value of the nitride indicated that Th_3N_4 had been formed, which being non-metallic in nature, also helped explain the increased distance to the Fermi edge in the unoccupied region, observed after exposure to the low energy electrons.

In addition to the differing stabilities of the two surfaces, the peaks detected in the IPE spectra of thorium and uranium after exposure to ammonia also differed in position and shape. Figure 6.6 shows a comparison between the spectra of the two metals, with the thorium result featured being the first acquired, before the low energy electron beam had altered the energy of the detected signal. The spectra from both metals featured a single prominent signal; however in the case of uranium; an additional three smaller signals were visible as shoulders. One of the shoulders, centred at approximately 0.8 eV, led to there being a greater intensity at the Fermi edge when compared to the spectra of thorium. The increased intensity was potentially due to the continuing delocalised nature of the 5f electrons, evidence of which was observed in the UV photoemission spectra. The lack of intensity of the signal, when compared to that seen in the occupied valence region, was due to the photoionisation cross-section towards the 5f orbitals being negligible at the energy detected [12,13].

In summary, the exposure of uranium and thorium to ammonia at 298 K resulted in the formation of nitride and NH_2 species upon their surfaces. The over layer formed on the uranium surface was 25 % thicker than that formed on thorium, with a greater proportion of the total being made up of nitride when compared to the over layer formed on the other metal. At 100 K the reaction between the uranium surface and ammonia was largely inhibited by a combination of oxide contamination, surface rearrangement, and band bending. The corresponding reaction on thorium did not encounter the same issue, with the total surface coverage matching that seen at 298 K. The most significant difference brought about by uranium possessing valence 5f

electrons was the more intense signal seen at the Fermi edge when compared to the valence region of thorium.

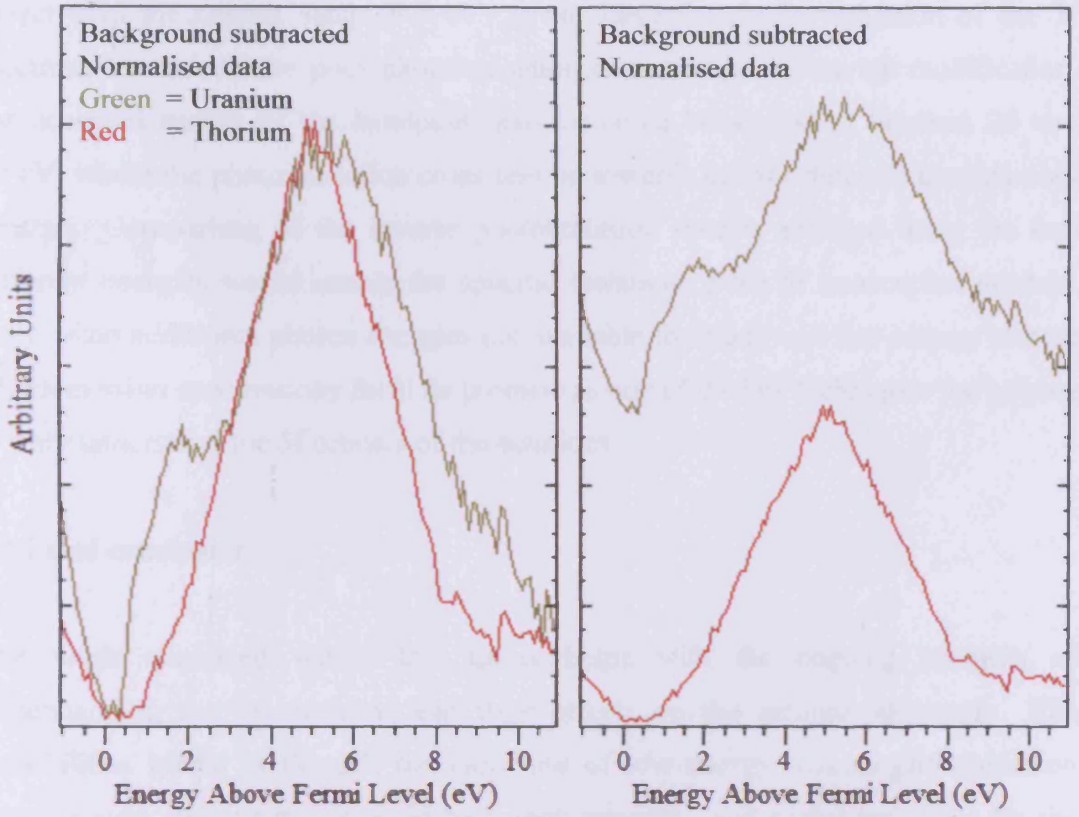

Figure 6.6: Inverse photoemission (IPE) spectra for clean uranium and thorium metal after exposure to 500 Langmuirs of NH_3

6.4 Inverse photoemission as a technique for the study of the actinides

In a review by Moore and van der Laan [18] of the 5f states in actinide metals, it was noted that there is a distinct lack of inverse photoemission studies. Only α-thorium and α-uranium had been studied at the time of writing, through the use of only high energy x-ray inverse photoemission spectroscopy (bremsstrahlung isochromat spectroscopy), as opposed to the low energy UV version of the technique. Moore and van der Laan [18] emphasised the need for additional inverse photoemission spectroscopy data, specifically the "great importance" of studying plutonium with the technique.

The work carried out in this study utilising low energy inverse photoemission spectroscopy to investigate the actinides is therefore amongst the first of its kind; however it is just the beginning of what still needs to be achieved. The energy detected in the current setup (9.5 eV) is not ideal for the investigation of the 5f electrons because of the poor photoionisation cross-section. Through modification, the accepted energy of the bandpass detector could be altered to between 20 and 30 eV, where the photoionisation cross-section towards the 5f orbitals is considerably greater. Comparison of the inverse photoemission spectra acquired using the two different energies would enable the specific isolation of the 5f unoccupied orbitals. Only when additional photon energies are available for study will low energy inverse photoemission spectroscopy fulfil its promise as one of the key techniques for helping to truly understand the 5f orbitals of the actinides.

6.5 Final conclusion

The work contained within this thesis helps with the ongoing problem of understanding the 5f electrons and their effects on the actinide elements. The possibilities hinted at through the early use of low energy inverse photoemission spectroscopy, suggest that it could be a very important and useful technique for the study of the 5f electrons, and as such deserves considerable further study.

6.6 References

1 W. McLean, C. A. Colmenares, R. L. Smith and G. A. Somorjai, *Physical Review B*, 1982, **25**, 8-24.

2 P. Nevitt, "Photoemission Studies of The Light Actinides", *Ph.D. Thesis*, University of Cardiff, **2006**.

3 G. C. Allen, P. M. Tucker and R. A. Lewis, *Journal of the Chemical Society-Faraday Transactions Ii*, 1984, **80**, 991-1000.

4 C. A. Colmenares, *Progress in Solid State Chemistry*, 1984, **15**, 257-364.

5 K. Winer, C. A. Colmenares, R. L. Smith and F. Wooten, *Surface Science*, 1987, **183**, 67-99.

6 E. L. Fuller, N. R. Smyrl, J. B. Condon and M. H. Eager, *Journal of Nuclear Materials*, 1984, **120**, 174-194.

7 M. Balooch and A. V. Hamza, *Journal of Nuclear Materials*, 1996, **230**, 259-270.

8 J. Jupille, J. Fusy and P. Pareja, *Surface Science*, 1984, **143**, L433-L438.

9 E. M. Stuve, S. W. Jorgensen and R. J. Madix, *Surface Science*, 1984, **146**, 179-198.

10 T. Gouder, J. Naegele, C. A. Colmenares and J. J. Verbist, *Inorganica Chimica Acta*, 1987, **140**, 35-36.

11 J. R. Naegele and J. Ghijsen, Actinides - Chemistry and Physical Properties, in *Structure and Bonding, Vol. 59/60* (Ed.: L. Manes), **1985**, Springer-Verlag: Berlin, p. 240-241.

12 T. Fauster and F. J. Himpsel, *Physical Review B*, 1984, **30**, 1874.

13 J. J. Yeh and I. Lindau, *Atomic Data and Nuclear Data Tables*, 1985, **32**, 1-155.

14 P. R. Norton, R. L. Tapping, D. K. Creber and W. J. L. Buyers, *Physical Review B*, 1980, **21**, 2572-2577.

15 G. C. Allen and N. R. Holmes, *Journal of Nuclear Materials*, 1988, **152**, 187-193.

16 L. Black, F. Miserque, T. Gouder, L. Havela, J. Rebizant and F. Wastin, *Journal of Alloys and Compounds*, 2001, **315**, 36-41.

17 T. Gouder, L. Havela, L. Black, F. Wastin, J. Rebizant, P. Boulet, D. Bouexiere, S. Heathman and M. Idiri, *Journal of Alloys and Compounds*, 2002, **336**, 73-76.

18 K. T. Moore and G. van der Laan, *Reviews of Modern Physics*, 2009, **81**, 235-298.